INAUGURAL - DISSERTATION
zur
Erlangung der Doktorwürde
der
Naturwissenschaftlich–Mathematischen
Gesamtfakultät
der
Ruprecht–Karls–Universität
Heidelberg

Draft version March 22, 2011

Vorgelegt von
Dipl.-Phys. Leonard Burtscher
aus Rum

Tag der mündlichen Prüfung: 23. Mai 2011

Mitt-Infrarot-Interferometrie an den Zentren Aktiver Galaxienkerne

Gutacher: Prof. Dr. Klaus Meisenheimer
Prof. Dr. Sebastian Wolf

Zusammenfassung In dieser Arbeit geht es um AGNs.

Summary

Mid-infrared interferometry of AGN cores

DISSERTATION

BY
Leonard Burtscher

Max-Planck-Institut für Astronomie

Heidelberg, April 2011

Contents

1. Mid-infrared interferometry

Interferometry is a wide field reaching from the basics of Fourier optics via the understanding of the atmospheric turbulence and instrument concepts to the intricate details and philosophies of data reduction. In this section I want to briefly present the most important concepts and basics of long-baseline stellar interferometry with a particular emphasis on those ideas that I believe newcomers to the field would like to understand but where the literature is scarce or explanations are inadequate. It is not my aim to present full derivations, but essential concepts and formulae. An excellent introduction to the theory of interferometry has been given by Haniff (2007) and a more general review of optical interferometry can be found in Quirrenbach (2001).

1.1. High resolution observing methods

Even the nearest and brightest AGN tori have apparent sizes of $\lesssim 100$ mas in the mid-infrared. In models, the spectral energy distribution of AGN tori has a broad peak between about 2 and $\gtrsim 100$ μm with the prominent Silicate absorption feature at ≈ 10 μm (e.g. Schartmann et al. 2008).

One might expect it then to be best to use the shortest possible wavelengths to study and resolve tori since the resolving power of optical systems is inversely proportional to λ. However, tori generally are expected to appear larger at longer wavelengths (i.e. they have a radial temperature distribution). There is no simple way to determine the best trade-off between resolving power and size of the torus as its surface brightness depends on intricate details such as the possible clumpy or filamentary structure of the dust.

A number of high-resolution techniques have been devised to reach the diffraction limit of a single telescope, e.g. Speckle Interferometry (Labeyrie 1970; Weigelt 1977; Saha 1999) or Adaptive Optics (attaining the diffraction-limit in the near- and mid-infrared, e.g. Arsenault et al. 2003), or even gain a factor of $\lesssim 2.5$ [1] through Aperture masking (Baldwin et al. 1986; Tuthill et al. 2000, 2010)

Since the FWHM of the PSF of an 8m single-dish telescope in the mid-infrared (≈ 10 μm , see 1.3) is ≈ 300 mas, none of these techniques are sufficient to resolve AGN tori.

In the time-domain: Reverberation mapping An interesting way of probing very small scales in AGNs is a method called Reverberation Mapping (Blandford & McKee 1982; Peterson 1993). In the spectrum of a type 1 AGN there are, among other constituents,

[1] due to the selection of only the highest-spatial-frequency elements in the optical transfer function, see e.g. Hecht (2001)

contributions from the accretion disk very close to the black hole (the optical/UV/X-Ray continuum) and from gas further out in the broad line region (BLR). Variations in the continuum (it is known to be variable in many AGNs) take the lag time τ to reach the radius of the BLR, $R_{\rm BLR} = c\tau$. One can now monitor changes in the continuum and line fluxes and cross correlate the two to get an estimate of the lag time τ. The width of line σ further gives the velocity of the gas at $R_{\rm BLR}$ so that the virial mass of the BH can be estimated to $M_{BH} \approx f R_{\rm BLR}\sigma^2/G$ with the geometric factor f that is unknown.

This method has been applied successfully in a number of bright AGNs to derive black hole masses (Peterson et al. 2004) and even the motion of the nuclear gas (e.g. Bentz et al. 2008). It is an observationally very challenging method, however, since it requires a dense and smooth temporal (and spectral) coverage. So far it was not possible to derive details about the spatial structure of the nuclear gas with this method.

The highest resolutions in the optical–infrared wavelength regime are nowadays achieved using optical long baseline interferometry which is discussed in the next section.

1.2. Interferometry

1.2.1. Historical Notes / Introduction

Ever since Galileo Galilei pioneered the use of a telescope for astronomical purposes in 1609, astronomers have built ever bigger telescopes to gain both sensitivity and resolution. Notable milestones in the quest for the biggest telescope were William Herschel's 40-foot (1.2 m) telescope, built in 1789, the 100-inch (2.5 m) Hooker telescope on Mt. Wilson built in 1917, famous for its use by Edwin Hubble and also for the first stellar interferometer (see below). Further notable milestones of biggest telescopes were the 200-inch (5.1 m) Hale telescope on Mt. Palomar (1949) and the 6.0 m "Big Telescope Alt-Az" (BTA) in Russia (1975). The era of the 8-10 m class telescopes has begun with the 10 m Keck I telescope in 1993.

The sensitivity of a telescope[2] with diameter D increases as D^2, the resolution only increases with D, but it is said that the cost of a telescope roughly scales with D^3.

It is therefore very expensive (and technically challenging) to obtain higher resolution images by building larger telescopes. For sources with sufficiently large surface brightnesses, a number of smaller telescopes, separated by a baseline $B \gg D$ can increase the resolution while still providing sufficient sensitivity, using the principle of interferometry.

Although the principle of stellar interferometry had been suggested by Hippolyte Fizeau already in 1868, Michelson & Pease (1921) were the first to successfully resolve the diameter of Betelgeuse with a 6-meter interferometer in front of the Mt. Wilson 100-inch (2.5 m) telescope. The determined diameter of 47 mas is in good agreement with the

[2] A major factor in the sensitivity calculation used to be the efficiency of the detector. But since CCDs have practically reached 100% efficiency in the visual wavelength regime, further sensitivity enhancements can only be reached by increasing the telescope diameter.

current value (e.g. Ravi et al. 2010). Michelson and Pease's attempts with building a larger interferometer with a baseline of 7 meters did not produce any further significant results and the further development of stellar interferometry was hindered mostly due to sensitivity and construction problems. It effectively came to a halt until it restarted with the development of the "intensity interferometer" (Brown & Twiss 1957).

Nowadays optical stellar interferometers are an integral part of the astronomical research landscape. A non exhaustive list of current stellar interferometers includes the Keck Interferometer (KI Colavita & Wizinowich 2003), the Naval Prototype Optical Interferometer (NPOI Armstrong et al. 1998), the Center for High Angular Resolution Array (CHARA ten Brummelaar et al. 2000), the Cambridge Optical Aperture Synthesis Interferometer (COAST Haniff et al. 2000) and of course the Very Large Telescope Interferometer (VLTI Glindemann et al. 2000b) which I am going to discuss now.

1.2.2. Interferometry basics

A schematic cartoon of a two-telescope interferometer is given in Figure 1.1. The vector connecting the telescopes on the ground is $\vec{B}$. The pointing direction of the two telescopes is given by $\hat{s} = \vec{S}/|\vec{S}|$ where $\vec{S}$ is the vector from the geometrical center of the two telescopes to the distant source, $|\vec{S}| \gg |\vec{B}|$. Unless the telescopes point towards zenith, an optical delay $\hat{s} \cdot \vec{B}$ (the geometric delay) exists between the light rays reaching the two telescopes.

The separation of the two telescopes as seen from a source constitutes the projected baseline vector $\vec{B_p}$. At zenith angle α the length of this vector, the projected baseline length is $\vec{B} \cdot \cos\alpha$. It is often simply referred to as "baseline length". The term "baseline" has therefore at least three meanings: (1) The ground separation vector combining the two telescopes in question, the vector quantity $\vec{B}$, (2) the projection of this as seen from the source, the projected baseline length (a scalar), and also (3) the name of the interferometer made up of the two telescopes (as in "the UT2–UT4 baseline"). In the following "baseline" stands for (2), the projected baseline, unless specific telescope names are given when it stands for (3), the interferometer made up of the two telescopes. $\vec{B}$ will be referred to as the "ground separation vector".

At the basis of optical long-baseline interferometry is an important identity between the normalized source brightness distribution $I(\alpha, \beta)$, that we would like to observe, and the so-called spatial coherence function or normalized complex visibility $V(u_\lambda, v_\lambda)$, that an interferometer measures. (α, β) are co-ordinates on the sky, parallel to (RA, DEC) and measured in radian. (u_λ, v_λ) are the reciprocal co-ordinates to (α, β), pointing in the same direction ($u_\lambda \parallel$ RA and $v_\lambda \parallel$ DEC). They are *spatial frequencies* and given in fringe cycles / rad. At a given wavelength λ they make up the projected baseline vector:

$$\begin{pmatrix} u_\lambda \\ v_\lambda \end{pmatrix} = \frac{\vec{B_p}}{\lambda} = \frac{1}{\lambda} \cdot \begin{pmatrix} u \\ v \end{pmatrix} \tag{1.1}$$

The normalization of the source brightness distribution is in the sense that $1 = \int_\alpha \int_\beta I(\alpha, \beta)\, \mathrm{d}\alpha\, \mathrm{d}\beta$.

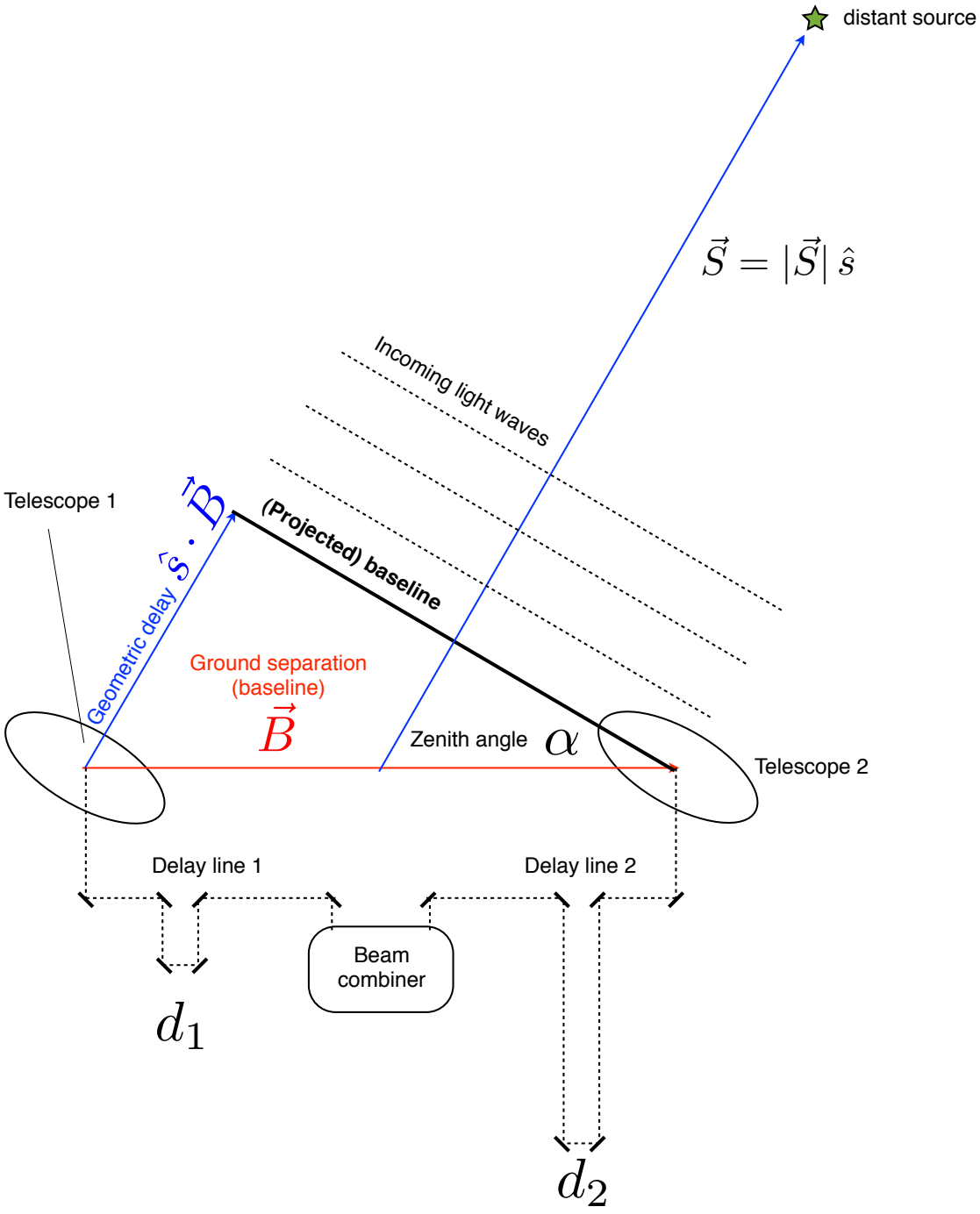

Figure 1.1.: Schematic cartoon of a two-telescope interferometer, see text for explanations.

The visibilities $V(u_\lambda, v_\lambda)$ are normalized in the sense that $V(0,0) = 1$.

The van Cittert Zernike theorem states that the two are related through a Fourier transform:

$$V(u_\lambda, v_\lambda) = \int_\alpha \int_\beta \mathrm{d}\alpha \, \mathrm{d}\beta I(\alpha, \beta) \exp(-\imath 2\pi(u_\lambda \alpha + v_\lambda \beta)) \tag{1.2}$$

Delay lines act to relay the light from the two telescopes to a beam combiner and to introduce the extra delays d_1 and d_2 respectively in order to correct for the geometric delay (see Figure 1.1).

In stellar interferometers, beam combination is either performed in the image plane ("Fizeau interferometer") or on parallel beams. The latter is called a Michelson interferometer. Such an interferometer may be combined with fringe *detection* in the image plane (such as done in MIDI at the VLTI).

In any case, the electric fields of the incoming waves collected at telescopes 1 and 2 with frequency $\omega/(2\pi)$ at beam combiner are given at time t by:

$$\Psi_1 = A \exp(\imath k[\hat{s} \cdot \vec{B} + d_1]) \exp(\imath \omega t)$$

$$\Psi_2 = A \exp(\imath k[d_2]) \exp(\imath \omega t)$$

where A is proportional to the collecting area of the telescopes (assumed to be equal) and $k = 2\pi/\lambda$.

After beam combination, the detected intensity is

$$I = \langle |\Psi_1 + \Psi_2|^2 \rangle \propto 2 + 2\cos(k[\hat{s} \cdot \vec{B} + d_1 - d_2]) \propto 2 + 2\cos(kD)$$

where $\langle \cdot \rangle$ denotes the time average and the optical path difference (OPD) has been set to $D = \hat{s} \cdot \vec{B} + d_1 - d_2$.

This co-sinusoidal variation of intensity as a function of D is the essential observable of an interferometer. More precisely, from the fringe pattern, the fringe amplitude and the phase offset at zero OPD can be obtained (see Figure 1.2). The fringe amplitude defines the Michelson visibility

$$V_{\mathrm{Michelson}} = \frac{I_{\max} - I_{\min}}{I_{\max} + I_{\min}} \tag{1.3}$$

The crucial point here is that the Michelson visibility and the phase offset directly measure the amplitude and phase of the normalized complex visibility V.

In practice, however, D has the additional term D_{atm} that is introduced by the atmosphere and that irrecoverably scrambles the phase information in a two-telescope interferometer[3].

[3]So called dual-beam interferometers try to 'lock' the phase of the target on a nearby reference star and can thus measure the visibility phase of the target. An example of such an instrument is PRIMA at the VLTI that is currently under commissioning.

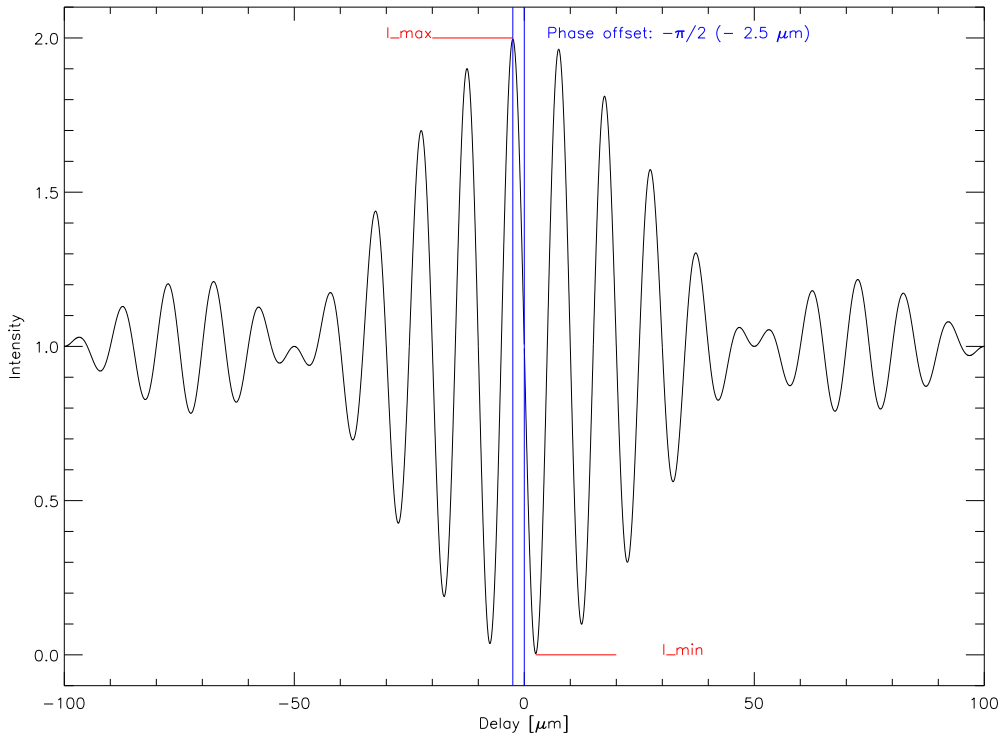

Figure 1.2.: Resulting fringe pattern for a polychromatic source with a finite bandwidth detector. In this case the Visibility amplitude is 1 and the phase offset is $-\pi/2$, corresponding to a delay offset of 2.5 μm at $\lambda_0 = 10$ μm. The resolution $R \equiv \lambda_0/\Delta\lambda = 5$, leading to a coherence length $\Lambda_{\rm coh}$ of 50 μm, easily recognizable by the first null of the sinc function.

So far we have implicitly assumed that our detector is monochromatic, leading to a fringe contrast $V_{\rm Michelson}$ that is independent of D. In reality, detectors (and the atmosphere) have a finite bandpass $\Delta\lambda$ at λ_0 leading to a modulation of the fringes by a sinc function called the "coherence envelope":

$$\begin{aligned} I' &= \int_{\lambda_0-\Delta\lambda/2}^{\lambda_0+\Delta\lambda/2} 2[1+\cos(2\pi D/\lambda)]\mathrm{d}\lambda \\ &\propto \Delta\lambda\left[1+\frac{\sin(\pi D\Delta\lambda/\lambda_0^2)}{\pi D\Delta\lambda/\lambda_0^2}\cos(k_0 D)\right] \\ &\propto \Delta\lambda\left[1+\frac{\sin(\pi D/\Lambda_{\rm coh})}{\pi D/\Lambda_{\rm coh}}\cos(k_0 D)\right] \end{aligned}$$

where we have introduced the coherence length $\Lambda_{\rm coh} = \lambda_0^2/\Delta\lambda$. See Haniff (2007) for a derivation.

This explains why delay lines are required at all: Due to the attenuation by the coherence envelope the optical path difference between the two telescopes D must be $\ll \Lambda_{\rm coh}$[4].

In order to recover the source brightness distribution $I(\alpha, \delta)$, one could imagine to simply invert Equation 1.2, given the measured values of $V(u, v)$. This is indeed done in radio interferometry (Högbom 1974; Cornwell 2009).

In our case this is, unfortunately, not practical for two reasons: (1) In a two-telescope interferometer (without phase-referencing) only the amplitude of the complex visibility is measured[5] and (2) since we will typically only be able to sample the visibility function at a few well selected (u, v) co-ordinates, the visibility function is not well defined.

Since inverting is not possible, the visibilities need to be modeled (see below, Section 1.2.5).

Heterodyne vs. direct interferometry The reader familiar with radio interferometry may wonder why optical interferometrists make these huge efforts (see Section 1.4) to directly interfere the light from the two telescopes while in radio interferometry a technically much easier solution is used. In radio interferometry, the single-dish signal is mixed with a so called "local oscillator" (e.g. a maser source) of similar frequency as the signal frequency so that the latter is converted into the lower beat frequency which can be easily amplified and recorded. The recorded signals are later transferred to a correlator (a fast computer) and brought to interference there. The obvious advantage of this technique, called *heterodyne interferometry* is that no "delay lines" need to be built and the baselines between the telescopes can therefore be very large as long as accurate clocks are available to relate the various recorded signals to each other. Additionally, the sensitivity improves with number of telescopes (often called antennae) added to the array.

In direct detection, on the other hand, complicated delay lines and beam-combiners have to be built to bring the light from two or more telescopes to interference. Also, the signal is diluted when adding more telescopes to the array.

However, it is not much a matter of choice which type of interferometry one prefers, but fundamental physics sets the advantage of heterodyne vs. direct detection signal/noise rate (SNR). The Heisenberg principle, in the form $\Delta N \cdot \Delta\phi \leq 1$ (radian), states that the precision with which we can measure the phase of a photon is inversely proportional to the number of photons used for that measurement. But the number of photons in one oscillator mode is given by Bose statistics as $(\exp(h\nu/(kT)) - 1)^{-1}$ where T is the temperature characteristic of the received radiation. In the radio it is the so called 'antenna temperature' (usually in the range of 10-100 K) and in the mid-IR it is given by the atmosphere (that is the dominant noise source), i.e. $T \approx 300$ K. That makes $(\exp(h\nu/(kT)) - 1)^{-1}$ to be of order 10^3 at 1.4 GHz but only 10^{-3} at 10 μm and it is immediately clear that measuring the phase in the mid-IR at both telescopes individually is impossible.

The two techniques have roughly the same SNR at ≈ 100 μm; at 10 μm, direction detection provides already a ten times larger SNR over heterodyne detection and at 2 μm the advantage is $> 10^3$. See Townes (2000) for a detailed account of noise and sensitivity in interferometry.

Heterodyne detection of fringes in the mid-IR has been successfully used in a scientific instrument (ISI, Bester et al. 1990) but has been limited to the observation of very bright objects ($\gtrsim 100$ Jy). All current

[4]The reason why *both* beams have to pass a delay line is that this is the easiest way to control for polarization equality. Only equally polarized rays interfere.

[5]Actually Fienup (1978) has shown that it is possible to reconstruct an image given only the amplitude of the visibility – but in *every* point.

infrared interferometers use direct detection.

1.2.3. Spatial resolution of an interferometer

For a single-dish telescope, the Rayleigh criterion describes two point sources of light as resolved if the center of one source's Airy disk falls onto the first minimum of the other. This leads to the well known formula for the minimum angle between two resolved sources $\Theta_{\mathrm{min}} = 1.22\lambda/D$ for a telescope with aperture diameter D.

In an interferometer, the angle between crests of the fringe pattern, the so-called fringe spacing, is $\Theta_{\mathrm{fringe}} = \lambda/BL$. Applying Rayleigh's criterion to an interferometer therefore leads to $\Theta_{\mathrm{min}} = \lambda/2BL$.

More than in the single-telescope case, though, the resolution of an interferometer depends not only on λ and D or BL, but also on the signal to noise ratio of the observation. In the single telescope case, features slightly smaller than $1.22\lambda/D$ can be discriminated if the signal to noise ratio is high (and the PSF of the telescope known). In an interferometer, a source is considered to be "partially resolved" as soon as the visibility is measured to be < 1 which of course depends on the signal/noise of the observation. For realistic signal/noise values the visibility will deviate from 1 for source sizes $\ll \lambda/2BL$.

Models can therefore be discriminated at resolutions $\ll \lambda/2BL$ and in this work the sensitivity to model parameters is assumed to be $\approx \lambda/3BL$ and will be called "resolution of the interferometer" henceforth. There is some ambiguity in this definition of resolution but it seems to be widely adopted by interferometrists (W. Jaffe, pers. comm.) and it serves our purpose. To put it in Lord Rayleigh's words: "The rule is convenient on account of its simplicity and it is sufficiently accurate in view of the necessary uncertainty as to what exactly is meant by resolution."

1.2.4. The (u, v) plane

The (u, v) co-ordinates, i.e. the components of the projected baseline vector, span the (u, v) plane (or "Fourier plane") that is best imagined as the aperture of the (huge) telescope that will be synthesized by the interferometer observations. It is used to mark the (u, v) co-ordinates of observations and serves to to quickly get an overview about the observed (projected) baseline lengths and angles. The (u, v) coverage describes how well the (u, v) plane has been sampled.

At a given wavelength, the (u, v) plane can be filled by any combination of:

- observing with various telescope combinations
- repositioning the telescopes
- using the earth's rotation to change the projected baseline

The process of filling the (u, v) plane with observations is called aperture synthesis and if this is done by using the rotation of the earth it is sometimes referred to as "Earth rotation aperture synthesis".

A point in the (u, v) plane is either referenced by its (u, v) co-ordinates or by its (projected) baseline length BL and the position angle PA, where PA is defined as usual in degrees east of north.

(BL, PA) and (u, v) are trivially connected by

$$BL = \sqrt{u^2 + v^2} \tag{1.4}$$
$$PA = \tan^{-1} u/v \tag{1.5}$$

The (u, v) co-ordinates, on the other hand, are defined by[6]:

$$u = B_E \cos h - B_N \sin\phi \sin h \tag{1.6}$$
$$v = B_E \sin\delta \sin h + B_N(\sin\phi \sin\delta + \cos\phi \cos\delta) \tag{1.7}$$

where the ground separation vector $\vec{B}$ was decomposed in its components B_E and B_N, h is the hour angle of the source, δ the declination of the source and ϕ the latitude of the interferometer (Dyck 2000).

(u, v) coverages are point symmetric with respect to the origin because the telescope positions are interchangeable.

The (u, v) coverages of the observations are displayed in the respective chapters, Figures ??.

1.2.5. Visibility modeling with geometrical image components

It is important to mention a caveat in this reasoning: The visibility of most simple models is very similar at spatial resolutions that are large compared to the source size $\theta \gg 1/BL_\lambda$ (see Figure 1.3). In order to confidently determine the nature of the source it is therefore necessary to observe very close to $1/BL_\lambda$.

Conversely, at the relatively visibilities that we will be probing our sources, the exact shape

, however, visibilities always drop as BL_λ^{-2} and therefore the nature of the source cannot be constrained. E.g. the visibility patterns produced by a Gaussian and a uniform disk only differ from a parabola shape at vis $<$ ...

The goal of visibility modeling with geometrical image components is to quantitatively model the source brightness distribution (the image) when it is not possible to directly reconstruct the image from the inverse transform of Equation 1.2.

The basic idea is to decompose the image into simple "building block" functions, such as points, (elongated) disks and rings and fit their properties (fluxes, sizes, elongations, offsets[7]) by comparing the visibility data to the Fourier Transform of the model image.

[6] This assumes that all telescopes have the same elevation. Otherwise additional terms need to be considered, see Dyck (2000).

[7] With phase-less data only relative astrometry within the interferometric field of view is possible, see discussion in Section 2.4.

The Fourier transform of the source brightness distribution, the visibility, is generally a complex quantity. Since we cannot measure the visibility phase, however, we will restrict ourselves to point-symmetric (even) functions since the Fourier transform of a real-valued even function is real (and even).[8]

Here the Fourier transforms of some often used components are given. The geometrical form describes the source brightness distribution.

In the following, α, β are co-ordinates in real space (in radian or milli-arcseconds) and the inverse co-ordinates are given as spatial frequencies u_λ, v_λ.

Most of the models are circularly symmetric and are therefore given in the radial co-ordinate $\rho = \pm\sqrt{\alpha^2 + \beta^2}$ and $\mathrm{BL}_\lambda = \pm\sqrt{u_\lambda^2 + v_\lambda^2}$.

The models and their Fourier transforms are displayed in Figure 1.3.

The point source The intensity distribution of a point source at a position α_0, β_0 relative to the center of the interferometric field of view, may be written with the Dirac-δ function as

$$I(\alpha, \beta) = I_0 \delta(\alpha - \alpha_0, \beta - \beta_0). \tag{1.8}$$

This is the only non-point-symmetric function shown here. It can be seen that the Fourier transform of it,

$$V(u_\lambda, v_\lambda) = \exp(-2\pi\imath(u_\lambda \cdot \alpha_0 + v_\lambda \cdot \beta_0), \tag{1.9}$$

is a complex-valued function whose amplitude is 1. This re-iterates what we have stated before: In a two-telescope interferometer, that measures only the amplitude of the visibility, it is not possible to determine the position of a point source in the interferometric field of view. It is nevertheless interesting to look also at the phase of this visibility function. It is linear in u_λ and v_λ with slope α_0, β_0, respectively, i.e. it contains the information of *where* on the image plane a source is located. This gives an impression why some measurement of the visibility phase is crucial for reconstructing realistic images.

Uniform disk The uniform disk is the first order description of a star that is useful for example to model the diameter of the (nearly unresolved) calibrator stars when calibrating the instrumental visibility (see below). For highly resolved stars, a better description of the source brightness distribution takes into account limb-darkening (Hajian et al. 1998).

$$I(\rho) = \begin{cases} I_0 & |\rho| \leq \Theta/2 \\ 0 & |\rho| > \Theta/2 \end{cases} \tag{1.10}$$

where the normalization $I_0 = \frac{4}{\pi\Theta^2}$ (for two dimensional models) and $I_0 = 1/\Theta$ (for one dimensional models).

[8] For completeness we note that an image in general is of course always a real-valued (but not necessarily point-symmetric) function and its Fourier transform is hermite, i.e. $V(u, v) = V^*(-u, -v)$. This is sometimes referred to as the "reality condition".

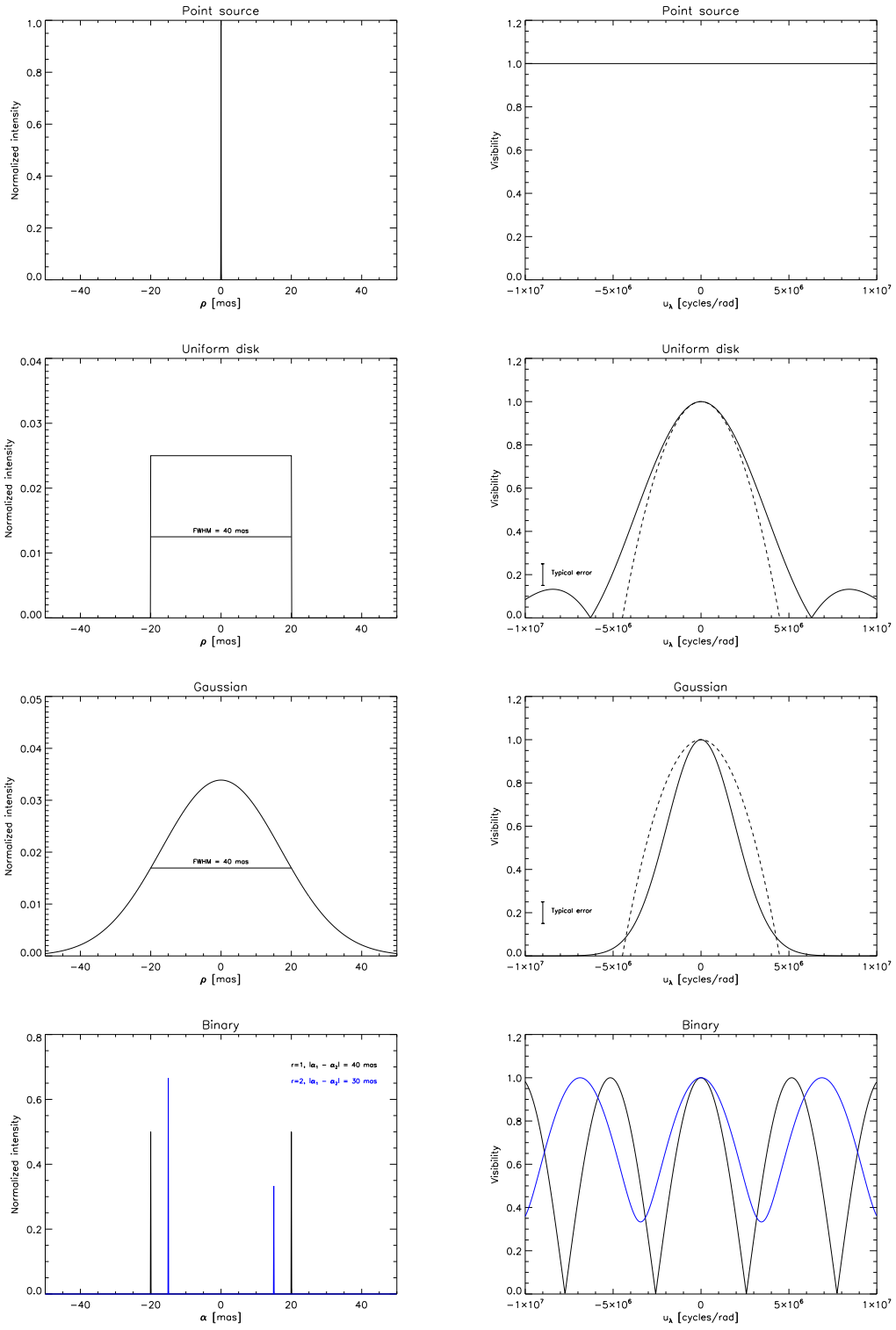

Figure 1.3.: Simple models for the source's surface brightness distribution and their Fourier transforms. For the uniform disk and Gaussian models a parabola of fixed width is overplotted to demonstrate that the two can hardly be distinguished at the given errors. See text for further details.

The visibility is given by

$$V(BL_\lambda) = \left| 2 \cdot \frac{J_1(\pi\Theta BL_\lambda)}{\pi\Theta BL_\lambda} \right| \tag{1.11}$$

where J_1 is the Bessel function of first kind and of integer order 1.

The circularly symmetric Gaussian disk The circularly symmetric Gaussian disk is a very popular representation of the "envelope" (i.e. the smoothed version) of a more complex source brightness distribution. It has the advantage to be smoother than the uniform disk in (u, v) space and it is therefore less likely to fit spurious signals even at moderately high resolutions. It is very useful for a first-order, reliable size estimate.

We give the equations for the Gaussian disk with zero mean both in terms of its standard deviation σ and in terms of the Full Width at Half Maximum (FWHM) $\Theta = 2\sqrt{2\ln 2}\cdot\sigma \approx 2.35 \cdot \sigma$.

Note how the size of the source (σ or Θ) enters the visibility function reciprocally to the real-space function, i.e., at a given BL_λ, smaller sources have larger visibilities.

$$I(\rho) = I_0 \exp\left(-\frac{\rho^2}{2\sigma^2}\right) = I_0 \exp\left(-\frac{4\ln 2\rho^2}{\Theta^2}\right) \tag{1.12}$$

$$V(BL_\lambda) = \exp(-2(\pi BL_\lambda\sigma)^2) = \exp\left(\frac{-(\pi\Theta)^2 BL_\lambda^2}{4\ln 2}\right) \tag{1.13}$$

$I_0 = \frac{1}{2\pi\sigma^2} = \frac{4\ln 2}{\pi\Theta^2}$ (in two dimensions) and $I_0 = \frac{1}{\sigma\sqrt{2\pi}} = \frac{2\sqrt{\ln(2)}}{\Theta\sqrt{\pi}}$ (in one dimension)

Binary The binary system of point sources is the simplest compound object and serves to demonstrate the visibility function of more general, complex systems.

$$I(\alpha, \beta) = I_1 \cdot \delta(\alpha - \alpha_1, \beta - \beta_1) + I_2 \cdot \delta(\alpha - \alpha_2, \beta - \beta_2) \tag{1.14}$$

$$V(u_\lambda, v_\lambda) = \sqrt{\frac{1 + r^2 + 2\,r\,\cos(2\pi\vec{a}\cdot\vec{\mathrm{BL}}_\lambda)}{(1+f)^2}} \tag{1.15}$$

with the normalization $1 = I_1 + I_2$ and the intensity ratio $r = I_1/I_2$, the separation vector of the binary $\vec{a} = \binom{\alpha_1-\alpha_2}{\beta_1-\beta_2}$ and the projected baseline vector $\vec{\mathrm{BL}}_\lambda = \binom{u_\lambda}{v_\lambda}$.

The formula can easily be rewritten for the more general case of any two structures that are separated by $\vec{a}$ for which the "building block" visibility functions $V_1 = V_1(u_\lambda, v_\lambda)$, $V_2 = V_2(u_\lambda, v_\lambda)$ are known (Berger & Segransan 2007):

$$V(u_\lambda, v_\lambda) = \sqrt{\frac{V_1^2 + r^2\cdot|V_2|^2 + 2\,r\,|V_1|\,|V_2|\,\cos(2\pi\vec{a}\cdot\vec{\mathrm{BL}}_\lambda)}{(1+f)^2}} \tag{1.16}$$

1.2.6. χ^2 fitting

To determine the best-fitting model, a (not necessarily unique) parameter set is desired for which the deviations between the modeled visibilities, V_i^{model}, and the observed visibilities, V_i^{data} are approximately as large as expected by the observational errors σ_i.

The quadratic sum over all observations N_{data} of the so normalized deviations is given by

$$\chi^2 = \sum_i^{N_{\mathrm{data}}} \frac{\left(V_i^{\mathrm{data}} - V_i^{\mathrm{model}}\right)^2}{\sigma_i} \tag{1.17}$$

The χ^2 distribution depends on the number of degrees of freedom $N_{\mathrm{free}} = N_{\mathrm{data}} - N_{\mathrm{params}}$ with N_{params}, the number of (free) model parameters. It has mean N_{free} and variance $2N_{\mathrm{free}}$ (Barlow 1989). Its normalized variant is called the "reduced χ^2 function" and is given by

$$\chi_r^2 = \frac{\chi^2}{N_{\mathrm{free}}} \tag{1.18}$$

The minimization of this quantity is a non-trivial procedure as χ^2 can be a highly complex, multi-dimensional function where the global minimum is not easily found. A numerical solution to this minimization problem is provided by the Levenberg-Marquardt algorithm (Marquardt, D 1963).

1.3. The mid-infrared wavelength region

The wavelength band of relatively low atmospheric absorption between about 8 and 13 μm (23-37 THz) is called the N band or the "mid-infrared" region[9]. It is also referred to as thermal infrared since a blackbody of room temperature ($\approx$ 300 K) has its maximum flux density $F_\lambda \equiv \mathrm{d}F/\mathrm{d}\lambda$ at 10 μm.[10] I will follow the astronomers' habit and mostly refer to the flux density simply as "flux" in the following.

A transmission spectrum of the earth's atmosphere (at the atmospherically privileged place of Mauna Kea, Hawaii) in this band for excellent conditions is shown in Figure **??** (Lord 1992). The N band is bounded by H_2O and CH_4 absorption at short wavelengths and by CO_2 absorption at long wavelengths (Cox 2000).[11] It is dominated by a prominent double-peaked absorption feature at 9.7 μm caused by the Ozone in the earth's stratosphere. The average transmission through the feature is $\approx$ 40% at airmass of 1 and decreases to $\approx$ 15 % at an airmass of 2. As the rest of the transmission spectrum, it is highly variable.

[9] Actually, the mid-infrared is normally defined as the region from 5 – 25 μm (e.g. PROCESSING & ANALYSIS CENTER IPAC). However outside the N band the earth's atmosphere makes ground-based mid-IR observations nearly impossible.

[10] Note that, in the usual representation of flux density for mid-IR spectra, $F_\nu \equiv \mathrm{d}F/\mathrm{d}\nu$, a blackbody of $\approx$ 500 K has its maximum flux density at 10 μm.

[11] More details about atmospheric spectral lines can be found at http://www-atm.physics.ox.ac.uk/group/mipas/atlas/.

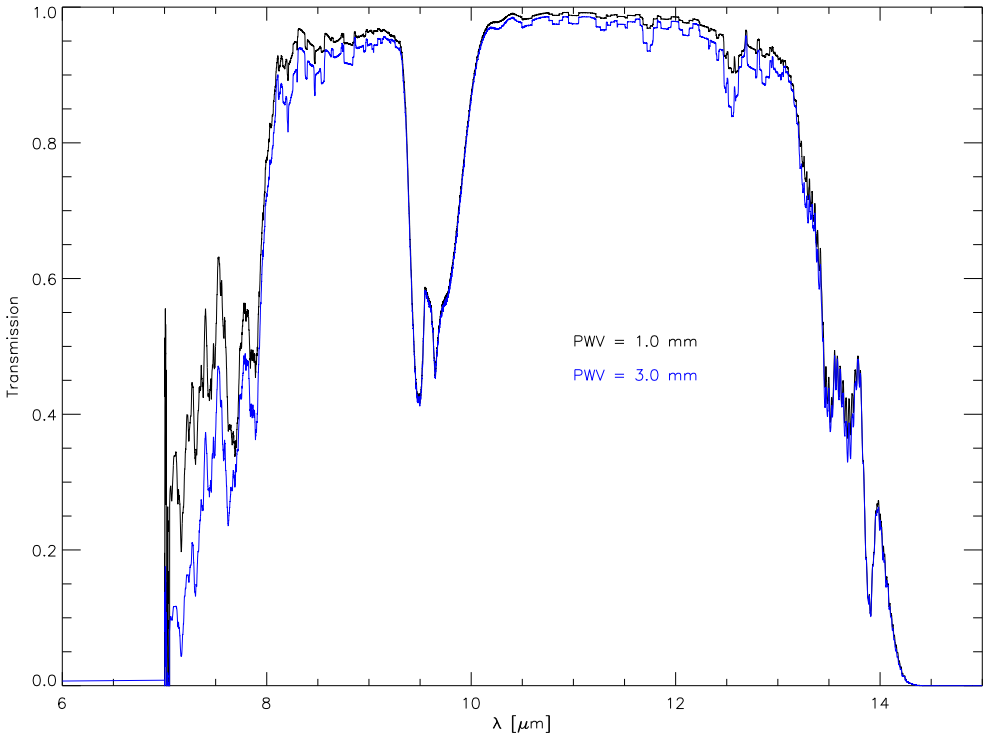

Figure 1.4.: An N band atmospheric transmission spectrum taken at the Gemini observatory (Mauna Kea, Hawaii) at airmass 1.0 and a precipitable water vapor (PWV) column of 1.0 mm (black) and 3.0 mm (blue), respectively (Lord 1992). The effect of increased water vapor is seen most clearly at short wavelengths. The spectral resolution has been downsampled to 0.2 μm to increase readability. At higher resolutions, a huge number of absorption bands are seen.

Emission lines in the N band relevant for AGN research include the forbidden lines [Ar II] 8.99 μm, [S IV] 10.51 μm and [Ne II] 12.81 μm and a number of Polycyclic Aromatic Hydrocarbon (PAH) lines indicative of star forming regions (e.g. Sales et al. 2010). The most prominent spectral feature in the mid-infrared, though, is the broad absorption feature caused by vibrational resonance of the Si–O bond in Silicates.

The transmission spectrum in the N band depends strongly on water vapor. An increase in water vapor leads to a reduction in transmission and a subsequent increase in sky background emission (via Kirchhoff's law of thermal radiation). At any water content in the air, the sky background dominates almost any signal as a typical value of the sky brightness is $N \approx -3$ mag where the brightest sources studied in this work are $N \approx 4$

(1 Jy). Taking into account additional background from the telescope mirrors that also shine brightly in the mid-infrared, only of order 10^{-4} of the detected photons will actually have originated from the 1 Jy source under study.

Fortunately there are a number of ways to reduce this noise. In single-dish observations the most widely applied technique is the chopping (and nodding) of the telescope where the telescope's pointing is switched repeatedly between the target and an off-target (sky) position. This technique works under the assumption the the mid-infrared background varies slower than feasible chopping frequencies of a few Hz and is constant over regions larger than the extent of the relevant sources. Solid numbers about the statistics of atmospheric variations in the mid-IR are hard to find in the literature but a number of individual studies, mostly conducted in preparation for a specific observing site or instrument, suggest that the minimum frequency should be several Hz and the maximum angle should be around $10''$ (Kaeufl et al. 1991; Robberto & Herbst 1998). An good introduction to techniques relevant for observations in the infrared is given by Glass (1999).

Chopping and nodding can reduce the sky background by a factor of $> 10^4$ for all values of PWV observed in single-dish N band observations at Gemini (Mason et al. 2008).

At longer wavelengths, $\approx 16 - 25\mu$m , there is another region of atmospheric transmission, dubbed the Q band. The transmission is less than 40 % over the band and it is not widely used. For completeness, the central wavelengths of the near infrared wavelength bands are 1.3 μm (J), 1.65 μm (H), 2.2 μm (K), 3.8 μm (L), 4.5 μm (M).

One of the advantages of observing in the mid-IR from the ground (compared to observations at shorter wavelengths) is that observations are less affected by atmospheric turbulence in comparison with observations at shorter wavelengths since the relevant quantities scale favorably with wavelengths: The characteristic length scale of atmospheric fluctuations, the Fried parameter, scales as $r_0 \propto \lambda^{6/5}$ and the coherence time as $\tau \propto r_0/v_w$ with the wind speed v_w. However, the FWHM Θ of a seeing-limited point-spread-function does not have a strong dependence on wavelength: $\Theta \propto \lambda^{-1/5}$ (e.g. Quirrenbach 2000).

1.4. The Very Large Telescope Interferometer

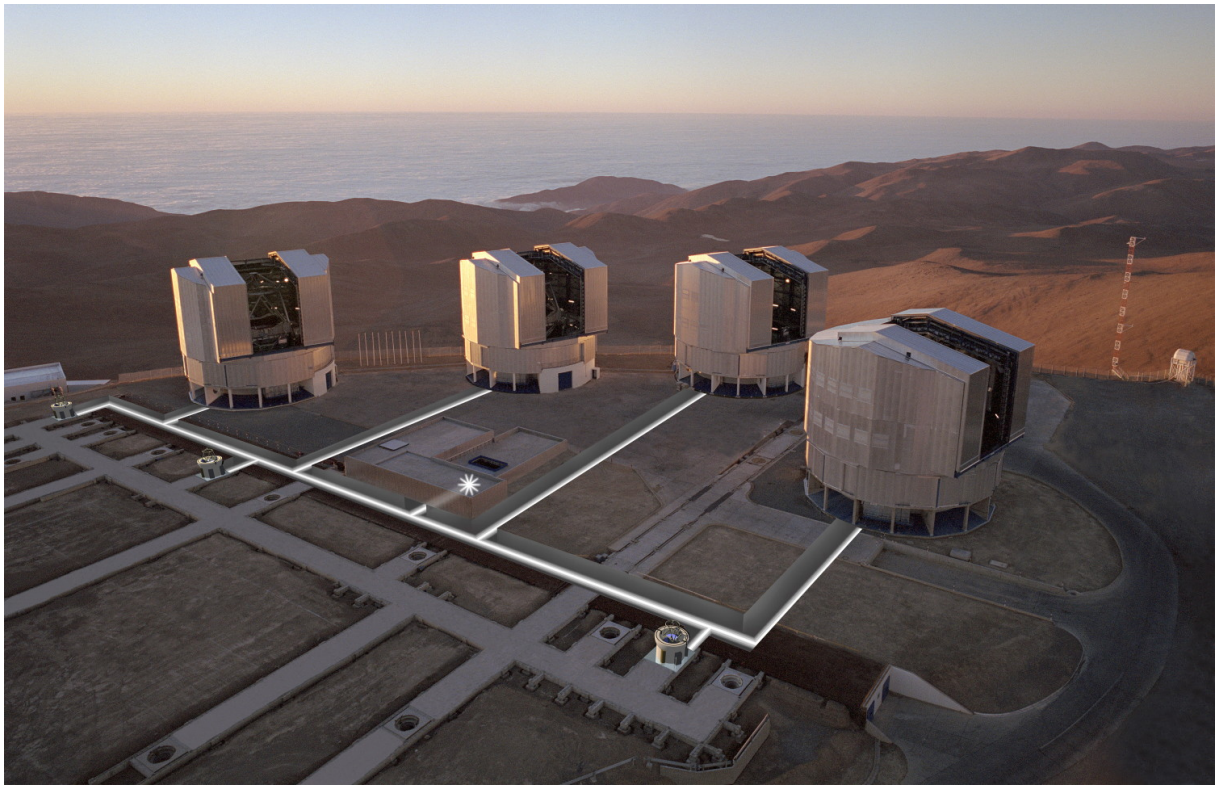

Figure 1.5.: Aerial view of the VLT platform on the flattened mountain top of Cerro Paranal with a graphical description of how the light from the individual telescopes is guided via the light ducts to the delay line tunnel to the VLTI laboratory marked with a star. Mock-up images of three ATs are superimposed (the fourth AT was granted later). Image credit: ESO

Among the 8-10 m class telescopes, the Very Large Telescope (VLT) is unique in the sense that it actually consists of four 8.0 m[12] so called Unit Telescopes (UTs) and four 1.8 m Auxiliary Telescopes (ATs). Together they make up the Very Large Telescope Interferometer (VLTI, Figure 1.5, Glindemann et al. 2000a) that is arguably the most advanced and most productive[13] optical interferometer in the world.

It is located on Cerro Paranal in the Chilean Atacama desert, about 120 km south of Antofagasta and 12 km from the Pacific coast at an altitude of 2635m above sea level. The site was selected for its many clear nights, excellent median seeing and dry atmosphere (ground-layer humidity is on average 15 %). Typical current values characterizing the atmospheric turbulence at Paranal are $\Theta(N) = 0.6''$, $r_0(N) = 5.0$ m and $\tau(N) = 130$ ms (Sarazin et al. 2008).

[12]The primary mirror diameter is 8.2 m, but the relevant clear aperture for the input pupil is 8.0m.

[13]Roughly every fourth paper that is based on results from optical interferometry used data from VLTI, see http://apps.jmmc.fr/bibdb/ for detailed statistics.

Due to its latitude $\phi = -24^\circ\,37'\,38''$, it offers full access to the southern hemisphere and to objects as north as $\delta \approx +40^\circ$. The observatory is run by the European Southern Observatory (ESO), an intergovernmental research organization financed by 14 European countries and Brazil.

The maximum ground separation of the UTs is 130 m (UT1–UT4 baseline) providing a maximum effective spatial resolution $\lambda/3$ BL = 4 mas at 8 μm. A more realistic number is probably $\approx$ 7 mas for a (projected) baseline length of 100 m at 10 μm. As a graphic comparison: 1 mas corresponds to the size of a man at the distance of the moon.

The $N_{\rm Tel} = 4$ UTs provide $N_{\rm BL} = 1/2 \cdot (N_{\rm Tel} \cdot (N_{\rm Tel} - 1)) = 6$ different two-telescope combinations with ground separations ranging from 47 to 130 m[14].

All sources studied in this thesis are too weak to be observed with the ATs, requiring the use of the large UTs that offer about 20$\times$ the collecting area of the ATs and supreme optics including a more sophisticated Adaptive Optics (AO) system.

1.4.1. VLTI subsystems

The VLTI's complexity is slightly underestimated as depicted in Figure 1.5. In reality, about 50 computers (S. Morel, pers. comm.) in a number of subsystems must work together faultlessly to record a fringe on the detector.

Let us follow the path of light from the first reflection to the detector: The plane wave that illuminates the apertures of the single-dish telescopes is guided through the Coudé optical trains where the AO system Multi-Application Curvature Adaptive Optics (MACAO, Arsenault et al. 2003) corrects the wavefront for atmospheric distortions. Since, in good conditions, the diameter of the seeing disk at 10 μm is almost equal to the UT diameter, MACAO is not absolutely necessary for mid-IR interferometry as such. It is required, though, for those the VLTI subsystems that operate at wavelengths < 10 μm.

The seeing-corrected beam enters the Delay Line Tunnel (see Figure 1.6), where the compensation for the geometrical delay $\hat{s} \cdot \vec{B}$ occurs (see Figure 1.1).

Distortions of the wavefront are not only introduced by atmospheric turbulence but also in the air-filled Delay Line tunnels (so called "tunnel seeing"). To reduce their deteriorating effect on the fringe detection, the Infrared Image Sensor (IRIS) detects and corrects tip–tilt wavefront aberrations in the tunnels.

After having been reflected off 16 mirrors, the beam of light reaches the VLTI lab where it undergoes another series of reflections to shape the beam and guide it into the interferometric instrument.

The VLTI is one of the most versatile interferometers in the world: it uses UTs that are normally used in single-dish mode, but it can also be used with ATs, and it combines the light of two, three or four beams in the near or mid-infrared. While this flexibility has operational advantages, it also limits the sensitivity of the interferometer, mostly because

[14]The ATs, on the other hand, can be placed on 30 different pre-defined positions, offering AT–AT ground separations from 8 to about 200m. This way several hundred (but, for technical reasons, less than $N_{\rm BL}$) telescope combinations can be achieved. In principle, hybrid observations involving one or several UTs and one or several ATs are also possible, but currently not offered as a standard mode.

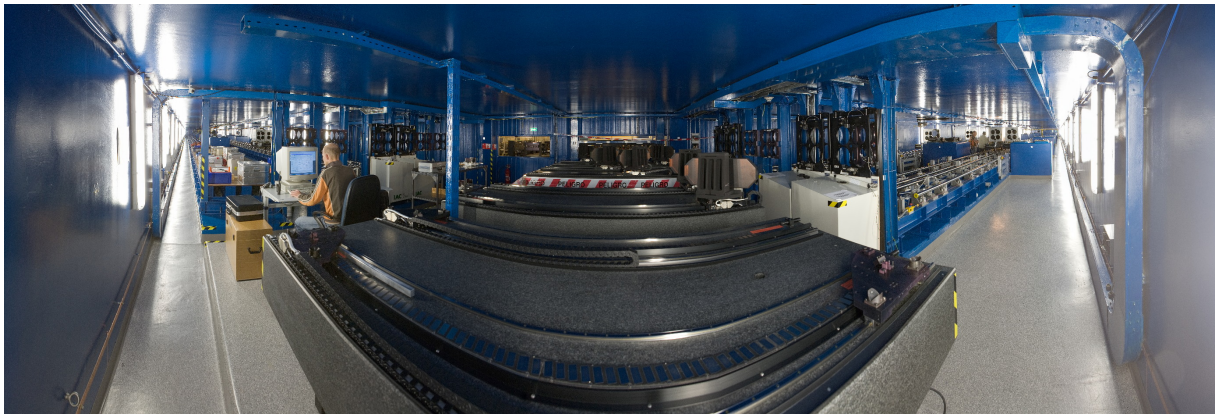

Figure 1.6.: Panoramic view of the four VLTI Delay Lines in the Delay Line Tunnel. Variable Curvature Mirrors (VCMs) and other retroreflectors ensure that the telescope pupil arrives at a fixed position in the VLTI lab (seen in the center of the image). The VCMs are mounted on carriages that glide on the delay line rails. The requirement for their position accuracy is ≈ 1 μm over the entire length of the delay lines (67m in both directions). It can be seen that there is room for more delay lines, providing an upgrade path for the VLTI to combine the light from more than four telescopes, should an appropriate interferometric instrument be built. Image credit: ESO

of the large number of reflections. In the mid-infrared, for example, the throughput of the VLTI is $\approx 30\%$ (Leinert et al. 2003) and this is further reduced in the lab so that only about 20% of the target flux that reaches the primary mirror is recorded in the interferometric instrument (C. Leinert, pers. comm.).

1.4.2. The MID-infrared interferometric Instrument (MIDI)

All observations reported in this thesis have been performed with MIDI, the adaptive-optics (MACAO) assisted interferometer in the mid-infrared for the VLTI. MIDI was built by an international collaboration led by C. Leinert at the Max Planck Institute for Astronomy in Heidelberg (Leinert et al. 2003). It was the first instrument to do direct combination interferometry at 10 μm in the world and also the first scientific instrument at the VLTI (first on-sky fringes were seen in 2002). An image of the instrument in the VLTI lab, showing mainly the warm feeding optics and the dewar on a rather compact optical bench, is shown in Figure 1.7. Selected basic parameters of the instrument are given in Table 1.1.

A schematic sketch of the instrument is shown in Fig. 1.8 and the instrument principle is briefly described there. A more detailed description of the instrument is given by Leinert et al. (2003) and a mathematical treatment of the beam combination in MIDI was given by Przygodda (2004).

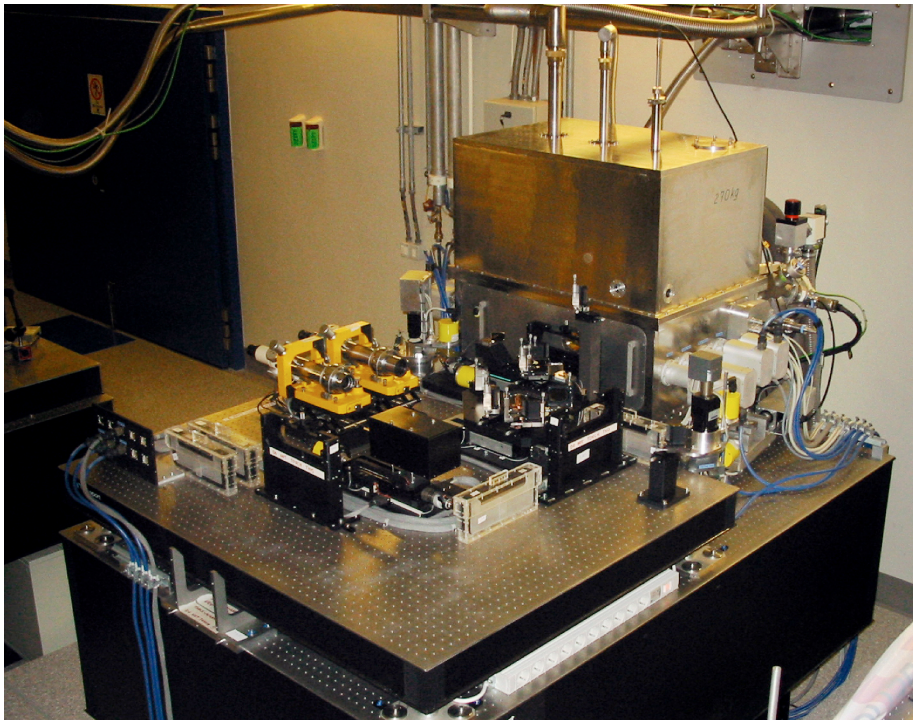

Figure 1.7.: MIDI in the VLTI lab. After having undergone a number of reflections in the VLTI lab, the beams arrive at the MIDI table. There, they pass the so called "internal delay line" (piezo-driven roof mirrors, seen in the center of the image) and then enter MIDI through the dewar window. Figure courtesy C. Leinert

Field of view The field of view (FOV) of a Michelson interferometer with finite spectral resolution $R \equiv \lambda/\Delta\lambda$ is limited to $\approx R$ resolution elements in diameter (Quirrenbach 2001). Even at relatively low resolutions, this value is normally much larger than other limits to the beam size such as a field stop. The MIDI field of view that is transmitted through the delay line tunnels is $2''$.

1.4.2.1. Sensitivity What limits MIDI's sensitivity?

limits come from a number of subsystems

MACAO: limiting magnitude for guiding: $V = 17$ (from ESO), Delta(RA,DEC) $< 58''$. The source morphology does not matter as long as it is not too extended[15].

IRIS: works in H/J/K, for MIDI: use IRIS in K mode (closest to N band) normally: use magnitude given in OB to determine IRIS DIT, but for weak sources: doesn't matter what you write into OB since integration times longer than 0.1 s are not automatically used; you need to manually set IRIS to those very long integration times (e.g. 1s, 2s, ...); then: don't use ACQ for centering source but only IRIS; limiting magnitude: K $\lesssim$ 11

[15]Mars' polar cap ice was also used as a 'guide star' once (A. Mérand, pers. comm.)

Table 1.1.: Relevant basic parameters of MIDI and the VLTI. Wavelength-dependent values are given at 10.0 μm

VLTI	
Telescope aperture D	8.0 m
UT–UT ground separations	47 . . . 130 m
Resolution $\lambda/3$ BL	5.4 – 16 mas
MIDI	
Selected filters	
SiC	11.8 ± 2.5 μm
[S IV]	10.5 ± 0.2
[Ne II]	12.8 ± 0.2
Spectral resolution	$R \equiv \lambda/\Delta\lambda = 30$ (with PRISM)
(Interferometric) field of view	$\pm$ 1 $''$
Airy disk FWHM	315 mas
Pixel scale with field camera	λ/3D $\approx$ 100 mas
Pixel scale with spectral camera	λ/2D $\approx$ 200 mas (in spatial direction)
Selected slit width	200 μm (520 mas on sky)
Detector quantum efficiency	34 %

(detector is not very good)

MIDI itself (fringe tracking): source needs to be acquired, needs to be bright enough to be seen above noise in MIDI acquisition images (this is the most strict limit and is probably at around 100-200 mJy and weather-dependent) or in K to see it in IRIS (K < ...)

The short atmospheric coherence time τ_0 limits the sensitivity of interferometric observations using incoherent data reduction to $\approx$ 1 Jy. Fainter sources can be tracked using fringe group delay recovery techniques and coherently integrating many thousand frames in the data processing step. This way sources as faint as $F_{\mathrm{corr}} \approx 100$ mJy can be observed.

Probably more a question of: which data can be reliably reduced than which fringe can just so be tracked. No point in tracking a weak fringe when it cannot be calibrated / the error cannot be determined reliably.

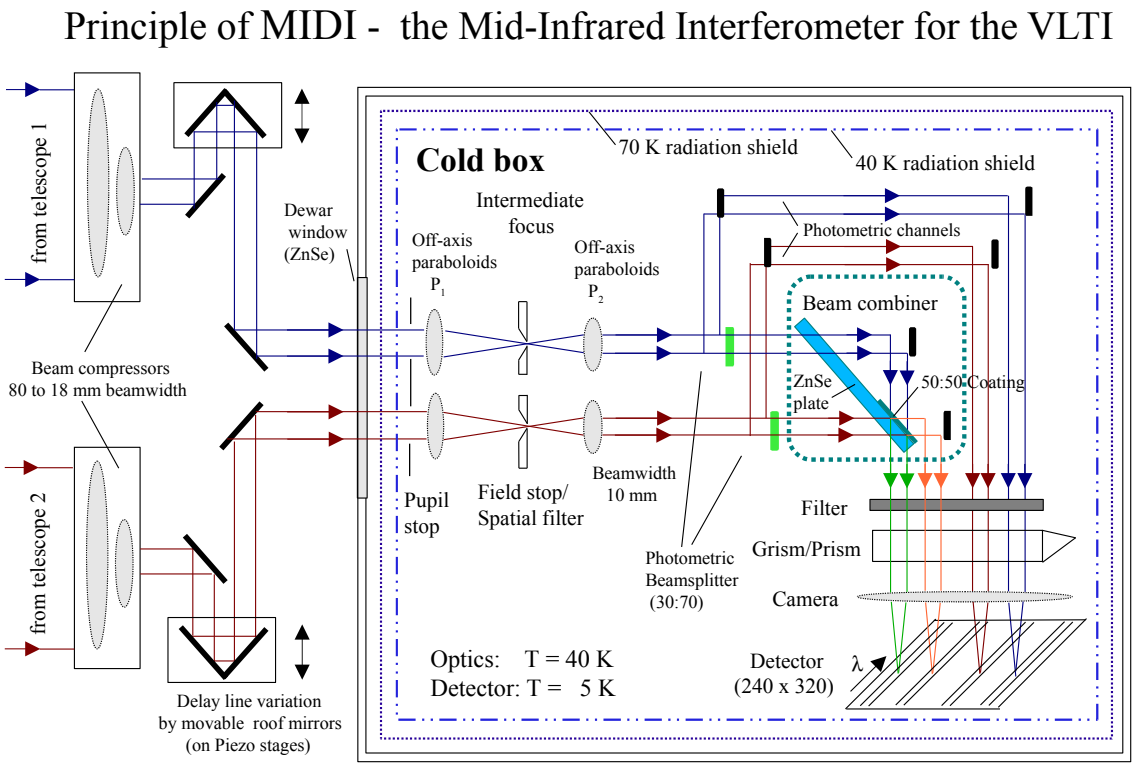

Figure 1.8.: Schematic view of MIDI: The beams pass the instrument-internal delay lines that are used as lock-in amplifiers before entering the cold optics through the dewar window. In the modes relevant to this thesis, the photometric beamsplitters are absent to gain maximum sensitivity. During interferometric observations, a 50/50 beam splitter acts as beam combiner to produce the fringe signal. The signal is recorded on the detector after dispersion by a prism (the grism was not used in this work – again for maximum sensitivity). Figure courtesy U. Graser

1.4.2.2. Overheads / What limits MIDI's efficiency?

The reason why it takes so long to acquire a source with MACAO is that MACAO has very sensitive APD that need careful adjustment of neutral filters to not burn them. The switching in and out of numerous filter combinations takes time. If the neutral density filter setting could be stored, observing time could be saved.

1.5. Observing procedure

describes non-standard observing procedure, only possible in visitor mode when you are at the telescope

Figure 1.9.: Observing at the VLTI

Preparation Proposal writing, proposal review through OPC, OB preparation in P2PP, service vs. visitor mode

A MIDI observation consists of multiple steps involving several observing modes which have been described by Bakker et al. (2003). The ones relevant for this work are briefly introduced below.

Preset and acquisition IR Interferometry: Due to Rayleigh scattering (angle proportial to $1/\lambda^4$) IR astronomy is much less sensitive for scattered solar light in the atmosphere and could in principle also be done during daytime. But: For AO a guide star is needed and MACAO works in the R band, also there is the danger that the sun's flux collected by an 8 meter telescope can do considerable damage if something goes wrong

Fringe Search OPD model for ZOPD position for each baseline and some pointing directions, good to a few millimeters.

Slow / fast Fringe Search depending on source flux. Fast = use grism with higher resolution, i.e. larger coh. length – faster OPD stepping possible, find fringe faster

Once fringe is found (for a certain baseline and at a certain pointing in the sky), it normally 'stays' there to within a few hundred microns. Can start the MIDI track at

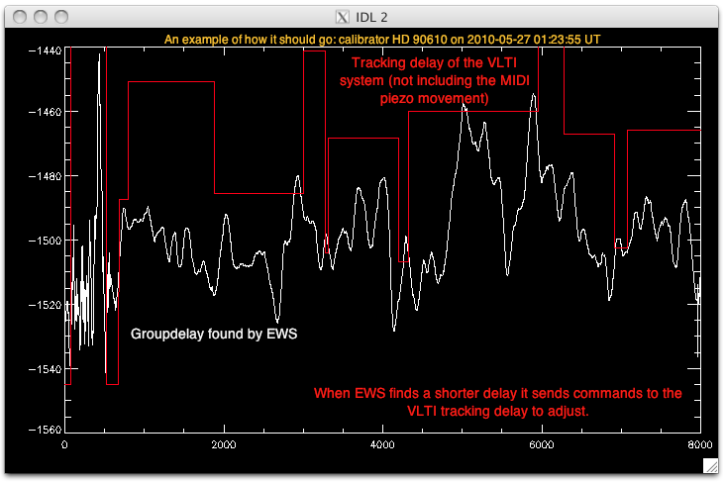

Figure 1.10.: How the MIDI internal fringe tracker and the VLTI delay line work together if everything works

presumed ZOPD - 200 μm , then the track will automatically run into the fringe, saves observing time.

Fringe Track two modes: external fringe tracker (FINITO, PRIMA – not sensitive enough or not yet ready, respectively) or self-fringe tracking.

Self-tracking means: groupdelay is determined nearly real time from the recorded fringe track data.

Requirement: sampling time $<$ 100 ms (coherence time of atmosphere in N band)

Procedure: internal delay lines step the OPD from 0 + a few micron to 80 + a few micron (offset tracking). Offset tracking better than zero-fringe tracking for weak sources because no white light noise (at the cost of somewhat reduced fringe contrast, due to coherence envelope); off-zero tracking introduces a shift in the fringes with respect to wavelength that does not occur at the white fringe position. It is therefore easier to determine the background (that doesn't vary with wavelength).

So we have D_{atm} and D_{ins}, where the latter is deliberately introduced by the interferometer to remove the former and to reduce signal/noise drastically (lock-in-amplifier).

nscan, scanlength, stepsize

Photometry Objective: measure the uncorrelated flux, for bright sources: also measure the atmospheric / VLTI transmission very close in time to fringe measurement

Procedure: close shutter for beam from telescope 1 / 2, respectively

However: very large background due to large number of reflections in VLTI / atmosphere / MACAO / IRIS / VCMs / unknown really.

Not so relevant for weak sources and can potentially be skipped because data is normally bad and analytic power (for the question what went wrong?) is very limited due to very large uncertainty.

Images of blobs in ACQ pictures? Blobs ≫ PSF? must come from inside VLTI!

There are various theories where the background fluctuations might come from: - Atmosphere (unlikely, too large) - MACAO (unlikely, ???) - IRIS / VCMs (???) - remaining tunnel seeing? - edges of M1 imaged by M2? (but defocused)?

Calibration The procedure is then repeated for a nearby star. Star has requirements: - largely unresolved / diameter known - ideally same flux as target source (seldom possible since stars with same low surface brightness as AGNs are normally more complicated objects than uniform disks)

1.6. Data reduction

link to wiki?

Objective: Describe the MIDI data reduction for weak sources. Using relatively new and not yet stable EWS snapshot version Jan 2011 as reference. Some parts have not yet been fully tested and some have not been implemented.

In principle there are two different ways of estimating the visibility from the data. Either one can look at the incoherent fringe power spectrum. This estimator is proportional to the square of the visibility (or correlated flux).Köhler & Jaffe (2008)

One can also try to estimate the groupdelay for each frame, derotate each frame by that number and coherently average all frames to get a signal that is linear in visibility. The latter is implemented in EWS.

Excellent introductions to MIA, the incoherent data reduction part of MIA+EWS, and to the standard EWS reduction have been given by Schuller (2002); Ratzka (2005); Tristram (2007).

1.6.1. The basic idea

SPIE documents: meisner2004, jaffe2004

EWS: phase = object (Fourier) phase + atmospheric phase, removed! group delay = slope of phase – can be determined from data

Modifications for very weak sources : removed biases due to water vapor etc., also increase signal/noise using slow and slope fitting (powerdelay)

1.6.2. Outline

outline graph?

1.6.3. Compression of data / application of a mask

Masks... Generate automatically using auto-correlation of template mask with the real, observed spectrum.

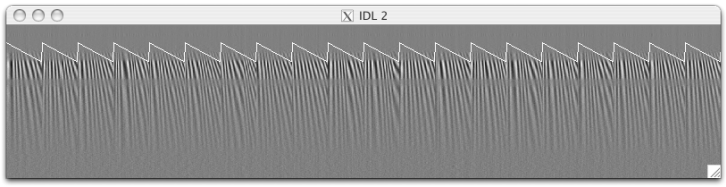

Figure 1.11.: Fringes after high pass filtering including a plot of the MIDI internal delay line position – for a calibrator. Frame number (time) is to the right (about 1000 are displayed) and wavelength runs from top to bottom

For Cen A: used EWS mask, shifted in y to cal position For LP: constructed averaged mask from PSF of all cals of one observing epoch (ca. 1 month), then shifted this mask to the respective position of the observation using the corresponding calibrator observation.

Even better (future versions of EWS): FringeImage as alternative way. Example where normal masking went wrong: 3C 273 2007-02-06/s24: sci fringe at diff. position than cal, had to be rejected.

1.6.4. Formation of fringes and high-pass filtering

Real fringes are modulated by internal delay lines (80 μm in 20 steps – double check, 1 frame 18 ms). Signal that is not modulated must be noise. Effectively provides a high frequency chopping.

Running a high pass filter (i.e. subtracting a smoothed version of the data from the data) removes most of the noise and makes fringes visible.

value of smooth, smooth = 10 is good.

1.6.5. Determination of group delay

Recorded data is

$$I = I_{\mathrm{src}} \cdot V(BL_\lambda \cdot \sin(kd + \phi)) \tag{1.19}$$

where

$$d = d_{\mathrm{ins}} + d_{\mathrm{atm}} \tag{1.20}$$

Now: remove d_{ins} by 'rotating' the data by $\exp(-\imath k d_{\mathrm{ins}})$. Data then becomes complex

$$\begin{aligned} I_{\mathrm{rot}} &= I \cdot \exp(-\imath k d_{\mathrm{ins}}) && (1.21)\\ &= fIV(BL_\lambda)\frac{1}{\imath}\left(\exp(\imath k d_{\mathrm{atm}} + \imath\phi) - \exp(\imath k(d_{\mathrm{atm}} + 2d_{\mathrm{ins}}) - \imath\phi)\right) && (1.22) \end{aligned}$$

Next: Fourier transformation from frequency (k) to delay (d) space – we want to determine d!

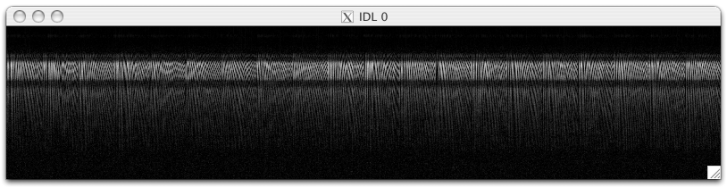

Figure 1.12.: Fringes after removal of instrumental OPD. This is the absolute value of the resulting complex quantity.

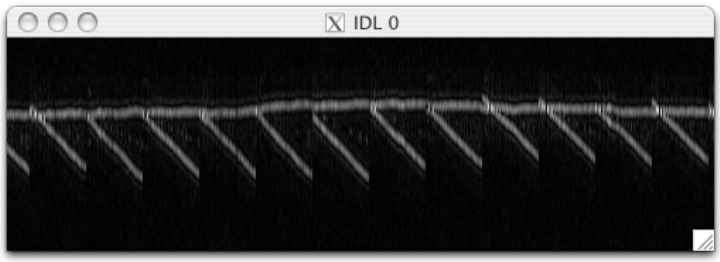

Figure 1.13.: The delay function. Frame number to the right, delay from top to bottom. The intensity is the amplitude of the respective Fourier component.

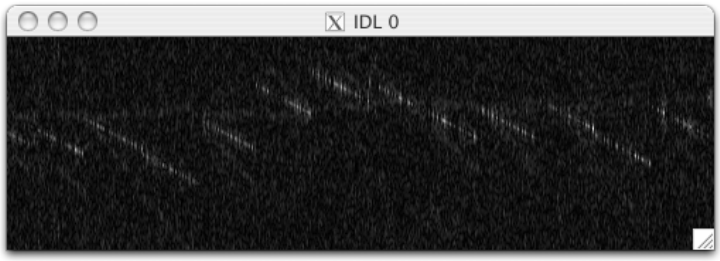

Figure 1.14.: The same as Figure 1.13 but for a weak calibrator (NGC 4151 in this case). Three peaks per column can be seen: a slowly varying function with time (the atmospheric delay), one that varies like $2d_{\mathrm{ins}}$, (that's the instrumental delay peak that was rotated in the wrong direction) and one that varies just like d_{ins}. This can be removed by applying dave.

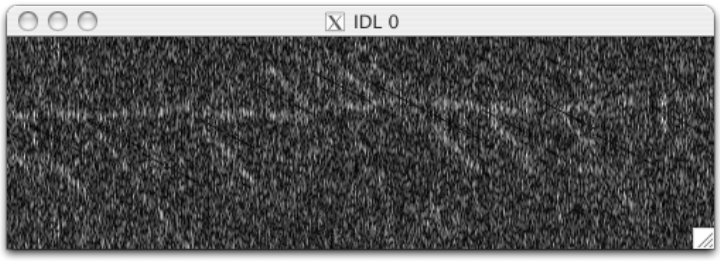

Figure 1.15.: The same as Figure 1.14 but with dave applied (requires offset tracking).

Now smooth the delay function to gain signal/noise

For bright sources the peak shows up very clearly in the image, for weak sources ($\approx$ 100 mJy correlated flux) where the signal/noise is not much larger than unity, it can be hard to find the signal peak among the many noise peaks.

Weak routine modification: For bright sources one can therefore simply search the groupdelay peak for every frame and apply some selection criteria for the value that results. E.g. it should not be more than say 10 μm different from the previous value and it should also not be too far away from the tracking OPD. For weak sources too many frames are discarded in that way and the signal to noise is low. In order to improve on this, one can run the groupdelay fitting in two steps: In the first approximation, the true groupdelay is found by averaging the Fourier transformed images by a large time ($\approx$ 10 seconds). This removes most of the noise, but returns a delay function that is only accurate to ≈ 10 μm . With this delay approximation, we run another groupdelay search, now with a narrower averaging width, and look only in an envelope of ≈ 10 μm around the previously found estimate. This is a reasonable way of finding the group delay of weak sources under not too bad conditions where the true atmospheric OPD does not change by more than ≈ 1 μm per second. The remaining, larger, OPD jumps are due to instrumental glitches. They do not depend on the source brightness and can therefore be assumed to affect the target and calibrator signal in about the same way. This technique runs under the names *powerdelay* or *slow fitting*.

An extra way of improving the signal to noise in groupdelay searches for coherent integration is the so called *slope fitting*. In this way, the OPD that was determined for each scan, is allowed to show a linear drift between the scans. The routine looks for various different changes of OPD versus time between the frames and picks the one that maximizes the signal.

1.6.6. Removal of phase biases and de-rotating group delay

1.6.7. Coherent averaging

1.6.8. Frame selection (flagging)

1.6.9. Single-dish spectra

Mask data

remove estimated background

Background reduction imperfect: In extreme cases, Ozone feature can be seen in the calibrated spectra as it leads to an absorption or emission feature in the wavelength range of telluric Ozone absorption if the background level has been over- or under-estimated respectively.

1.6.10. OIFITS

Standardized data format for storing, exchanging visibility data is OIFITS, still in version 1, cfluxes are missing but update should be coming. Cite pauls paper

1.7. Calibration and error discussion

1.7.1. Calibration

$$F = \frac{C_{\mathrm{target}}}{C_{\mathrm{cal}}} \cdot F_{\mathrm{cal}} \tag{1.23}$$

C: counts (detected), calibration requires knowledge of F_{cal}
Calibrator list: Roy's Ph.D. thesis / Cohen
Alternative way to calibrate:

$$V = \frac{V_{\mathrm{ins,target}}}{V_{\mathrm{ins,cal}}} \cdot V_{\mathrm{cal}} \tag{1.24}$$

Visibilities vs. correlated fluxes Calibration of visibilities means: dividing corr. flux by subsequently taken single-dish spectra. Advantage: not very sensitive to fluctuations in the atmospheric transfer function since both obs are taken shortly after each other. At a larger time separation, the calibrator visibility is determined which basically allows to correct for instrumental visibility losses. Since they are assumed to vary only on longer timescales as atmospheric variations; this is the usual way to calibrate interferometric data of bright sources.

For weak sources such as the ones described in the following chapters, the errors of the single-dish measurements are much larger than for the correlated flux observations and a different strategy has to be taken; otherwise huge errors of a single photometry measurement (as large as 30 %!)

precondition: uncertainty introduced by variations in atm. transfer functions between sci corr and cal corr must be smaller than photometric errors.

This has been tested extensively and is described in the next subsection.

1.7.2. Atmospheric stability / gains

Gains can be determined from calibrator measurements only every so often (typically once per hour). Good nights: gain seems to be stable more or less over the whole night (and sky)

Bad nights: gain can change a lot within a short time!

This factor limits our calibration accuracy! (in the calibrated corr. flux method)

In good nights not so much: In the April 2008 nights, typical variations of the transfer function between a calibrator and a target observation were $\approx$ 3%, as determined by

linear interpolation of the transfer function between the calibrator observations that surrounded the target observations. This is about half the statistical error of the averaged visibilities. We tried to remove this systematic error by using these interpolated values of the transfer function to calibrate the target observations. The consistency of repeated visibility observations could not be increased, however, if correcting for the transmission fluctuations in this way. In bad nights might be different.

Therefore: Would be desirable to find a proxy for the gain in order to improve calibration accuracy.

Atmospheric proxies for interferometer stability? Looked for correlations between gain and various determinations of the atmospheric turbulence that are measured more often (DIMM, MACAO, coherence time as seen by MIDI), however: no strong correlation found that would significantly improve the calibration accuracy.

In conclusion, no proxies for the atmospheric transmission of mid-infrared interferometric observations were found that are measured more frequently than the calibrator star.

1.7.3. Statistical error / error budget

The statistical error of the corr. flux and of the single-dish flux is estimated by splitting an observation in five equal parts and deriving the variance of these sub-observations.

For the phots: the larger part of the error seems to occur on longer timescales, not seen by an individual obs (see LP error discussion in LP chapter)

1.7.4. Systematic errors – Repeated observations

So can we trust the pure photon-noise error given by the EWS data reduction routines? A good test for systematic errors is again the re-observation of a (u, v) point on a different baseline and in a different night. For the Centaurus A observations this has already helped to gain confidence in the correlated flux measurements (see Figure ???). Among the Large Programme targets, there is one source, NGC 1365, that has been observed at different baselines. The fluxes are identical within the errors – although the data have been taken three years apart. It appears that the errors determined from the variance within one fringe track are a good estimation to the true uncertainty of the correlated flux measurements.

Centaurus A Systematic errors in MIDI observations can arise for a number of reasons.

A good test for the overall systematic error of MIDI observations is to re-observe a (u, v) point. Due to the southern declination of Cen A, the U1U3 and U2U4 baselines cross at $(u, v) \approx (65, 50)$ m. This offers the possibility to observe the same (u, v) point not only on different days but also with different telescope combinations. The comparison of the visibilities measured at this crossing point is displayed in Figure 1.16.

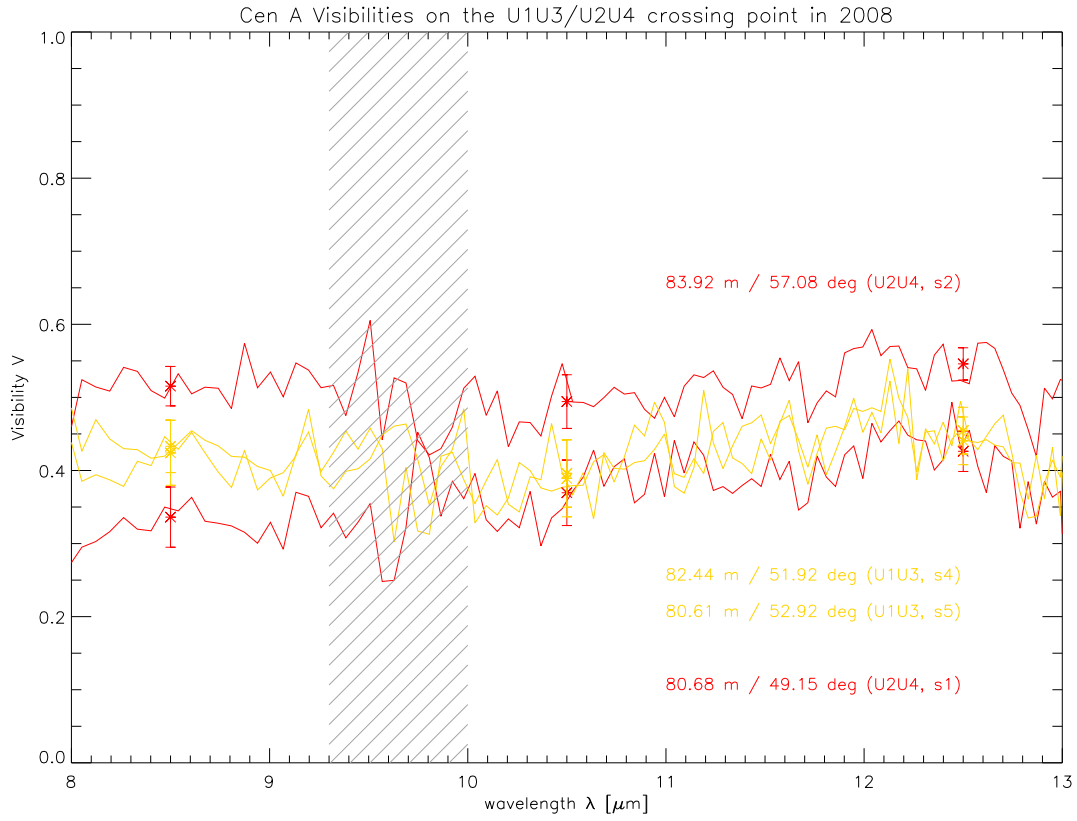

Figure 1.16.: Test for systematic errors using observations of Centaurus A. The (u, v) point at which the upper red spectrum has been taken is separated by about 8m from that of the yellow spectra. The yellow spectra are separated by only about 2m in (u, v) space and the separation between the lower yellow spectrum and the lower red spectrum is about 5m. The data points and error bars show the averaged visibilities that have been used for the model fits (see Table 2.2).

The two points that are closest together in (u, v) position (s4/s5 on U1U3, separation: 2m, yellow curves) show identical spectra. s1 on U2U4 (lower red spectrum) and the two yellow spectra are also (almost) identical within the errors – only at 8.5 micron they are slightly more separated than 1 σ. s2 on U2U4 (upper red spectrum), finally, shows a significantly larger visibility at all wavelengths than the other spectra – it is also separated by about 8m from the next nearest one. It is therefore reasonable to take this offset as real and conclude that systematic errors do not dominate over the statistical ones.

Note that between the two red spectra, a calibrator has been observed, while there has not been a re-acquisition of the source in between the two yellow curves. Since the lower red curve, taken on a different baseline and in a different night than the yellow curves, shows a very similar visibility as the yellow curves, however, we assume that this effect is negligible.

Large Programme image of NGC 1365 (u, v) crossing point (3 years apart! only with newest EWS)

1.7.5. What can go wrong?

- Overlap (OK with IRIS) / positioning of source on the detector (see 3C 273 example, mentioned above (s24/2007-02-06) - Ambient Conditions: e.g. 2010-04-28: clouds! - Beam overlap: probably not a problem (IRIS) - data reduction biases: not easily assessible, see weak star test (but they are stars that have higher MACAO performance, because they are blue(r than AGNs)), example: difference between 2009Dec02 and 2011 EWS versions?

Other sources of errors include the atmosphere and differences in the quality of the AO correction. The AO correction is normally better for type 1 AGNs (where the nucleus can be used for guiding) and for sources with nearby bright guide stars. Airmass and atmospheric conditions also play a role in the reliability of determining a single-dish spectrum as well as the conditions in the delay line tunnels and the VLTI lab. These additional sources of error are very hard to quantify and cannot be taken into account here.

somewhere: demonstration that new EWS is better than old in uv clusters

2. Centaurus A: Dissecting the nuclear mid-infrared emission in a radio-galaxy

2.1. Introduction

2.1.1. A unique galaxy

Centaurus A is a unique astrophysical object that can serve as a laboratory for many sub-disciplines of (astro)physics.

While the peculiar nature of NGC 5128 was already noticed by William Herschel in 1847, only Bolton et al. (1949) identified Centaurus A, the largest extragalactic radio source, with the giant elliptical galaxy by using the sea interferometer at Dover Heights near Sydney, Australia.[1] Its giant radio lobes, that span about $5^\circ \times 9^\circ$ (270 kpc $\times$ 480 kpc) on the sky, have now been mapped in detail in large radio-synthesis images (e.g. Feain et al. 2009). Its huge size is testimony of its proximity rather than its intrinsic power: The distance to Centaurus A is now very well determined from a combination of various distance indicators to just 3.8 ± 0.1 Mpc (Harris et al. 2010), making it one of the closest AGNs known. At this distance, one parsec corresponds to 54 mas. Its black hole mass of $M_{\rm BH} = 4.5^{+1.7}_{-1.0} \times 10^7 M_\odot$ (from gas kinematics, but with similar values from stellar kinematics Neumayer et al. 2007; Cappellari et al. 2009) is rather low compared to its peers, such as M87 that has $M_{\rm BH} = (6.6 \pm 0.4) \times 10^9 M_\odot$ (Gebhardt et al. 2011).

The radio source Centaurus A is classified as a low luminosity radio galaxy. In the context of unified models for low-luminosity radio galaxies (see **??**), Chiaberge et al. (2001) have described Centaurus A as a "misaligned blazar" (due to the similarity of its spectrum with that of (other) blazars) but had to employ a spine-sheath structure of the jet in order to fit the unexpectedly low values of the Doppler factor δ. In this scenario, the jet emission from Cen A seen by us is dominated by the slower moving sheath of the jet, but a faster moving spine (with $\gtrsim 0.45c$) was inferred from the short-time variability of individual components (Tingay et al. 1998) and actually seen from the proper motions of knots in the X-Ray jet (at ≈ 0.5 c, Hardcastle et al. 2003a). In a long-time VLBI study, Tingay et al. (2001) determined the proper motion of jet knots to be relatively slow at ≈ 0.1 c and confirmed variability of the jet components on a time-scale of months

[1] In a strict sense, "Centaurus A" therefore denotes the *radio* source and NGC 5128 the elliptical / irregular galaxy. In the following, the identifiers "NGC 5128" and "Centaurus A" (or "Cen A") will be used synonymously, however.

to years. This variability was explained as the result of perturbations in the jet flow near the base of the jet as modeled by Agudo et al. (2001). Such a perturbation would cause enhanced synchrotron emission as it crosses slower moving shocks downstream in the jet.

Centaurus A is one of a few AGNs that have been continually monitored for over twenty years with space-based observatories (Rothschild et al. 2011). From X-Ray observations, Evans et al. (2004) inferred an efficiency for Bondi accretion of the hot gas of $\approx 0.2\%$, lower than the expected efficiency for a standard disk (Shakura & Syunyaev 1973), but much larger than expected for Bondi accretion. Evans et al. (2004) therefore favor an accretion mode via a geometrically thin, optically thick disk for Cen A. This stands against the current view (e.g. Best 2009) that low-luminosity radio galaxies work through slow, radiatively-inefficient accretion of hot gas from their X-Ray halos. Maybe Cen A is special in this respect because the merger has accelerated the slow accretion process? Struve et al. (2010) find, though, that the kinematics of the HI disk in Cen A is very regular (down to ca. 100 pc, the resolution limit of their observations) and does not show any evidence of an accretion flow.

On the highest energy end of the spectrum, Cen A has also been detected in Very High Energy γ-rays (HESS Collaboration: F. Aharonian 2009) and due to both the extent of its radio structure and its proximity, Centaurus A is now discussed as one of the few plausible sites where those Ultra High Energy particles got accelerated that have been detected by the AUGER Cosmic Ray observatory (e.g. Hardcastle et al. 2009; Nemmen et al. 2010). Therefore and due to the wealth of other observations, Centaurus A is one of only few astronomical sources that are privileged to have become the theme of an international conference[2].

The merging history of Centaurus A was already evident from optical images (see Figure 2.1). The prominent dust lane is interpreted as the remainder of a disk galaxy that merged with the much larger elliptical galaxy. An impressive demonstration of the disk galaxy's impact on the elliptical galaxy was achieved by Malin et al. (1983) and Peng et al. (2002) who took very deep optical images and discovered a system of shells from which the merger was derived to have started several hundred million years ago.

The most recent comprehensive review of this source was given by Israel (1998). More recently Morganti (2010) have summarized "the many faces of gas in Centaurus A" and Struve et al. (2010) nicely review the timescales of the processes that might have formed Cen A's morphology. An extensive collection of Cen A resources can also be found on Helmut Steinle's webpage[3]. Images spanning a wide range of frequencies can be found at Caltech's "Cool Cosmos" webpage[4].

While some aspects of Centaurus A appear peculiar in comparison with other galaxies, it has already been noted by Bland et al. (1987) that these features would probably not attract our attention if Cen A were not at such a close distance to us.

[2]http://www.atnf.csiro.au/research/cena/
[3]http://www.mpe.mpg.de/Cen-A/
[4]http://coolcosmos.ipac.caltech.edu/cosmic_classroom/multiwavelength_astronomy/multiwavelength_museum

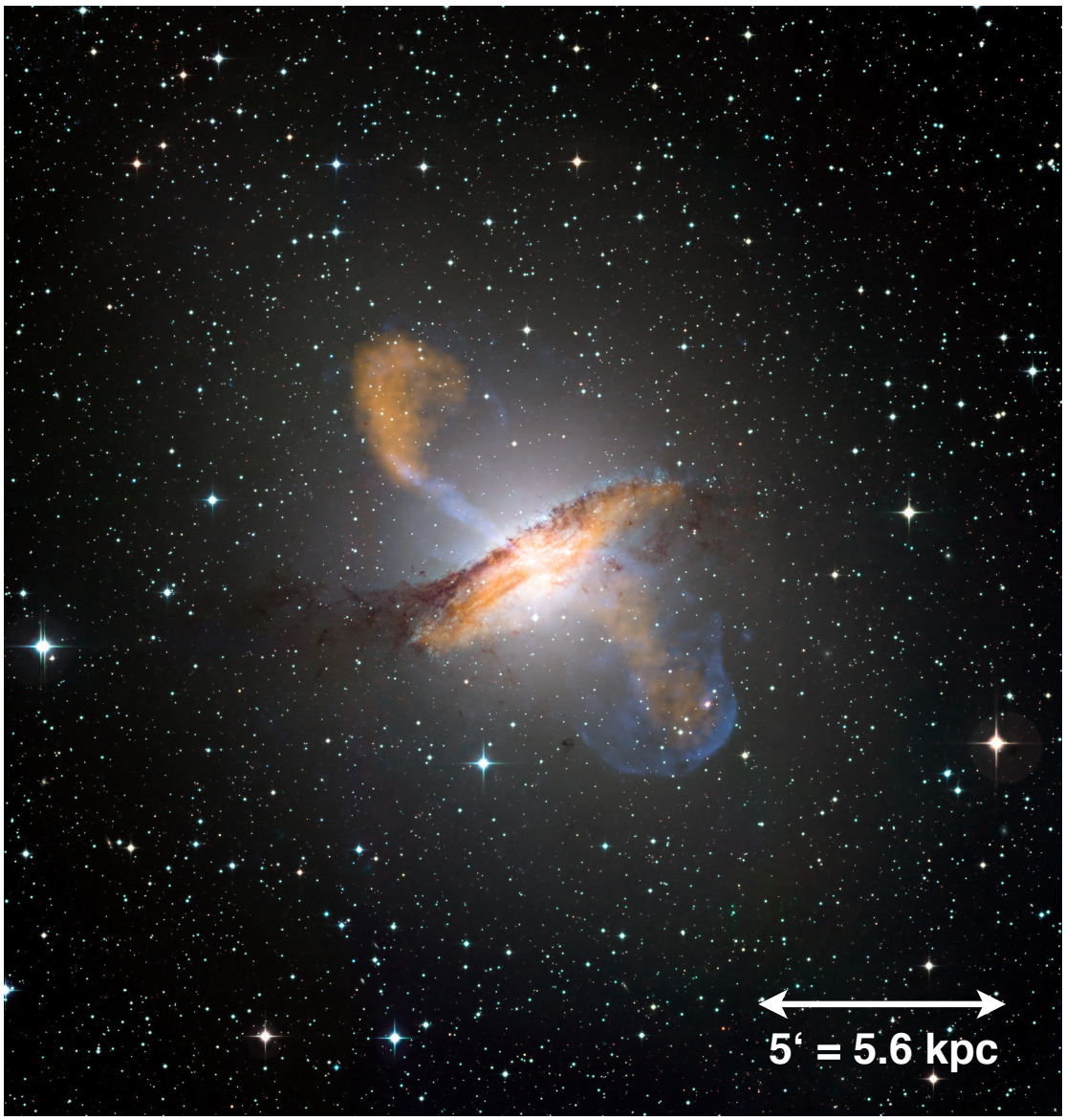

Figure 2.1.: Multi-frequency composit of Centaurus A showing the kpc-scale jet in sub-mm (orange) and X-Rays (blue). North is up and east is left. The northern jet, which is thought to be directed towards us at an inclination of $\approx 50°$ powers the northern inner lobe; in the south the jet is not visible in the X-Rays (but in the radio, not shown here). The merging spiral and elliptical galaxies are seen in true colors (optical) and the famous cold (≈ 30 K, Weiß et al. 2008) dust lane also glows in the sub-mm regime in front of the giant elliptical galaxy. Credit: ESO/WFI (Optical); MPIfR/ESO/APEX/A.Weiss et al. (Submillimetre); NASA/CXC/CfA/R.Kraft et al. (X-ray)

2.1.2. Centaurus A in the infrared

The nucleus of Cen A is attenuated by $A_V \gtrsim 8$ mag as determined from an SED fit to HST photometry of the nucleus by Marconi et al. (2000); these authors also marginally detected the core in the V band. In order to study the nucleus of Cen A in the optical regime in detail, however, one must observe in the near- or mid-infrared.

Let us start with an overview of the infrared morphology of Cen A, zooming in from the kpc-scale. There, Spitzer observations have been successfully modeled as a warped disk ($r \approx 100''$, 2 kpc) of gas and dust (Quillen et al. 2006), following the original model by Bland et al. (1987). The disk is seen nearly edge-on and warps crossing our line of sight are thought to be responsible for bright absorption (near-IR) or emission (mid-IR) knots. There appears to be a gap in this disk at $6'' \lesssim r \lesssim 50''$, corresponding to ≈ 0.1 kpc $\lesssim r \lesssim 0.8$ kpc. Zooming further in, a 500 pc dust shell is seen in a Spitzer spectrographic map (Quillen et al. 2008). In the vicinity of this shell, the molecular hydrogen is found to have temperatures of 250 - 720 K, higher than in non-active galaxies, but similar to values found in Seyfert galaxies. At this distance, highly ionized species are found at position angles near the jet that are probably excited by radiation from the nucleus.

Neumayer et al. (2007) used adaptive optics assisted integral field spectroscopy in the near infrared to derive a model for the mass distribution of the central $3''$(60 pc) from the observation of molecular hydrogen emission. At their resolution limit of 120 mas (ca. 2 pc) in the K band, they find a PA of $(148.5 \pm 1)^\circ$ and an inclination of $(37.5 \pm 2)^\circ$ for the velocity field in their tilted ring model.

Espada et al. (2009) observed the central 1 arcmin (1 kpc) of Cen A in the $^{12}CO(2-1)$ emission line with the Submillimeter Array with a resolution of 100 pc x 40 pc. Using a warped thin disk model, they find that this molecular gas emission in the inner $20''$(400 pc) is elongated at a PA of $\approx 155^\circ$ and they interpret the observed axis-ratio of the presumably circular disk as an inclination of $i = 70^\circ$.

Attempts to resolve the core in the infrared have been made by Schreier et al. (1998) who found an unresolved (< 100 mas) nucleus in the K band using HST WFPC data. Using observations with HST NICMOS, Capetti et al. (2000) got a 3 σ upper limit on the core FWHM of 0.8 pc and found a high polarization of $(11.1 \pm 0.2)\%$, difficult to explain with dust scattering as it would require a much larger column density of dust (corresponding to $A_V \approx 50$) than is observed.

High-resolution ground-based observations of the nucleus of Centaurus A using the 8-10 m class observatories, finally, still find an unresolved nucleus in the mid-IR with upper limits of 190 mas at 8.8 micron (Radomski et al. 2008) or detect it as a point source (Horst et al. 2009; van der Wolk et al. 2010)

Taken together, long-baseline optical interferometry is obviously needed for getting closer to the infrared core of Centaurus A.

Fortunately, its relatively bright mid-IR core of $F_{\rm core}(12\mu{\rm m}) \approx 1.5 Jy$ (variable) puts it in the range of the MIDI sensitivity. Centaurus A is the only radio galaxy that can be studied with MIDI in great detail.

With limited (u, v) coverage, Meisenheimer et al. (2007) found from earlier MIDI data

that the mid-IR emission from the central parsec of Centaurus A is dominated (80% at 8 μm and 60% at 13 μm, respectively) by an unresolved point source (diameter < 10 mas). By comparison with multi-wavelength data, this emission was classified as being most likely non-thermal (synchrotron) in origin. The size of the resolved emission was estimated to be $\gtrsim 30$ mas (0.6 pc) roughly perpendicular to the axis of the radio jet and $\lesssim 12$ mas (0.2 pc) along the axis of the radio jet, respectively. The position angle of the major axis was approximated to be at about 127 ± 9 °. It was found to be consistent with a geometrically thin, inclined dusty disk. With only 4 (u, v) points, the PA of the inferred disk was fixed to the direction orthogonal to the PA of the maximum visibilities.

Here we report results from a more extensive set of (u, v) points that allows to fit model source brightness distributions to the nuclear mid-infrared emission and determine the parameters of the possible emission components more precisely.

2.2. Instrument, observations and data reduction

Observations were performed in the N band ($8\mu\text{m} < \lambda < 13\mu\text{m}$) with MIDI using the observing procedure described in Chapter 1.

For the observation log as well as the observational parameters, see Table 2.1. In total, 34 fringe track observations were made between 2004 and 2010. 13 of these observations are unusable due to various reasons. This leaves a total of 21 successful fringe track observations in two epochs: Four in 2005 and 17 in 2008. Of the ones that were observed in 2008, 7 are practically duplicates in the (u, v) plane and were taken either to increase signal-to-noise or to check for systematic errors.

These observations provide effective spatial resolutions (see Section 1.2.3) of $\approx 5 - 11$ mas at 8.5 μm and $\approx 7 - 16$ mas at 12.5 μm, respectively. Calibrators were selected to be close in airmass. Due to the orientation of the VLTI baselines and the declination of the source, there are unfortunately no long UT baselines in the lower left (and upper right) quadrant of the (u, v) plane (see Figure 2.2).

Data reduction was performed with the interferometric data reduction software *MIDI Interactive Analysis and Expert Work Station* (MIA+EWS, Jaffe 2004; Köhler & Jaffe 2008)[5] and the data reduction procedure was as described in Section 1.6.

The 2005 data were re-reduced with a more recent (in comparison to the one used by Meisenheimer et al. (2007)) EWS version. The results differ slightly from the previously published data reduction but the relative flux levels (between the various (u, v) points) remain the same.[6]

The 2005 data were first published in Meisenheimer et al. (2007). Averaged 12.5 μm visibilities of the 2008 data were published in Burtscher et al. (2010).

[5]The nightly build from Dec 02 2009 was used. It can be downloaded from http://www.strw.leidenuniv.nl/~jaffe/ews/index.html

[6]The data reduction was also compared to a data reduction with an even more recent EWS version (2010Nov20, including the so called "weak sources routines", see Section 1.6). Within the errors, the results were identical.

Table 2.1.: Overview of all successful NGC 5128 MIDI observations and related calibrators. Observation id, projected baseline length BL and position angle PA, effective spatial resolution of the interferometer $\Theta_{\min} \approx 8.5\mu\mathrm{m}\,/3BL$, Airmass and Seeing

Calculate lambda/3 BL resolution!?

Date and Time [UTC]	id	BL [m]	PA [°]	$\Theta_{\min}$ [mas (pc)]	Airmass	Seeing[a] ["]	Associated calibrator
2005-02-28:	UT3 – UT4						
06:07:16	s4	58.22	96.41	10.0 (0.19)	1.11	0.54	HD112213 (c7)
08:29:03	s6	62.37	119.79	9.4 (0.18)	1.08	0.87	HD112213 (c9)
2005-05-26:	UT2 – UT3						
00:16:26	s3	46.51	27.96	12.6 (0.24)	1.12	0.68	HD112213 (c3)
02:27:21	s6	44.11	46.72	13.3 (0.25)	1.07	0.69	HD112213 (c5)
2008-04-18:	UT1 – UT3						
02:54:31	s1	101.35	22.43	5.8 (0.11)	1.10	1.07	HD112213 (c6)
04:51:38	s2	96.72	38.11	6.1 (0.11)	1.06	1.05	HD112213 (c6)
05:03:06	s3	95.92	39.48	6.1 (0.12)	1.07	1.10	HD112213 (c6)
07:03:41	s4	82.44	51.92	7.1 (0.13)	1.28	1.71	HD119193 (c8)
07:15:19	s5	80.61	52.92	7.3 (0.14)	1.32	1.22	HD119193 (c8)
2008-04-19:	UT1 – UT4						
02:09:13	s2	128.74	40.33	4.6 (0.08)	1.17	0.95	HD112213 (c3)
02:20:33	s3	129.17	42.48	4.6 (0.08)	1.15	1.10	HD112213 (c3)
2008-04-21:	UT3 – UT4						
01:47:30	s1	53.46	87.27	10.9 (0.20)	1.20	0.66	HD111915 (c2)
03:55:10	s4	61.85	108.28	9.5 (0.18)	1.06	0.65	HD112213 (c4)
05:26:40	s5	62.02	123.96	9.5 (0.18)	1.10	0.60	HD112213 (c4)
05:38:02	s6	61.77	126.06	9.5 (0.18)	1.12	0.68	HD112213 (c4)
08:48:03	s9	55.44	169.34	10.5 (0.20)	1.98	0.57	HD119193 (c7)
08:59:20	s10	55.27	172.34	10.5 (0.20)	2.12	0.54	HD119193 (c7)
2008-04-23:	UT2 – UT4						
01:06:08	s1	80.68	49.15	7.3 (0.14)	1.30	1.17	HD119193 (c4)
01:42:35	s2	83.92	57.08	6.9 (0.13)	1.20	0.69	HD111915 (c5)
04:52:34	s8	87.18	91.22	6.7 (0.12)	1.08	1.00	HD112213 (c7)
06:16:51	s9	78.88	106.62	7.4 (0.14)	1.21	1.08	HD119193 (c10)

[a] at 0.5 μm from the VLT seeing monitor

Unsuccessful observations of NGC 5128 For completeness, the unsuccessful observations and observing attempts are listed below. Six fringe tracks had to be discarded because the telescopes were still in chopping state. This data is hard to reduce because the chopping state is not stored in the fringe track files (in MIDI's HIGH SENSE mode), making it hard to flag the "sky" frames. Apart from that, even if the data could be reduced, the reduced data would be unreliable as it is unclear what effect the chopping has on the estimation of the correlated flux. Chopping during HIGH SENSE mode is not foreseen, but it apparently occurs sometimes when an observation template is not completely executed (e.g. if "Phot B" is aborted). In future observations one must take care to verify the chopping state before starting the fringe track observation.

- 2004-06-01 (43m, 43°, UT2 – UT3), 02:31:28: no fringe found
- 2005-05-26 (46m, 31°, UT1 – UT3), 00:37:35 (s4): M2 was chopping during fringe track
- 2006-01-20 (130m, 49°, UT1 – UT4), 08:50:46 (s1): fringe was not tracked
- 2008-04-16 (99m, 33°, UT1 – UT3), 04:05:48 (s1): very bad seeing, very low signal
- 2008-04-18 (54m, 61°, UT1 – UT3), 09:26:26 (s6): very high airmass, very low signal
- 2008-04-19 (114m, 79°, UT1 – UT4), 06:08:06 (s8): M2 was chopping during fringe track, photometry useable
- 2008-04-19 (113m, 80°, UT1 – UT4), 06:11:55 (s9): M2 was chopping during fringe track, photometry useable
- 2010-05-30 (72m, 117°, UT2 – UT4), 04:39:38 (s3): experimental GRISM observation
- 2010-05-30 (71m, 118°, UT2 – UT4), 04:47:32 (s4): M2 was chopping during fringe track
- 2010-05-30 (70m, 121°, UT2 – UT4), 04:57:57 (s5): M2 was chopping during fringe track
- 2010-05-30 (69m, 122°, UT2 – UT4), 05:01:40 (s6): M2 was chopping during fringe track
- 2010-05-30 (62m, 134°, UT2 – UT4), 05:45:59 (s7): bad track
- 2010-05-30 (61m, 136°, UT2 – UT4), 05:52:22 (s8): bad track

2.3. Results

2.3.1. (u, v) coverage

The resulting (u, v) coverage is displayed in Figure 2.2. It was conceived to be as uniform as possible. Even when using all available UT baselines, however, the south-eastern (= north-western) quadrant of the (u, v) coverage is less uniformly sampled than the north-eastern (= south-western) quadrant due to the orientation of the VLT Unit Telescopes. Also, some of the planned observation failed for technical reasons.

We observed visibilities on virtually identical (u, v) points and in the same epoch (2008) at the crossing point between the U1U3 and U2U4 baselines and re-observed, on the U3U4 baseline, some of the visibilities observed in 2005. This observing strategy proved to be a very important test for systematics and variability.

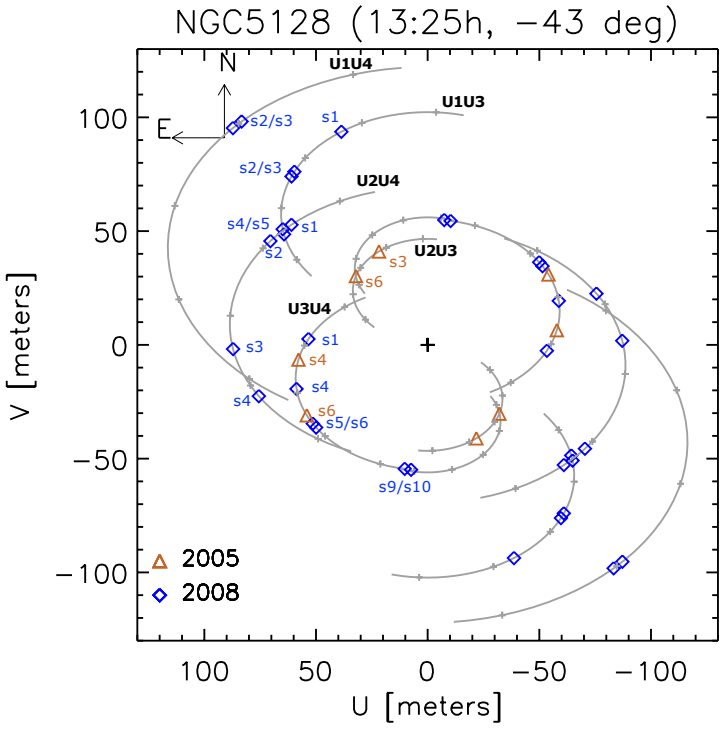

Figure 2.2.: (u, v) coverage of the successful 2005 and 2008 MIDI observations of Cen A. Every visibility appears twice in this plot (because the telescope positions are interchangeable). The solid lines are the (u, v) positions traced by the various baselines (UT combinations are labelled) as a result of earth's rotation. (u, v) plane tracks are followed CCW if $\delta < 0$, CW if $\delta > 0$. They are truncated at telescope elevations of 30 degrees above the horizon, the elevation limit of the VLT Unit Telescopes. Small grey crosses denote Hour Angles = -4, -2, 0, 2, 4.

2.3.2. Correlated fluxes

The resulting calibrated correlated fluxes are displayed in the left panels of Figure 2.3. Besides the deep Silicate absorption feature, the most prominent result of the correlated fluxes is that they are always much larger than our detection limit ($\approx$ 50 mJy). At 8.5 μm , for example, they are $\gtrsim$ 300 mJy, even on the longest baselines.

2.3.3. Single-dish spectra

Single-dish spectra were taken after every correlated flux observation. The accuracy of these observations is limited by imperfect thermal background reduction and they have a much larger scatter than the correlated flux measurements. We show both the 2005 and 2008 single-dish spectra in Figure 2.4. The 2005 spectra differ (within the errors) from the ones shown in Meisenheimer et al. (2007) since they have been reduced using a slightly different data reduction technique (especially: a different mask), as described in Section 1.6.

All Cen A single-dish spectra (per epoch, i.e. for 2005-02, 2005-05 and for 2008-04) were stacked and combined to one average spectrum. This is possible since only the correlated flux depends on the projected baseline length and position angle and it is not expected that the N band source changes within a few days (the 2008 observations were scheduled within one week to exclude variability). The single-dish flux of 2005-05-26 was found to be too low because of background subtraction problems (see Figure 2.4). It was discarded for the further analysis.

The single-dish spectra are dominated by a broad Silicate absorption feature. They also show emission from the [Ne II] 12.81 μm forbidden line, that is absent in all correlated flux spectra and most likely originates in the dust shell discovered by Quillen et al. (2008).

2.3.4. Visibilities

Finally, the calibrated correlated spectra were divided by the calibrated and averaged single-dish spectra to derive calibrated visibilities. Differing from the usual technique to determine the visibility for each measurement by dividing the correlated flux by the subsequently taken single-dish spectrum, we use our averaged single-dish spectra (of the relevant epoch) to derive the visibilities. This greatly reduces the statistical error of the visibility at the cost of an increased systematic calibration uncertainty. Since the nights of observation were stable in terms of total mid-infrared atmospheric throughput, the additional systematic error introduced by averaging total fluxes over several nights is considered to be small compared to the gain in statistical precision (see Section 1.7 for a further discussion of calibration issues). These visibilities are shown in the right panels of Figure 2.3. For the two observations on 2005-05-26, the single-dish fluxes observed on 2005-02-28 were taken to derive visibilities, since the 2005-05-26 single-dish measurements are not correct.

For this work, the visibilities were then averaged at 8.5 ± 0.2 μm , 10.5 ± 0.2 μm and 12.5 ± 0.2 μm . They are given in Table 2.2 and visualized in the (u, v) plane in Figure 2.5

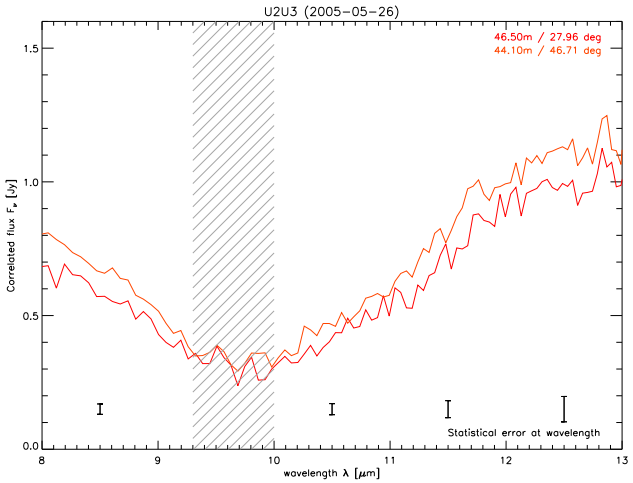

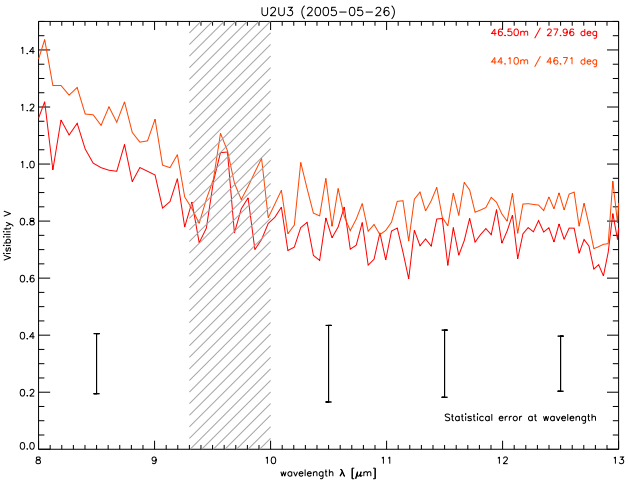

(b) Note the different visibility axis scale for this plot.

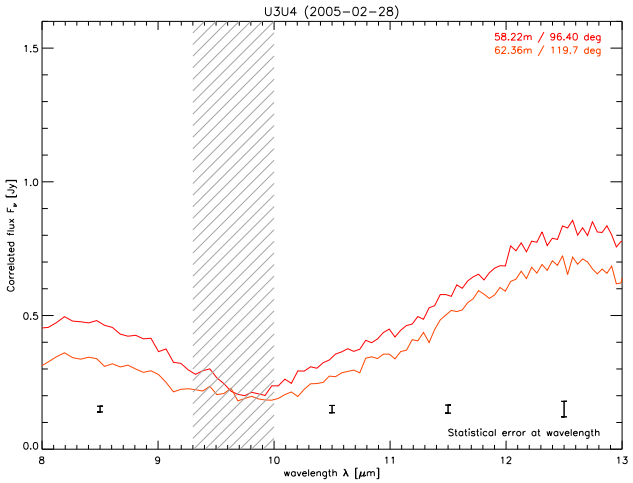

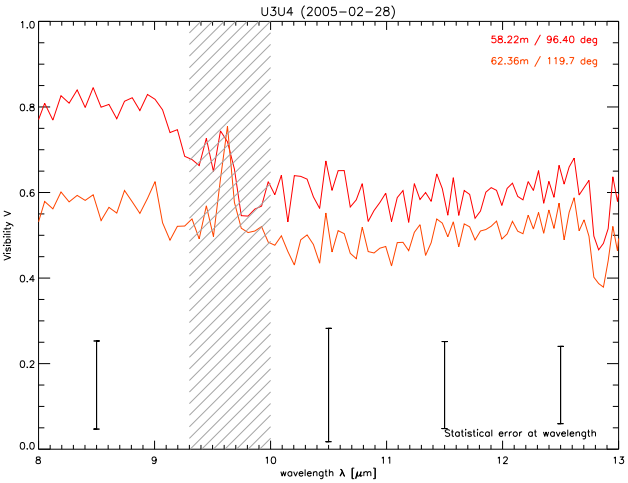

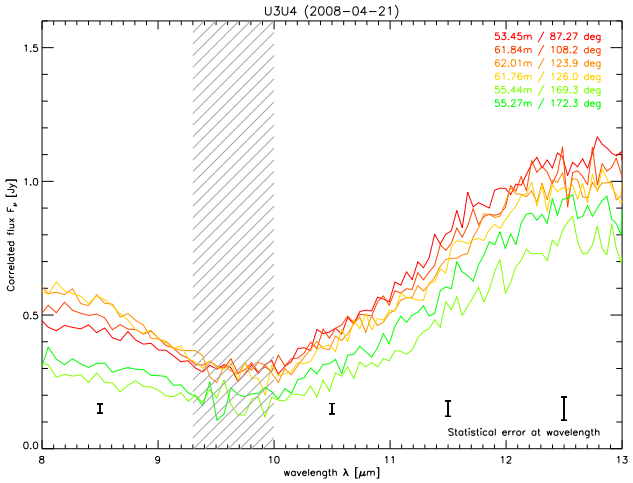

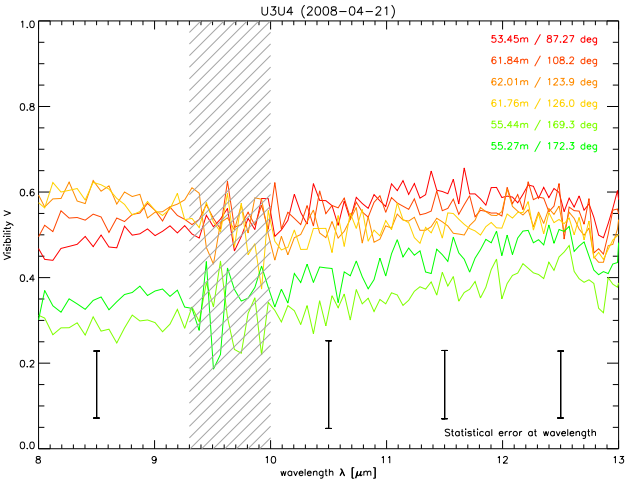

Figure 2.3.: MIDI observations of Centaurus A of 2005 and 2008. The days of night begin and baselines are given in the plot headers. Left: Correlated Fluxes, Right: Visibilities (using averaged photometries), see text for details. Note that the U3U4 baseline has been used for observations in both 2005 and 2008. The spectra taken on this baseline in 2005 and in 2008 are shown next to each other for better comparability. The average errors of all spectra shown in each graph are displayed at the bottom of each plot at four wavelengths (the error bars are $\pm 1\sigma$). The region of the telluric Ozone absorption feature is hatched (see Section **??**). *Continued on next page*

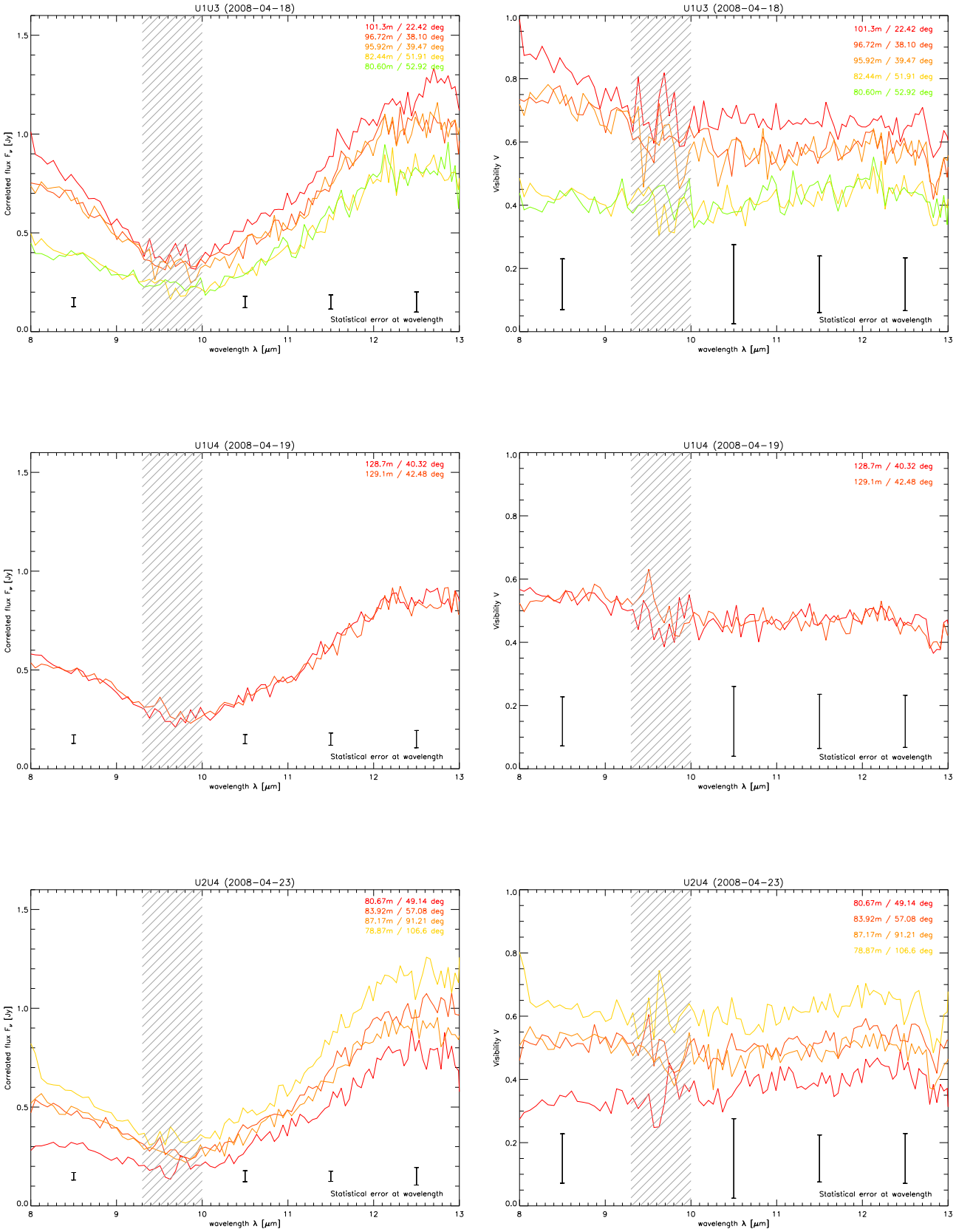

Figure 2.3.: — *Continued*

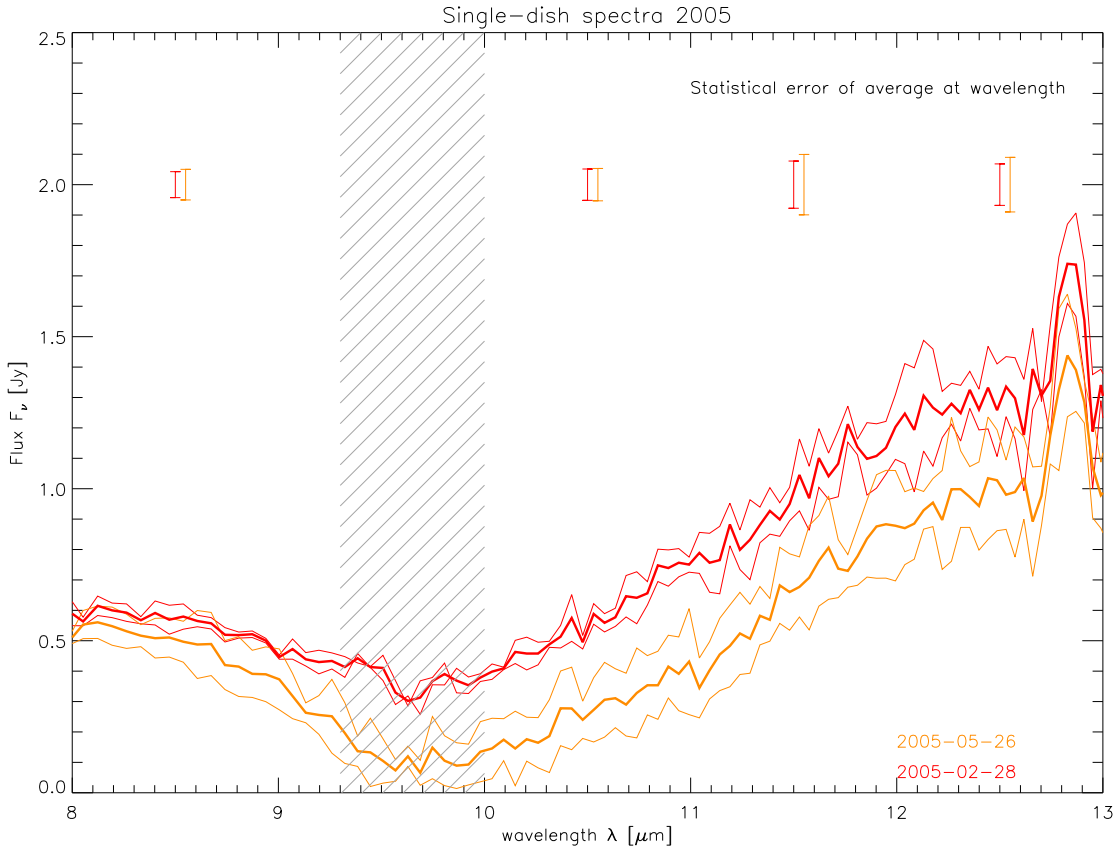

(a) 2005

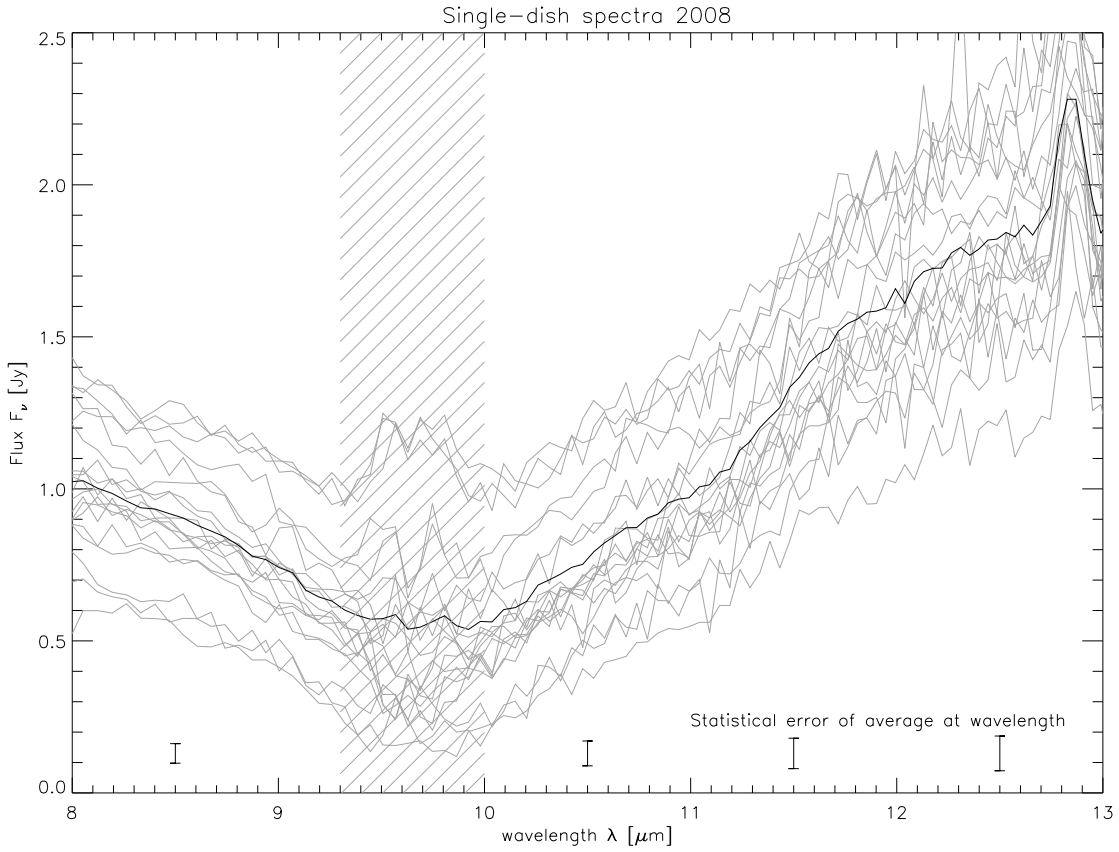

(b) 2008

Figure 2.4.: Single-dish (total flux) observations of Centaurus A in 2005 (a) and in 2008 (b). The dates of observations in 2005 are marked, in 2008 the individual observations are shown in grey and the averaged total flux in black. The statistical errors at selected wavelengths is plotted on top and below the spectra for each epoch (the error bars are $\pm 1\sigma$). The single-dish spectra of 2005-05-26 were discarded due to their low flux and incorrect shape.

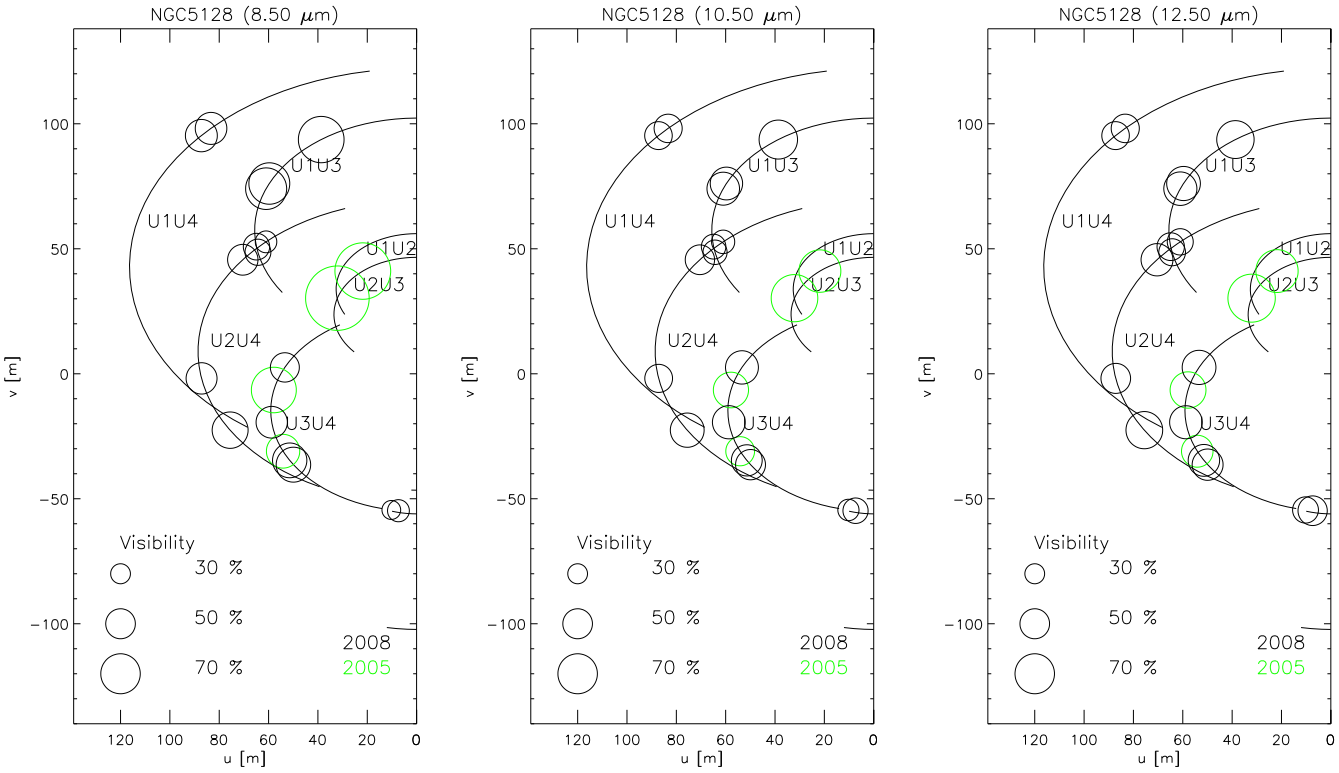

Figure 2.5.: Visibilities from the 2005 and 2008 epochs in the (u, v) plane. Each symbol represents a visibility measurement, the radius denotes the visibility amplitude. Note that only half of the (u, v) plane is shown (the other half is point-symmetric to the one shown).

where the radius of each ring represents the visibility amplitude of the observation at these (u, v) coordinates.

The error of the calibrated, averaged visibility is composed of the statistical error of the correlated flux and that of the averaged photometry (see Section 1.7.3) as well as the error of the calibration templates (assumed to be 5 %, R. van Boekel, pers. comm., see also Section 1.7.2). These errors were propagated using the rules of propagation of uncertainty (e.g. Barlow 1989, Chap. 4.3).

Systematic errors were studied extensively and also specifically for this source. The investigation was explained in Section 1.7 and the main result was (from re-observing a point on the (u, v) plane) that systematic errors do not dominate over statistical errors for these observations.

2.3.5. Variability

Cen A clearly increased its mid-infrared flux between our 2005 and 2008 observations. This is most directly seen by comparing the total fluxes between the two epochs (Figure

Table 2.2.: Averaged visibilities of the 2005 and 2008 observations of Centaurus A, used for the model fits described below.

id	u [m]	v [m]	BL [m]	PA [°]	$V((8.5 \pm 0.2)\mu)$	$V((10.5 \pm 0.2)\mu)$	$V((12.5 \pm 0.2)\mu)$
2005-02-28 U3U4							
s4	57.9	-6.5	58.2	96.4	0.811 ± 0.035	0.613 ± 0.043	0.627 ± 0.030
s6	54.1	-31.0	62.4	119.8	0.575 ± 0.039	0.483 ± 0.048	0.539 ± 0.032
2005-05-26 U2U3							
s3	21.8	41.1	46.5	28.0	1.188 ± 0.055	1.550 ± 0.096	0.994 ± 0.045
s6	32.1	30.2	44.1	46.7	1.371 ± 0.050	1.749 ± 0.091	1.130 ± 0.040
2008-04-18 U1U3							
s1	38.7	93.7	101.3	22.4	0.827 ± 0.025	0.679 ± 0.035	0.657 ± 0.022
s2	59.7	76.1	96.7	38.1	0.728 ± 0.028	0.556 ± 0.036	0.583 ± 0.026
s3	61.0	74.0	95.9	39.5	0.732 ± 0.027	0.560 ± 0.041	0.570 ± 0.025
s4	64.9	50.8	82.4	51.9	0.433 ± 0.036	0.396 ± 0.046	0.454 ± 0.032
s5	64.3	48.6	80.6	52.9	0.424 ± 0.044	0.389 ± 0.052	0.441 ± 0.033
2008-04-19 U1U4							
s2	83.3	98.1	128.7	40.3	0.540 ± 0.026	0.469 ± 0.039	0.470 ± 0.025
s3	87.2	95.3	129.2	42.5	0.547 ± 0.029	0.458 ± 0.038	0.459 ± 0.025
2008-04-21 U3U4							
s1	53.4	2.5	53.5	87.3	0.487 ± 0.034	0.566 ± 0.033	0.584 ± 0.022
s4	58.7	-19.4	61.8	108.3	0.534 ± 0.028	0.564 ± 0.033	0.561 ± 0.023
s5	51.4	-34.6	62.0	124.0	0.595 ± 0.025	0.524 ± 0.035	0.537 ± 0.024
s6	49.9	-36.4	61.8	126.1	0.599 ± 0.027	0.506 ± 0.037	0.526 ± 0.023
s9	10.3	-54.5	55.4	169.3	0.279 ± 0.041	0.329 ± 0.048	0.424 ± 0.028
s10	7.4	-54.8	55.3	172.3	0.342 ± 0.036	0.410 ± 0.038	0.493 ± 0.025
2008-04-23 U2U4							
s1	61.0	52.8	80.7	49.1	0.336 ± 0.041	0.369 ± 0.045	0.426 ± 0.028
s2	70.4	45.6	83.9	57.1	0.515 ± 0.027	0.494 ± 0.037	0.546 ± 0.022
s8	87.2	-1.8	87.2	91.2	0.527 ± 0.031	0.462 ± 0.038	0.500 ± 0.024
s9	75.6	-22.6	78.9	106.6	0.628 ± 0.029	0.585 ± 0.038	0.644 ± 0.023

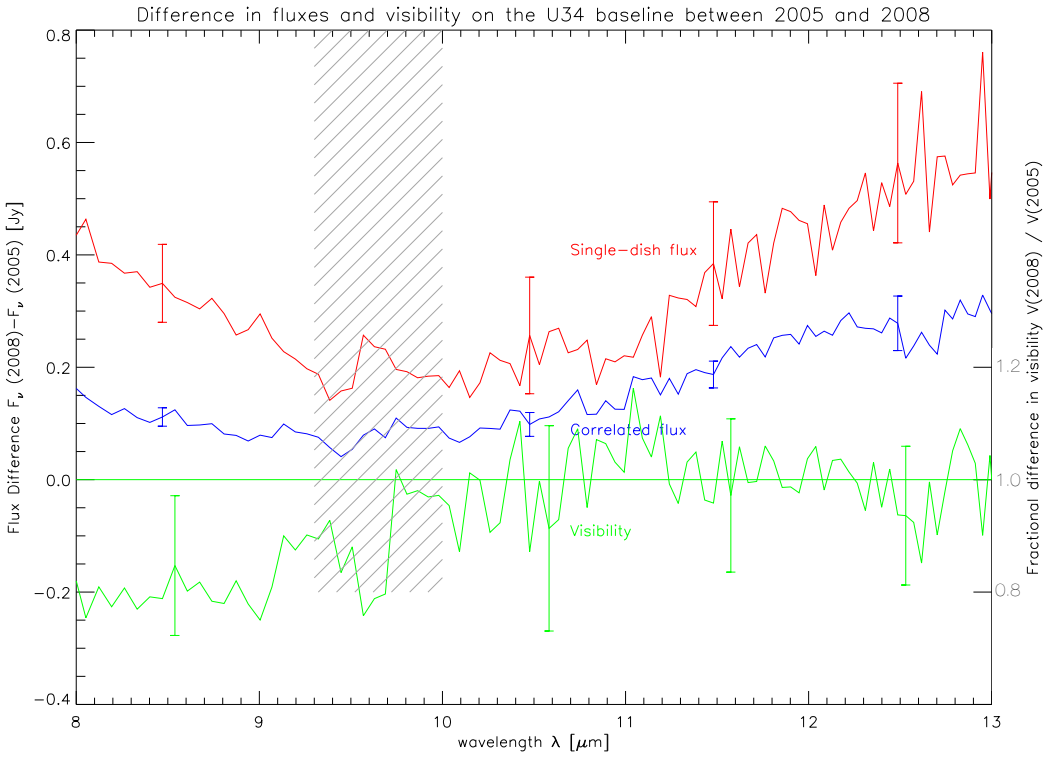

Figure 2.6.: Difference of the correlated (blue curve) and single-dish fluxes (red curve) and visibilities (green curve) between the 2005 and 2008 observations. For the correlated fluxes and visibilities, the average of the fringe tracks s1, s4, s5, s6 for the observations on 2008-04-21 and the average of the fringe tracks s4 and s6 (on 2005-02-28) were taken into account. They were observed at very similar (u, v) points (see Figures 2.2 and 2.5). The difference in visibility is consistent with no change (green straight line). The region of telluric ozone absorption is hatched as it is untrustworthy, especially in the single-dish fluxes and the visibilities. The error bars of the three curves are slightly offset for clarity.

2.4). In Figure 2.6 the increase in the average correlated and total flux is plotted (together with the difference in visibility). The source increased its total flux by ≈ 350 mJy at 8.5 μm , ≈ 250 mJy at 10.5 μm and ≈ 550 mJy at 12.5 μm .

The correlated flux also increased. However, comparing correlated fluxes requires some caution. Since they, in general, depend on (u, v) coordinates, one must take observations at sufficiently similar (u, v) coordinates to compare them over time. In other words: The maximum separation two (u, v) points may have to still show identical correlated fluxes depends on the structure of the source: For an unresolved or over-resolved source, the correlated flux is identical at all (u, v) points (namely V=1 or V=0, respectively); for a complex source, though, it may vary already between two points that are separated by about one telescope diameter. Since the detailed structure of the source was unknown in advance, we re-observed three (u, v) points on the U3U4 baseline in 2008 (s1, s4, and s5/s6) that are interlaced with two observations that were taken in 2005 (s4 and s6), see the (u, v) coverage in Figure 2.2. As can be seen from Figure 2.3, the two red spectra of the 2005 U3U4 measurements are comparable to each other and the same is true for the three orange/red spectra of the 2008 U3U4 measurements. In order to compare them, we therefore compute from them an averaged 2005 and an averaged 2008 correlated flux of this (u, v) region and plot the difference. This is shown in Figure 2.6. The increase of correlated flux at ≈ 60m/100° in April 2008 with respect to February / May 2005 is ≈ 100 mJy at 8.5 μm and 10.5 μm and ≈ 250 mJy at 12.5 μm .

In terms of visibility change, the source's brightness increase is consistent with no change in visibility at all wavelengths, i.e. the correlated flux increased roughly by the same *factor* as the total flux.

2.4. Modelling

2.4.1. Considerations for model fitting

With phase-less data on sparsely sampled (u, v) planes (see Figure 2.2), it is impossible to reconstruct meaningful images directly, i.e. images that show more than just the properties of the synthesized beam. We therefore model the source brightness distribution (the "image") with simple geometrical components (e.g. point sources, Gaussians, rings, ellipses etc.) and constrain the parameters of the model with the observed visibilities, see Section 1.2.5 and, e.g., Berger & Segransan (2007).

Here we present our model fit to the averaged visibilities at 8.5, 10.5 and 12.5 μm. The wavelengths were chosen to be safely outside the low signal/noise regions at the edges of the N band and outside of the region of ozone absorption. They also avoid the [Ne II] 12.81 μm forbidden line that is seen in the single-dish spectra. The fits were performed with Lyon's Interferometric Tool prototype (LITpro), an interferometric model fitting tool, provided by the Jean-Marie Mariotti Center (JMMC, Tallon-Bosc et al. 2008)[7]. It is based on a modified Levenberg-Marquardt algorithm to find the least χ^2 value (within

[7]The online version of LITpro can be found at http://www.jmmc.fr/litpro_page.htm

given parameter boundaries) and provides a graphical user interface to examine the (u, v) plane with a number of geometrical models.
Since the brightness increase between the 2005 and 2008 observations could have caused a change in the structure of the source, we treat the two epochs as probing separate source states and only take into account the data from the 2008 epoch for the geometric fits. We cannot perform the same kind of fit for the 2005 observations since this exploratory observation sampled the (u, v) plane too sparsely to constrain model parameters in a geometrical model fit.
From examining the visibilities of the 2008 epoch on the (u, v) plane (Figure 2.5), it is not obvious which structure they probe. To nonetheless get a reliable impression of the source brightness distribution responsible for the visibility pattern, we will approach it with a set of geometrical models based on the following observations:

- The visibilities are not very different over the entire (u, v) plane. They are significantly larger than 0 and lower than 1 at every point. This suggest a combination of an (unresolved) point source and an (over-resolved) larger source.
- The visibilities in the north-east ($0° < \mathrm{PA} < 90°$) tend to be larger than the ones at $90° < \mathrm{PA} < 180°$. This effect is strongest at 8.5 μm and could indicate an elongated structure.
- Furthermore, and again most readily seen at 8.5 μm, not all visibilities in the north-east are larger than the ones in the south-east. Rather, they seem to show a co-sinusoidal pattern in the (u, v) plane, centered at (0,0), with a period of roughly 50m. Its normal is at a position angle of ca. 45° (see below for a more detailed explanation and figures).
- Between 2005 and 2008 the source brightened considerably, but the visibility (on one baseline) stayed more or less constant (see Figures 2.5 and 2.6). We will discuss potential scenarios for the luminosity increase in Section 2.5.

2.4.2. Geometrical models for the surface brightness distribution

Starting from these observations, we will add complexity to the simple-most model by adding (free) parameters until we reach a satisfactory fit with a reduced χ^2_r of the order of 1.

The model geometries are shown in Figure 2.7 and the coordinate system used to describe the locations of the components in real space is (x, y) = (RA, DEC) in units of mas. Analytic transforms of some of the "building block" functions which constitute the models were given in Section 1.2.5. A critical discussion of the model fits is given in Section 2.5.

Model a: Point source + concentric circular Gaussian The simple most explanation of the visibilities, model *a*, consists of a point source that contributes the flux fraction f_p

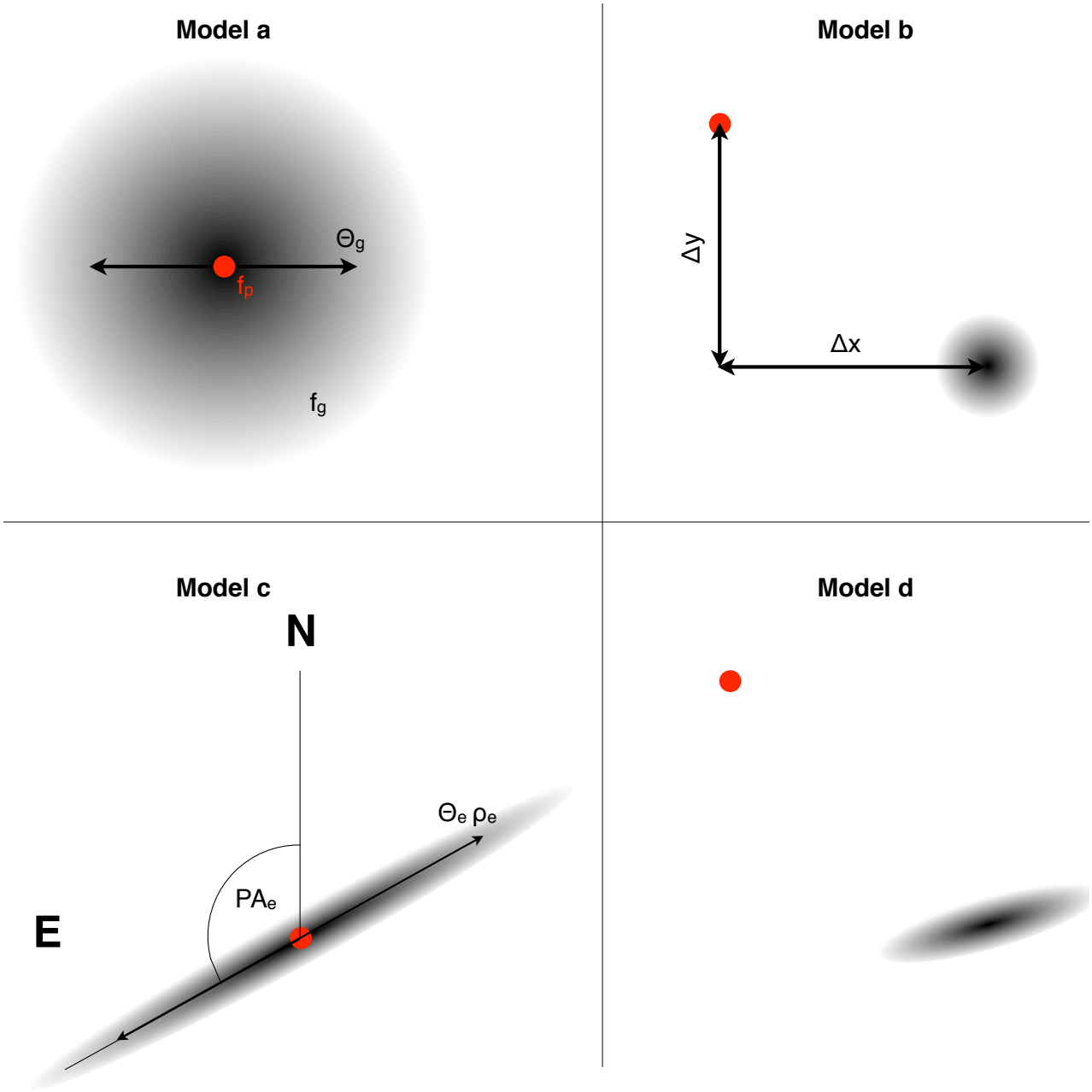

Figure 2.7.: Geometrical models for the visibilities (here in real space). The fitted parameters are marked in the model images (where they are introduced) and explained in Section 2.4 for the various models.

Table 2.3.: Best-fitting parameters for the fits of the geometrical models *a* and *b* to the averaged visibilities of Centaurus A at 8.5, 10.5 and 12.5 μm . Fixed parameter values are given in brackets. For convenience, the flux contributions of the two components are also given in units of Jy (F_p and F_g). See the text for an explanation of the parameters of the model components point source (p) and Gaussian source.

	model	a			b		
	λ	8.5 μm	10.5 μm	12.5 μm	8.5 μm	10.5 μm	12.5 μm
p	f_p	0.57 ± 0.14	0.51 ± 0.12	0.53 ± 0.13	0.59 ± 0.14	0.50 ± 0.12	0.53 ± 0.13
	F_p [Jy]	0.51 ± 0.13	0.40 ± 0.09	0.97 ± 0.24	0.52 ± 0.13	0.40 ± 0.09	0.97 ± 0.24
Gauss	f_g	0.43 ± 0.10	0.49 ± 0.12	0.47 ± 0.11	0.41 ± 0.10	0.50 ± 0.12	0.47 ± 0.11
	F_g [Jy]	0.39 ± 0.09	0.39 ± 0.09	0.86 ± 0.20	0.37 ± 0.09	0.40 ± 0.09	0.86 ± 0.20
	Δx	(0)	(0)	(0)	26.0 ± 0.2	4.9 ± 1.7	5.2 ± 2.5
	Δy	(0)	(0)	(0)	23.4 ± 0.4	20.7 ± 3.3	25.5 ± 4.7
	Θ_g	($\gtrsim$ 40)	($\gtrsim$ 50)	($\gtrsim$ 60)	9.6 ± 0.4	20.7 ± 3.3	31.4 ± 1.9
	# DOF	15			12		
	χ^2	348	84	134	169	51	104
	χ^2_r	23.2	5.6	8.9	14.0	4.2	8.7

(flux F_p) and a circularly symmetric Gaussian with a FWHM of Θ_g that contributes the flux fraction f_g (flux F_g) to the total flux (see Figure 2.7 for a sketch of the model). The two sources are concentric, i.e. Δx, Δy are fixed at 0.

In the (u, v) plane, this transforms to a Gaussian drop-off of the visibilities from 100 % at $(u, v) = (0, 0)$, asymptotically reaching f_p at baselines $\gg \lambda/\Theta_g$.

The (u, v) plane fit is visualized in Figure 2.8 and the best-fitting parameters for this model are given in Table 2.3.

Since the visibilities do not show a radial drop-off, we cannot constrain Θ_g with this model, but only give a *lower* limit that corresponds to a fully resolved Gaussian component at the shortest baselines. Note that this limit increases from ≈ 40 mas at 8.5 μm to 60 mas $\approx 12.5/8.5 \cdot 40$ mas at 12.5 μm , i.e. the size is less well constrained at 12.5 μm because the resolution is lower. Within the errors, the point source and the over-resolved Gaussian contribute the same to the total flux at all wavelengths. With 15 degrees of freedom (N_{free}), this model yields $\chi^2_r = \chi^2/N_{\text{free}}$ values of 23.2, 5.6 and 8.9 for the 8.5 μm , 10.5 μm , 12.5 μm fit respectively. Following tests of systematic errors and a careful treatment of the statistical errors, this model must be excluded. In other words: the model residuals are much larger than any reasonable estimate of the uncertainties of the data. A more complex model is needed.

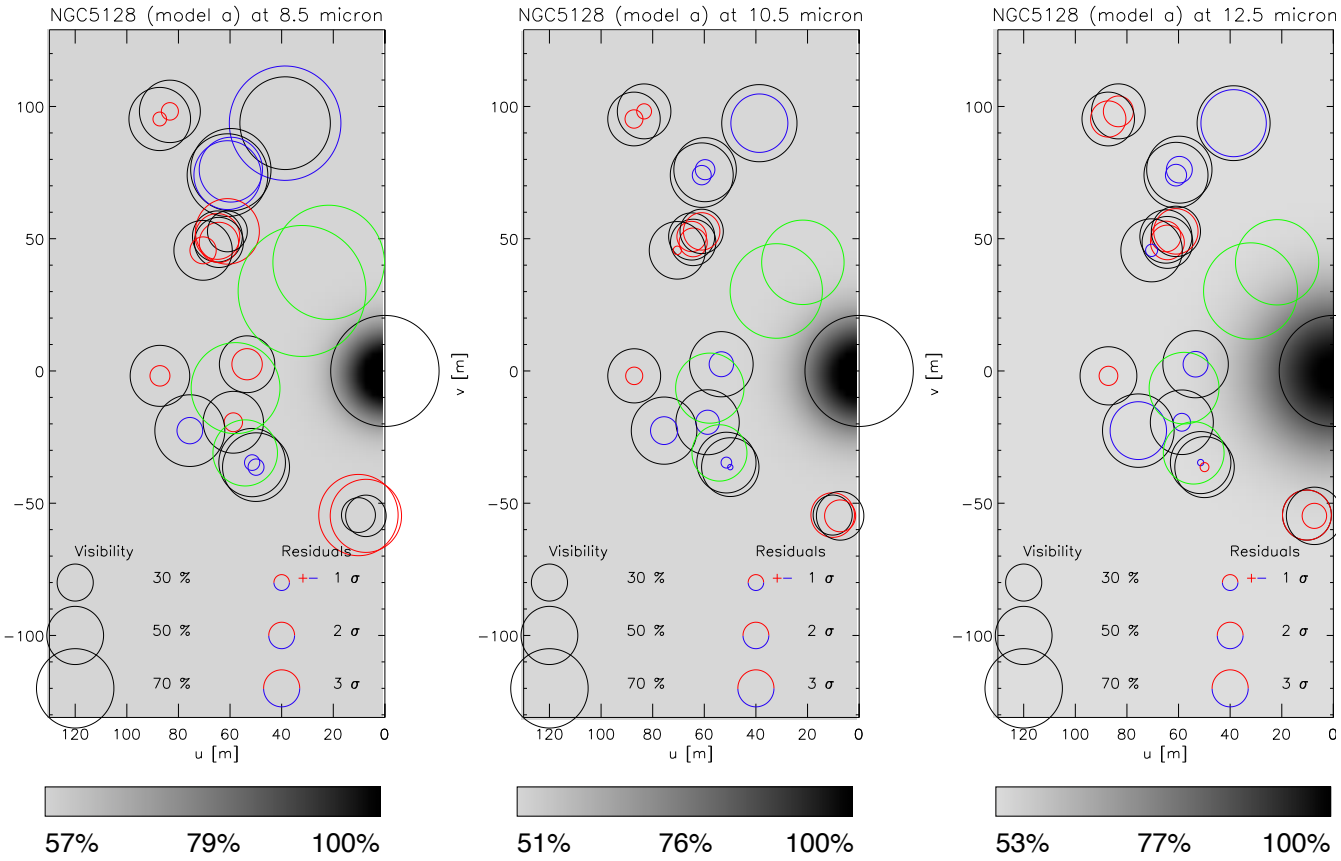

Figure 2.8.: *Model a:* Visibilities, averaged at 8.5 ± 0.2 μm , 10.5 ± 0.2 μm and 12.5 ± 0.2 μm in the (u, v) plane. Each circle (green: 2005, black: 2008) represents a visibility measurement; the radius denotes the visibility amplitude (see legend in plot). The large circle at the origin stands for the single-dish flux that corresponds to $V = 1$. The statistical errors of these visibilities are given in Table 2.2 and are not shown in the plot for clarity. Concentric to each black circle is a second circle whose radius denotes the model residual $|V_{\rm obs} - V_{\rm model}|$ (in units of σ, see legend in plot) at this point in (u, v) space. If $V_{\rm obs} - V_{\rm model} > 0$, this circle is plotted in blue, otherwise in red. The model visibilities are shown in greyscale in the backdrop image and the scaling is given below the (u, v) plane plot.
In real space, this model consists of a circularly symmetric Gaussian and a concentric, unresolved point source. The best fitting parameters of this model are given in Table 2.3.
Note that only half of the (u, v) plane is shown (the other half is point-symmetric to the one shown).

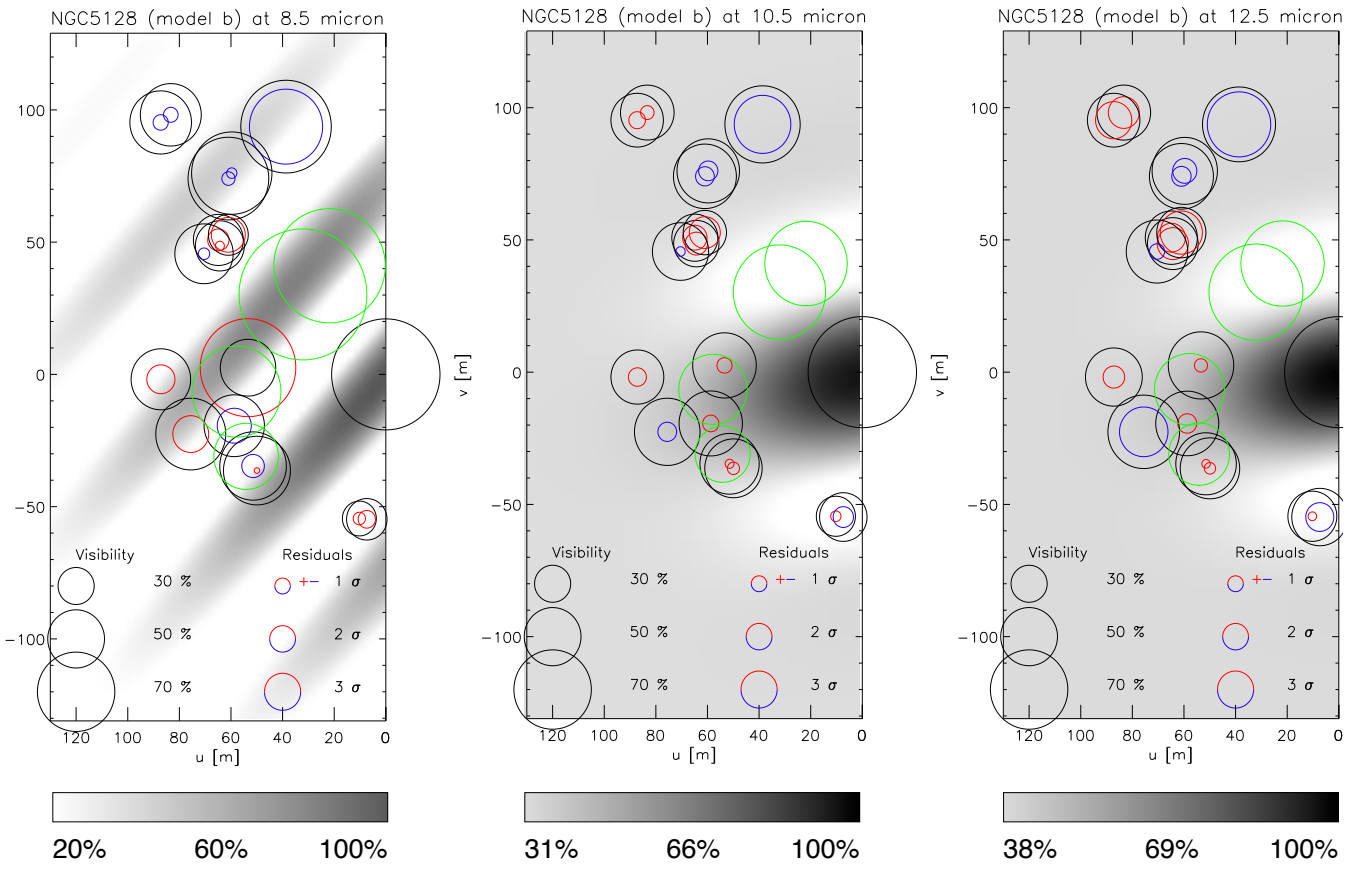

Figure 2.9.: *Model b:* Visibility model and residuals plot in the (u, v) plane (see the caption of Figure 2.8 for details).
In real space, this model consists of an unresolved point source and a circularly symmetric Gaussian that is offset from the point source by 35, 21, 26 mas at a position angle of 45°, 13°, 12° at 8.5 μm, 10.5 μm, 12.5 μm, respectively. The best fitting parameters of this model are given in Table 2.3.

Model b: Point source + offset circular Gaussian In model b the same components as in model a are employed, but we no longer fix the center of the Gaussian component to $(x, y) = (0,0)$. Due to the lack of absolute astrometry and phase information, we can in fact only constrain an offset between the two sources and not their absolute positions. This implies that the source positions are interchangeable. We therefore give *offsets* $(\Delta x, \Delta y)$ *between* the components rather than their *positions*. See Figure 2.7 for a sketch of the model.

The best-fitting parameters for this model are given in Table 2.3 and the (u, v) plane fit is visualized in Figure 2.9.

For the 8.5 μm visibilities, the best-fitting offset is $(\Delta x, \Delta y) = (26.0, 23.4)$ mas or $\sqrt{\Delta x_{p2}^2 + \Delta y_{p2}^2} \approx 35$ mas at a position angle $\tan^{-1}(\Delta x_{p2}/\Delta y_{p2}) \approx 45°$ east of north. This offset matches well the co-sinusoidal pattern described before but the fringe contrast of that pattern decreases too fast because the Gauss is constrained to be large due to the low visibilities at short baselines. At other wavelengths, this pattern is not seen so strongly and the best fit is found for smaller offsets of 21 and 26 mas and for smaller position angles of 13° and 12° for the 10.5 μm and 12.5 μm fits, respectively. The sizes of the Gaussian range from a marginally resolved one at 8.5 μm to almost over-resolved ones at 10.5 μm and 12.5 μm . Within the errors, the point source and the over-resolved Gaussian contribute the same to the total flux at all wavelengths.

This model yields a significantly reduced χ^2 value of 14.0 at 8.5 μm but is only a minor improvement at the other two wavelengths.

Apparently, allowing an offset between the point source and the circular symmetric Gauss doesn't help since this model is torn between an under- and an over-resolved Gaussian: The first is needed to produce high visibilities ($\gtrsim$ 80% at 8.5 μm) at $(u, v) \approx (40, 100)$, the latter for shallow fringe contrasts ($\lesssim$ 30% at 8.5 μm) at $(u, v) \approx (10, -50)$ (see Figure 2.9). This cannot work and large residuals remain. The fact that the best-fit offset changes so drastically with wavelength is hard to explain physically and most probably a sign that this offset is not real.

Model c: Point source + concentric elongated Gaussian Model c explores the possibility of an elongated structure. It consists of a point source and a concentric elongated Gauss, i.e. it is the model discussed by Meisenheimer et al. (2007). The elongated Gauss is described by its axis ratio ρ, the FWHM of its *minor* axis Θ_e and the position angle PA (east of north) of the *major* axis (see Figure 2.7 for a sketch of the model). In fact, we cannot constrain ρ and Θ_e in any of the fits and only their product, i.e. the FWHM of the major axis is a meaningful number.

The best-fitting parameters for this model are given in Table 2.4 and the (u, v) plane fit is visualized in Figure 2.10.

In this model, the major axis is $> \lambda/B$, i.e. over-resolved at the shortest baselines, and the minor axis is found to be point-like and responsible for the visibility variations in the north-eastern quadrant of the (u, v) plane. In effect, this fit describes a narrow "bar" in (u, v) space (see Figure 2.10) where visibilities are ≈ 1. Outside of the bar they drop

Table 2.4.: Best-fitting parameters for the fits of the geometrical models *c* and *d* to the averaged visibilities of Centaurus A at 8.5, 10.5 and 12.5 μm. Fixed parameter values are given in brackets. For convenience, the flux contributions of the two components are also given in units of Jy (F_p and F_e). See the text for an explanation of the parameters of the model components point source (p) and elongated Gaussian source.

	model	c			d		
	λ	8.5 μm	10.5 μm	12.5 μm	8.5 μm	10.5 μm	12.5 μm
p	f_p	0.51 ± 0.12	0.48 ± 0.12	0.52 ± 0.13	0.57 ± 0.14	0.52 ± 0.13	0.55 ± 0.13
	F_p [Jy]	0.46 ± 0.11	0.38 ± 0.09	0.95 ± 0.24	0.51 ± 0.13	0.41 ± 0.10	1.00 ± 0.24
Elong. Gauss	f_e	0.49 ± 0.12	0.52 ± 0.13	0.48 ± 0.12	0.43 ± 0.11	0.48 ± 0.12	0.45 ± 0.11
	F_e [Jy]	0.44 ± 0.11	0.41 ± 0.10	0.88 ± 0.22	0.39 ± 0.10	0.38 ± 0.09	0.82 ± 0.20
	Δx	(0)	(0)	(0)	25.0 ± 0.7	27.7 ± 1.3	32.2 ± 1.6
	Δy	(0)	(0)	(0)	23.4 ± 0.5	28.6 ± 1.2	34.3 ± 0.7
	PA_e	119.2 ± 0.4	118.8 ± 1.3	119.2 ± 1.7	105.7 ± 3.6	111.7 ± 4.3	115.5 ± 1.5
	$\Theta_e \cdot \rho_e$	≈60	≈100	≈ 130	≈ 22	≈ 35	≈ 48
	# DOF	12			10		
	χ^2	141	51	89	46	16	41
	χ^2_r	11.7	4.2	7.4	4.6	1.6	4.1

quickly to f_p. The best fitting position angle of this structure is 119° (at all wavelengths) in real space which translates to 119°-90° = 29° in (u, v) space. Within the errors, the point source and the over-resolved Gaussian again contribute the same to the total flux at all wavelengths. The PA is not well constrained in this model. In fact, Burtscher et al. (2010) found a fit to the 12.5 μm visibilities with very similar χ^2_r for a position angle of 15°.

Compared to model *b*, this model yields another significant reduction of χ^2_r at 8.5 μm, but only a minor improvement at 12.5 μm and no change at 10.5 μm.

Model d: Point source + offset elongated Gaussian Finally, we allow an offset $(\Delta x, \Delta y)$ between the point source and the elongated Gauss of model *c* (see Figure 2.7 for a sketch of the model). For the offset, the same restrictions apply as mentioned above for model *b*.

This model has two almost equally good (in terms of χ^2_r) solutions for very different values of $(\Delta x, \Delta y)$. The formally best model (with χ^2_r = 3.3, 1.4, 4.0) is found for offsets of $(\Delta x, \Delta y) \approx (20, -12), (30, -16), (41, -24)$ at 8.5 μm, 10.5 μm, 12.5 μm, respectively. The second best model (with χ^2_r = 4.6, 1.6, 4.1) is found for offsets of $(\Delta x, \Delta y) \approx (25, 23), (28, 29), (32, 34)$. The other fitted parameters $(f_g, f_e, PA, \Theta_e, \rho_e)$ are similar for

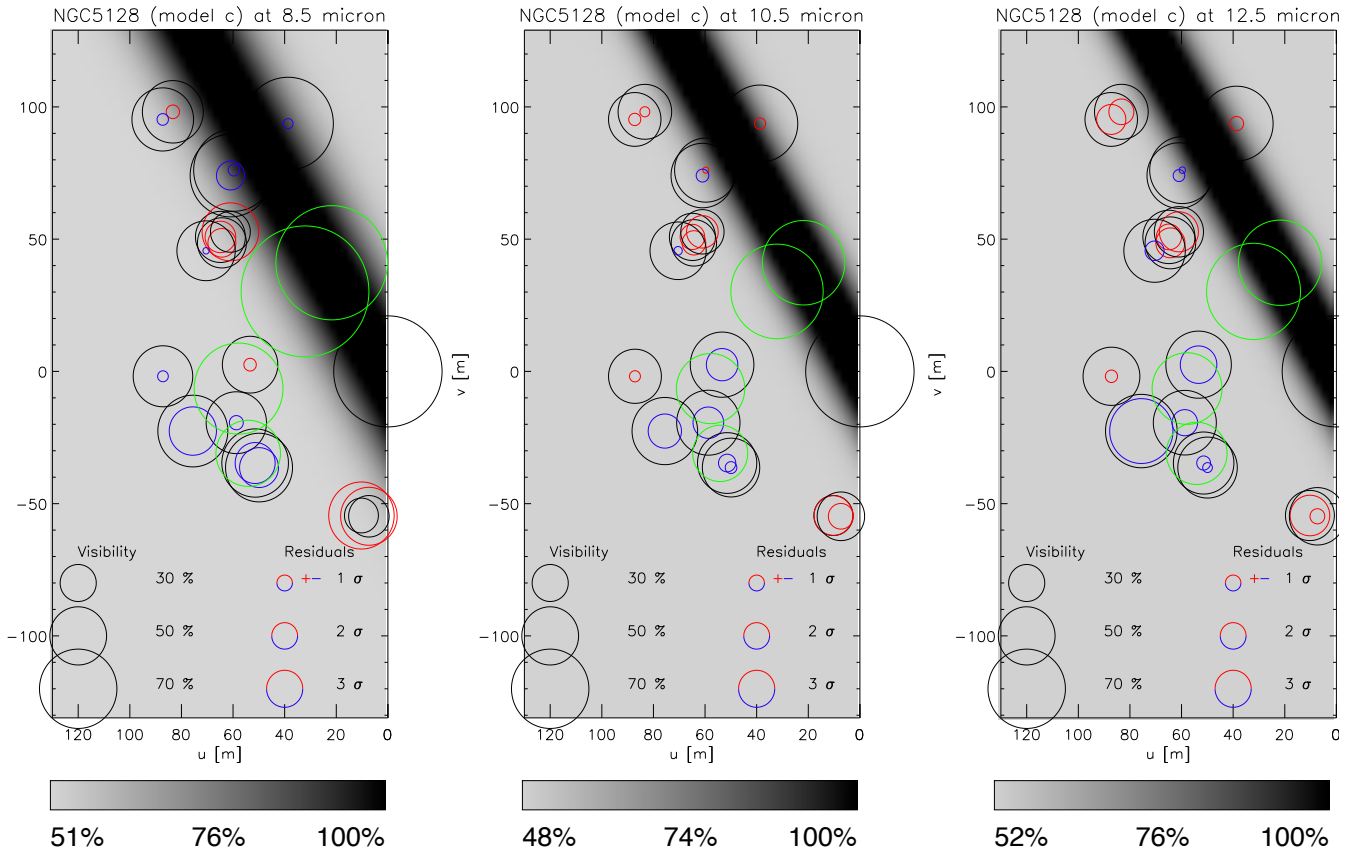

Figure 2.10.: *Model c:* Visibility model and residuals plot in the (u, v) plane (see the caption of Figure 2.8 for details).
In real space, this model consists of an unresolved point source and a concentric elongated Gaussian. The position angle of the elongated Gaussian is 119°; its minor axis is point-like and the major axis is nearly over-resolved. This results in a narrow bar in the (u, v) plane at a position angle of 119°-90° = 29°. The best fitting parameters of this model are given in Table 2.4.

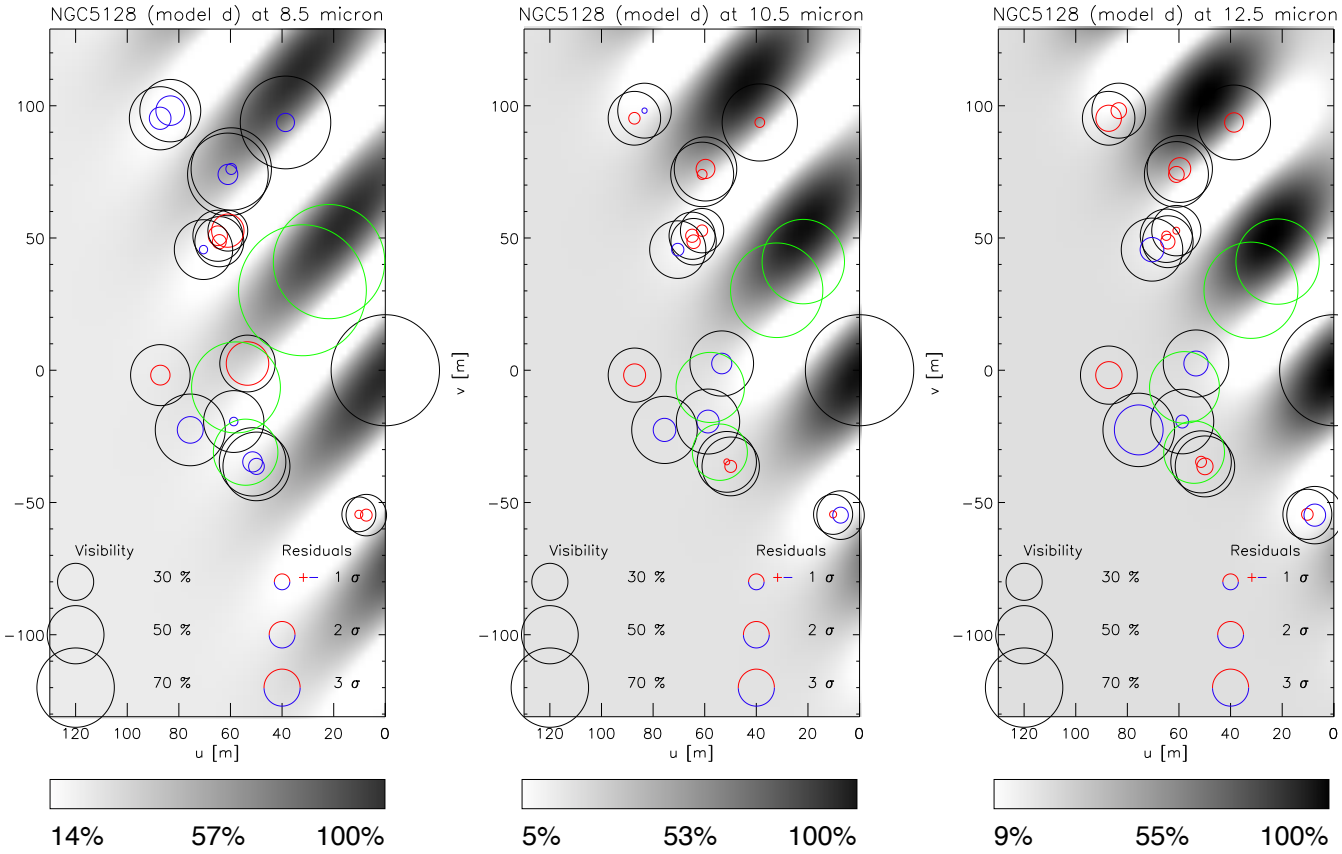

Figure 2.11.: *Model d:* Visibility model and residuals plot in the (u, v) plane (see the caption of Figure 2.8 for details).
In real space, this model consists of an unresolved point source and an elongated Gaussian that is offset from the point source by 34, 40 and 47 mas at $47°, 44°$ and $43°$ for the 8.5 μm , 10.5 μm and 12.5 μm fits respectively. The position angle of the elongated Gauss is $\approx 110°$; its minor axis is point-like and the major axis is nearly over-resolved. Together with the offset point source, this results in a co-sinusoidal pattern in the (u, v) plane at a position angle of $\approx 110° - 90° \approx 20°$. The fringe contrast in that direction does not decrease because of the point-like minor axis; in the orthogonal direction it decreases rapidly due to the relatively large major axis of the elongated Gauss. Note that the visibility decreases to very low values where the offset point source interferes destructively with the elongated Gaussian component. The best fitting parameters of this model are given in Table 2.4.

the two models. The ambiguity in $(\Delta x, \Delta y)$ can be most clearly seen in the respective χ^2 planes, shown in Figure 2.12: At 8.5 μm, actually three minima can be seen (the ones given above and additionally at $\approx$ (20,-45)).[8] The latter minimum is not seen at other wavelengths and therefore rejected.

With regard to the width of the χ^2_r distribution for this model, $\sigma_{\chi^2_r} = \sqrt{2/N_{\rm free}} = 0.45$, only at 8.5 μm a marginally significant difference can be claimed for the goodness of fit between the two offsets.

However, in the model with the formally best fit, the offset position changes drastically between the wavelengths. This is not expected for a real source. In the second best fit, the offset position also changes with wavelength, but roughly according to the wavelength ratio which can be understood as an effect of the sparsely sampled (u, v) plane.[9]

We therefore report the best fitting parameters of the fit with the more consistent $(\Delta x, \Delta y)$ values over wavelength. These parameters are given in Table 2.4 and the (u, v) plane fit is visualized in Figure 2.11. Again, the elongated Gauss' minor axis is point-like and the major axis is close to being over-resolved at all wavelengths. This leads again to a "bar-like" structure as in model *c* – but now co-sinusoidally modulated due to the offset of the two source components. The offsets found in this fit correspond to $\sqrt{(\Delta x)^2 + (\Delta y)^2} \approx 34$, 40 and 47 mas at 47°, 44° and 43° for the 8.5 μm, 10.5 μm and 12.5 μm fits respectively. The position angle of the elongated Gauss is smaller than in model *c*. Within the errors, the point source and the over-resolved Gaussian contribute the same to the total flux at all wavelengths.

This model, that has lost two degrees of freedom in comparison with model *c*, is a significant improvement in terms of χ^2_r at all wavelengths, leading to acceptable values of $\chi^2_r = 4.6$, 1.6, 4.1 at 8.5 μm, 10.5 μm and 12.5 μm respectively.

Cuts through the χ^2 space (Figure 2.12) demonstrate the parameter constraints: The position angle and the relative flux levels of the point source and the elongated Gaussian are well defined. Regarding ρ and Θ, only their product is constrained and the $(\Delta x, \Delta y)$ χ^2 plane is complex.

[8] In Figure 2.12, the $(\Delta x, \Delta y)$ landscape is plotted only for Δx = [0,50] mas and Δy = [-50, 50] mas, since it repeats for larger offsets, see Figure 2.13 for a demonstration at 10.5 μm. For this model, the distance between the maxima of the fringe pattern in the (u, v) plane (see Figure 2.11) is set by the offset of the two components. Multiples of this offset lead to accordingly decreased distances in the (u, v) plane (cf. "harmonics of a wave"). Offsets $\gtrsim$ 50 mas lead to fringe patterns that show variations on scales $\lesssim$ the telescope diameter in the (u, v) plane and are therefore likely to fit noise rather than real structure. We therefore choose the smallest offsets compatible with the data.

[9] If the offsets were identical at all wavelengths, then the true maximum of the fringe pattern produced by the offset source (see Figure 2.11) would be at the same spatial frequencies at all wavelengths. In a (u, v) plot in units of meters (such as Figure 2.11), the maximum would then move to longer baselines for longer wavelengths. Due to the sparsely sampled (u, v) plane, this cannot be excluded by the data: It is quite possible that the true maximum is only seen at 8.5 μm (at $(u, v) \approx$ (50,80)), where the visibilities are highest, and that at other wavelengths only the wings are seen. The errors of $(\Delta x, \Delta y)$ only describe the statistical uncertainties of the offset position. The systematic uncertainties due to the asymmetric and sparse (u, v) coverage are larger but hard to quantify. For the same reason, the derived position angle must be taken with care.

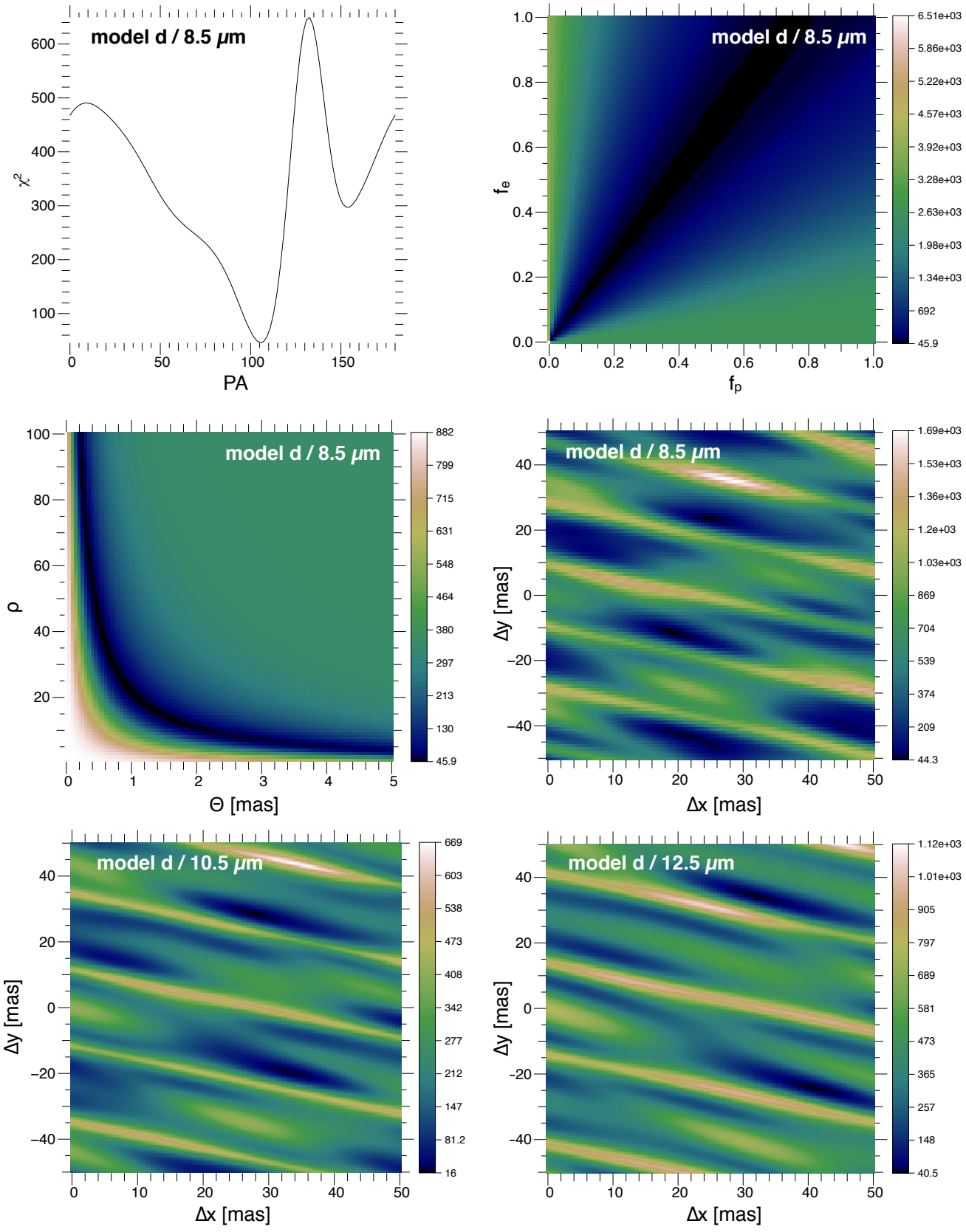

Figure 2.12.: Cuts through the χ^2 landscape for model *d*. See text for details.

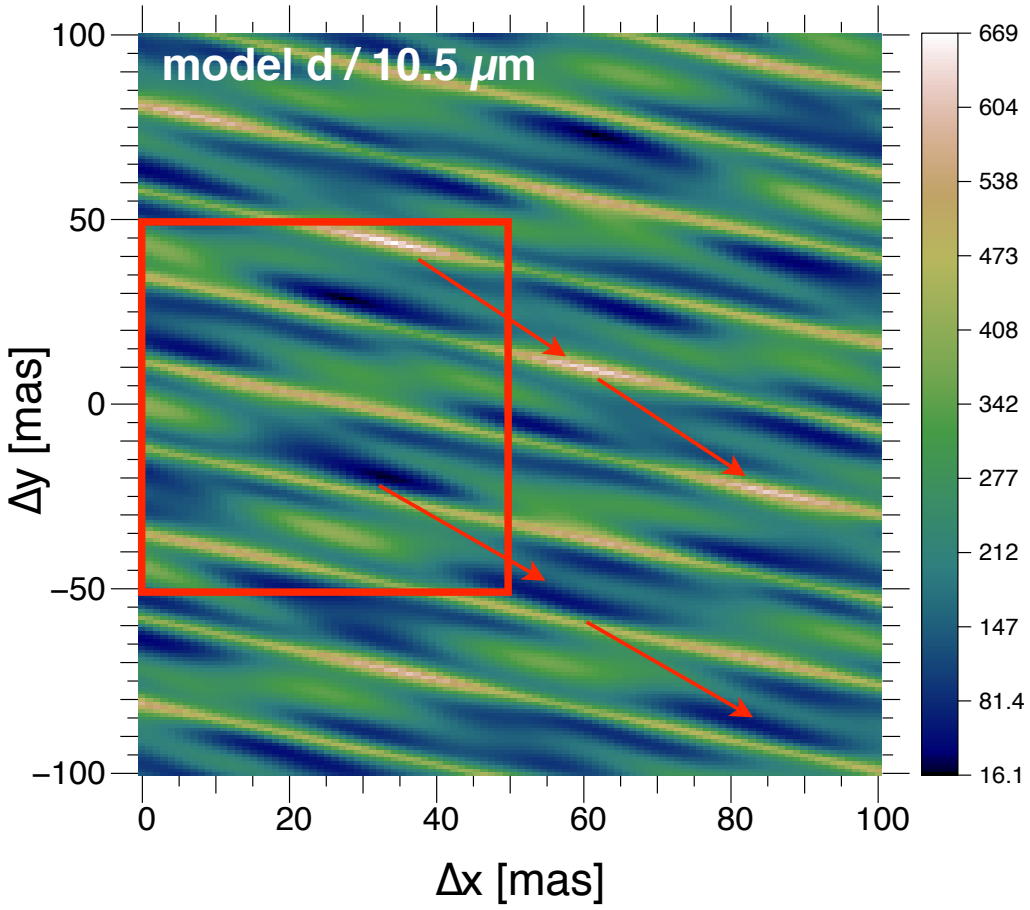

Figure 2.13.: Cut through the χ^2 landscape for model d at 10.5 μm with a larger plot range showing that the χ^2 landscape is repeated beyond $(\Delta x, \Delta y) \approx (50, 50)$ mas (the red box). An example for a repeated maximum and for a minimum in the χ^2 plane are drawn with arrows.

2.5. Discussion

The discussion is structured as follows: First, a critical discussion of the model fits is given and the spectra of the source components are briefly discussed. Next, variability is studied. Taken together, astrophysical scenarios are sketched. At the end, we compare these observations to other MIDI observations of AGNs.

2.5.1. Geometrical model fits

Summary One of the most crucial aspects of χ^2 fitting is the correct determination of the statistical errors. Only with realistically estimated uncertainties can the value of χ^2_r be used to estimate the quality of the fit. For the data modeled here, the errors have been computed taking into account the rms noise of the individual observations and the uncertainties of the calibration templates. By repeating an observation we made sure that systematic errors do not dominate over the statistical ones.

In conclusion, models *a* (concentric point source and circularly symmetric Gaussian), *b* (offset point source and circularly symmetric Gaussian) and *c* (concentric point source and elongated Gauss) must be rejected because no fit could be found that results in a χ^2_r near the desired value of 1.

This leaves us with model *d*, the point source and offset elongated Gaussian. It has two equally good solutions for $(\Delta x, \Delta y)$. In both, the offset between the two sources differs significantly from wavelength to wavelength. While the marginally better fit has offset differences that cannot be explained, the second solution's offset differences can be explained as effects arising from the sparse (u, v) sampling. Model *d*, with the parameter values reported in Table 2.4, is therefore our best geometrical explanation for the visibility pattern.

It is worth noting, that in all models the best fit is achieved at 10.5±0.2 μm. The reason for this is simple: At this wavelength regime, near the bottom of the pronounced Silicate absorption trough, the signal-to-noise ratio is lowest (the errors are largest) and therefore the residuals in units of σ are smallest. However, since there is no reason why the structure should be better described by our model geometry at 10.5 μm than at 8.5 μm or 12.5 μm, we conclude that either the errors at 10.5 μm are *over*-estimated by a factor of $\sqrt{\chi^2_r(8.5\mu\text{m})/\chi^2_r(10.5\mu\text{m})} \approx 1.7$ or the errors at 8.5 μm and 12.5 μm are *under*-estimated by the same factor.

Spectral Index of the model components So far we have concentrated on fits at three distinct wavelengths. Combining the results at these wavelengths gives an estimate of the spectral index[10] of the fitted components. The contributions of the two components of model *d* are consistent with both the point source and the extended source having similar

[10]Note that calculating a spectral index out of a fit of a geometrical model to interferometric data can be dangerous since the resolution is higher at 8.5 μm than at 12.5 μm. Effectively we are observing with a larger aperture at 12.5 μm compared to 8.5 μm. The fitted 12.5 μm flux is thus an upper limit to the "true" 12.5 μm flux (that would be observed with a hypothetical, smaller, 8.5 μm effective aperture).

spectra, e.g. a flat, $F_\nu \propto \nu^{-0.36}$, power-law spectrum (as inferred from the synchrotron model of Meisenheimer et al. (2007) for the point source) or a warm ($\approx$ 500K) blackbody spectrum.

The visibilities show no Silicate feature, because the depth of this feature is identical (within the errors) in the single-dish spectra and the correlated spectra. In the context of geometrical model *d*, this implies that the optical depth to dust obscuration is constant within the central ca. 50 mas (see Figure 2.16).

The 2005 observations Although the 2005 observations were not included in the fit, they are also plotted in the model images, Figure 2.8 - 2.11, for comparison. Models *a* and *b* are even stronger rejected when adding the 2005 observations. Model *c* was discussed in Meisenheimer et al. (2007) as a possible interpretation for the 2005 visibilities. For the following discussion, it is interesting to note that model *d*, optimized just for the 2008 visibilities, seems to be a relatively good model for the 2005 visibilities, too (see Figure 2.11).

2.5.2. Variability

The correlated and total flux of Centaurus A changed in such a way between our 2005 and 2008 observations as to leave the visibilities on the U34 baseline unchanged. What does this tell us about the source morphology, if we assume that model *d* is a valid description of the 2008 morphology?

Basically, two scenarios are possible

1. Either the *geometry did not change*, implying that both components brightened. In the context of model *d*, the minimum separation between the two source components is 34 mas, corresponding to about 2 light years in Cen A. Since the observations are about 3 years apart, the brightness increase in the two components can be causally connected. Also, the 2005 observations are compatible with the existence of a point source and an elongated Gauss.

2. The other possible scenario is that only one component increased its flux, implying a *change in geometry* to keep the visibilities constant. Would that mean that one of the components moved? In this case the three years of time difference between the two epochs would require velocities near *c*, too fast for a moving dust cloud (the dust would be rapidly destroyed by shocks) and untypically fast for the moving knots in the jet.

In order to understand the origin of the variability, it would therefore be helpful to get an estimate of *when* the increase in flux occurred.

Variability time constraints from an IR-X-Ray correlation Since Cen A is not continually monitored in the mid-infrared, the precise date of flux increase in this waveband cannot easily be reconstructed. However, there is one observation that directly helps to

Table 2.5.: Correlation between X-Ray counts and mid IR flux for Centaurus A

Date	MJD	MIR flux [Jy] at 11.7 μm	XTE counts at MJD-50	IR flux / X-Ray counts Jy / (counts/s)	Reference & Notes
2002-01-30	52304	≈ 1.3	0.89	1.5	(1)
2002-06-28	52453	1.6 ± 0.2	0.78	2.1	(2)
2005-02-28	53429	1.10 ± 0.08	0.50	2.2	(3)
2006-03-15	53809	1.150 ± 0.005	0.57	2.0	(4)
2006-12-27	54096	≈ 1.1	0.58	1.9	(5)
2008-04-20	54576	1.50 ± 0.05	0.95	1.6	(3)

References: (1): Siebenmorgen et al. (2004) measured 650 mJy at 10.4 μm using the TIMMI2 mid-infrared camera at the ESO 3.6 m telescope. Using a factor of 2 (derived from our 2005 and 2008 spectra) to convert this 10.4 μm flux to an 11.7 μm flux, we arrive at the quoted 1.3 Jy.[11]
(2): Whysong & Antonucci (2004); Keck I telescope
(3): our observations
(4): Reunanen et al. (2010); VISIR/VLT
(5): van der Wolk et al. (2010); VISIR / VLT. Their flux was given at 11.85 μm and a spectral correction factor of ≈ 0.9 was applied to estimate an 11.7 μm flux.

constrain the date. On 2006-12-27, van der Wolk et al. (2010) used the VISIR instrument on the VLT UT3 and observed a core flux at 11.85 μm of (1200 ± 47) mJy, very compatible with our 2005 photometry and significantly lower than our 2008 observation. Since the VISIR aperture is very similar to the one used for the MIDI total flux observations and since van der Wolk et al. (2010) saw Cen A essentially as a point source, we can directly compare their flux to our total flux measurement and find that the bulk of the flux increase must have occurred after van der Wolk et al. (2010)'s observation.

In 2007 there was unfortunately no observation of Centaurus A in the mid-infrared with a high-resolution camera (e.g. VLT / VISIR or Gemini-South / T-ReCS). In order to further constrain the date of flux increase, we therefore looked at monitoring data of the All Sky Monitor (ASM) onboard the Rossi X-Ray Timing Explorer (RXTE), see Figure 2.14. With this satellite, Cen A is monitored every day at 2-10 keV. When applying a time lag between the X-Ray counts and the IR flux of about 50 days (in the sense that the IR radiation follows the X-Ray radiation), then the IR flux appears to be correlated with the X-Ray counts since 2002 (see Table 2.5). The time lag of ≈ 50 days could be understood as the light travel time from the inner hot accretion disk (Evans et al. 2004) to the innermost radius of dust. The sublimation radius in Cen A was estimated by Meisenheimer et al. (2007) to be $\gtrsim 0.013$ pc (≈ 13 light days).

Turning again to Figure 2.14, the most prominent feature of this lightcurve actually is the strong outburst in mid-November 2007. Taken together with the apparent correlation between X-Ray counts and IR flux, we speculate that this outburst was responsible for the increase in IR flux between the two MIDI observations. The time difference between

the X-Ray flare[12] and our 2008 observations is then $\lesssim 8$ months.

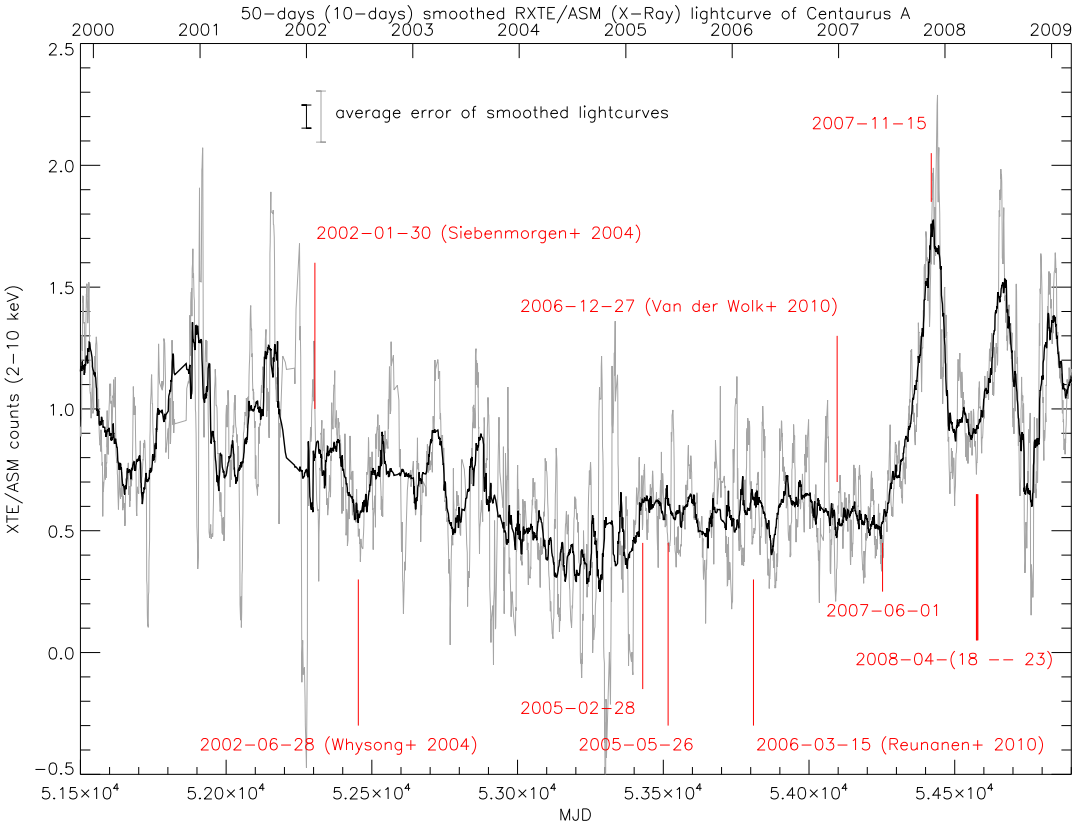

Figure 2.14.: X-Ray lightcurve from the All-Sky-Monitor (ASM) onboard the Rossi X-Ray Timing Explorer (RXTE), summed over all bands of the instrument and smoothed by 50 days (black curve) and 10 days (grey curve), respectively. The lower x axis displays the Modified Julian Date (MJD). The nights of the MIDI observations are marked. A rather quiescent X-Ray phase in 2005 is followed by a strong outburst in mid November 2007, five months before the second MIDI observations. The averaged X-Ray count rate is taken to be 0.6 (per second) at the 2005 observations and 0.9 in April 2008. For the other marked dates, see Table 2.5 and text.

VLBI monitoring For Cen A, correlations of flares in hard X-Rays with the appearance of new knots in the radio jet have been reported by Tingay et al. (1998). It is therefore tempting to look for new components that might have followed the X-Ray outburst in November 2007 and that could explain the increase in mid-IR flux. Tingay et al. (1998)

[12]Taking the half-rise date, i.e. when the X-Ray counts first reached the high level.

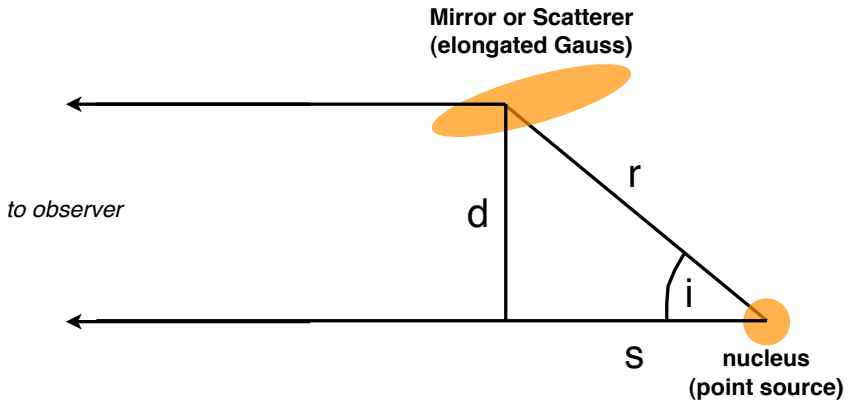

Figure 2.15.: Derivation of the position of the elongated Gauss, see text for explanation

also observed short-term (≈ months-scale) variability of the jet components in an 8.4 GHz light curve. Can we find a radio counterpart to the components of model *d* and did the radio morphology change between our two observations?

Although Centaurus A is very frequently observed using the highest resolution radio technique, Very Long Baseline Interferometry (VLBI), there have been no observations between the extensive monitoring campaign of Tingay et al. (2001) that ended in January 2000 and Tingay & Lenc (2009) who published a 2.3 GHz map of June 2007, i.e. five months before the X-Ray flare (Steven Tingay, pers. comm.). Müller et al. (2010) and Müller (2010) report a series of VLBI observations at 8.4 GHz from the time of the X-Ray flare in late 2007 until about a year after. Comparing VLBI maps between 1997 and 2008, they find that no new (bright) components appeared (see Figure 5.24 of Müller (2010)), but they caution that due to different beams and sensitivities it is difficult to compare the observations. Still, this leaves little room for the appearance of a new component between 2005 and 2008. Furthermore, if a new component had been ejected at the X-Ray outburst in Nov 2007, it would be unlikely that it had already reached a separation of ≈ 30 mas in April 2008, since the bulk motion of the jet is only 0.5 c (8 mas/yr) and proper motion of the components is even slower (≈ 2 mas/yr, (Tingay et al. 2001)).

A projection effect? *Movement of material* from the nucleus to the offset position found in model *d* cannot have occurred in less than 8 months time (without employing extreme apparent superluminal motions that have not been observed for Cen A so far).

Therefore, it seems reasonable to assume that the mid-IR emission geometry did not change between 2005 and 2008 (and that model *d* is a valid description for both epochs). We further assumed (see above) that the IR outburst was *triggered* by the X-Ray flare in November 2007. The flux increase then occurred first in what we model as point source and then gets reflected (scattered or re-emitted) by what we model as elongated Gauss. In this case, we can constrain the angle i between our line of sight and the elongated Gauss' line of sight to the nucleus by using simple geometrical relations in a triangle with

known sides, see Figure 2.15.

We have measured d to be $\gtrsim 34$ mas (from model d at 8.5 μm , i.e. at highest resolution) and we have a constraint from the X-Ray monitoring for $r - s \lesssim c \cdot 8$ months (taking the half-rise time of the X-ray flare) ≈ 10 mas. This allows us to estimate i since $(r-s)/d = (1-\cos i)/\sin i \lesssim 10/34$ or $i \lesssim 40°$.

2.5.3. The elongated source and overall geometry

From our geometrical model fits, only the offset between the elongated source and the unresolved point source is determined. The offsets found were compatible with the source lying either in the north-east or in the south-west.

However, taking the variability considerations seriously, the elongated source must be located "in front of" the point source for the projection effect to work. Due to the history of non-thermal flux variations in Cen A and the inferred (projected) proximity of the elongated Gauss structure to the jet, it is likely that the extended component is actually connected with the jet region. In this case, the structure must be to the north-east of the nucleus since that part of the jet points in our direction. In fact the inclination implied from the variability consideration $i \lesssim 40°$ is in between the different inclinations inferred from radio and X-ray studies: In VLBI observations, Tingay et al. (2001) found an inclination (angle to the line of sight) of $50° - 80°$ (Tingay et al. 1998) but in combined radio and X-ray observations, Hardcastle et al. (2003b) find that only small inclinations of $\approx 20°$ are consistent with both X-rays and radio observations from combined constraints on apparent motions and sidedness of the jet (components).

We note that it is unlikely that the elongated structure is connected to the nuclear disks found by Neumayer et al. (2007) and Espada et al. (2009) in molecular hydrogen and CO emission, respectively.

Our best model scenario, together with the VLBI radio data is sketched in Figure 2.16.

2.5.4. Comparison with other MIDI AGN observations

In the two other AGNs that have been studied extensively with MIDI, the Circinus galaxy and NGC 1068, "scatter" of the visibilities in the (u, v) plane has only been seen at very low visibility levels ($\lesssim 20$ %) where the source is almost completely resolved (cf. Figure 4 of Tristram et al. (2007)). In the Circinus galaxy, a fit with two Gaussian components leads to a $\chi^2 \sim 16600$ with 451 degrees of freedom (Tristram et al. 2007); in NGC 1068 especially the data at longer baselines are also not well described by a model of two Gaussian components (Raban et al. 2009). These small scale structures can, for example, arise from clumpiness in the dusty disk as has been demonstrated by Tristram et al. (2007).

It is easily understandable that deviations from the usual Gauss fits only arise at low visibilities because at large visibilities most simple geometries (Gaussians, disks, rings, ...) lead to $V \propto (BL/\lambda)^{-2}$. But subtracting the point source flux fraction in Cen A ($\approx 50\%$) from the visibilities, leaves also only very low visibility values. Therefore, we

are effectively observing the extended component in Cen A at visibilities $\lesssim$ 20 % or, equivalently, probing the extended component at relatively high spatial resolutions which are most sensitive to small-scale structures and not well described by simple structures. This is the explanation why the simple smooth fits (Gaussian, elongated Gaussian) cannot explain the visibility pattern: Large, smooth structures are probably only good estimates for the real surface brightness distribution at large visibilities (there, they describe the envelope of the true, probably more complicated, visibility function). Taking into account that the nuclear region of Cen A, especially around the jet, is very complex (Neumayer et al. 2007), it is actually not too surprising that no perfect fit can be found with simple model components.

2.6. Conclusion

- The simplest geometrical models (a,b,c) cannot explain the complex visibility pattern of Cen A. After having studied systematic errors, including calibration errors and propagating them to the final visibilities, we are convinced that the residuals from these models are not caused by underestimated errors.

- Acceptable fits are achieved at 8.5 μm , 10.5 μm and 12.5 μm for the elongated Gauss + offset point source model. There are two solutions for the offset of which one was discarded because the offset changed excessively with wavelength. In this fit, the major axis of the elongated Gaussian is at a position angle of $\approx 110^\circ$ and is in fact almost over-resolved with a FWHM of 22 - 48 mas; the minor axis is unresolved. Both components contribute roughly the same amount of flux. In this model, the remaining scatter can be explained because such a simple structure (especially the extended component with un- and almost over-resolved axes) is obviously not a very good fit for the complex nuclear region of Cen A, especially close to the jet. More complex geometrical models lead to a very low number of degrees of freedom.

- The nucleus of Cen A brightened considerably between the 2005 and 2008 MIDI observations. Repeated observations on one baseline showed that the visibilities did not change between these epochs suggesting that the mid-IR emitting geometry stayed the same. An alternative explanation that is compatible with the datasets from both epochs would be that a component newly appeared in 2008 (where the model with the offset component results in a good fit). This scenario seems to be excluded by X-Ray and radio observations.

- Assuming that the mid-IR geometry is well explained by the offset two-component model and indeed did not0 change between 2005 and 2008, leads to the question *when* the two components brightened. A mid-IR observation at the end of 2006 showed no increase in flux relative to our 2005 observation. In November 2007, a bright X-Ray flare was detected in Cen A suggesting that this could be responsible for the outburst. In a possible scenario, the X-Ray outburst is caused by an event

in the very center of Cen A which we then identify with our point source. Using a light travel time argument, the extended component must then be positioned *in front of* the the point source which puts it near the jet of Cen A.

2.7. Outlook

Fitting procedure The employed fit (using LITpro) was not a global grid-search (but we tried to scan the parameter space manually as good as possible). As the model χ^2 planes turned out to be highly complex (see Figure 2.12), a more robust fitting algorithm is needed.

A Monte Carlo fitting algorithm would allow us to select models with greater confidence. It would help to separate more clearly the errors arising from single-dish and from interferometric measurements, such as demonstrated in Chapter 3 for the Seyfert 1 galaxy NGC 4151 where the single-dish error was several times larger than the correlated flux errors.

A spectro-interferometric model might be able to disentangle the model components more clearly and determine their spectra. However, with the current uncertainties in the geometry of the structure, it is hard to imagine a robust solution to a spectro-interferometric model.

(u, v) **coverage** The most promising way to better constrain the source brightness distribution is to better sample the (u, v) plane. Especially short baselines are missing at the moment to discriminate models with over-resolved sources from models with offsets.

Observations with very short baselines ($\lesssim$ 40 m) require the use of the flexibly positionable Auxiliary Telescopes of the VLTI. Such a study is currently under considerations. Due to their smaller mirror diameter in comparison with the larger Unit Telescopes ($D^2_{\mathrm{AT}}/D^2_{\mathrm{UT}} \approx 1/16$) and their poorer optical properties, these observations will be very challenging. The correlated fluxes of Cen A at short baselines can be expected to be $\lesssim$ 1.5 Jy (at 12.5 μm; the level of the total flux in bright state). This "AT flux" corresponds to a "UT flux" of $\lesssim$ 100 mJy. With an improved online data system at the VLTI, such observations might be just so possible, but it probably needs to be paired with new UT observations to control the longer baselines.

Such observations could provide important clues on the nature of the emission. For example, the geometrical models *c* and *d* should be easily discernible with the new observations: If there really is an offset point source (model *d*) then the visibility should decrease considerably below 50% at baselines shorter than 20m at position angles near 40°, but stay at high values near 130° out to 30m (compare Figures 2.10 and 2.11).

Variability In the context of multi-wavelength monitoring of Centaurus A it would be important to determine the nuclear flux from Cen A by mid-IR interferometry with as few (u, v) points as possible. To make this possible, it is first necessary to have a reliable model of the mid-IR visibilities.

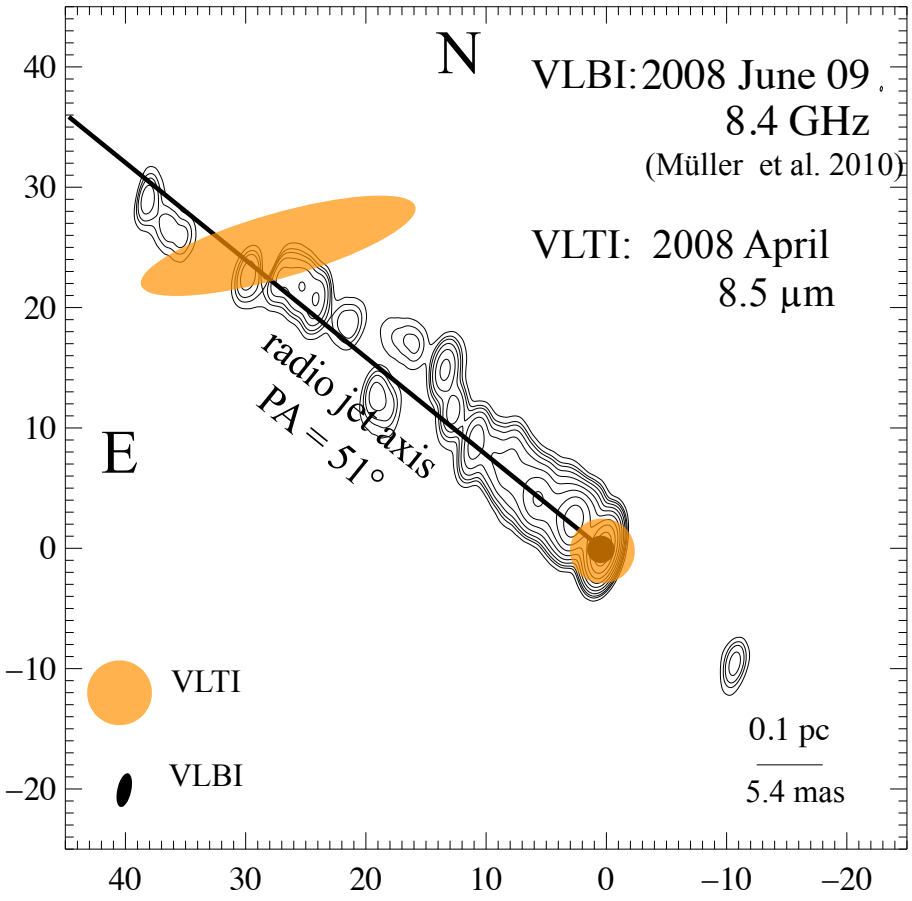

Figure 2.16.: Best-fitting two-component geometrical model d (at the highest resolution, i.e. 8.5 μm) for the nuclear mid-infrared emission of Centaurus A consisting of an elongated Gaussian disk and an unresolved point source. The major axis of the disk is ≈ 22 mas or ≈ 0.4 pc, the minor axis of the disk is smaller than the VLTI resolution of about 5 mas at 8.5 μm . The position angle of the disk is found to be $105.7 \pm 3.6°$ in this model. The dark grey circle that is concentric with the elongated disk is the point source. It has previously been identified with the synchrotron core (black point) by Meisenheimer et al. (2007). The radio radio jet axis is PA $\sim 51°$ (e.g. Tingay et al. 2001) and the radio contours are from Müller et al. (2010). The PA of the X-ray jet is $\sim 55°$ (Kraft et al. 2000). The relative positioning of the VLTI and VLBI structures follows from the variability scenario (see text).

3. NGC 4151: The first resolved nuclear dust in a type 1 AGN[1]

3.1. Introduction

MIDI observations have been successful in testing the unified model of active galaxies by resolving warm dust in their nuclei (see Section **??**). So far, however, no Sy 1s have been observed in sufficient detail[2] to test the central premise of the unified models: type 1 and type 2 dust distributions are identical and the observed differences are only due to differences in orientation with respect to the line of sight.

At a distance $D = (14 \pm 1)$ Mpc (i.e. 1 mas ≈ 0.068 pc)[3], NGC 4151 is the closest and brightest type 1 galaxy (classification: Seyfert 1.5) – unfortunately at a declination of $\approx +40°$, which puts constraints on its observability from Paranal. It is also one of the most variable Seyfert galaxies: The UV continuum flux varies on scales of days and weeks (Ulrich 2000) and the reverberation time to the hot dust on the sub-parsec scale varies on yearly timescales (Koshida et al. 2009).

Sy 1 galaxies have been observed previously with MIDI (NGC 3783, Beckert et al. 2008), (NGC 7469, Tristram et al. 2009), see also Kishimoto et al. (2009), but NGC 4151 is the first multi-baseline case where the size of the nuclear dust distribution is clearly indicated.

NGC 4151 was also the first extragalactic target to be observed successfully with optical interferometry: Swain et al. (2003) reported near-IR, 2.2μm, observations with the Keck interferometer. They find that the majority of the K band emission comes from a largely unresolved source of ≤ 0.1 pc in diameter. Based on this small size, they argued that the K band emission arises in the central hot accretion disk. They note, however, that their result is also consistent with very hot dust at the sublimation radius. This view is supported by the K band reverberation measurements of Minezaki et al. (2004) who find a lag time corresponding to ≈ 0.04 pc.

In general, reverberation-based radii $r_{\rm rev}$ were found to be *systematically* smaller by a factor of ≈ 3 than the predicted dust sublimation radii $r_{\rm sub}$ (Kishimoto et al. 2007). On the other hand, interferometrically determined radii seem to be roughly equal or only slightly larger than $r_{\rm rev}$ (Kishimoto et al. 2009).

[1] adapted from Burtscher et al. (2009)

[2] Since the space density of Seyfert 2 galaxies is larger than that of Seyfert 1s (Maiolino & Rieke 1995, estimate a factor of 4), there are more nearby and bright type 2 galaxies.

[3] from the NASA Extragalactic Database: http://nedwww.ipac.caltech.edu; distance from redshift with H_0=73 km/s/Mpc; other estimates range to 20 Mpc

Figure 3.1.: SDSS *gri* image of NGC 4151. The active nucleus is easily spotted. The central part of the galaxy is dominated by a "fat bar" (Ulrich 2000). The weak spiral arms can be seen in blue extending almost to the top and bottom of the image. The image is 13 × 9.5 arc minutes (53 × 39 kpc) wide. Five arc minutes to the NE, group member NGC 4156 can be seen. Credit: David W. Hogg, Michael R. Blanton, and the Sloan Digital Sky Survey Collaboration

Reverberation techniques have also been used by Bentz et al. (2006) to derive an estimate for the mass of the supermassive black hole: $M_{BH} = \left(4.57^{+0.57}_{-0.47}\right) \times 10^7 M_\odot$.

Riffel et al. (2009) modelled the near-infrared spectrum of this source and found it to be composed of a powerlaw accretion-disk spectrum and a component likely arising from hot dust (T = 1285 K). The hot dust component dominates at $\lambda \gtrsim 1.3\mu$m, consistent with the interpretation of hot dust emitting at 2μm. They measured a K band flux of ≈ 65 mJy.

An early attempt to resolve the nucleus in the mid-IR is reported by Neugebauer et al. (1990). They observed NGC 4151 at 11.2 μm using the f/70 Cassegrain focus of the 200 inch (5 m) Hale telescope. They claim to have determined the size of the resolved emitter at 11.2μm to (0.16 $\pm$ 0.04) $''$– less than a third of the diffraction limit of the telescope. After careful study of their paper and references therein and after discussions with researchers familiar with similar high-resolution techniques (Ch. Leinert, pers. comm.), we decided not to take the resolved scale reported by Neugebauer et al. (1990) into account for our further discussion.

This is corroborated by high-resolution observations by Soifer et al. (2003) who studied the nucleus with the Keck I telescope with a measured PSF FWHM of 0.36$''$at 12.5 μm and found it unresolved. Radomski et al. (2003) presented images of NGC 4151 at 10.8μm with the Gemini North telescope (aperture: 4.5$''$, measured PSF FWHM: $\approx$0.55 $''$). They find that the majority (73%) of the N band flux comes from an unresolved point source with a size ≤ 35 pc, and the rest is extended emission from the narrow line region.

In this letter we report new mid-infrared interferometric observations of NGC 4151 which clearly resolve a thermal structure.

3.2. Instrument, observations and data reduction

Observations were performed in the N band ($\lambda \approx 8 \ldots 13\mu$m) with the MID-infrared Interferometric instrument (MIDI, Leinert et al. 2003) at the ESO Very Large Telescope Interferometer (VLTI) on Cerro Paranal, Chile, using pairs of 8 m Unit Telescopes (UTs). The observables with MIDI are the single-dish spectra and the correlated flux spectrum that is obtained from the interference pattern generated by the two beams. The spectra were dispersed with a NaCl prism with $R \equiv \lambda/\delta\lambda \approx 30$.

Observations were taken in the nights of April 21 and 23, 2008 with projected baseline length BL of 61 m and 89 m at position angles of 103° and 81° respectively. These provide effective spatial resolutions [4] ($\lambda/3BL$) at 10.3μm of 11 and 7 milliarcseconds (mas), respectively. The calibrators HD 133582 and HD 94336 were selected to be very close in airmass with $\Delta z \lesssim 0.15$. This is especially important for NGC 4151 (DEC $\approx +40°$) which, at Paranal, never rises higher than $\approx 25°$ ($z \gtrsim 2.3$) above the horizon. The northern declination of the source also limits the projected baselines and fringe patterns to essentially East-West orientation at Paranal (see Figure 3.2). The N band spectrum

[4] see Section 1.2.3

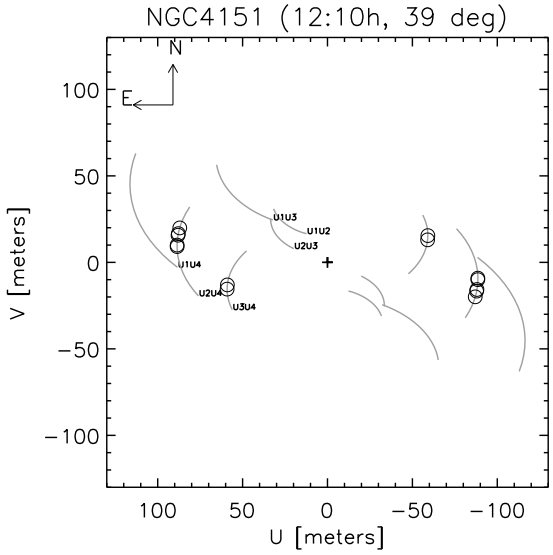

Figure 3.2.: Observed (u, v) coverage for NGC 4151. The open circles denote the (u, v) coordinates of the fringe tracks on the two baselines. Their diameter corresponds to the telescope diameter D of the VLT UTs, $D = 8$m. The thin lines are the (u, v) tracks that are traced by the various telescope combinations as a result of earth's motion. They are plotted for elevations $> 20°$. (u, v) plane tracks are followed CCW if $\delta < 0$, CW if $\delta > 0$. Small grey crosses denote Hour Angles = -4, -2, 0, 2, 4.

of HD 133582 (K2III) was taken to follow a Rayleigh-Jeans law, while that of HD 94336 (MIII) was taken from Cohen et al. (1999).

Data reduction was performed with the interferometric data reduction software *MIDI Interactive Analysis and Expert Work Station* (MIA+EWS, Jaffe 2004) and followed the procedure described in Section 1.6.

3.3. Results and modelling

3.3.1. Single-dish spectrum

The resulting single-dish spectrum with an effective aperture of $\approx$ 300 mas is shown in Figure 3.3 together with a Spitzer IRS spectrum for this source (observed 8 Apr 2004; aperture $\approx 3.5''$, Weedman et al. 2005). The higher Spitzer flux most likely indicates emission from the Narrow Line Region (cf. Radomski et al. 2003).

The color temperature of the spectrum is (285^{+25}_{-50}) K, slightly warmer than the 201 K estimated from IRAS 12 and 25 μm data by Soifer et al. (2003). The reason for this is probably that the large aperture IRAS data contain not only the warm nuclear material but also colder material from larger scales. Additionally, we detect the [Ne II] 12.81 μm line commonly seen in star forming regions. The [S IV] 10.51 μm line, clearly seen in the Spitzer spectrum, is not significant in the MIDI spectrum. The errors in the MIDI spectrum arise from incomplete thermal background subtraction and hence rise steeply with increasing wavelength.

3.3.2. Correlated spectra

The two correlated flux spectra are shown in Figure 3.4.

The correlated flux observed with $BL = 61$m rises from (0.13 ± 0.01) Jy at 8.5 μm to (0.43 ± 0.05) Jy at 12.5 μm. The second spectrum ($BL = 89$m), rises from (0.12 ± 0.02) Jy at 8.5 μm to (0.30 ± 0.05) Jy at 12.5 μm. Correlated flux uncertainties arise primarily from background photon noise and increase with wavelength but are smaller than the single dish errors.

The correlated flux on the shorter baseline (the one that has a higher flux) shows a broad "bump" between 9 μm and 12 μm that we interpret as a silicate emission feature (see section 3.3.3). No [Ne II] emission is seen, indicating that this arises on a scale that is fully resolved by the interferometer (i.e. $\gtrsim 20$ mas ≈ 1.3 pc). The fact that the correlated flux is lower on the longer baseline is a clear sign that the source is resolved by the interferometer.

Since the resolution of the interferometer $\theta_{min} \approx \lambda/3BL$ changes with wavelength, the correlated flux reflects both the source spectrum and the source structure. It is not possible to draw any conclusions from the spectral slope of a correlated flux spectrum without assuming a source geometry.

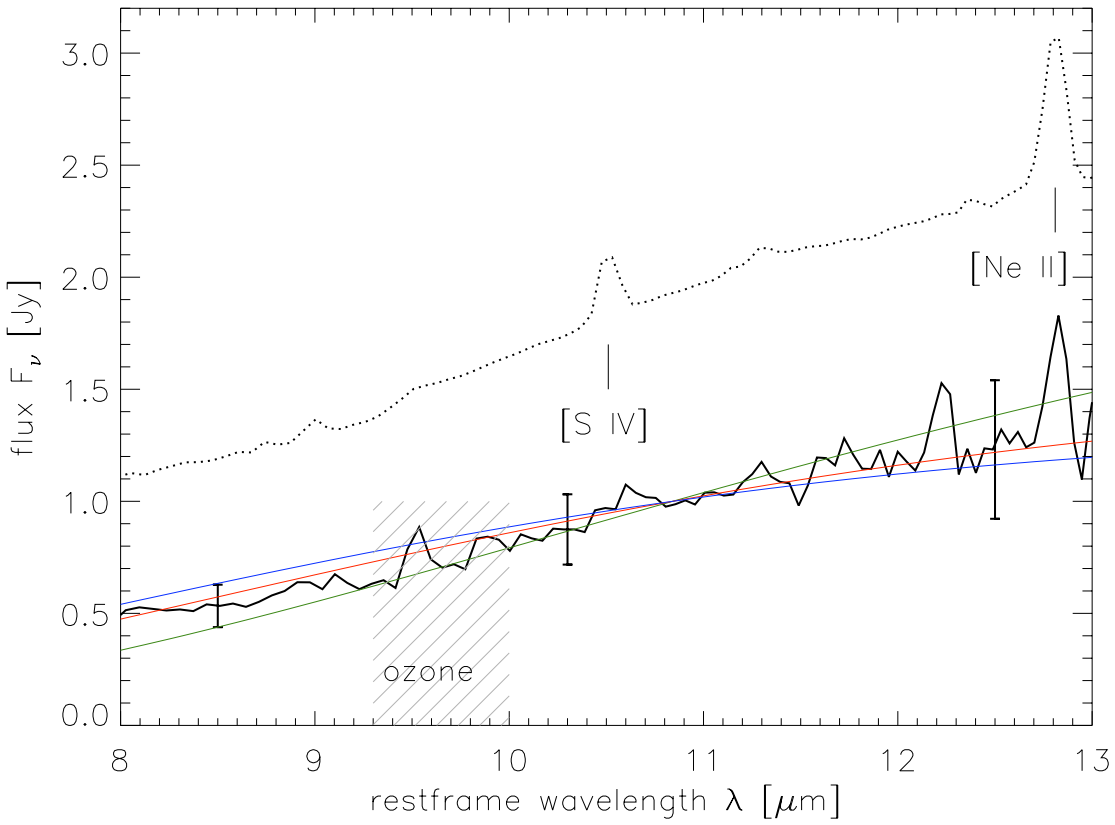

Figure 3.3.: Single-dish spectra for NGC 4151. Spitzer spectrum (3.5″, dotted, Weedman et al. 2005), MIDI spectrum (0.3″, black line with error bars). The MIDI single-dish errors were taken as the error of the mean from five observations. Also plotted are blackbody emission curves at $T = 235, 285, 310$ K (green, red, blue). The region of atmospheric ozone absorption, between 9.3 and 10 μm (hatched), is uncertain and not taken into account for the later analysis.

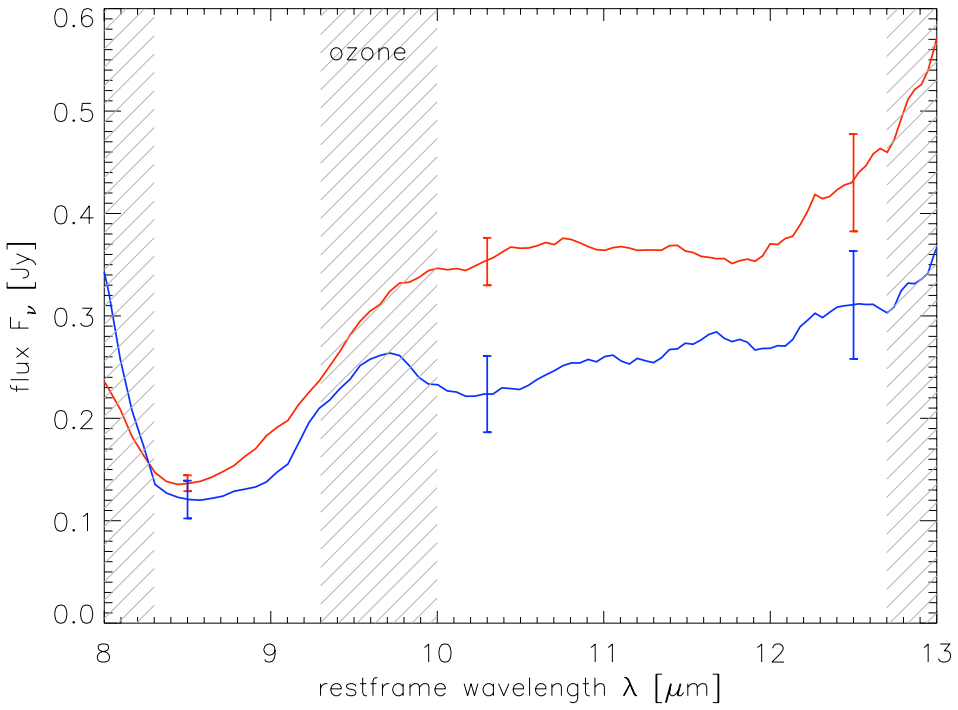

Figure 3.4.: Smoothed ($\Delta\lambda \approx 0.3\mu$m) correlated MIDI spectra at two different East-West projected baselines: 61m (red, average of two fringe track observations) and 89m (blue, average of three fringe track observations). The errors are the errors of the mean of the individual observations. The region of atmospheric ozone absorption, between 9.3 and 10 μm (hatched), is uncertain and not taken into account for the later analysis, as are the regions $\lambda < 8.3\mu$m and $\lambda > 12.7\mu$m (hatched), which have very low S/N.

3.3.3. A possible silicate emission feature

Although the silicate absorption feature has often been detected in type 2 nuclei, the emission feature, predicted for type 1 nuclei by torus models (e.g. Pier & Krolik 1992; Schartmann et al. 2005), has not been detected except in a handful of objects, most of them quasars (Hao et al. 2005; Weedman et al. 2005; Buchanan et al. 2006).

As noted by Weedman et al. (2005) and Buchanan et al. (2006), Spitzer spectra (with an aperture of $\approx 3.5''$) of NGC 4151 show weak excess emission at 10 μm and 18 μm that is most easily seen when plotted as $\nu^2 F_\nu$ with a sufficiently large wavelength range. In Figure 3.5 we plotted our spectra (that are limited to the atmospheric N band) in such a way together with a Spitzer spectrum.

The hypothesis of silicate emission is not inconsistent with our single dish spectrum (aperture $\approx 0.3''$) but since this spectrum suffers from incomplete background subtraction, especially at longer wavelengths, it is probably hidden in the resulting uncertainties. The emission feature seems to be most prominent in our observations on the 61m baseline observation and is clearly not detected on the 89m baseline.

This suggests that at least some fraction of the silicate emission feature observed in type 1 AGNs is located on scales ≈ 1 pc as derived from the 10.5 μm Gaussian model (see 3.3.4). Recent observation of bright quasars, in combination with dusty Narrow Line Region models, have suggested that the Silicate emission feature may be produced in the Narrow Line Region, although a contribution from the parsec-scale is not excluded (Schweitzer et al. 2008).

3.3.4. Simple Gaussian model

With the limited baselines available from Paranal, it is not possible to reconstruct an *image* of NGC 4151 from our data. Instead we consider simple model distributions of the emission on the sky and compare the predicted interferometric and single dish spectra with our measurements in order to fix parameters in such a model. We chose a model containing an unresolved point source (flux F_p) and an extended Gaussian distribution (flux normalization F_g, FWHM θ). Although we might expect the mid-IR brightness distribution in Sy 1 galaxies to have a hole in the middle, the fluxes do not change as long as the hole, whose radius is determined by the sublimation radius of the dust, is unresolved. This is certainly the case in NGC 4151 where $r_{\mathrm{rev}} = 0.04$ pc, roughly four times smaller than our highest resolution observation (see section 3.4). An upper limit to the size of our point source is given by the effective resolution of the interferometer; this corresponds to a diameter of $\approx \lambda/3BL \approx 7$ mas, i.e. a radius of ≈ 0.2 pc, at 10.3 μm.

Because of the East-West baseline orientation, the North-South distribution of emission is undetermined. Equivalently, we assume the source to be circularly symmetric on the sky.

The model correlated flux density at wavelength λ is then given by $F_\nu(\lambda) = F_p(\lambda) + F_g(\lambda) \cdot \exp(-(BL/\lambda \cdot \pi/2 \cdot \theta)^2/\ln(2))$. With the given data points this model is uniquely determined. We calculated the parameters of such a model separately at 8.5, 10.3 and

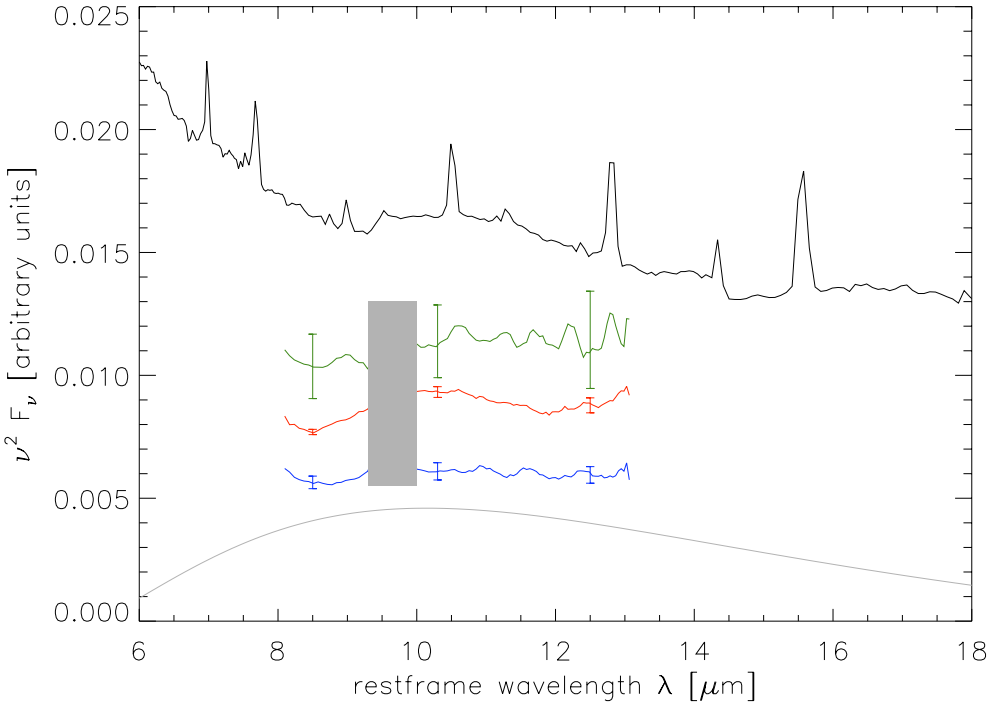

Figure 3.5.: The silicate emission feature as seen in $\nu^2 F_\nu$. In the Spitzer spectrum (black, Weedman et al. 2005), a broad weak emission feature at around 11 μm is clearly seen. The three MIDI spectra (green: single-dish, red: 61m baseline, blue: 89m baseline) are plotted with offsets. The grey line shows a 285 K blackbody. The region between 9.3μm and 10 μm is hard to calibrate in the MIDI spectra due to the atmospheric ozone feature and has been greyed to not mislead the eye.

Table 3.1.: Parameters for the Gaussian models (see text).

λ [μm]	F_g [Jy]	θ [mas] (diameter [pc])	F_p [Jy]
8.5 ± 0.2	0.41 ± 0.10	$29^{+3}{}_{-6}$ ($2.0^{+0.2}{}_{-0.4}$)	0.119 ± 0.016
10.3 ± 0.25	0.70 ± 0.16	23 ± 4 (1.5 ± 0.3)	0.194 ± 0.061
12.5 ± 0.3	1.03 ± 0.30	32 ± 6 (2.1 ± 0.4)	0.290 ± 0.070

12.5 μm where we are safely away from the regions of very low signal to noise (at the edges of the N band) and the ozone feature. At 10.3 μm the parameter values may be affected by the silicate feature. The modelled visibilities are shown in Figure 3.6 and the resulting parameters are given in Table 3.1.

The errors of these parameters were estimated from a Monte-Carlo simulation in which we resampled our data by randomly placing 10 000 measurements in a Gaussian distribution around the measured value with the σ as determined from our data reduction. The parameter errors are then given by the standard deviations of the resulting model solutions to the simulated data.

3.4. Discussion

3.4.1. The extended source and the Sy 1 / Sy 2 paradigm

In the strictest version of unified models, we expect for both a Sy 1 and a Sy 2 galaxy an extended dust structure with the same size, morphology and temperature distribution (at a given UV luminosity $L_{\rm UV}$). In less strict versions this is only true statistically (e.g. Elitzur & Shlosman 2006). Additionally, Sy 1 galaxies should have an unobscured point source (the unresolved accretion disk and inner rim of the torus) – but the relative strength of these two components in the mid-IR is model-dependent.

To test this, we can compare our observations with other MIDI observations: In the Circinus galaxy ($L_{\rm UV} \approx 4 \times 10^{36}$ W, $L_{\rm torus} \approx 5 \times 10^{35}$ W), Tristram et al. (2007) found a warm ($T \approx 330$ K) disk with major axis FWHM ≈ 0.4 pc and a larger, similarly warm, component of ≈ 2 pc FWHM.

In NGC 1068 ($L_{\rm UV} \approx 3 \times 10^{37}$ W, $L_{\rm torus} \approx 10^{37}$ W), Raban et al. (2009) found a hot ($T \approx 800$ K) disk of 1.35 x 0.45 pc and a warm component 3 $\times$ 4 pc in FWHM. They identified the disks with the densest parts of the torus of the unified model.

For NGC 4151 ($L_{\rm UV} \approx 1.5 \times 10^{36}$ W – variable (from NED), $L_{\rm torus} \approx 4\pi D^2 \nu F_g \approx 6 \times 10^{35}$ W) we determined a torus size (FWHM) of $\approx (2.0 \pm 0.4)$ pc and a dust temperature of (285^{+25}_{-50}) K.

When scaled to the accretion disk luminosity $L_{\rm UV}$, these values agree well with the torus sizes ($r \approx {L_{\rm UV}}^{1/2}$) and torus luminosities ($L_{\rm torus} \approx L_{\rm UV}$) of the two Seyfert 2 galaxies and the temperatures are also very similar. Note, however, that the torus luminosity used

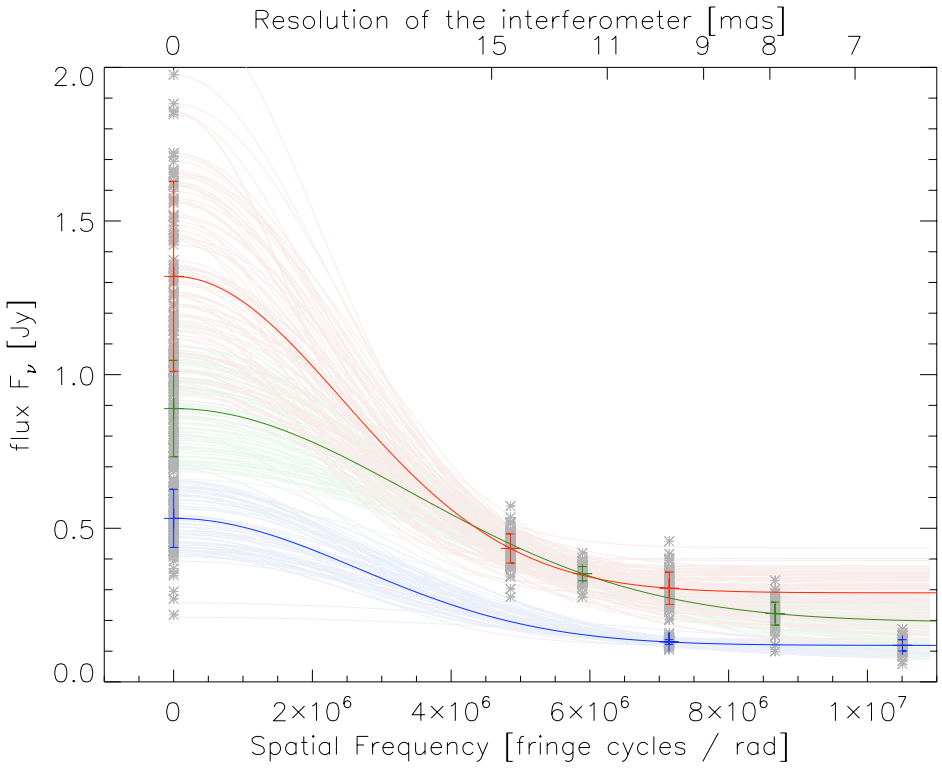

Figure 3.6.: Gaussian model for NGC 4151. On the upper x axis the resolution (i.e. sensitivity to model parameters) of the interferometer $\lambda/3BL$ is given. The three curves correspond to uniquely determined models at 8.5 μm (blue), 10.3 μm (green) and 12.5 μm (red). Data points and errors are taken from the single-dish (i.e. "0-baseline", Figure 3.3) and correlated fluxes (the other two data points per wavelength, Figure 3.4). The many thin lines represent the Monte-Carlo-like error determination for the Gauss model. For details see text.

here is calculated from the 12μm flux density, not taking into account emission at longer wavelengths.

3.4.2. Greybody models and the nature of the extended source

In addition to the single-wavelength Gaussian models discussed above, we can also connect the various wavelengths together by constructing *greybody* models where we assume a smooth power-law dependence of temperature with radius: $T(r) = T_0(r/R_{\rm min})^{-\alpha}$, and an essentially constant emissivity ϵ with radius and wavelength. The model flux is then given by

$$F_\nu = \int I_\nu \, \mathrm{d}\Omega = \frac{2\pi}{D^2} \int I_\nu r \, \mathrm{d}r = \frac{2\pi}{D^2} \int_{R_{\rm min}}^{R_{\rm max}} \frac{2\pi h\nu^3}{c^2} \frac{\epsilon}{\exp\left(\frac{h\nu}{kT(r)}\right) - 1} \mathrm{d}r$$

where the inner integration boundary $R_{\rm min}$ is given by the reverberation radius ≈ 0.04 pc and the outer boundary is set to the resolved scale $R_{\rm max} \approx 0.2$ pc / 0.35 pc (for the correlated flux at 8.5 μm and 12.5 μm respectively) and 1 pc (for the total flux). The integral is very sensitive to the inner boundary (where the temperature is maximal), the outer boundary is not so critical. The temperature at $R_{\rm min}$ is fixed to the value derived by Riffel et al. (2009) from a fit to the near-IR spectrum (see below).

With such models we get acceptable fits (reduced $\chi^2 \approx 1$) for both the total and the correlated flux spectra with $T(1\mathrm{pc}) \approx 250$ K and $\alpha \approx 1/2.8 \approx 0.36$. This value of α is consistent with dust receiving direct radiation from a central source (e.g. Barvainis 1987), i.e. an optically thin medium with optically thick clumps in it.

These models can be extrapolated to shorter wavelengths to check their consistency with the K band measurements. All plausible extrapolations of the MIDI data yield K band fluxes of < 10 mJy, much less than observed by Swain et al. (2003) and Riffel et al. (2009) (see below). On the basis of these greybody models, we therefore conclude that the K band emission arises from structures which can probably not be extrapolated from the larger structure seen in the N band.

From the greybody models one can further infer an emissivity $\epsilon \approx 10^{-1}$ – similar to what has been seen in NGC 1068 and Circinus.

To conclude: The resolved nuclear mid-IR structure in NGC 4151 has a size, temperature and emissivity that is comparable to those in type 2 objects where the existence of clumpy tori is established. Apart from the similarities with type 2 tori and the temperature profile of the greybody models, there is further evidence for clumpiness in the NGC 4151 torus from radio observations: Mundell et al. (2003) measured HI absorption against the radio jet ($PA \approx 77°$) and found a structure of ≈ 3 pc in size. From the velocities they further suggest that the gas is distributed in clumps. Warm dust possibly traces the HI gas in the mid-IR.

It therefore seems reasonable to identify the warm dust structure resolved now in NGC 4151 with the clumpy tori seen in Sy 2 galaxies. Due to the limited observing geometry

and the limited amount of observations we cannot reconstruct its apparent shape nor can we constrain a model with more than the two components discussed above.

3.4.3. The point source and its relation to K band measurements

K band interferometry measurements by Swain et al. (2003) and, with higher significance, more recent Keck observations (Pott et al. 2010) revealed a marginally resolved source, compatible with hot dust at the sublimation radius of ≈ 0.05 pc. Reverberation measurements by Minezaki et al. (2004) and Koshida et al. (2009) find lag times Δt between the UV/optical continuum and the K band corresponding to a radius of ≈ 0.04 pc (variable) which they interpret as the sublimation radius of dust.

Riffel et al. (2009) measured a flux of ≈ 65 mJy at 2.2 μm and from spectral fitting they found that, at 2.2 μm, this flux is entirely dominated by a blackbody with a temperature of (1285 ± 50) K – again consistent with hot dust at the sublimation radius and the K band interferometry, taking into account that L_{UV} is variable by at least a factor of 10 (Ulrich 2000). To account for that variability when comparing our observations with these K band observations of different epochs, we looked at the X-Ray flux as a proxy for the UV–optical radiation[5] and find that, at the date of our observations, the source was probably in a higher state than at the time of Riffel et al. (2009)'s observations and emitted ≈ 0.2 Jy in the K band (see Figure 3.7).

Since the flux density F_ν of a $\approx$ 1285 K blackbody is roughly the same at 2.2μm as at 8.5 μm, we can compare the flux in the K band ($\approx$ 0.2 Jy at the time of our measurement) with our point source flux at 8.5 μm ($\approx (0.119 \pm 0.016)$ Jy). From this it seems likely that hot dust is contributing to our point source at 8.5 μm. The spectrum of the point source rises by more than a factor of two from 8.5 μm to 12.5 μm, however, and thus requires emission from an additional small, "red" component. This could be core synchrotron emission, although such sources usually have flat spectra, or emission from a small, cool, optically thick central dust structure, possibly shadowed from direct accretion disk radiation.

3.5. Conclusions

Using mid-IR interferometry, we have resolved a warm dusty structure in NGC 4151. Its FWHM size (2.0 ± 0.4 pc – from comparing the data with a Gaussian model), temperature (285^{+25}_{-50} K) and emissivity (≈ 0.1) are in good agreement with the clumpy tori seen in type 2 AGNs and are thus consistent with the unified model of Active Galaxies. Excess emission around 10.5 μm on the intermediate baseline indicates that silicate emission might arise from scales of ≈ 1 pc in AGNs.

Using simple models we compare our mid-IR fluxes with observations in the K band and find that the structure we resolve is probably not the smooth continuation of the nuclear source detected in the K band

[5] Data from the All-Sky-Monitor (ASM) on the Rossi X-Ray Timing Explorer (RXTE), available online[6].

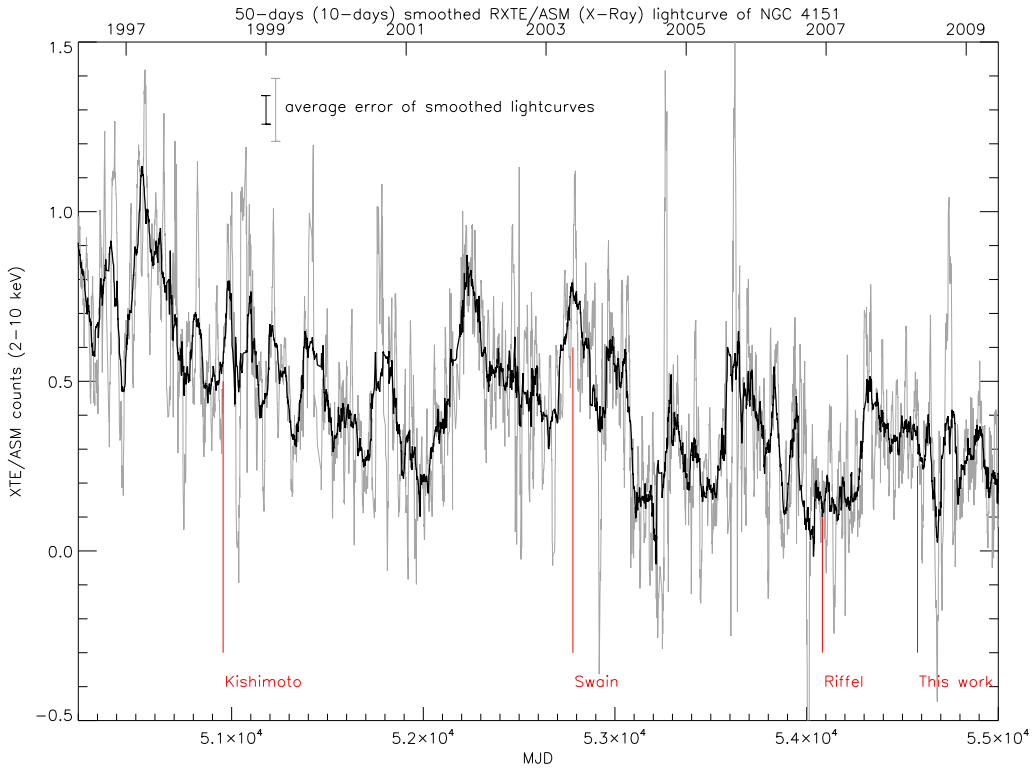

Figure 3.7.: X-Ray lightcurve from the All-Sky-Monitor (ASM) onboard the Rossi X-Ray Timing Explorer (RXTE), summed over all bands of the instrument and smoothed by 50 days (black curve) and 10 days (grey curve), respectively. The lower x axis displays the Modified Julian Date (MJD). The nights of relevant observations are marked: Riffel et al. (2009) seem to have observed the source in a rather low state compared to the earlier observations of Kishimoto et al. (2007) and Swain et al. (2003). See also Figure 2.14 for the X-Ray-IR-variability correlation in Centaurus A.

Due to the limited number of measurements, no two-dimensional information could be gathered and questions about the unified model (such as: is the dust structure in Sy 1 galaxies thick and torus-like or rather disk-shaped?) remain unanswered. Since nuclear dust distributions are different even within the same class of AGNs, the ultimate question whether or not the unified model is valid will not be answered before a statistical study of numerous tori is performed. First results from such a study are presented in Section 4.

Acknowledgements

This research is based on observations collected at the European Organisation for Astronomical Research in the Southern Hemisphere, Chile, programme number 081.B-0092(A). The authors wish to thank the anonymous referee for many comments that helped to improve the paper. I would like to thank Roy van Boekel, Marc Schartmann, Gaëlle Dumas and Carole Mundell for helpful discussions.

4. The MIDI AGN Large Programme: A statistical sample of resolved AGN tori

4.1. Introduction[1]

The first detailed interferometric studies of the brightest AGNs in the mid-IR have resolved their nuclear dust distributions. They showed that warm dust exists on the parsec scale, that their geometry and temperature are not universal and that their structure is probably clumpy (a summary of these studies has been given in Section **??**).

In addition to the three mid-IR brightest sources, another dozen, weaker, galaxies had been examined in the MIDI GTO time, but generally only one or two (u, v)-points were observed (Tristram et al. 2009). Therefore, this 'snapshot' survey served more to prove the observability of weaker targets than to provide a statistical basis for size and structure analysis.

It was clear that a large and systematic observational campaign was needed to collect the basic observational information necessary to understand dusty tori on a statistical basis. This is the aim of the MIDI AGN Large Programme (LP).[2]

The questions to be addressed in the LP are:

1. How does the measured mid-IR morphology of AGN tori depend on wavelength, nuclear orientation and luminosity? This is the key to understanding the radiation transfer effects in the dust structure. Is there a common torus size – AGN luminosity relation for all types of AGNs as suggested by the GTO study (Tristram et al. 2009)? Understanding and properly calibrating this relation with local AGNs is the only way to safely apply the relation to the wealth of distant spatially unresolved AGNs.

2. Are other "parameters" important to the morphology, such as mass feeding rate from circumstellar star clusters, or dust chemistry?

3. Is the Sy 1 and Sy 2 dichotomy only an orientation effect or a simplified view of a wide variety of different intrinsic morphologies? Are 10 μm silicate features always seen in absorption in Sy 2s and in emission in Sy 1s?

[1] This section and subsection 4.2.1 were adapted from the Large Programme proposal 184.B-0832 (PI: Meisenheimer)

[2] So far this is the only Large Programme for any VLTI instrument.

4. Is the apparent "two component" structure of a compact dense disk and an extended almost round (spherical?) distribution (see Figure **??**, left panel) a general property? Is the dust distribution patchy / clumpy (as found in Circinus)? In which AGNs does maser emission coincide with the dust emission?

5. Is the inner rim at the sublimation radius? So far hot dust ($T \sim 900\,\mathrm{K}$) has been detected in only one object (NGC 1068).

Some of these questions (e.g. on the size–luminosity relation) can be answered directly from the interferometric data, others, such as questions on the structural properties of the dust (e.g. clump sizes and distributions), require a more detailed understanding of the spectra through radiative transfer models. The most far-reaching astrophysical questions, involving accretion mechanisms from the kpc scales of nuclear star cluster to the parsec-scale dust and further in, require comparisons with hydrodynamical models, or at least a study of the physical mechanisms responsible on these scales. The various participating researchers in the Large Programme have planned to perform these studies in the near future.

Here, the first full data reduction of the Large Programme, a set of one-dimensional models and some direct implications from these model fits are presented.

4.2. Observations and Data Reduction

4.2.1. Large programme observational strategy

While the size and shape of the nuclear dust distribution can be derived from very few (u, v) points, a more detailed study is required to investigate the *structure* of the dust distribution and particularly measure clumpiness and warping.

To answer both the questions on detailed structures and on statistical relationships within reasonable time limits, the Large Programme therefore had two objectives:

1. Determine the basic properties for a sample of 8 sources (the *extended snapshot* subsample) and

2. obtain *detailed maps* for three more sources where preliminary data indicated that MIDI achieves good spatial resolution.

The three galaxies for which detailed maps already existed (NGC 1068, the Circinus galaxy and Centaurus A) are some of the closest Active Galaxies. By extending the sample, more distant galaxies with higher luminosities needed to be included. While, on first sight, it may appear that the ability to resolve the dust structure is a strong function of distance, this is not the case, if the "torus" sizes s follow the very basic scaling relation expected for centrally heated dust with heating luminosity L, $s \propto L^{1/2}$: Then, the apparent size at distance D is $\Theta = s/D = \mathrm{const} \cdot L^{1/2}/D$. The luminosity L relates to the observed flux F as $L = 4\pi D^2 F$. Thus $\Theta \propto \sqrt{F}$, independent of the distance D.

Studies of more distant AGNs therefore are feasible with the VLTI, if the above relations hold.

4.2.2. Target list

Some of the LP targets had been observed before in the GTO programmes and were included to complement their (u, v) coverage. Others had not been observed with MIDI before. For selecting those sources, similar criteria had been applied as for the original GTO study: Besides being well observable from Paranal (Declination $\lesssim 25°$), the sources were required to have an unresolved core flux $\gtrsim 200$ mJy[3] at ≈ 12 μm as determined from high-resolution imaging observations (such as Krabbe et al. 2001; Siebenmorgen et al. 2004; Gorjian et al. 2004; Galliano et al. 2005; Haas et al. 2007; Raban et al. 2008; Horst et al. 2009; Gandhi et al. 2009; Prieto et al. 2010; Reunanen et al. 2010). To predict observability with MIDI, it is essential to take nuclear fluxes only from high-resolution observations, as large aperture observations (such as from the IRAS, ISO or Spitzer satellites) are very often contaminated by non-nuclear mid-infrared emission, e.g. from starburst regions.

These selection criteria resulted in a very high success rate of MIDI observability (Raban et al. 2008; Tristram et al. 2009).

In the LP, one quasar, six type 1 and six type 2 galaxies have been observed. Most of them have total fluxes $\lesssim 1$ Jy and all of them have correlated fluxes significantly < 1 Jy. They are therefore among the weakest sources ever observed with MIDI. The (angular size) distances of these sources range from 18 Mpc (NGC 1365) to the cosmological distance of 546 Mpc (3C 273, $z = 0.158$) with the median at 52 Mpc. The most relevant information of the Large Programme targets has been collected in Table 4.1 and the individual targets are introduced in Section 4.4.1.

4.2.3. The observations

Observations were carried out in Visitor Mode between December 2009 and August 2010. Since the targets were much fainter than supported by standard ESO service mode observations, Visitor Mode was required in order to ensure an optimum observing strategy. For the following analysis all other data for the LP targets, that was available through the ESO archive, has also been taken into account. The observing log together with the ESO programme numbers are given in the appendix, Section B.1.

A total of 13.1 nights, corresponding to 151.5 hours (including twilight time[4]), were scheduled of which about 25 % were lost due to technical problems and bad weather. The programme profited from two excellent low-seeing and large-coherent-time nights (2010-03-26 and 2010-03-27), experienced many average nights (with less than 1 hour losses due to technical problems or weather) and a relatively large number of very bad nights (such

[3]The GTO criterium was $\gtrsim 400$ mJy.

[4]ESO's conversion factor between nights and hours only counts hours after/before astronomical twilight, but mid-IR observations can already be started, respectively carried on, in twilight time.

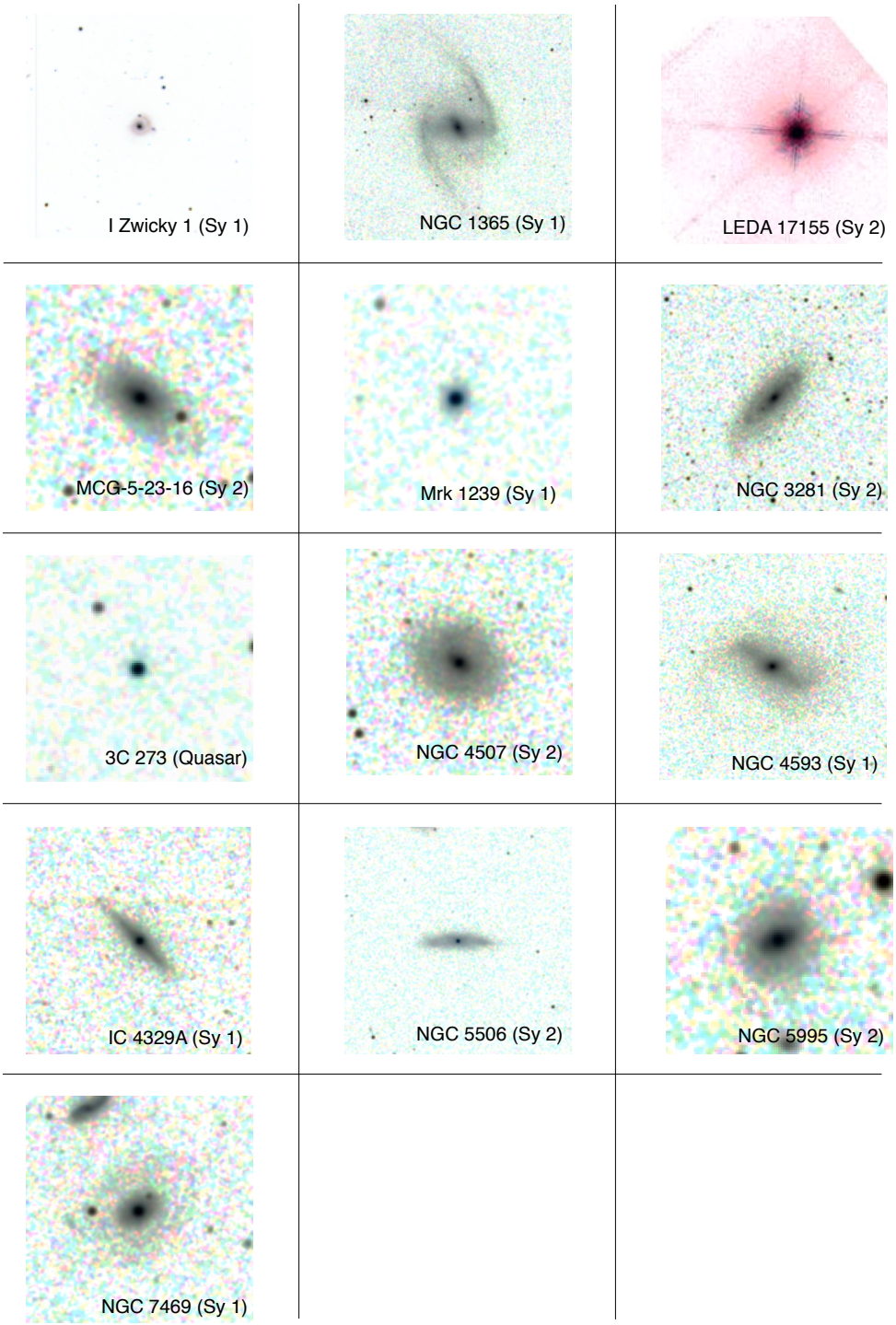

Figure 4.1.: Inverted color images of the Large Programme targets at nearly identical resolutions and wavelengths (with the exception of IZwicky 1 that is a BVR composite from the EFOSC2/ESO 3.6 m telescope, Courtesy I. Saviane and the EFOSC2 gallery). All others are infrared images: LEDA 17155 (IRAS 05189-2524) is an HST NICMOS image (courtesy N. Scoville) from Scoville et al. (2000); all others are 2MASS JHK_s composite images (Credit: NASA/IPAC Infrared Science Archive).
The box sizes of the images are 5' (I Zwicky 1), 9.6' (NGC 1365), 12' (LEDA 17155), 1.8' (MCG-5-23-16), 1.7' (Mrk 1239), 5' (NGC 3281), 1.5' (3C 273), 2.5' (NGC 4507), 5.1' (NGC 4593), 3' (IC 4329A), 6.5' (NGC 5506), 1.5' (NGC 5995), 2.6' (NGC 7469)

Table 4.1.: Large Programme targets and other AGNs studied with MIDI (NGC 1068 (Raban et al. 2009), NGC 4151 (see Chapter 3) and the Circinus galaxy (Tristram 2007))

Name	RA	DEC	type	type	D	scale	$F_\nu^{12.5\mu m}$	Coudé star		$n_{(u,v)}$	$N_{(u,v)}$
	[h m s]	[° ' "]	(1)	(2)	[Mpc]	[mas/pc]	[Jy]	Ψ["]	V [mag]		
I Zw 1	00 53 35.1	+12 41 34	Sy 1	Sy 1	222	0.93	0.44±0.04	0	14.1	9	18
NGC 1365	03 33 36.4	-36 08 25	Sy 1.8	Sy 1	18.1 ± 2.6	11.40	0.41±0.04	0	13.5	12	25
LEDA 17155	05 21 01.7	-25 21 45	Sy 1h	Sy 2	167	1.24	0.31±0.06	0	16.5	6	8
MCG-05-23-16	09 47 40.2	-30 56 54	Sy 1i	Sy 2	38.8	5.32	0.64±0.05	11	13.5	11	22
Mrk 1239	09 52 19.1	-01 36 43	NL Sy 1	Sy 1	84.5	2.44	0.43±0.05	0	14.4	5	9
NGC 3281	10 31 52.1	-34 51 13	Sy 2	Sy 2	47.6	4.33	0.63±0.09	15	15.7	3	7
3C 273	12 29 06.7	+02 03 08	Sy 1.0	Quasar	546	0.38	0.33±0.09	0	12.9	3	4
NGC 4507	12 35 36.6	-39 54 33	Sy 1h	Sy 2	51.7	3.99	0.39±0.08	28	16.0	4	7
NGC 4593	12 39 39.4	-05 20 39	Sy 1.0	Sy 1	44.0 ± 6.4	4.69	0.20±0.07	0	13.9	3	6
IC 4329 A	13 49 19.3	-30 18 34	Sy 1.2	Sy 1	68.3	3.02	1.00±0.04	0	12.9	8	12
Mrk 463 E	13 56 02.9	+18 22 19	Sy 1h	Sy 2	197	1.05	0.34	0	14.3	0	0
NGC 5506	14 13 15.0	-03 12 27	Sy 1i	Sy 2	28.9 ± 0.2	7.14	1.16±0.08	0	12.4	4	8
NGC 5995	15 48 25.0	-13 45 28	Sy 1.9	Sy 2	102	2.02	0.35±0.13	26	13.0	2	4
NGC 7469	23 03 15.6	+08 52 26	Sy 1	Sy 1	60.9	3.39	0.44±0.08	0	13.3	2	8
NGC 1068	02 42 40.7	-00 00 48	Sy 1h	Sy 2	14.4	14.32	16.00±1.00	0	12.0	12	16
NGC 4151	12 10 32.6	+39 24 21	Sy 1.5	Sy 1	14	14.73	1.30±0.30	0	12.3	3	7
Circinus	14 13 09.9	-65 20 21	Sy 1h	Sy 2	4	51.57	14.00±0.50	50	12.5	11	21

(1) AGN type as classified in NED (Véron-Cetty & Véron 2006): The classification of intermediate Seyfert types (1 < type < 2) is defined by the ratio of Hβ to [OIII]λ5007 fluxes. Sy 1h are 'hidden' Seyfert 1 galaxies (i.e. where broad lines have been seen in polarized light), In the Sy 1i type, broad Pa β lines are detected
(2) AGN type from SIMBAD
D (without given uncertainty): angular-size distance derived from redshift using the CMB reference frame and a concordance ΛCDM cosmology, D (with given uncertainty): redshift-independent distance measurement (average over several observations, see NED), the distances of NGC 1068, NGC 4151 and of the Circinus galaxy have been taken from the respective publications.
$F_\nu^{12.5\mu m}$: flux at $12.5 \pm 0.2\mu$m as seen by MIDI (the Mrk 463E flux is from Raban et al. (2008))
Ψ: Coudé (MACAO) guide star separation from science target (0: guiding on nucleus)
$n_{(u,v)}$: number of good fringe tracks at (u, v) points separated by $\gtrsim 1$ telescope diameter ($D = 8.2$m) from each other

$N_{(u,v)}$: total number of good fringe tracks

as most of the nights in May 2010) during which strong wind, extreme seeing, fog and even rain made observations impossible.

4.2.4. Data reduction, selection and handling

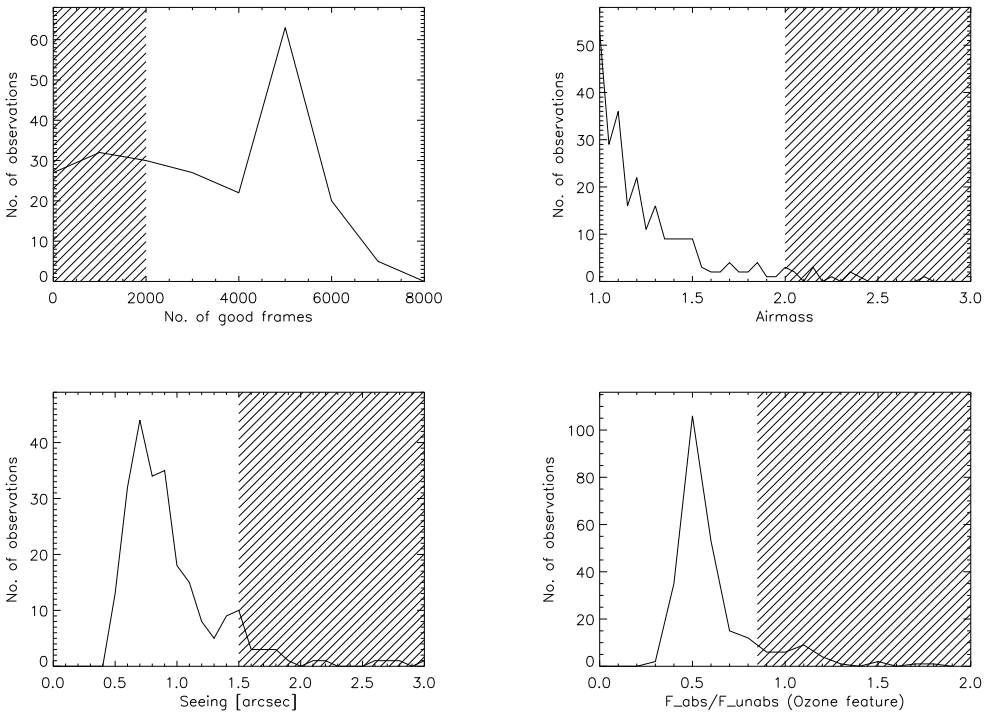

Figure 4.2.: Histogram for the quality of the fringe track observations measured by the number of good frames (top left), airmass (top right), seeing (bottom left) and $F_{\rm abs}/F_{\rm unabs}$ in the telluric Ozone feature (bottom right). Observations in the hatched areas were rejected. See text for details.

Data selection Selection criteria were applied to both raw and reduced data to reject bad observations and spurious results. The criteria were based on experience with other datasets and tests of systematic errors (see Section 1.7.4) and they were rather strict in order to get a *first reliable overview* of the whole LP dataset, not to keep the maximum number of datasets.

Seven fringe tracks were rejected on the raw-data level because the telescope was in chopping mode (such data is not reducible reliably) and two were rejected because they were accidentally taken in the wrong tracking mode[5] and no suitable calibrators were available.

[5]Weak source fringe tracks are best taken in off-zero tracking mode, see Chapter 1.

For the data selection in the reduced data stage, automatic selection criteria were applied to prevent (or at least control) the introduction of biases due to the selection. Out of the 253 fringe tracks (228 from the Large Programme and 25 from the archive) taken into account, 138 were identified as good and 115 were flagged as bad for the following reasons (some tracks were rejected for multiple reasons, see the observing log, Section B.1):

- number of good frames (as determined by EWS, see Section 1.6.8) N_{good} was required to be > 2000. For the weak sources ($F_{\mathrm{corr}} \approx 300$ mJy), 8000 frames roughly correspond to a signal/noise of only 5. If there are less than 2000 frames, not only does the signal to noise decrease to unacceptable levels, but often this is also indicative of other, maybe undetected, problems with this dataset. (59 tracks were rejected for this reason)

- The airmass z was required to be < 2.0. For very high airmasses (and weak sources), the adaptive optics correction by MACAO works considerably less well, possibly loosing overlap between the two beams. In some cases, the correlated fluxes have reached unrealistically low values for very high airmass observations. (13 tracks)

- Only observations taken at a seeing $< 1.5''$were accepted. The seeing values were taken from the DIMM observations in the optical near zenith. While MIDI observes in a different waveband and possibly at a different location on the sky than the DIMM, this value proved to correlate with the calibration errors for MIDI (see Section 1.7.4). Besides affecting the beam overlap, large seeing values also imply low values for the atmospheric coherence time, leading to correlation losses. (40 tracks)

- The Ozone feature depth was required to be well visible above the noise in the raw counts: The telluric Ozone feature should produce a pronounced decrease of flux at (9.65 ± 0.25) μm so that the ratio between the measured flux, F_{abs}, to the expected unabsorbed flux, $F_{\mathrm{unabs}}^{\mathrm{expected}}$, should be ≈ 0.4. By linearly interpolating between (9.0 ± 0.1) μm and (10.3 ± 0.1) μm, a rough estimate of the "unabsorbed" count rate, F_{unabs} is found. If $F_{\mathrm{abs}}/F_{\mathrm{unabs}} > 0.85$, not a large portion of the signal went through the earth's atmosphere and the observation is probably spurious. (37 tracks)

Apart from these automatic selection criteria, data were manually inspected if the calibrated fluxes showed unexpected results. This way 13 fringe track observations were manually rejected due to clouds (as seen from the ESO ambient conditions database), obvious signs of correlation losses (extremely low fluxes at 8 μm, not seen in other correlated flux spectra of this source), extremely low signal/noise ratios or large variations in the OPD during the fringe track.

For the single-dish spectra, similar criteria were applied, but the seeing limit was relaxed to 2.0. Out of 148 single-dish spectra (130 from the Large Programme, 18 from the archive), 79 were identified as good and 69 as bad. Out of the latter, 37 were flagged

for their excessive flux in the Ozone feature, 5 due to high seeing, 6 due to high airmass. Further 24 single-dish spectra were rejected due to very uneven backgrounds, clouds or problems that affected only one of the two photometric channels.

The bad data flags are included in the observing log in the appendix, Section B.1.

Data reduction The data reduction procedure followed the outline given in Section 1.6. For the very weak targets observed during the Large Programme, the most recent (2011) versions of MIA+EWS produced different results than older versions (especially the ones released before 2009) because of the various modifications of the data reduction routines for weak targets as described in that Section 1.6.

Data reduction and handling Data reduction of such a large amount of data (ca. 300 GB of raw data or roughly 10 million individual frames) requires a considerable amount of book-keeping. For this purpose a database was set up to hold all information required for the data reduction and analysis (see Figure 4.3). The database consisted essentially of four tables:

- *Observations* – Information extracted directly from the raw data headers
- *Calibrators* – Spectra and other information of about 800 N band calibrators, kindly provided by Roy van Boekel
- *Corr_fluxes* – Storage of all reduced and calibrated fringe track data
- *Photometries* – Storage of all reduced and calibrated single-dish data

The data reduction for a Large Programme source would then follow the outline given in Figure 4.3.

For example, the best calibrator for any target observation (fringe track or photometry) was found automatically by using a weighting function that takes into account both the angular and temporal distance of the calibrator star from the science target. References for reasonable values for the relative weighting of these two distances are hard to find in the literature. At the Keck Interferometer it is assumed that either $t_0 = 1$ hour temporal distance or $\phi_0 = 15$ degree sky distance lead to an increase of variance in the calibration by a factor of two.[6] These values were used to determine the 'penalty' function p for a calibrator observation given a target source's position and time. p was defined as a function of time difference Δt and angular difference on the sky $\Delta\phi = \sqrt{(\Delta RA \cdot \cos\delta)^2 + (\Delta\delta)^2}$

$$p = \frac{\Delta t}{t_0} + \frac{\Delta phi}{\phi_0} \tag{4.1}$$

The calibrator with the lowest value of p was chosen to calibrate the science observation. Normally these were simply the calibrators observed specifically for the science source.

[6] http://nexsci.caltech.edu/software/V2calib/wbCalib/index.html

However, this simple function replaced the tedious procedure of manually matching target and calibrator observations for several hundred observations. Besides, for repeated calibrator – target – calibrator observations, it made sure that each target observation was matched with the closest calibrator observation.

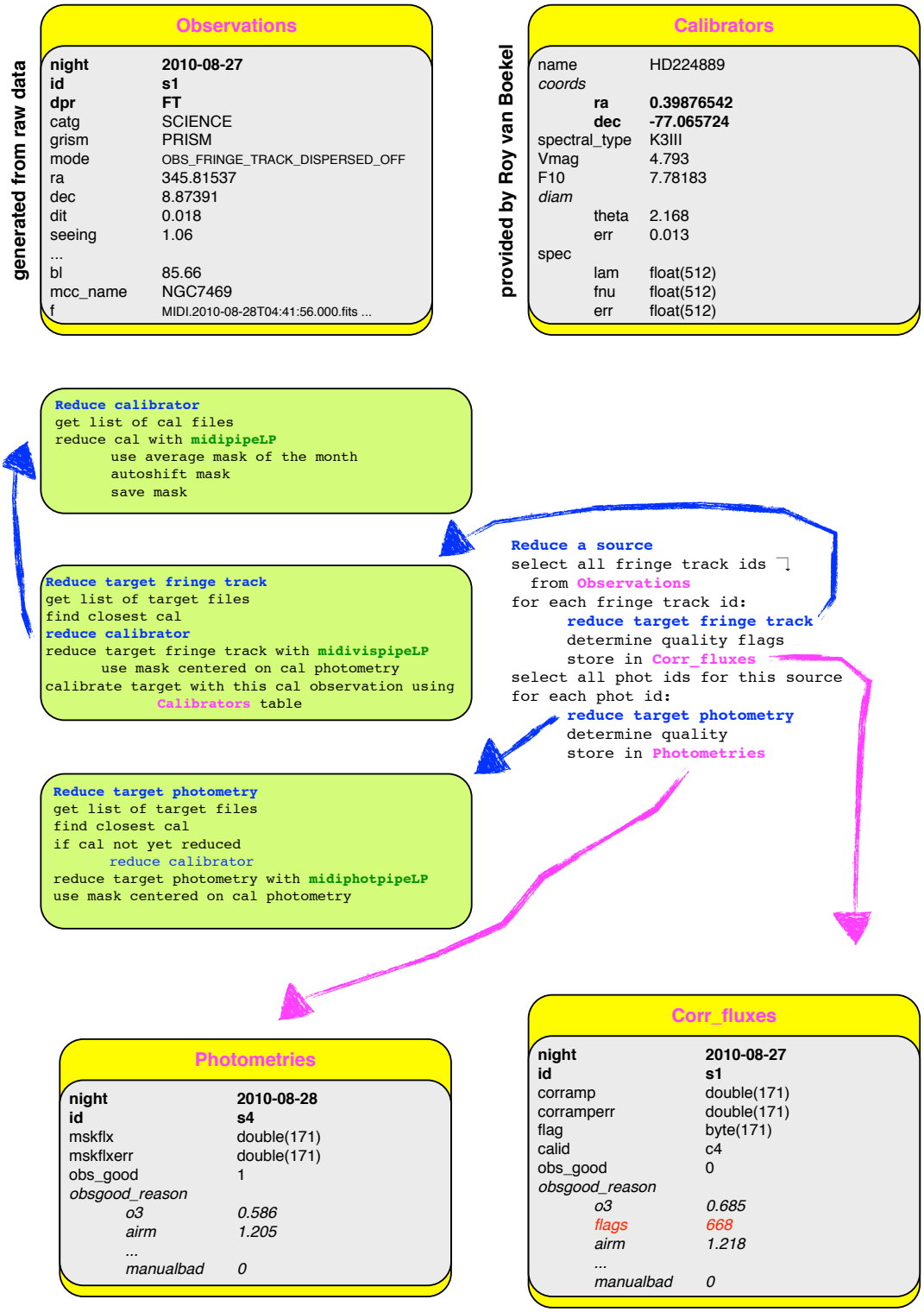

Figure 4.3.: Scripts (blue, in pseudocode) and selected fields of database tables (magenta) used for the LP data reduction, the midi*pipeLP scripts are a part of EWS and were described in Section 1.6. A combination of entries (printed in bold) served as unique identifiers of a dataset in a table, see text for details

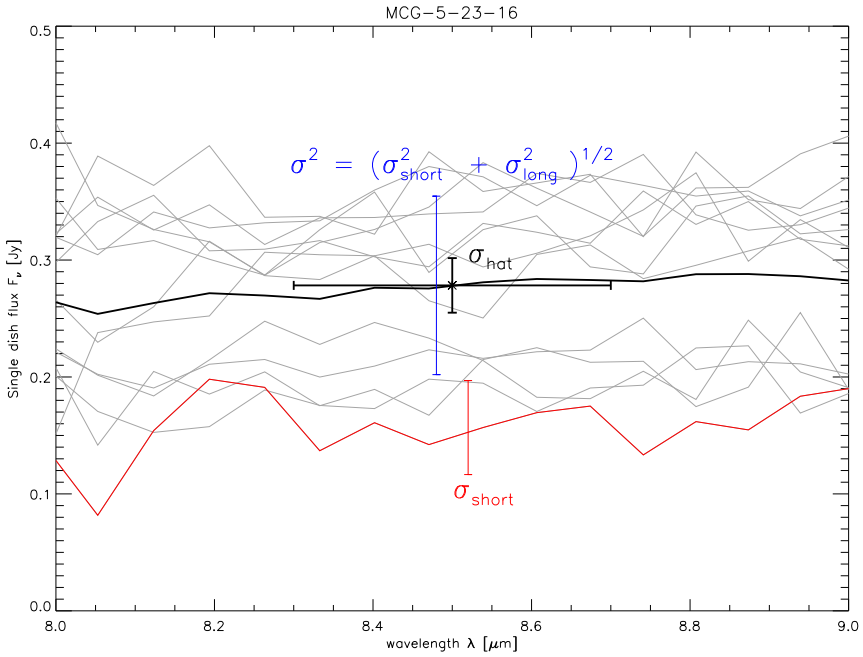

Figure 4.4.: Explanation of the error sources using the example of a set of MCG-5-23-16 single-dish observations (grey lines): A short-timescale error σ_{short} (red) can be determined from an individual observation, the total error measured on a set of observations (blue) is assumed to be the quadratic sum of this error and a long-timescale error σ_{long}. Using this error decomposition the error of the flux averaged over both all observations and a certain wavelength range (black, $\sigma_{hat} = \widehat{\sigma}(\lambda \pm \Delta\lambda)$) can be determined. The blue and red error bars were slightly offset for readability. See text for details.

4.2.5. Uncertainties in the calibrated data

Single-dish spectra MIDI single-dish spectra of all but the strongest sources ($F_\nu \gg 10$ Jy) have large uncertainties. This affects all targets of the Large Programme. However, since we have taken $N_{\mathrm{obs}} \gg 1$ such spectra per source in the course of the Programme, we are able to reduce the error (for most sources) significantly by using averaged fluxes. Yet when averaging both between observations and within one observation (i.e. over a wavelength range $\pm\Delta\lambda$), one must take into account that the uncertainty of the single-dish spectra has two main components that occur on different timescales and have to be treated differently in the averaging process (see Figure 4.4):

1. $\sigma_{\mathrm{short}}(\lambda)$, an error that occurs on relatively short timescales ($\ll t_{\mathrm{obs}} \approx 2$ min) and is probably dominated by photon noise. It can be estimated reliably by computing

the variance[7] between subsets of one observation (see Section 1.7.3).[8]

2. $\sigma_{\rm long}(\lambda)$, an error that is negligible for one observation but affects offsets *between* repeated observations. It is probably dominated by the imperfect background subtraction of single-dish observations (see Section 1.6.9) and it is reasonable to assume that this error follows a Gaussian distribution with zero mean.

Since we have taken multiple observations, we can determine both $\sigma_{\rm short}(\lambda)$ (out of each individual observation) and the total error $\sigma(\lambda)$ (from the variance of multiple observations) empirically. Thus we can determine $\sigma_{\rm long}(\lambda)$ under the assumption

$$\sigma^2(\lambda) = \sigma^2_{\rm short}(\lambda) + \sigma^2_{\rm long}(\lambda). \tag{4.2}$$

Figure 4.5 shows this decomposition for the five sources for which we have seven or more good single-dish spectra. It is evident that $\sigma^2_{\rm long}(\lambda)$ (the blue curve) dominates in all sources except in MCG-5-23-16.[9]

The error $\widehat{\sigma}(\lambda \pm \Delta\lambda)$ of the flux averaged at a certain wavelength and over many observations is then given by

$$\widehat{\sigma}^2(\lambda \pm \Delta\lambda) = \frac{1}{N_{\rm obs}} \left(\frac{\langle \sigma^2_{\rm short} \rangle_{\rm obs,\lambda}}{N_\lambda} + \langle \sigma^2_{\rm long} \rangle_\lambda \right) \tag{4.3}$$

where $\langle \cdot \rangle_{\rm (obs,)\lambda}$ denotes a variance, averaged over (all observations and) $\lambda \pm \Delta\lambda$. N_λ is the number of bins in the wavelength range $\lambda \pm \Delta\lambda$.

Since eight of our thirteen sources do not have a sufficiently large number (≥ 7) of single-dish observations to derive $\sigma_{\rm long}(\lambda)$ from the spread of the data, we use the average value of $\sigma_{\rm long}(\lambda)$ from the more frequently observed sources (Figure 4.5). This basically sets a lower limit to the derived values of $\widehat{\sigma}^2(\lambda \pm \Delta\lambda)$.

If $\sigma_{\rm long}$ is really determined by imperfect background subtraction, it should be independent of source brightness (so that the relative error decreases). And if $\sigma_{\rm short}$ is dominated by shot noise, the signal/noise ratio is $\propto \sqrt{N}$ where N is the number of counts on the detector. Between 9 and 11.5 μm the brightest source, IC 4329A ($F_\nu^{12.5\mu{\rm m}} \approx 1$ Jy), indeed has a larger total error than the other sources – but the lowest $\sigma_{\rm short}(\lambda)$. We conclude that – in the range of fluxes studied here – other factors than the source flux seem to determine the errors and thus justify the approximation of applying the same value of $\sigma_{\rm long}$ for all sources.[10]

[7] The variance is defined as $\sigma^2(\lambda) = \langle \sigma^2(\lambda) \rangle - \langle \sigma(\lambda) \rangle^2$, where $\langle \cdot \rangle$ denotes the arithmetic average.

[8] Photon noise follows Poisson's statistics, but in this case it can be well approximated by Gaussian statistics due to the large number of counts (even for weak sources).

[9] This is the only type 2 source in this sample and the only source for which the adaptive optics was set to off-target guiding. A correlation between AO guiding mode and source quality was not further investigated.

[10] The flux errors for much brighter sources, such as the Circinus galaxy or NGC 1068 (see Section 4.4.1.2) show that single-dish errors in MIDI remain a nuisance even for moderately bright sources ($F_\nu \approx 10$ Jy) where the relative errors are still comparable to the weak LP targets.

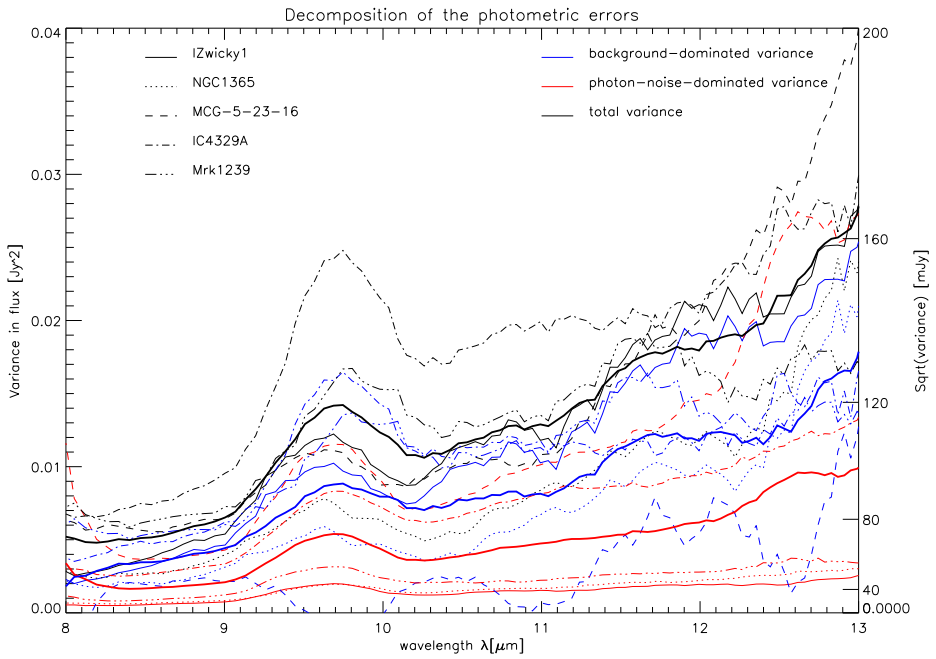

Figure 4.5.: Decomposition of the error in MIDI single-dish spectra of weak sources: Total observed variance $\sigma^2(\lambda)$ (black), short-time fluctuations $\sigma^2_{\text{short}}(\lambda)$ (red), long-time fluctuations $\sigma^2_{\text{long}}(\lambda)$ (blue), see text for details. The sum of the red and the blue curve are the black one. Thin lines with various linestyles: individual sources (indicated in the plot); thick lines: average values for all sources. In the average curves a local maximum can be seen in the region of telluric Ozone absorption. A boxcar-smoothing with a width of about 0.2 μm has been applied to all curves for readability.

Correlated flux spectra Correlated fluxes are less affected by an uneven background since most of the background is removed through high-pass filtering (see Section 1.6.4). Experiments with repeated observations of identical (u, v) points (Section 1.7.4) have suggested that, for correlated fluxes, $\sigma_{\text{long}} \lesssim \sigma_{\text{short}}$. The errors in correlated fluxes are therefore simple errors of the mean, i.e. the flux averaged over the given wavelength regime.

Systematic errors Systematic errors have been studied specifically for the LP dataset. The tests and results have been described in Section 1.7.4.

4.3. Results

4.3.1. (u, v) coverages

The resulting (u, v) coverages are displayed in Figure 4.6.

For the "detailed map sources" NGC 1365, MCG-5-23-16 and IC 4329 A, continuous fringe tracks[11] on at least one baseline were planned but only partially achieved for NGC 1365 and MCG-5-23-16. In IC 4329 A no continuous fringe track was observed but a good overall coverage of the (u, v) plane was reached.

For the sources of the "extended snapshot" sample, six (u, v) points were planned so that two or three position angles would be sampled by two or three baseline lengths each. It was attempted to span a right angle between two of these directions in order to detect elongation.

For two sources, the desired coverage has been reached (I Zwicky 1 and LEDA 17155). For the others, gaps remain, mostly as a result of weather loss. Follow-up observations are scheduled to compensate for this loss (see Section 4.7).

4.3.2. Correlated flux and single-dish spectra

All correlated flux and single-dish spectra are given in the appendix B.2.

The single-dish spectra are colored by year to show that the variability in these fluxes is $\lesssim$ errors of the individual photometries. In other words: To the accuracy of the single-dish uncertainties ($\approx 30\%$), we can exclude flux variability in the mid-infrared between the respective observations.

Neither the single-dish nor the correlated flux spectra show any spectral lines (not even the often seen [Ne II] 12.81 μm forbidden line, indicative for star forming regions). The only feature present in some of the spectra is that of Silicates. It can be seen most clearly in emission in I Zwicky 1 and in Mrk 1239 and in absorption in LEDA 17155, NGC 3281 and in NGC 5506.

4.3.3. Visibilities on the (u, v) plane

In Section B.3 in the appendix, the visibilities are displayed on a (u, v) plane (and again colored by year) to give an overview of the level and range of the visibilities in the targets. From these plots, it can also be seen that there are no signs for elongation in any of the targets, with the possible exception of MCG-5-23-16.

4.4. Radial visibility models

With phase-less visibilities (correlated fluxes) on sparsely sampled (u, v) planes, *images* cannot be reconstructed. We therefore compare the observed fluxes to models (see Sec-

[11] A continuous fringe track is a dense sampling of the target (u, v) plane, only intercepted for one calibrator observation per hour.

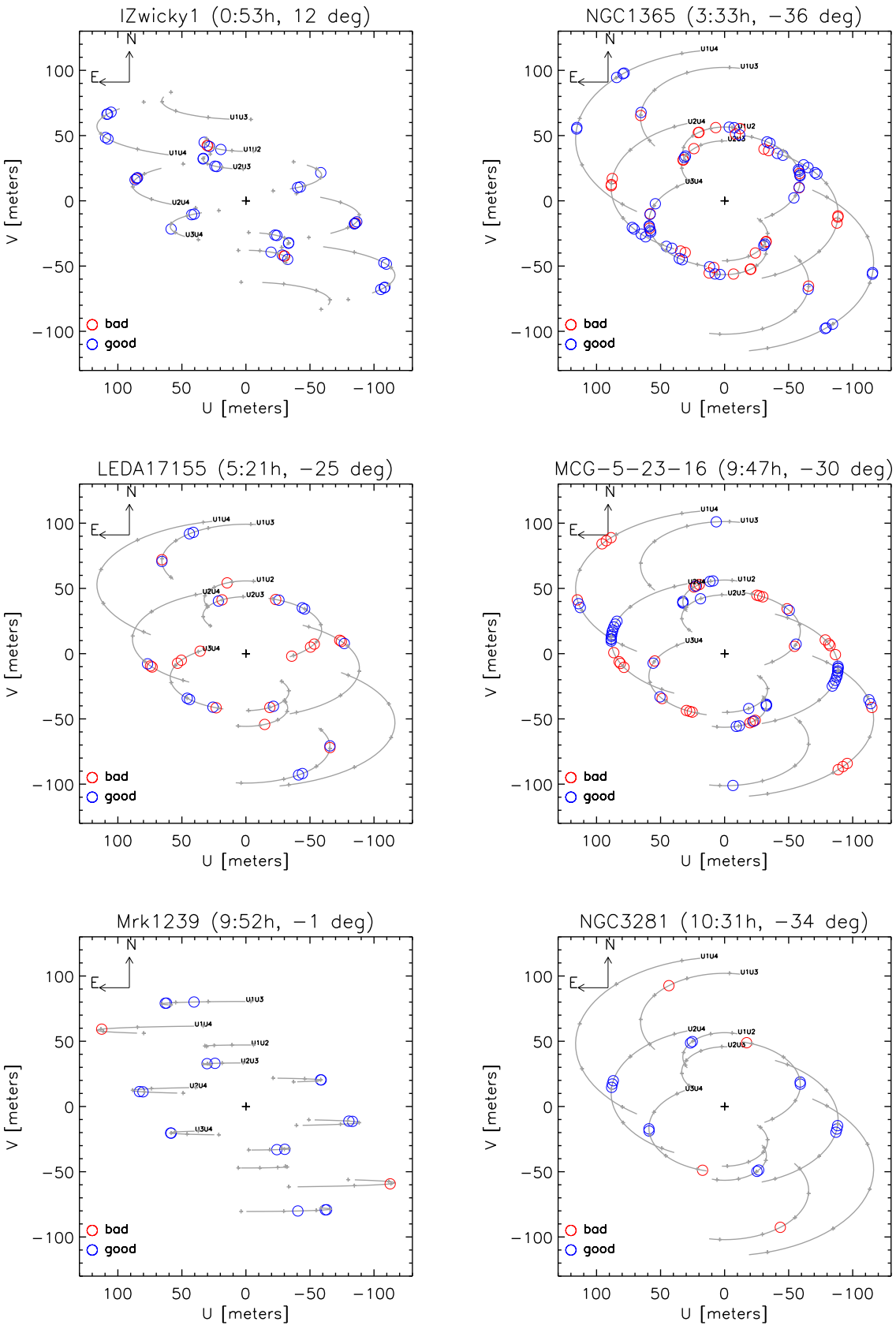

Figure 4.6.: (u, v) coverages of LP targets. Observations flagged as good according to the above mentioned criteria are displayed in blue, others in red. The diameter of the circles corresponds to 8 m, the diameter of the VLT UTs. Small grey crosses denote Hour Angles = -4, -2, 0, 2, 4. (u, v) plane tracks are followed CCW if $\delta < 0$, CW if $\delta > 0$. *Continued on next page*

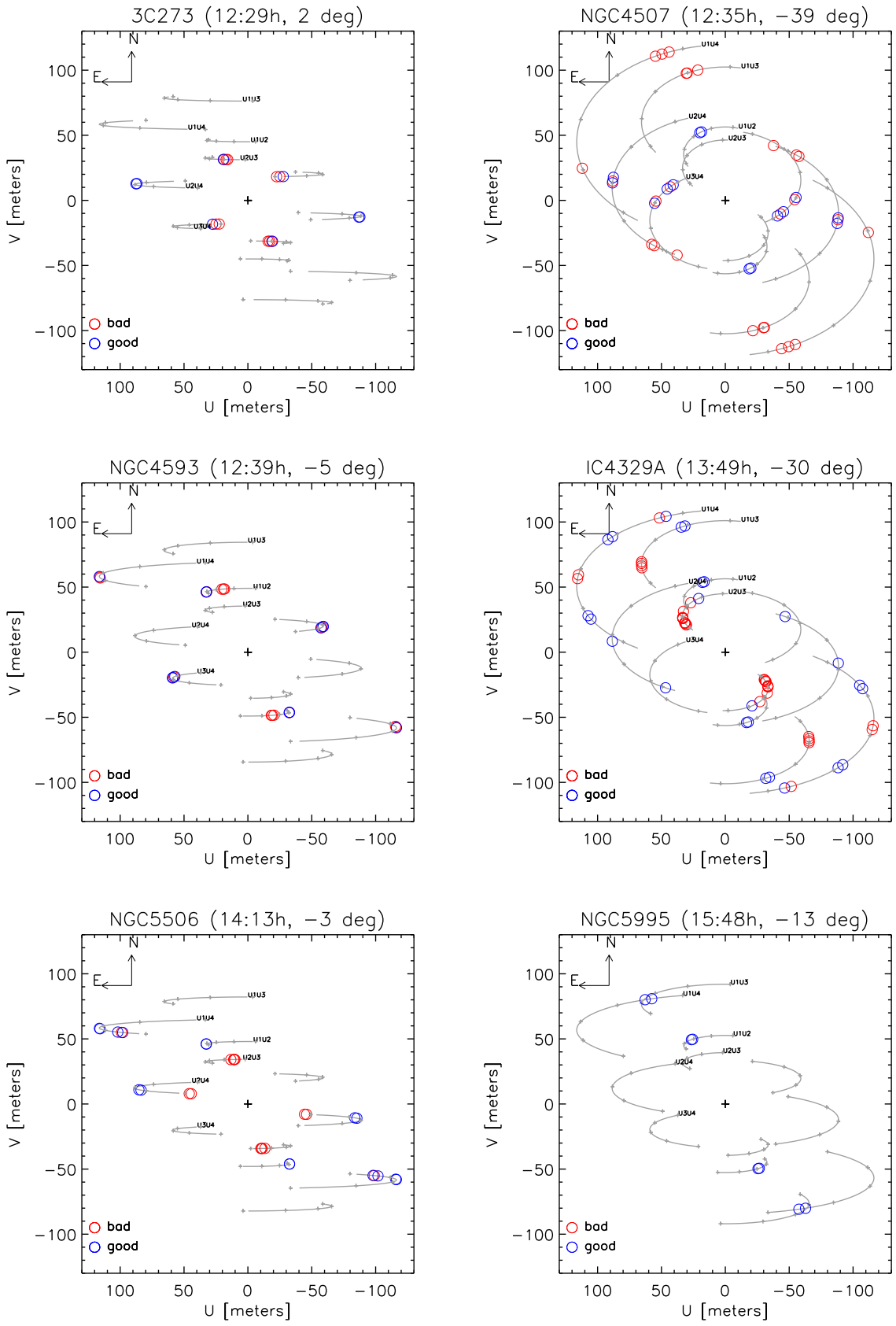

Figure 4.6.: — *Continued*

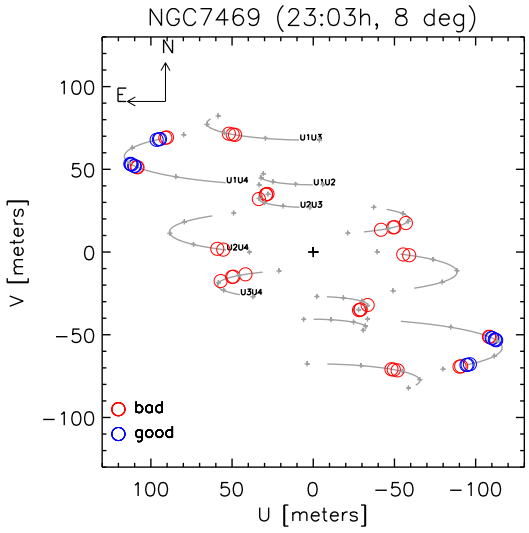

Figure 4.6.: — *Continued*

tion1.2.5). The goal of these first model fits to the LP targets is to derive reasonable estimates (with errors) of the size and flux of the resolved emitter, if it exists, and an estimate of the unresolved flux. To this end we are looking for a decrease of correlated flux with increasing baseline length and fit a Gaussian profile to it.

We fit fluxes and not visibilities (see also discussion in 3). This way the (relatively large) error of the single-dish flux (taken as the 'zero baseline' point) is cleanly separated from the errors of the correlated fluxes.

Since no pronounced dependence of visibility on position angle is visible from the visibility plots on the (u, v) plane (Appendix B.3), circular symmetry is assumed for all model geometries and we can reduce our co-ordinate system to one dimension, the spatial frequency in radial direction $\mathrm{BL}_\lambda = \sqrt{u^2 + v^2}/\lambda$.

We employ the following radial models for the (correlated) fluxes and fit the parameters of the models at three wavelengths: $8.5 \pm 0.2\ \mu$m, $10.5 \pm 0.2\ \mu$m and $12.5 \pm 0.2\ \mu$m, avoiding regions of low signal/noise and the telluric ozone feature, but probing the region of Silicate absorption with the $10.5\ \mu$m fit.

a) Point source + Gaussian This model consists of an unresolved point source with flux contribution F_ν^p (in mJy) and a (partly) resolved Gauss with flux F_ν^g (in mJy) and FWHM Θ. It seems to be an adequate fit for many of our observations.

$$F_\nu(\mathrm{BL}_\lambda, F_\nu^p, F_\nu^g, \Theta) = F_\nu^p + F_\nu^g \cdot \exp\left(-\frac{(\pi\Theta\mathrm{BL}_\lambda)^2}{4\ln 2}\right) \tag{4.4}$$

This model has been applied e.g. for I Zwicky 1 (Figure 4.7).

b) Point source + lower limit for over-resolved Gaussian In sources where the correlated flux may be lower than the single-dish flux, but no decrease of correlated flux with increasing baseline length is visible, the source is assumed to consist of a point source and an over-resolved Gaussian component to explain the difference between the correlated and single-dish fluxes. In this case, only a lower limit to the FWHM of this Gaussian component Θ (with flux F_ν^g) is given by requiring that the over-resolved component has dropped in flux at least to the level of the standard deviation of the correlated fluxes σ_c at the lowest observed spatial frequency $\mathrm{BL}_{\lambda,\mathrm{min}}$, i.e.

$$F_\nu(\mathrm{BL}_{\lambda,\mathrm{min}}, F_\nu^p, F_\nu^g, \Theta) \lesssim F_\nu^p + \sigma_c \tag{4.5}$$

Substituting Equation 4.4 and rearranging gives a limit for Θ:

$$\Theta \gtrsim \frac{2\sqrt{2\ln F_\nu^g/\sigma_c}}{\pi \mathrm{BL}_{\lambda,\mathrm{min}}} \tag{4.6}$$

This model has been applied e.g. for NGC 3281 and is further explained in Figure 4.13.

c) Point source + large Gaussian + small Gaussian In partly resolved sources where a shallow decrease of correlated flux with increasing BL_λ can be seen, we will consider to add a second, small, Gaussian component (flux F_{g2}, FWHM Θ_2) to the fit:

$$F_\nu(\mathrm{BL}_\lambda, F_\nu^p, F_\nu^{g1}, \Theta_{g1}, F_\nu^{g2}, \Theta_{g2}) = F_\nu^p + F_\nu^{g1}\cdot\exp\left(-\frac{(\pi\Theta_1\mathrm{BL}_\lambda)^2}{4\ln 2}\right) + F_\nu^{g2}\cdot\exp\left(-\frac{(\pi\Theta_2\mathrm{BL}_\lambda)^2}{4\ln 2}\right) \tag{4.7}$$

This model has been applied for IC 4329 A (Figure 4.18) and NGC 5506 (Figure 4.19).

4.4.1. Results

4.4.1.1. Large Programme targets

IZwicky 1 – a very luminous narrow-line Seyfert 1 galaxy This type of AGN is thought to deviate from the $M_{\mathrm{BH}} - \sigma$ relation in the sense that they have 'undermassive' black holes and therefore no strong broad emission lines (Komossa 2008). However, I Zw 1 is also sometimes called a quasar (PG 0050+124, Weedman et al. 2005).

It has a nuclear starburst on kpc scales and a possibly connected circum-nuclear molecular ring (Schinnerer et al. 1998). It is believed that I Zwicky 1 is undergoing a merger with the nearby companion galaxy that is marginally detectable in Figure 4.1 to the west (Scharwächter et al. 2003).

I Zw 1 is well studied in many wavelength regimes: In the X-Rays, different modes of short-term variability are observed from which a two component accretion-disk corona is implied (Gallo et al. 2007). It is also a popular target for observations in the UV for its rich Fe II emission spectrum. (It is hoped to develop an understanding of the Fe II emission mechanism to use it as a diagnostic for BLRs, Bruhweiler & Verner 2008, .) In

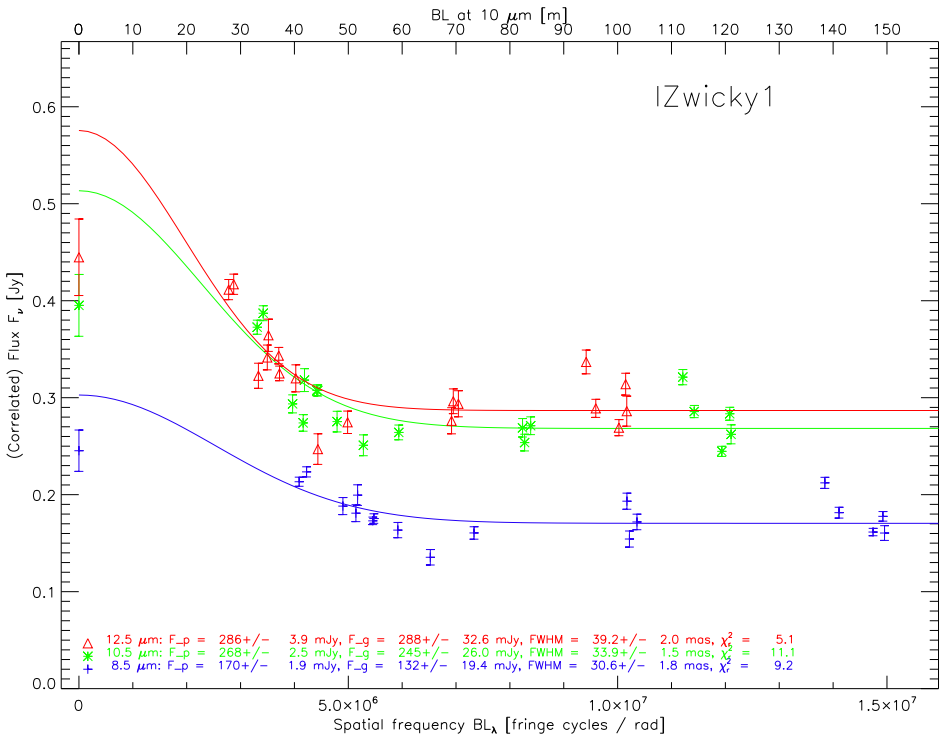

Figure 4.7.: Radial (1D) visibility model for I Zwicky 1. The single-dish ("0-baseline") and correlated fluxes are plotted as a function of spatial frequency for three wavelengths, together with the best fit for a Gaussian + point source model, see text for details. The best fitting parameters are given in the plot.

the infrared, I Zw 1 is found to have "strong Silicate emission and no PAH or emission lines" (Weedman et al. 2005). A dedicated review about this source does not seem to exist, but the introduction of Scharwächter et al. (2007) gives a concise overview over this source.

In our radial models, I Zwicky 1 is the perfect case for the point source + Gauss model (*a*). In all three wavelengths, a clear decrease in correlated flux is seen with increasing spatial frequency. At spatial frequencies $\gtrsim 6 \cdot 10^6$, the flux is at the point source level and does not decrease any more with increasing BL_λ. The fits predict larger single-dish fluxes than observed. This is a consequence of the small errors of the correlated fluxes in comparison with the single-dish fluxes. In this and in the following fits, we decided not to require the fits to meet the single-dish fluxes but to respect the derived statistical errors.

The best fitting values for I Zwicky 1 and for all other sources are given in the respective Figure and in Table 4.2 on page 123.

Figure 4.8.: The "Great Barred Spiral Galaxy" **NGC 1365** as seen in the infrared ($YJHK$ composite) by HAWK-I at the VLT. Image credit: ESO/P. Grosbøl

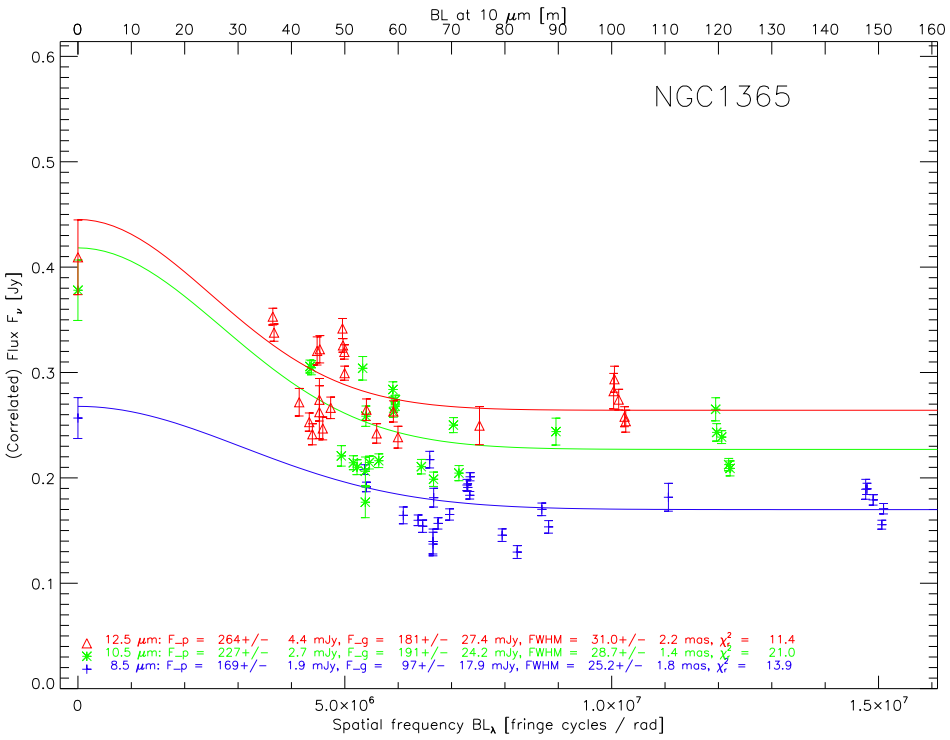

Figure 4.9.: Same as Fig. 4.7 but for **NGC 1365**

NGC 1365 – the one with black hole eclipses The supergiant barred galaxy NGC 1365 is the closest (and maybe the most beautiful, Figure 4.8) of the 13 targets observed in the Large Programme. It exhibits a wide variety of nuclear activity and has been studied, partly because of its prominent bar, in great detail. A radio jet emanates from the optical nucleus and is visible up to $\sim$ 500 pc from the center (Sandqvist et al. 1995) and CO observations have revealed a giant molecular torus of over 1 kpc in diameter (Sandqvist 1999). An excellent review has been given by Lindblad (1999).

Fits to the optical spectrum of NGC 1365 show that a broad component of Hα emission is required and that it is probably a Seyfert 1 galaxy seen through $A_V = 3$ absorption (Veron et al. 1980). However, the optical classification is somewhat vague as some classify it as a Seyfert 1.5 (i.e. 'type 1', Lindblad 1999) and others as a Seyfert 1.8 (i.e. 'type 2', Maiolino & Rieke 1995; Véron-Cetty & Véron 2006). So much seems to be clear: This source is between the type 1 and the type 2 class – and it may even change class due to intrinsic variations. This has been demonstrated very impressively from X-Ray observations when Risaliti et al. (2007) have seen a dramatic change in its X-Ray behaviour: The source changed from Compton-thin to reflection-dominated back to Compton-thin in just four days. This was interpreted as a Compton-thick cloud close to the broad line region that, on its orbit around the nucleus, eclipsed the broad line region while in our line of sight. The deduced size of these X-Ray absorbing clouds, $r \approx 10^{12}$m $\approx 0.1\mu$arcsec,

is clearly out of reach for MIDI, however.

In the mid-IR, [S IV] and [Ne II] were detected by ISO observations, but not in observations with smaller aperture (Siebenmorgen et al. 2004). These TIMMI2 observations also showed no sign of Silicate absorption.

In our radial models, NCG 1365 is, besides I Zwicky 1, the other case where both the decrease of correlated flux and the point source flux level can be clearly seen, i.e. model (a) is well defined. However, the scatter is much larger leading to much larger reduced χ^2 values than for the distant I Zwicky 1. A possible interpretation for some of the scatter is discussed in Section 4.5.2.

In the GTO study (Tristram et al. 2009) this source was found to be partially resolved (confirmed by the new data) and possibly elongated (this cannot be confirmed, see Fig. B.14).

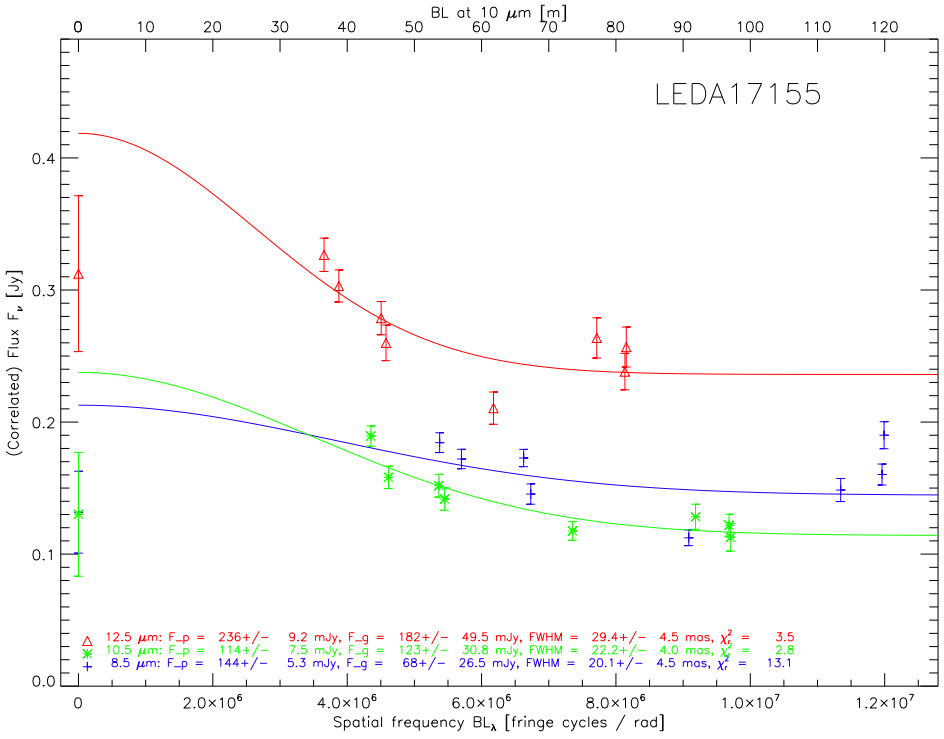

Figure 4.10.: Same as Fig. 4.7 but for **LEDA 17155**

LEDA 17155 – a ULIRG With $\log L(8-1000\mu\mathrm{m})/L_\odot = 12.10$, LEDA 17155 (= IRAS 05189-2524) is an ultraluminous infrared galaxy (ULIRG, Sanders et al. 1988). From optical spectroscopy, it was classified as a Seyfert 2 galaxy by Veilleux et al. (1995) and as a 'hidden Seyfert 1' galaxy by Young et al. (1996) due to the detection of a broad Hα line in polarized light. Deep HST/WFPC observations ($\approx B$ and I bands) reveal clumps

(probably star-forming regions) as well as "loops" and "horns" that are probably tidal features (Surace et al. 1998). In a recent X-Ray observing campaign, Suzaku observations did not show any short-term variability (like in NGC 1365), but revealed a change of flux compared to previous observations with other X-Ray satellites (Teng et al. 2009).

In the mid-IR, Spoon et al. (2002) identified a spectral feature due to water ice at 6 μm and Siebenmorgen et al. (2004) estimated $A_V \approx 12$ mag from the Silicate absorption feature.

The radial models at 10.5 μm and 12.5 μm provide good fits to the MIDI data. At 8.5 μm the source is essentially unresolved.

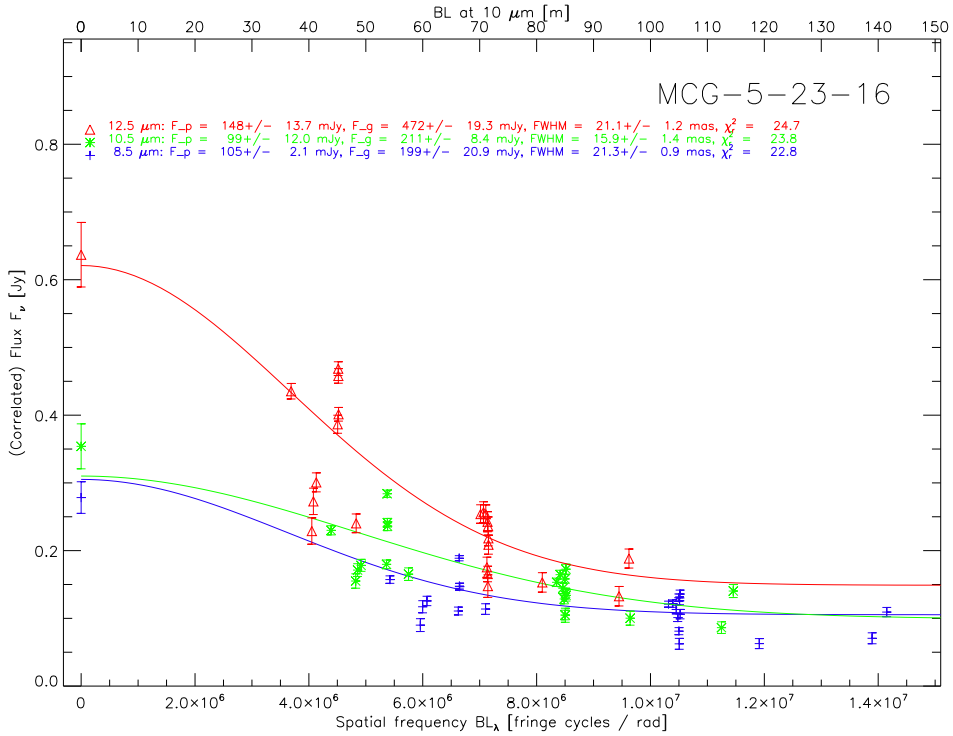

Figure 4.11.: Same as Fig. 4.7 but for **MCG-05-23-16**

MCG-05-23-16 MCG-05-23-16 probably has a hidden type 1 nucleus as suggested both by its original classification by Veron et al. (1980) who found a broad component for the fit to the Hα line and by the current classification as a type 1i (Véron-Cetty & Véron 2006) meaning that a broad Paschen β line is detected. In the X-Rays, MCG-05-23-16 shows an unusual Fe Kα line profile that is difficult to fit with standard accretion disk models (Weaver et al. 1997).

In this relatively nearby source, again a clear decrease in fluxes with BL_λ is seen (model a). At two spatial frequencies, $4 \cdot 10^6$ and $7 \cdot 10^6$ for the 12.5 μm fit, the measured fluxes

show a large scatter around the best-fit value. While the spatial frequency is nearly the same for all of these values, the position angle changes by about 10 °. A possible dependence of correlated flux on PA is discussed in Section 4.5.2 and Figure 4.26.

Tristram et al. (2009) found the source partially resolved.

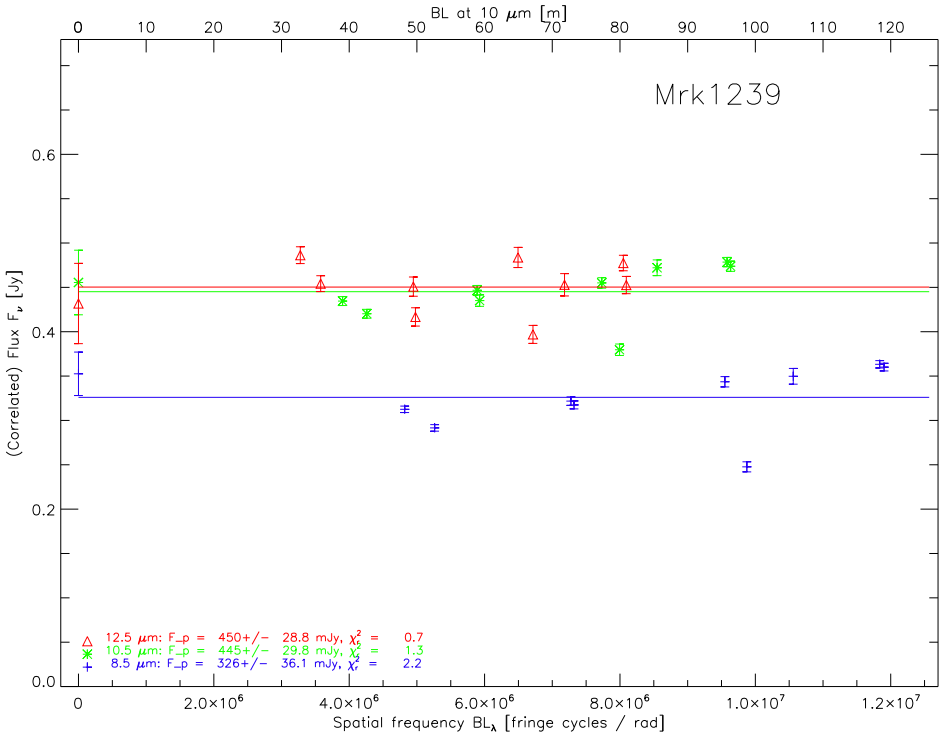

Figure 4.12.: Same as Fig. 4.7 but for **Mrk 1239**

Mrk 1239 In an infrared spectrum taken with the Infrared Telescope Facility (IRTF), Rodríguez-Ardila & Mazzalay (2006) find an unusually strong bump of emission peaking at 2.2 μm that is well fitted by a 1200 K blackbody. In the mid-infrared, no PAH emission is seen (indicating the absence of star formation) – probably because the infrared flux of the whole galaxy is dominated by emission from the AGN (Reunanen et al. 2010).

In this source, all MIDI correlated fluxes are on the same level as the single-dish fluxes: Mrk 1239 is unresolved in the mid-IR on $\approx$ 10 mas scales, confirming the result found from the GTO observations (Tristram et al. 2009). In this case, a Gaussian component is not required and we defined the point source flux and error as the average and rms error of the average, respectively.

NGC 3281 NGC 3281 is notable for its highly obscured nucleus and its relatively small ratio of visual extinction A_V to absorbing hydrogen column (1/50 the Galactic value)

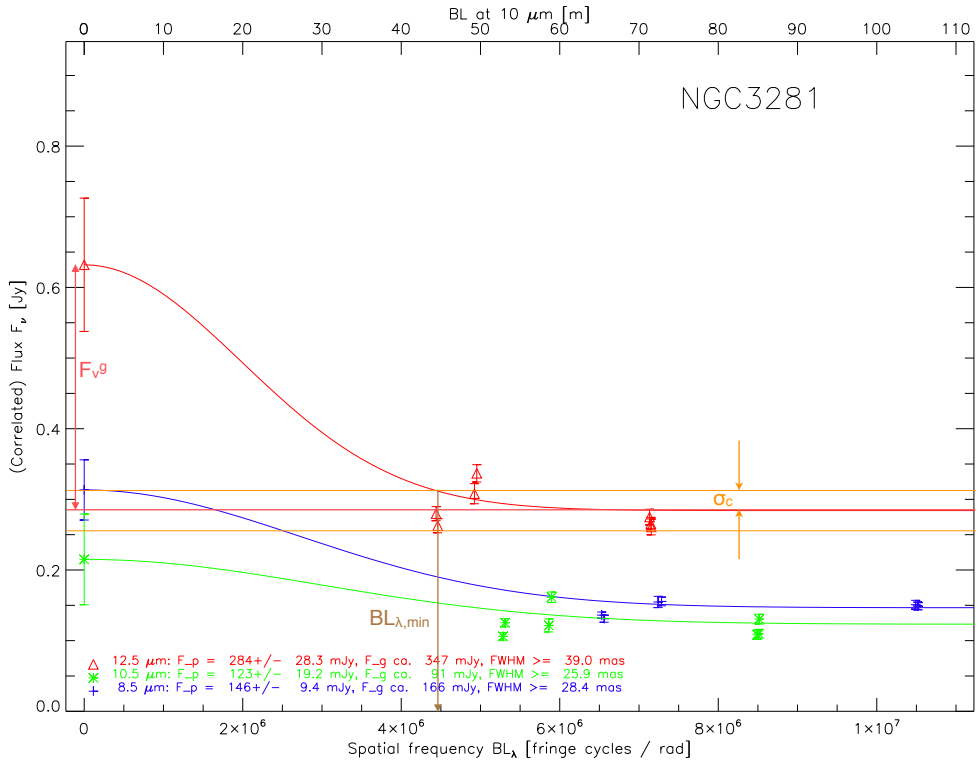

Figure 4.13.: Same as Fig. 4.7 but for **NGC 3281**. Model *b* is explained using the example of the 12.5 μm fit. A lower limit for the size of the over-resolved component with flux F_ν^g is derived by requiring the model visibility curve (red) to have dropped to the point source level + the spread in point source flux σ_c at the lowest spatial frequency $\mathrm{BL}_{\lambda,\mathrm{min}}$. In other words: the red curve is required to intersect the upper yellow curve at $\mathrm{BL}_{\lambda,\mathrm{min}}$.

density N_H as found by Simpson (1998) in a near-IR and X-Ray study of this galaxy. This finding was explained by Vignali & Comastri (2002) with a special geometry of the obscuring material, although this must not necessarily be the case since a large range in A_V/N_H, and especially values lower than the Galactic value, have been found in AGNs by Maiolino et al. (2001). In the respect of anomalous A_V/N_H values, see also the discussion for the 'unabsorbed Seyfert 2' NGC 5995. While there is no direct evidence of a broad line region in this galaxy (it is classified as a Seyfert 2.0), Storchi-Bergmann et al. (1992) argue that it most probably has a hidden type 1 nucleus as derived from a well-defined biconical ionization region and emission line models.

In NGC 3281 the point source level is adequately well defined by the MIDI correlated fluxes. By requiring that the contribution from the Gaussian component is lower than the rms of the correlated fluxes (model b), we can constrain a lower limit to the size of the Gaussian component.

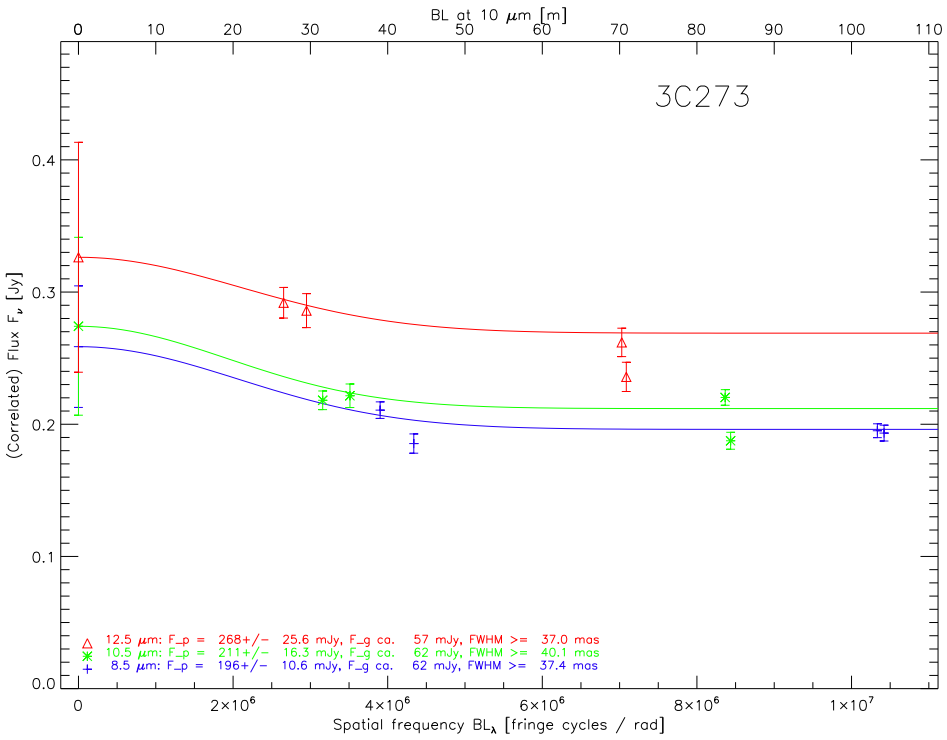

Figure 4.14.: Same as Fig. 4.7 but for **3C 273**

3C 273 – an extremely luminous, cosmological source The only cosmological source in the LP is the quasar 3C 273. It is also the most luminous source accessible with MIDI. With a luminosity $\nu L_\nu \approx 4 \cdot 10^{38}$ W (at $\lambda = 12\,\mu$m), it is about an order of magnitude brighter than the second most luminous galaxy in our sample. At the cosmological redshift of $z = 0.158$ ($D_a \approx 546$ Mpc) it is the most distant object that can be studied with MIDI.

Strictly, it was not part of the Large Programme, because at the time of proposal submission, it was scheduled for observations on a DDT programme (282.B-5071). Unfortunately, that programme was only partly executed due to bad weather and timing constraints. During the LP time, 3C 273 was successfully observed in 2010-01-30 as a backup target.

3C 273 is one of the most well-studied quasars and was the first to be identified with a cosmological source due to its high redshift by Schmidt (1963). The literature for 3C 273 is rich, an overview is given in the review by Courvoisier (1998).

In the infrared, a bump at 3 μm had already been noticed by Neugebauer et al. (1979) and was attributed to the presence of hot dust. On the other hand, this radio-loud quasar has a prominent jet that shines brightly from radio to gamma rays with contributions also in the infrared and shows variability across the electromagnetic spectrum (Soldi et al. 2008). The infrared quiescent flux level has been interpreted as being due to dust emission, however (Robson et al. 1993). This interpretation was confirmed by an observation in a

historic minimum in the sub-millimeter emission of 3C 273's jet where Türler et al. (2006) identified three thermal components of dust at various temperatures ($T \approx 40$, 250, 1300 K). Apart from that, Hao et al. (2005) presented Spitzer spectra that showed Silicate emission features at 10 and 18 μm in 3C 273, requiring the presence of hot dust.

From early MIDI data, the source appeared to be possibly resolved. Tristram et al. (2009) gave two *upper* limits for the size (<67 pc / < 108 pc). The reasoning for this limit was that the correlated flux appeared significantly different at the two baselines observed. This flux difference could not be reproduced with the more extensive LP. Instead, evidence for a decrease of correlated flux with increasing baseline length is marginal and the new observations are comparable with an over-resolved Gaussian that, at the distance of 3C 273, would have to be $\gtrsim$ 100 pc. Most of the emission is unresolved, i.e. on scales $\lesssim \lambda/3BL \approx 7$ mas ≈ 20 pc.

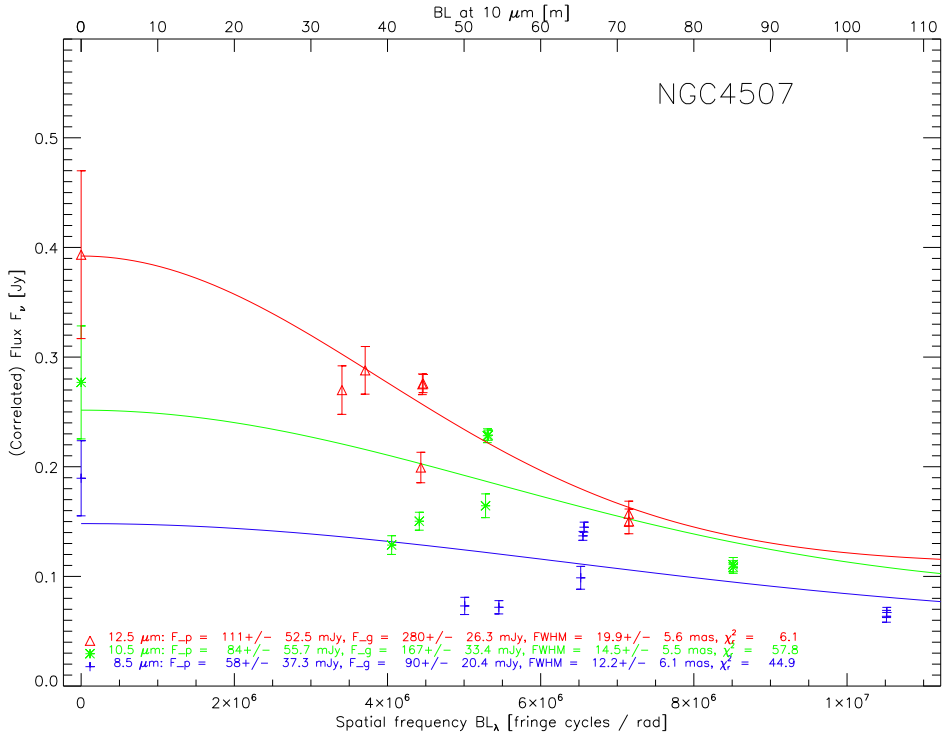

Figure 4.15.: Same as Fig. 4.7 but for **NGC 4507**

NGC 4507 NGC 4507 is another hidden Seyfert 1 galaxy as seen by broad lines in polarized flux (Moran et al. 2000). This Compton-thin, X-Ray bright galaxy has been studied in detail with XMM-Newton and Chandra by Matt et al. (2004). In the mid-infrared the source is unresolved with single-dish observations (Horst et al. 2009).

In NGC 4507, only at 12.5 μm is a clear decrease of correlated flux seen with increasing spatial frequency. But is it real? The two lowest spatial frequency fluxes at 12.5 μm are,

also relatively, higher than at other wavelengths. Their errors, given in the fit in Figure 4.15, are the largest correlated flux errors in this source. These fluxes are probably overestimated due to the spurious "emission feature" at $\lambda \approx 12.5\mu$m seen in the spectra in Figure B.8. Reassuringly, however, the fitted FWHM sizes would not change dramatically if these two points were placed at lower fluxes. Also, all sizes are compatible with each others within the errors.

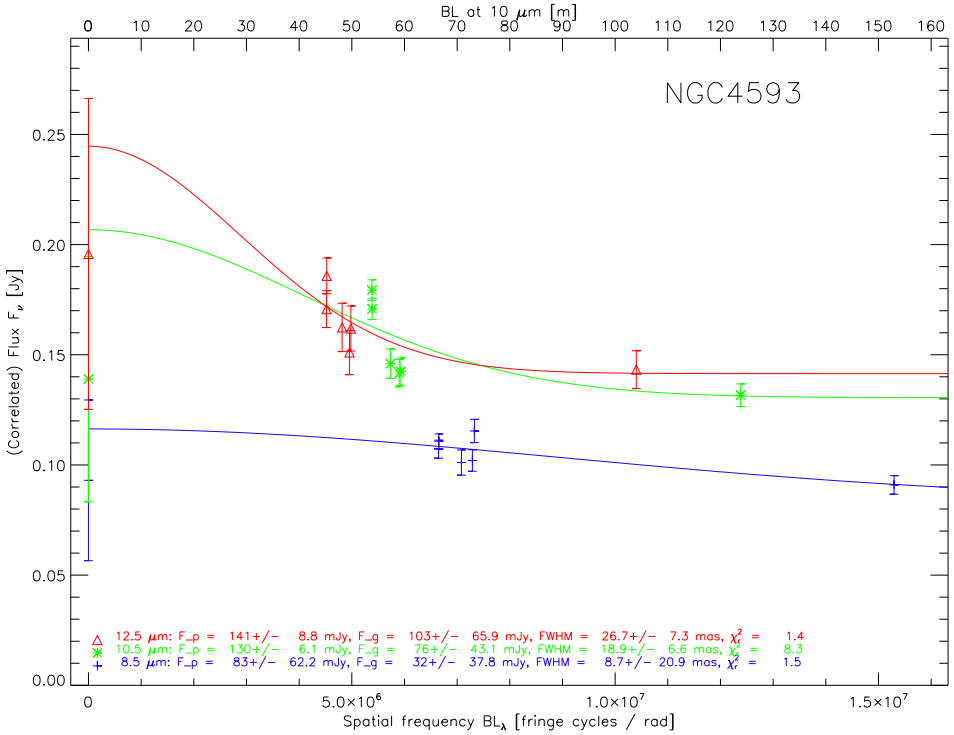

Figure 4.16.: Same as Fig. 4.7 but for **NGC 4593**

NGC 4593 The Seyfert 1 galaxy NGC 4593 is an example of a so called "pseudobulge galaxy" (Kormendy et al. 2006) whose dense nuclear region might be mis-interpreted as a merger-built bulge but is actually thought to be the product of secular evolution. NGC 4593 is a popular target in reverberation-mapping campaigns due to its emission line variability (e.g. Greene et al. 2010). In Spitzer IRS spectra, the 9.7 μm Silicate emission feature is seen, peaking at ≈ 10.5 μm (Horst et al. 2009).

NGC 4593 is among the weakest of all the LP targets with correlated fluxes between 100 and 200 mJy. Nevertheless, a clear decrease of correlated flux with baseline length is seen at all wavelengths, with the most prominent drops at 10.5 μm and 12.5 μm. At these wavelengths, the point source is well defined and the uncertainty in F_ν^g is driven by the large errors of the single-dish fluxes. At 8.5 μm the correlated flux drop is small and

the best fit is found for a very small Gaussian (with shallow decrease of correlated flux). The point source flux is not well defined at 8.5 μm .

Figure 4.17.: BVRI composite image taken at the VLT/FORS2 showing the interacting galaxy group IC 4329 A (left) + IC 4329. Is the activity in IC 4329 A triggered by the nearby elliptical galaxy? X-Ray images show a bridge of hot diffuse gas between the two galaxies (Read & Pietsch 1998). Image Credit: ESO/M. Mejias

IC 4329A The X-ray bright edge-on Seyfert 1 galaxy IC 4329 A (see Figure 4.17) is found near the center of Abell cluster A3574. Its variability has been studied (with little success) in the optical (Peterson et al. 2004) and with more success in the X-Rays (Markowitz 2009). The latter derived a black hole mass of $1.3^{+1.0}_{-0.3} \times 10^8 M_\odot$ from an empirical relation linking it to the break in the power spectral density function and the bolometric luminosity of the galaxy. In the mid-IR, Siebenmorgen et al. (2004) found the [S IV] and the [Ne II] line in TIMMI2 spectra. From the GTO data, the source appeared unresolved (Tristram et al. 2009).

In the LP data, IC 4329A is one of the two sources (besides NGC 5506) where the plot of correlated fluxes versus baseline (Figure 4.18) gives the impression of two resolved components: Clearly, there must be a very large ($\Theta \gtrsim 20 \ldots 40$ mas, depending on wavelength) component to explain the low level of correlated fluxes with respect to the single-dish fluxes. But when looking closer, one can also see a more shallow decrease of flux towards longer baselines – an indication for a second, much smaller and only partially resolved, Gaussian component?

Not really: Adding two parameters (F_{g2}, Θ_2) to accommodate for this component (i.e. moving from model a to model c), does not improve the goodness of fit as determined by the value of χ^2_r. While the absolute value of χ^2 decreases, the lower number of degrees of freedom leads to actually larger values of χ^2_r than for the simpler two component model. The χ^2_r values for model a are 27.0, 53.6 and 46.3 for the fits to the 8.5 μm , 10.5 μm and 12.5 μm data, respectively. In model c, $\chi^2_r = 27.9$, 54.1 and 54.1, respectively. Since our main aim here is to give reliable estimates of the sizes, we actually employ the much simpler model b and give a robust lower limit for the size of the resolved emitter. A large scatter remains around the point source flux level.

The fit with the two components as well as the more robust estimate of the extended component's size are displayed in Figure 4.18.

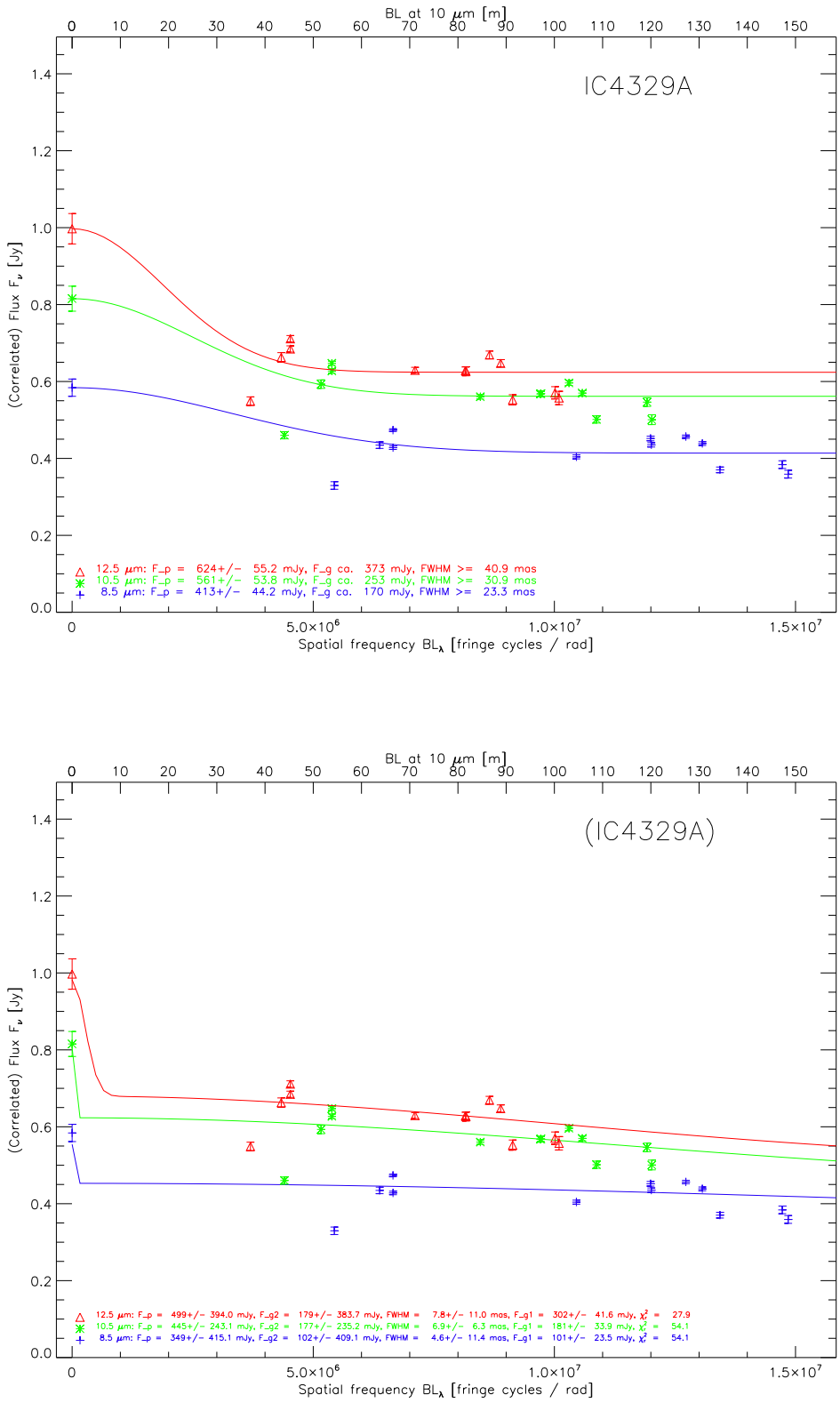

Figure 4.18.: Same as Fig. 4.7 but for **IC 4329 A**. Top panel: Model *b*. The size of the large Gaussian is not constrained in model *c* (lower panel) and only a limit can be given (model *b*). See text for details.

NGC 5506 – an obscured Narrow Line Seyfert 1? Nagar et al. (2002) are convinced to have found in NGC 5506 the first case of an optically-obscured Narrow-Line Seyfert 1: From IR spectroscopy they find permitted lines that, according to them, can only originate from the Broad Line Region. The FWHM of these lines, however, is < 2000 km/s admitting NGC 5506 indeed into the club of NL-Sy1 galaxies. NGC 5506 hosts a relatively luminous H_2O megamaser (Braatz et al. 1994; Henkel et al. 2005). Guainazzi et al. (2010) find a broad Fe Kα line in this galaxy and speculate that reprocessing of this line occurs in the AGN torus.

In this edge-on galaxy (see Figure 4.1), the nucleus is obscured by $A_V \approx 15$ mag as determined from the pronounced Silicate absorption feature (Siebenmorgen et al. 2004, , see also Figure B.11). From the unresolved nucleus at near-infrared wavelengths, Prieto et al. (2010) derive an upper limit to the FWHM size of the source of 0.1 arcsec (13 pc, FWHM). As in Mrk 1239, the IR flux of this galaxy originates almost exclusively from the nucleus (Reunanen et al. 2010).

NGC 5506 is the other candidate for a second, smaller, Gaussian component. In this case, a fit to model c leads to reasonably well defined values for the point source and the small (partially resolved) Gaussian component (see the two plots for this source in Figure 4.19). The over-resolved Gaussian component is not well defined. However, the χ^2_r values for model a are not much different and we *choose* to use the parameter values of the simpler model (a) for the following discussion.

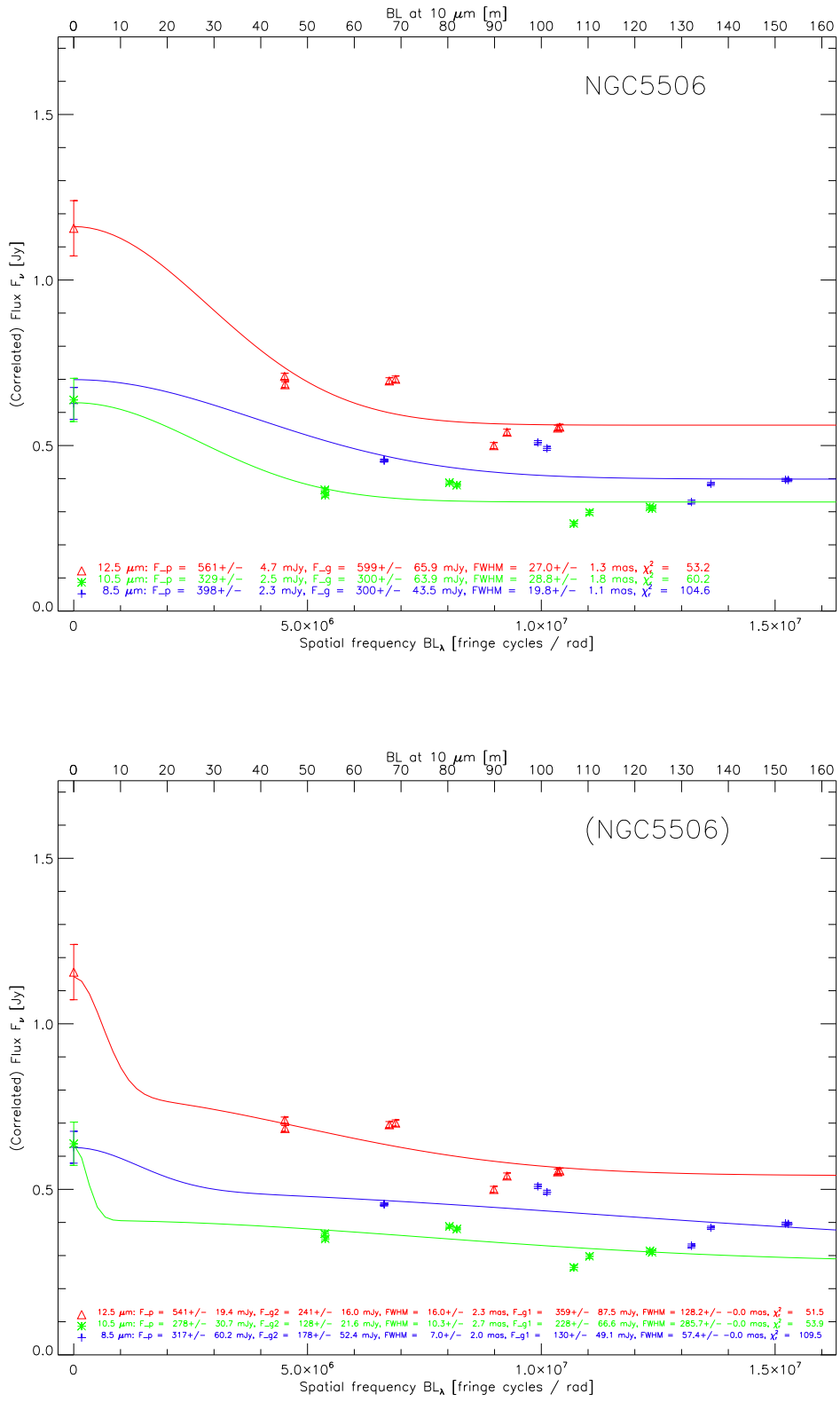

Figure 4.19.: Same as Fig. 4.7 but for **NGC 5506**. In model *c* (lower panel), the size of the large Gaussian component is not constrained, for a limit see model *a* (top panel). see text for details.

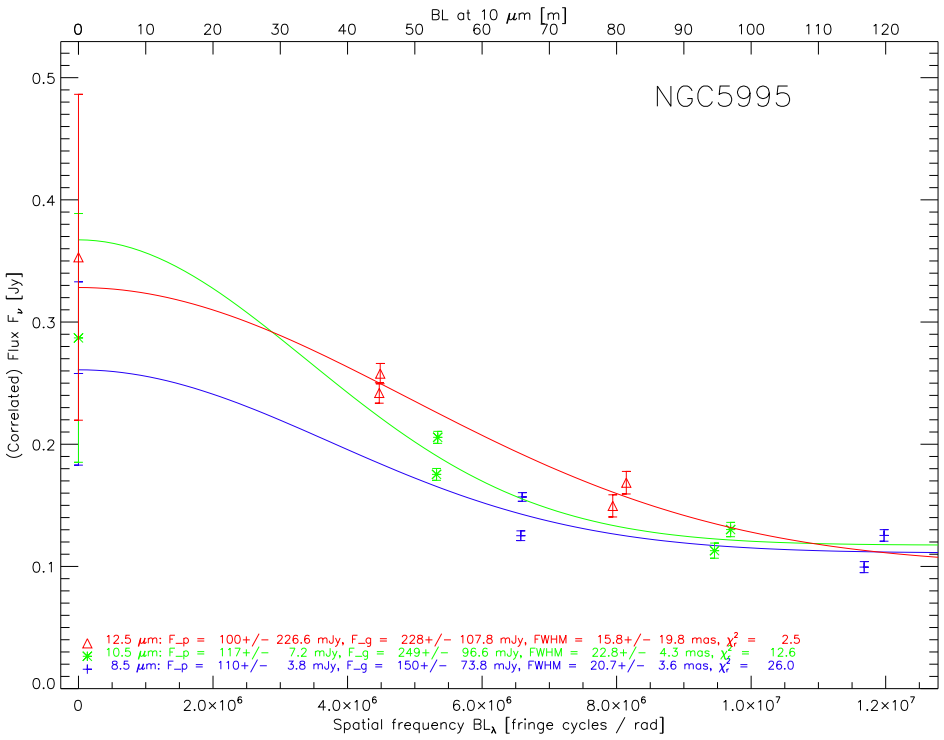

Figure 4.20.: Same as Fig. 4.7 but for **NGC 5995**

NGC 5995 – an unabsorbed Seyfert 2 NGC 5995 is among the few (4%, Risaliti et al. 1999) Seyfert 2 galaxies that have an X-Ray absorbing column $< 10^{22}$ cm^{-2} (a so called "unabsorbed Seyfert 2 galaxy"). Panessa & Bassani (2002) argue that the observed X-Ray absorbing column[12] can only be responsible for an extinction $A_V \approx 0.45$ (assuming the Galactic A_V/N_H value[13]) and that A_V/N_H would need to be a factor 10–50 larger in order to block our line of sight to the broad line region in the optical. The existence of such a broad line region is inferred from the detection of broad Hα emission in the polarized light (Lumsden et al. 2001). Other broad (FWHM $>$ 1000 km/s) permitted lines are not observed in this galaxy (Panessa & Bassani 2002). However, the direct spectrum also shows a broad component to the Hα line, i.e. it is a Seyfert 1.9 galaxy (Lumsden et al. 2001).

[12]The authors note that such a low column density would not necessarily imply obscuration in a torus, but a nuclear starburst or dust lanes on scales $\gg$ 1 pc would probably suffice. This is corroborated by the fact that most of the galaxies in their sample have large-scale bars or other dusty features that could provide the obscuration.

[13]From reddening in the NLR, Panessa & Bassani (2002) determined A_V and from X-Ray observations they found N_H. With these values they find no deviation from the Galactic value for A_V/N_H for their sample of unabsorbed Seyfert 2 galaxies. Besides, evidence for anomalous dust in AGNs points in the other direction than what would be needed to explain the observations of NGC 5995: the A_V/N_H value was found to be *lower* than the galactic value in X-Ray selected AGNs by Maiolino et al. (2001).

In this respect, it is remarkable that we see a clear decrease in correlated flux with increasing baseline length in the MIDI data, implying a resolved emitter of ≈ 3-4 pc in FWHM size. How can this be reconciled with the X-Ray classification as an unabsorbed Seyfert? Is NGC 5995 maybe simply a type 1 object with a weak broad line region, not requiring any obscuration in the optical at all? This would imply similar strengths for the broad polarized Hα and the broad component to the direct line. Unfortunately Lumsden et al. (2001) do not give a decomposition of the detected lines that would allow to test this hypothesis.

In single-dish mid-IR observations, Horst et al. (2009) find a slightly elongated nucleus at PA ≈ 110°. With the current dataset we cannot constrain any possible elongation as our observations so far only cover one position angle in (u, v) space.

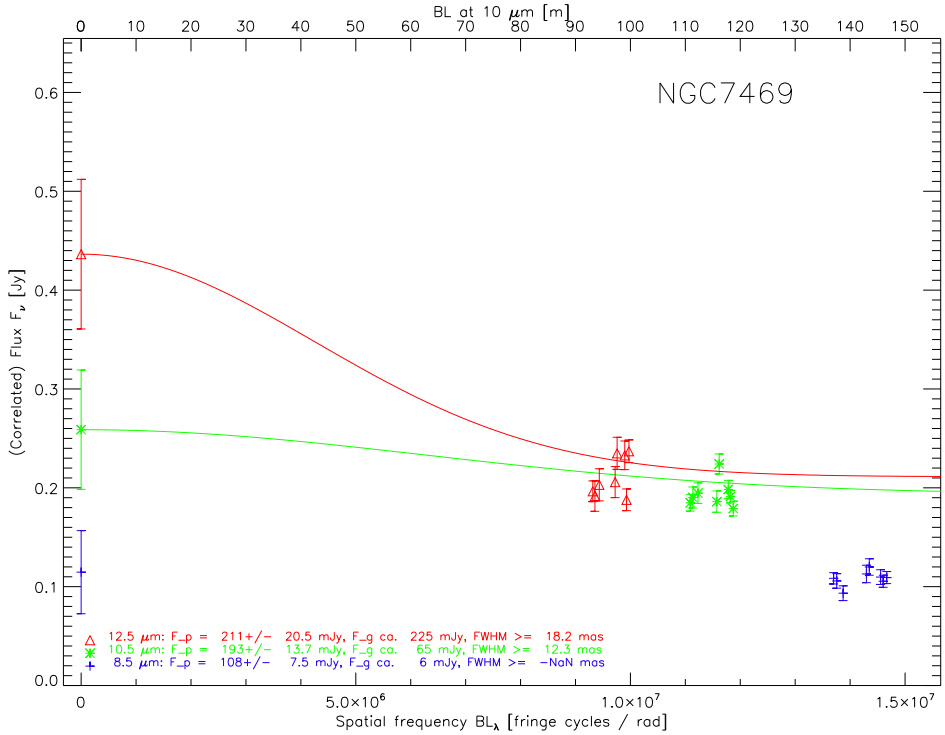

Figure 4.21.: Same as Fig. 4.7 but for **NGC 7469**

NGC 7469 NGC 7469 is an interacting Seyfert 1 galaxy and well known for its face-on starburst ring at a radius of ≈ 1″ (340 pc) from the nucleus (Díaz-Santos et al. 2007).

From its unresolved core in H band, Prieto et al. (2010) derive an upper limit to its FWHM size of 0.08″ (26 pc).

Soifer et al. (2003) observed NGC 7469 with the Keck I telescope and found a marginally resolved, elongated structure from the deconvolved image. They give a size of $< 40 \times 80$ mas ($< 13 \times 26$ pc) with the major axis of the structure at 135°.

In the GTO study the source was found to be well resolved (Tristram et al. 2009). For the LP analysis, the data from the GTO programme were not used, however, since it did not pass the aforementioned quality criteria (they have a very low number of good frames).

NGC 7469 is one of the weakest sources of the Large Programme. For it we only have very few successful observations on the long U1U4 baseline at PA $\approx 45°$, i.e. roughly the PA of the minor axis of the elongated structure found by Soifer et al. (2003). At 12.5 μm , the correlated fluxes are clearly lower than the single-dish flux, showing an extended component of Gaussian FWHM $\gtrsim$ 18 mas (5.4 pc). This limit is compatible with the upper limit in this direction of $<$ 13 pc, given by Soifer et al. (2003), constraining the size of the mid-IR emitter in that direction to 5.4 pc $\lesssim$ FWHM $\lesssim$ 13 pc. At 10.5 μm and 8.5 μm the source is compatible with being unresolved.

Mrk 463 E Mrk 463E is a well-known interacting galaxy (for an image of its double nucleus see Mazzarella & Boroson 1993).

It was the only target selected for the Large Programme for which no observation was successful.[14]

[14]S. Hönig noted about the run in the excellent night of 26 March 2010 that the fringe search failed already on the short U1U2 baseline, even after solving an initial confusing which of the two nuclei was the eastern one. No further observing attempts were made.

Table 4.2.: Fit results for the radial models, see text for explanations.

source	type	λ	F_ν^p	F_ν^g	Θ_g	χ_r^2
		μm	mJy	mJy	mas (pc)	$\chi^2/\#DOF$
IZwicky1	Sy 1	8.5	170± 1.9	132± 19.4	30.6± 1.8 (32.9± 1.9)	146/16= 9.2
IZwicky1	Sy 1	10.5	268± 2.5	245± 26.0	33.9± 1.5 (36.5± 1.6)	177/16= 11.1
IZwicky1	Sy 1	12.5	286± 3.9	288± 32.6	39.2± 2.0 (42.2± 2.1)	81/16= 5.1
NGC1365	Sy 1	8.5	169± 1.9	97± 17.9	25.2± 1.8 (2.2± 0.2)	320/23= 13.9
NGC1365	Sy 1	10.5	227± 2.7	191± 24.2	28.7± 1.4 (2.5± 0.1)	483/23= 21.0
NGC1365	Sy 1	12.5	264± 4.4	181± 27.4	31.0± 2.2 (2.7± 0.2)	262/23= 11.4
LEDA17155	Sy 2	8.5	144± 5.3	68± 26.5	20.1± 4.5 (16.3± 3.6)	78/ 6= 13.1
LEDA17155	Sy 2	10.5	114± 7.5	123± 30.8	22.2± 4.0 (18.0± 3.3)	16/ 6= 2.8
LEDA17155	Sy 2	12.5	236± 9.2	182± 49.5	29.4± 4.5 (23.8± 3.6)	21/ 6= 3.5
MCG-5-23-16	Sy 2	8.5	105± 2.1	199± 20.9	21.3± 0.9 (4.0± 0.2)	456/20= 22.8
MCG-5-23-16	Sy 2	10.5	99± 12.0	211± 8.4	15.9± 1.4 (3.0± 0.3)	475/20= 23.8
MCG-5-23-16	Sy 2	12.5	148± 13.7	472± 19.3	21.1± 1.2 (4.0± 0.2)	494/20= 24.7
Mrk1239	Sy 1	8.5	326± 36.1	≈ 0	—	2.2
Mrk1239	Sy 1	10.5	445± 29.8	≈ 0	—	1.3
Mrk1239	Sy 1	12.5	450± 28.8	≈ 0	—	0.7
NGC3281	Sy 2	8.5	146± 9.4	≈ 166	$\gtrsim 28.4$ ($\gtrsim 6.6$)	
NGC3281	Sy 2	10.5	123± 19.2	≈ 91	$\gtrsim 25.9$ ($\gtrsim 6.0$)	
NGC3281	Sy 2	12.5	284± 28.3	≈ 347	$\gtrsim 39.0$ ($\gtrsim 9.0$)	
3C273	Quasar	8.5	196± 10.6	≈ 62	$\gtrsim 37.4$ ($\gtrsim 98.9$)	
3C273	Quasar	10.5	211± 16.3	≈ 62	$\gtrsim 40.1$ ($\gtrsim$106.0)	
3C273	Quasar	12.5	268± 25.6	≈ 57	$\gtrsim 37.0$ ($\gtrsim 98.1$)	
NGC4507	Sy 2	8.5	58± 37.3	90± 20.4	12.2± 6.1 (3.0± 1.5)	224/ 5= 44.9
NGC4507	Sy 2	10.5	84± 55.7	167± 33.4	14.5± 5.5 (3.6± 1.4)	288/ 5= 57.8
NGC4507	Sy 2	12.5	111± 52.5	280± 26.3	19.9± 5.6 (5.0± 1.4)	30/ 5= 6.1
NGC4593	Sy 1	8.5	83± 62.2	32± 37.8	8.7± 20.9 (1.9± 4.5)	5/ 4= 1.5
NGC4593	Sy 1	10.5	130± 6.1	76± 43.1	18.9± 6.6 (4.0± 1.4)	33/ 4= 8.3
NGC4593	Sy 1	12.5	141± 8.8	103± 65.9	26.7± 7.3 (5.7± 1.6)	5/ 4= 1.4
IC4329A	Sy 1	8.5	413± 44.2	≈ 170	$\gtrsim 23.3$ ($\gtrsim 7.7$)	
IC4329A	Sy 1	10.5	561± 53.8	≈ 253	$\gtrsim 30.9$ ($\gtrsim 10.2$)	
IC4329A	Sy 1	12.5	624± 55.2	≈ 373	$\gtrsim 40.9$ ($\gtrsim 13.5$)	
NGC5506	Sy 2	8.5	398± 2.3	300± 43.5	19.8± 1.1 (2.8± 0.2)	627/ 6= 104.6
NGC5506	Sy 2	10.5	329± 2.5	300± 63.9	28.8± 1.8 (4.0± 0.3)	361/ 6= 60.2
NGC5506	Sy 2	12.5	561± 4.7	599± 65.9	27.0± 1.3 (3.8± 0.2)	319/ 6= 53.2
NGC5995	Sy 2	8.5	110± 3.8	150± 73.8	20.7± 3.6 (10.2± 1.8)	52/ 2= 26.0
NGC5995	Sy 2	10.5	117± 7.2	249± 96.6	22.8± 4.3 (11.3± 2.1)	25/ 2= 12.6
NGC5995	Sy 2	12.5	100± 226.6	228± 107.8	15.8± 19.8 (7.8± 9.8)	5/ 2= 2.5
NGC7469	Sy 1	8.5	108± 7.5	≈ 6	—	
NGC7469	Sy 1	10.5	193± 13.7	≈ 65	$\gtrsim 12.3$ ($\gtrsim 3.6$)	
NGC7469	Sy 1	12.5	211± 20.5	≈ 225	$\gtrsim 18.2$ ($\gtrsim 5.4$)	

Table 4.3.: Fit results for the three other targets, compare to Table 4.2 and see text for explanations.

source	type	λ μm	F_ν^p mJy	F_ν^g mJy	Θ_g mas (pc)
Circinus	Sy 2	10.5	570 ± 60	3070 ± 310	100 ± 10 (1.9 ± 0.2)
NGC1068	Sy 2	10.5	1700 ± 170	9500 ± 950	50 ± 10 (3.5± 0.4)
NGC4151	Sy 1	8.5	119± 16	410± 100	29± 5 (2.0± 0.3)
NGC4151	Sy 1	10.5	194± 61	700± 160	23± 4 (1.5± 0.3)
NGC4151	Sy 1	12.5	290± 70	1030± 300	32± 6 (2.1± 0.4)

4.4.1.2. Other targets

For the three other targets listed in Table 4.1, the results given in the literature were re-interpreted to be used in the context of the radial models.

The Circinus galaxy The Circinus galaxy has been studied in great detail, not only in the mid-infrared (see Tristram et al. 2007, and references therein). In the mid-IR, it is the second brightest southern galaxy and it was the second galaxy to be observed with MIDI. Its mid-IR emission is best fitted by a two component model consisting of a highly elongated disk and a large, round, component, according to Tristram et al. (2007). The elongated disk's major axis FWHM is 21 mas (0.4 pc) and the minor axis is unresolved. The large component was overresolved and contributes only marginally even at most of the shortest baselines. Its FWHM size is given as 100 mas (2 pc).

In their fit to the correlated and single-dish spectra, Tristram et al. (2007) determined *one* best-fit size of the emission (for each component) and did not fit a wavelength-dependent size like in our models. Since, in our models, the size of the emitter is almost always seen to be larger at 12.5 μm than at 8.5 μm , we interpret the fitted sizes of Tristram et al. (2007) as the average size that most likely corresponds to the size that we would give at 10.5 μm . To compare their results to the results from the 1-dimensional point source + Gauss models, we further identified their disk-like component with the point source of our models and the larger component as the circularly symmetric Gaussian component.

The motivation for this is twofold: (1) We do not detect any deviations from circular symmetry in most of the LP sources. Any disk-like component (should it exist) must be unresolved. (2) If a disk component exists and does not scale with AGN luminosity, it would be unresolved in all of the LP targets due to their large distances.

The 10.5 μm fluxes (+ errors) of the disk component and the overresolved Gauss component are taken from their Figure C.1 and are given in Table 4.3 together with the other relevant fit parameters. The error of the size of the large component is not given by Tristram et al. (2007) and therefore estimated to be $\approx$ 10 %.

NGC 1068 NGC 1068 is the mid-IR brightest extragalactic target in the southern sky and was the first galaxy to be studied with MIDI (Jaffe et al. 2004). As for the Circinius

galaxy Raban et al. (2009) also fitted a two component structure consisting of a hot disk-like component of ca. 20 × 6.5 mas (1.35 × 0.45 pc) ("Component 1") and a larger, less constrained, second component. This "component 2" is ca. 50 mas (3 × 4 pc) in Gaussian FWHM. The fluxes F_ν^p and F_ν^g are given in their Figure 2 and the errors of both the fluxes and the size of component 2 are estimated to be ≈ 10 %.

As in Circinus, their best model also gives one size for all wavelengths[15] and we interpret it as the 10.5 μm size. Also, their disk component will again be identified with the point source of our models. The resulting parameters are given in Table 4.3.

NGC 4151 The model applied for the mid-IR emission of NGC 4151 in Section 3 is very similar to the model *a* discussed here: In both cases the model consists of a point source and a resolved Gaussian source. However, since we have only 2 correlated flux observations, the model has no free parameters and is therefore an exact solution (and not a fit). The flux errors for NGC 4151 are considerably larger (≈ 20%) than for other sources of this magnitude because this source had to be observed at very high airmass where an accurate calibration is very challenging. See Chapter 3 for further discussion.

...and Centaurus A? We do not include Centaurus A in the analysis here since this source is of a very different kind: Its mid-IR emission is very weak and at least half of it is non-thermal. The resolved emission in this source is probably a very different entity than the resolved mid-IR emission in Seyfert galaxies. See Chapter 2 for further discussion.

[15] Raban et al. (2009) also fit a model with wavelength-dependent size of the emitter. For consistency with the Circinus model, the wavelength-independent model is used for the discussion here.

4.5. Discussion

4.5.1. Torus scaling relations

One of the goals of the Large Programme is to look for statistical evidence of unification on the parsec scale. There, the obscuring dust is a central ingredient in unified models. Strict unification models that require it to be identical in all AGNs, were already excluded by the variety of dust seen in the first MIDI observations (see Section **??**). Statistical unification models are less strict but still require the dust to appear differently in type 1 and type 2 galaxies. If such unified models contain any predictive power, the difference in appearance (e.g. the mid-IR size) of type 1 and type 2 tori must be dominated by class membership and not by individual properties of a galaxy.

Reverberation mapping studies (Suganuma et al. 2006; Landt et al. 2011) as well as near-IR interferometric observations (Kishimoto et al. 2007) suggest a relationship between the size of the innermost radius of hot dust and the illuminating luminosity, as predicted by theoretical models (Barvainis 1987).

It is expected that the radius of mid-IR emission also increases with illuminating radiation and that the study of the mid-IR size–luminosity relation will help to constrain torus models (Tristram & Schartmann 2011). Since the illuminating radiation, i.e. the UV / X-Ray flux, cannot be observed directly in type 2 objects, a relation between the mid-IR and the (absorption corrected) hard X-Ray luminosities of AGNs comes in handy (Krabbe et al. 2001; Horst et al. 2008) to relate observed to intrinsic properties. It implies that the mid-IR luminosity is a good tracer for the irradiating luminosity of the AGN.

Tristram et al. (2009) have shown a first size–luminosity relation for AGN tori (see their Figure 8) from the MIDI GTO sample of AGNs and confirmed the expected relation of $\Theta \propto \sqrt{\nu F_\nu}$. As expected from the diversity of dust distributions, the scatter in the relation is considerable. The GTO data are however incomplete in many respects: many data points are only limits, since the GTO observations did not provide the signal/noise and the (u, v) coverage to fit geometrical models to the visibilities. Only upper or lower limits were given when no correlated flux was observed or when no deviation from $V = 1$ was seen, respectively.

With the improved data set from the Large Programme we can now constrain a possible size–luminosity relation much better. Before turning to the results, however, let us briefly discuss which loci of such a size–luminosity diagram are actually observable with MIDI.

4.5.1.1. Observational constraints

Two obvious constraints limit the range of observability: (1) The total luminosity emitted by a blackbody (of constant temperature and emissivity) is proportional to its surface area (i.e. there are no small but luminous tori), (2) structures $\gg 1/BL_\lambda$ are over-resolved in an interferometer, leading to very low correlated fluxes. If there is no additional small component ("point source"), fringes cannot be tracked on such objects and they are not observable.

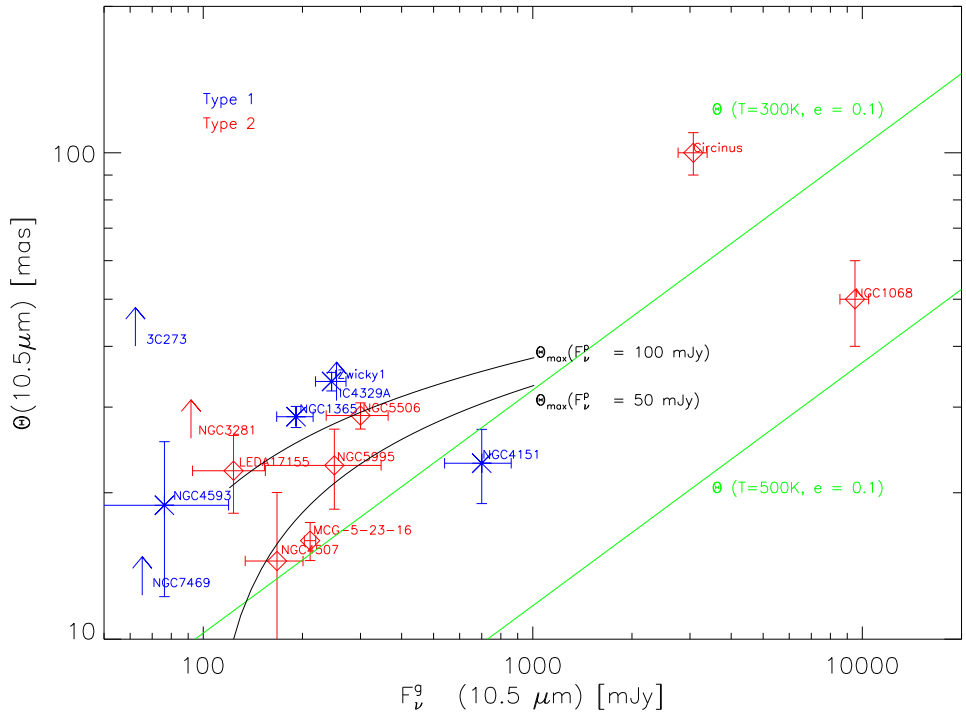

Figure 4.22.: Observability constraints for torus sizes with MIDI: Best-fit FWHM apparent size (Θ) as a function of resolved component flux (F_ν^g). Type 1 objects are plotted as blue stars, type 2 objects are plotted as red diamonds. Arrows are plotted where only a lower limit to the FWHM size can be given. Overplotted are the expected loci of blackbodies of constant temperature and emissivity (green lines) and sensitivity limits. Objects with a given point source flux F_ν^p can only be observed up to a maximum size $\Theta_{\rm max}$ indicated by the black lines. NGC 1068 and the Circinus galaxies show "point sources" of $> F_\nu^{\rm min} \approx 150$ mJy, so that the $\Theta_{\rm max}$ criterion is not applicable to them.

In Figure 4.22 we plot, logarithmically, the best-fit FWHM size Θ as a function of the best-fit flux of the structure of this size, F_ν^g. Overplotted are the observability constraints that are discussed below. In this plot only *observed* quantities are plotted to clearly separate the observational limitations from any astrophysical effects.

(1) The loci of constant temperature blackbodies A blackbody emitter with constant temperature $T \approx 300$ K, emissivity (covering factor) $\epsilon \approx 0.1$ and full-width half maximum size Θ produces a (total) flux F of

$$F \approx \nu F_\nu = \epsilon \sigma_{\mathrm{SB}} \Theta^2 T^4 / 4 \tag{4.8}$$

with the Stefan-Boltzmann constant $\sigma_{\mathrm{SB}} = 5.67 \cdot 10^{-8} \mathrm{Js}^{-1}\mathrm{m}^{-2}\mathrm{K}^{-4}$. The assumption $F \approx \nu F_\nu$ implies that the torus emits most of its flux at the observed wavelength. Rearranging the formula, a blackbody with an observed flux (density) F_ν has a Gaussian FWHM Θ of

$$\Theta = \sqrt{\frac{4\nu F_\nu}{\epsilon \sigma_{\mathrm{SB}} T^4}} \tag{4.9}$$

These are the straight green lines in Figure 4.22. It connects tori of constant temperature and emissivity.

(2) The flux limit For a given sensitivity limit $F_\nu^{\mathrm{min}} \approx 150$ mJy (at 10.5 μm), observable targets must obey the relation

$$F_\nu^p + F_\nu^g \cdot \exp\left(-\frac{(\pi \Theta B L_\lambda)^2}{4 \ln 2}\right) \gtrsim F_\nu^{\mathrm{min}} \tag{4.10}$$

This translates into a maximum size of the resolved emitter

$$\Theta_{\mathrm{max}} = \frac{2\sqrt{\ln 2 \ln(F_\nu^g / (F_\nu^{\mathrm{min}} - F_\nu^p))}}{\pi B L_{\lambda,\mathrm{min}}} \tag{4.11}$$

with the minimum spatial resolution of the observations $BL_{\lambda,\mathrm{min}} \approx 50\mathrm{m} \,/\, 10.5\ \mu\mathrm{m} \approx 5 \cdot 10^6$. For $F_\nu^p \geq F_\nu^{\mathrm{min}}$, Θ_{max} does not exist, i.e. tori of any size are observable. Whether any change of correlated flux with baseline length can be observed depends on the signal/noise of the respective observations.

At a given F_ν^g, the maximum size an object may have to still be observable is given by the point source flux: Objects with little point source contributions must have smaller sizes (leading to larger correlated fluxes) to be observable. These maximum sizes are plotted in Figure 4.22 for point source fluxes of 50 mJy and 100 mJy.

From this Figure it can be seen that all of the resolved objects (except NGC 1068) are larger than expected for a 300K blackbody with emissivity of 10%, i.e. the observed structures trace emitters with lower surface brightnesses than such a blackbody.

There appears to be an indication that type 1 objects trace larger structures than type 2 objects – contrary to the expectation (Tristram & Schartmann 2011). However, one must be careful when interpreting this bias: Since type 1 sources typically have larger point source fluxes than type 2 sources (see also Figure 4.24 below), observational constraints limit our ability to detect large tori in type 2 sources. Type 2 sources with very large tori are simply not observable.

The size–luminosity relation In Figure 4.23, the resolved emitter's size at 10.5 μm is plotted as a function of luminosity $L = \nu L_\nu$, estimated at 12.5 μm. The reason for choosing two different wavelengths here is that we only know the sizes for *all* sources at 10.5 μm (see subsection 4.4.1.2), but the flux is better estimated well outside any possible Silicate feature, e.g. at 12.5 μm.

Overplotted is the relation $s \propto L^{0.5}$. The offset has been set to 0 and the slope has not been fitted. It fits the data points remarkably well. What does the relation tell us? Does it imply that tori scale with luminosity?

First of all a size–luminosity relation of $s \propto L^{0.5}$ is the trivial outcome for blackbody emission (see Equation 4.9). The fact that the data points show relatively little scatter around that relation indeed implies that the observed tori all have similar surface brightnesses (i.e. the product of covering factor $\times\ T^4$).

As a future step, the observability constraints must be studied and discussed for such a diagram to better separate observability constraints from astrophysics.

4.5.1.2. Does distance matter?

In order to learn more about 'tori' (e.g. by studying their substructure, the 'clumpiness'), it is important to understand how the characteristic scale of their constituents ρ scales with source luminosity and distance r from the nucleus. While most toy models find or assume that $\rho \propto r^\beta$ with $\beta \approx 1$ (e.g. Hönig et al. 2006; Schartmann et al. 2008), this is not found in the hydrodynamical torus model of Schartmann et al. (2009) where the thickness of the filaments, which the torus is made of, is independent of distance. In this case, a fixed characteristic scale of the torus substructure, the notion that the torus geometry simply depends on the observed flux, is no longer correct and a certain spatial resolution would be needed in physical scales (pc). In this case, we need to observe the closest AGNs.

Does Figure 4.23 already imply that tori scale with luminosity?

Let us assume that tori are indeed made up of a relatively small disk component (as seen in NGC 1068 and Circinus) of size $\approx 0.1pc/\sqrt{L/L_{\rm Circinus}}$ and a larger "torus" component of $\approx 1pc/\sqrt{L/L_{\rm Circinus}}$. In that case – both components scale with luminosity – the "point source fraction" should be constant with distance, using the same arguments as before.

Now let us look at a plot of point source fraction f_ν^p as a function of resolved scale (Figure 4.24). Two observations strike the eye:

1. As expected, type 1 galaxies have on average higher point source fractions than type 2s. This should be a relatively robust result since the observational bias explained above is inverse: it biases against type 2 galaxies with very low point source fractions.

2. Contrary to the assumption made above, it is also evident that the point source fraction is a function of distance: The larger the scale, the more point source contribution we see, indicating that the sources *do not scale* strictly with luminosity (and would therefore be distance independent).

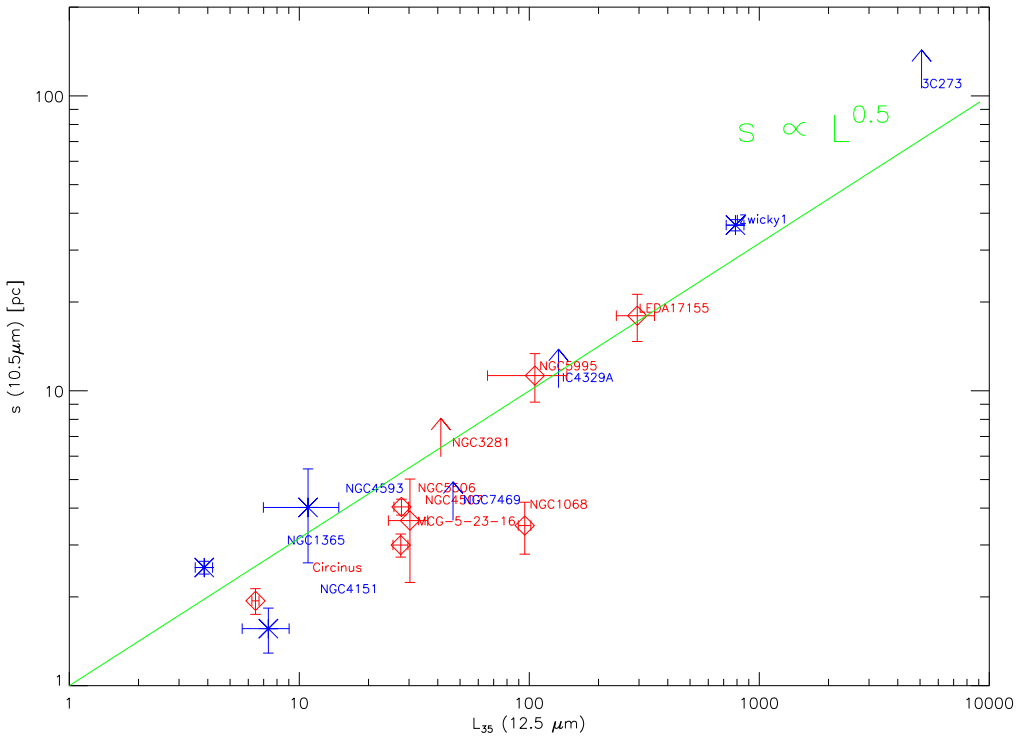

Figure 4.23.: Size–luminosity relation for the LP sample. The size s is given by $D_A \cdot \Theta_g$ where D_A is the angular-size distance, the luminosity is estimated from $L = 4\pi D_L^2 c/\lambda F_\nu$ at 12.5 μm, where D_L is the luminosity distance, $L_{35} = L/(10^{35}\mathrm{W})$. The green line is $s = L^{0.5}$, i.e. the expected relation $s \propto L^{0.5}$ with zero offset.

The observation that the point source fraction increases with luminosity (point 2), can be understood in the context of the so called "receding torus paradigm" (Lawrence 1991). It predicts that the inner radius of the torus r_{in} increases with the AGN's luminosity L_{uv} as $r_{in} = 1.3 L_{uv,46}^{1/2} T_{1500}^{-2.8}$ pc (Barvainis 1987) – this follows from the fact that r_{in} is given by the sublimation temperature of the dust. Larger r_{in}s lead to smaller torus half-opening angles and so, in the unified picture, the fraction of type 1 AGNs increases with luminosity. This is roughly compatible with source counts (Lawrence 1991). However, the exact form of the luminosity dependence of the type 1 fraction is inconsistent with the most simple receding torus paradigm in which the torus height h remains constant with luminosity (Simpson 2005).

In Figure 4.24, the scale axis is more or less identical with luminosity (for the LP targets) since they all have approximately the same observed flux.

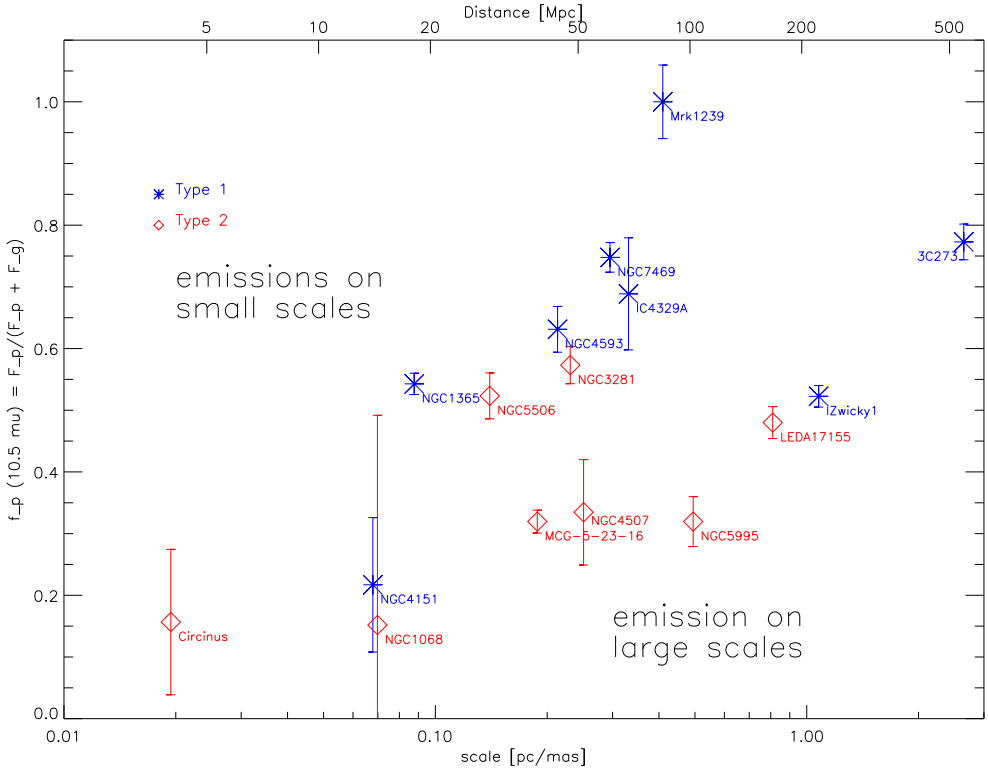

Figure 4.24.: Point source fraction as a function of resolved scale (distance). Type 1 objects have a larger point source fraction than type 2 objects. The more distant the source, the larger the point source fraction.

In the receding torus paradigm, the extinction at 10 μm to the inner parts of the torus would decrease (in the statistical average), i.e. the unresolved part gets brighter, offering a possible explanation for the increase in point source fraction.

4.5.2. The sub-structure of tori

4.5.2.1. Observational signs of torus substructure

A possible way to detect torus substructure was devised by K. Tristram: In a source where the baseline length does not change with position angle one can study the source at the same spatial resolution for various position angles. Such a source has to be at $\delta \approx -65°$ (if observed at the VLTI), like the Circinus galaxy). One can then compare these observations to fluxes from radiative transfer models to constrain torus parameters such as the characteristic size of the clumps. First results from such observations were

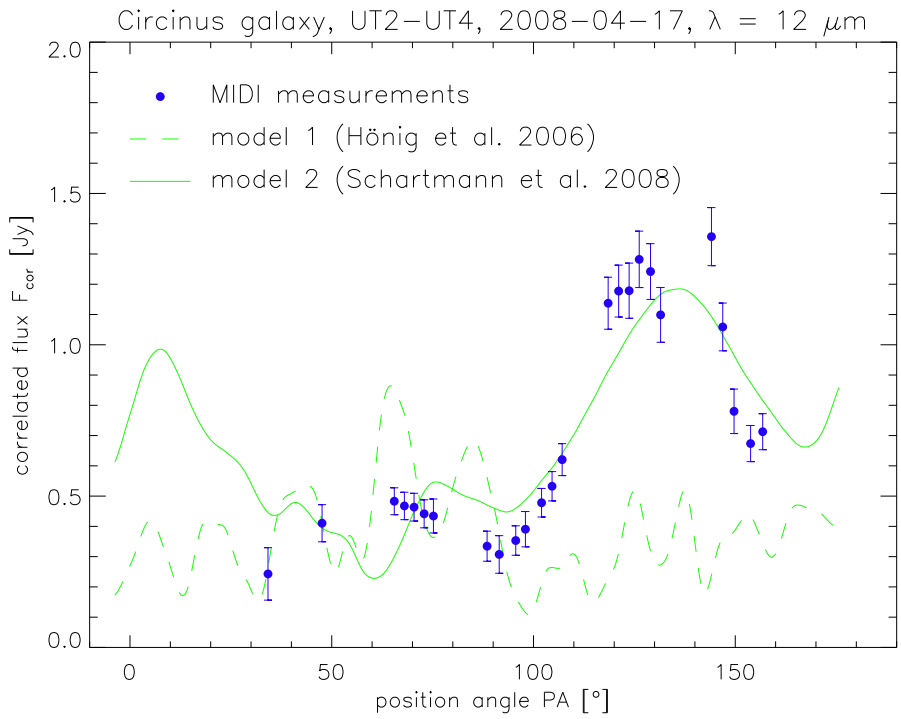

Figure 4.25.: Clumpiness in Circinus. The correlated flux increased about three-fold with a change of position angle of just about 30 °. This cannot be explained by a simple elongation (inclination) of a disk since the latter would only produce variations with a period of 180°.
The two radiative transfer model curves differ mainly by the size of the clumps where the clumps in the model by (Schartmann et al. 2008) were much larger than the clumps in the model employed by Hönig et al. (2006). Figure courtesy K. Tristram, to be published

promising, see Figure 4.25.

4.5.2.2. "Continous fringe tracks" in the Large Programme

Most of the radial fits are bad in the sense that $\chi^2_r \gg 1$. Have we under-estimated the errors? Probably not! Since we found no evidence for large systematic errors in the correlated fluxes[16], we argued that the statistical errors are an adequate description of the measurement uncertainties.

In other words, the models are too simple and the remaining scatter tells us that there is more structure in the sources that we have ignored by the Gaussian "envelope" function.

Supporting evidence comes from the desired signs for clumpiness. To detect clumpy tori, some sources have been sampled very densely on baselines where the projected baseline is not a strong function of position angle (e.g. NGC 1365, MCG-5-23-16). These two

[16]The single-dish flux mostly does not contribute very much to χ^2_r due to its relatively large error.

sources already showed evidence of non-centrosymmetric structures from Figures 4.9 and 4.11 respectively. Let us now look at plots of correlated flux as a function of *position angle*, at a certain (narrow) range of projected baseline.

MCG-5-23-16 MCG-5-23-16 has a well sampled (u, v) plane (Figure 4.6) and is the best case for small-scale structure (clumpiness) in the Large Programme (Figure 4.26). Here, the correlated flux seems to be a function of position angle, decreasing from ≈ 250 mJy $\pm$ 15 to $\approx 160 \pm 15$ mJy, or by a factor of 0.6 over only $\approx 10^\circ$ in projected baseline angle.

Not only because of the significance of the variation, but also because the observations show a continuous decrease of correlated flux, *even though* the points marked as '6' and '8' have been taken in different nights than the others – corroborating the argument that systematic errors do not dominate over statistical ones.

NGC 1365 NGC 1365 also has a region of densely sampled (u, v) space at around 50 $<$ BL $<$ 80m and $100^\circ <$ PA $< 120^\circ$ (Figure 4.6). If plotted against position angle, a decrease in flux can be observed, starting from the point labeled '4' to '9' and further to '10' and '11' Figure 4.27. However, point '6' in between does not fit to this trend.

According to our selection criteria, there is no reason to believe that point '6' should be excluded. This point is at a slightly larger baseline (about 1 telescope diameter larger than neighboring points 5 and 7). This can, however, not be the reason for it being a significant outlier (see Figure 4.9).

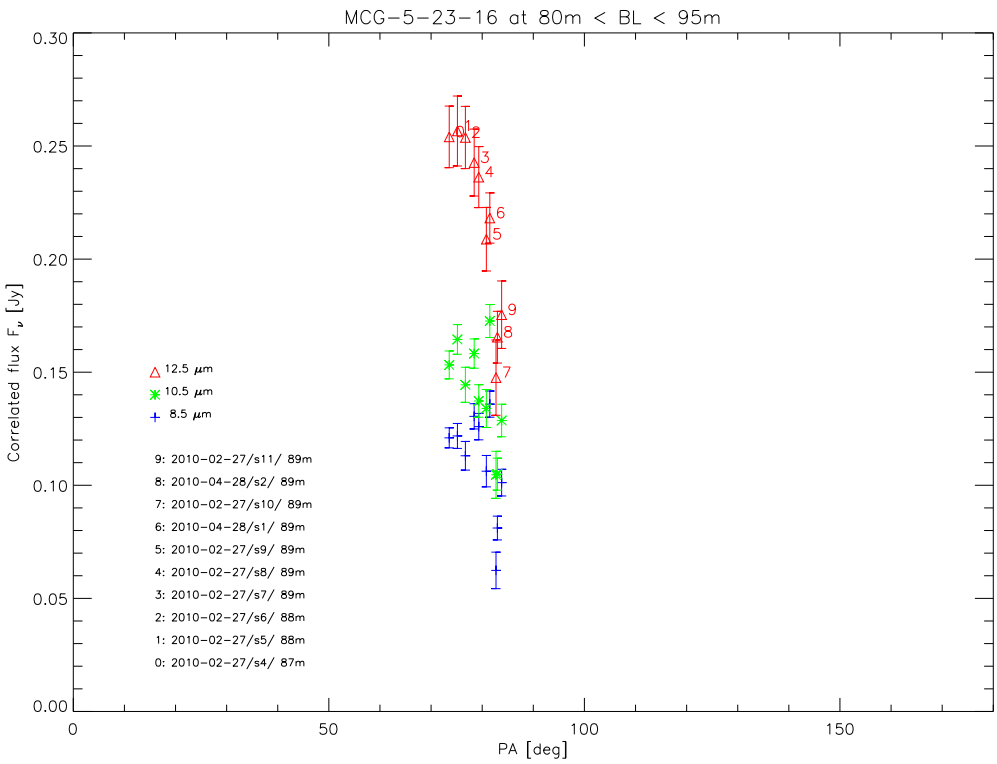

Figure 4.26.: Evidence for clumpiness in MCG-5-23-16?

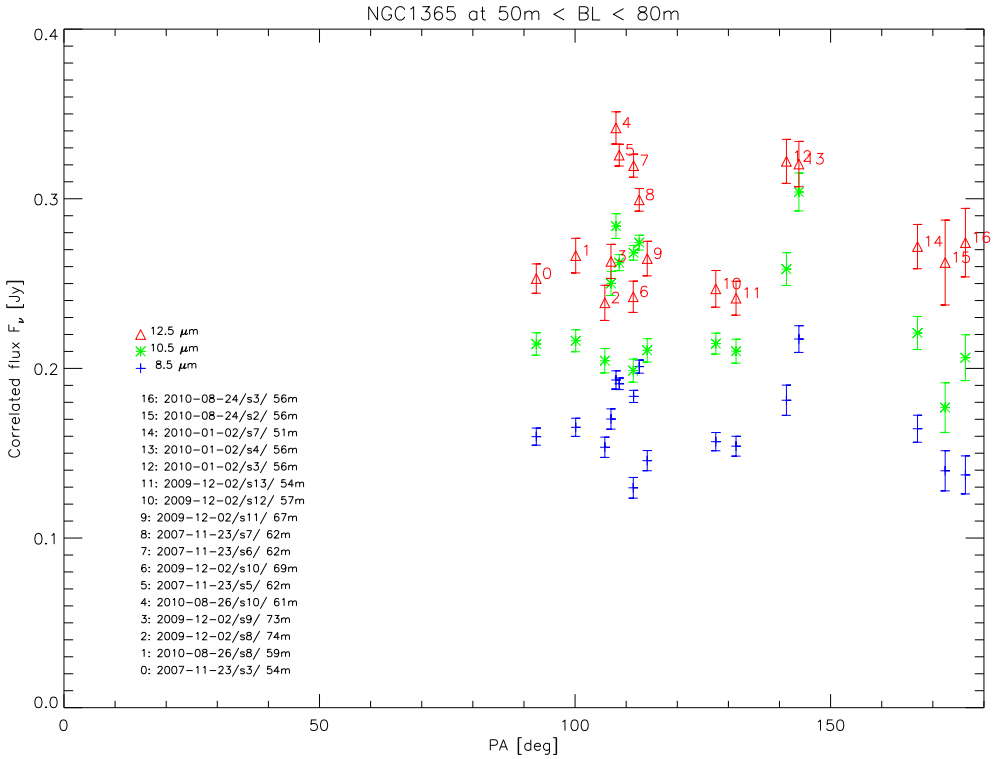

Figure 4.27.: Clumpiness??? An outlier (6) raises questions.

4.5.2.3. Torus size as a function of wavelength

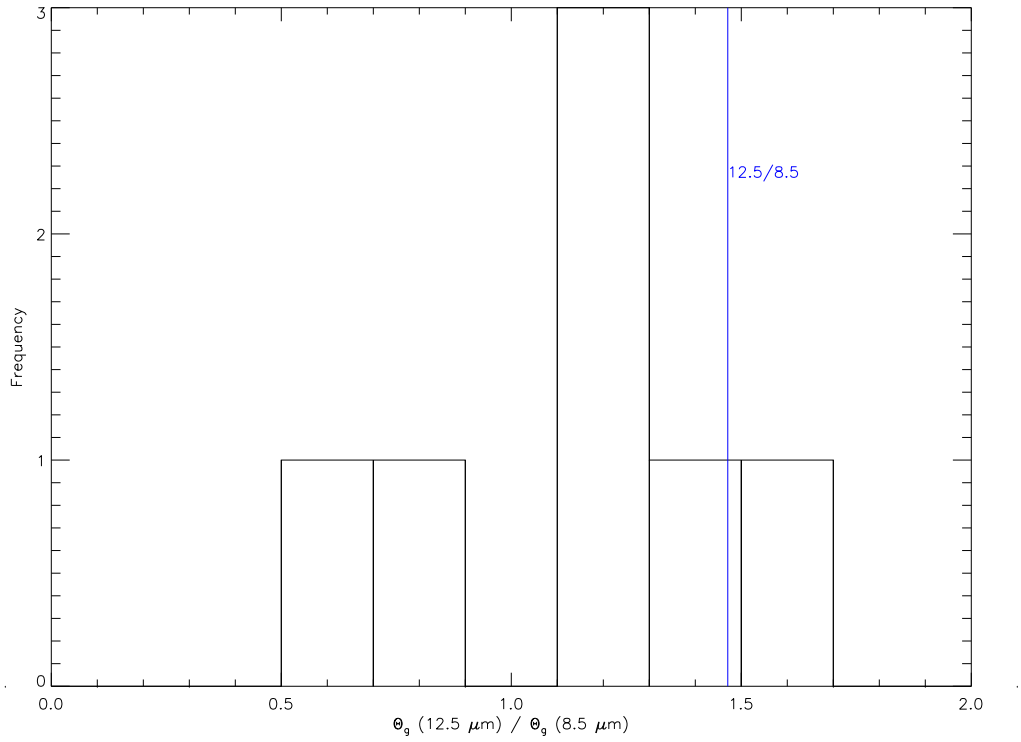

Figure 4.28.: Size-ratio histogram, 12.5/8.5 is expected

The histogram of torus size relations (Figure 4.28) shows that the size increase is roughly compatible with dust being heated from inside. Assuming greybody models where $T \propto r^{-\alpha}$ with $\alpha \approx 1/2.8$ (Barvainis 1987), the source size increases roughly proportional to λ since colder parts of the structure (that have their emission peak at longer wavelengths) are larger.

4.6. Conclusions

- The VLTI/MIDI AGN Large Programme is largest survey of resolved AGN nuclear dust so far.
- A huge amount of data has been selected and reduced and new, more robust, ways to determine errors in MIDI observations has been devised.

- The LP has been successful: most targets could be observed and showed signs for being resolved (albeit some only marginally). It is remarkable that correlated fluxes can now routinely be observed at the < 200 mJy level with MIDI!
- However, the range in visibilities is small and no elongation seen in the observed sources.
- For the first fits we therefore applied only 1D models to constrain the size and flux of the emitter and the flux of the unresolved source
- Statistical studies from MIDI data suffer biases due to the many observability constraints. They must be carefully studied and understood before claiming statistical relations. Near the flux limit of MIDI, large type 2 sources are harder to detect than large type 1 sources since the latter almost always have larger point source contributions, making it easier to track fringes on them.
- Blackbody emission size–luminosity relation is the natural outcome of
- Size–luminosity seems to be confirmed
- Overall structure (envelope) proportional to source luminosity (observational constraints apply!), substructure might not be! Possible explanation: Receding torus makes inner part better visible in high power sources, therefore f_p larger
- Indications for substructure in some sources (with a tendency of being the nearer ones?) *Check!!!*
- Get back to 5 questions in intro: 1 (size–luminosity): can be constrained with this dataset, (2): will need to wait for comparison with other programmes, (3, silicate feature): requires radiative transport, (4, two component structure): might well be the case, possible evidence for different scaling behavior or receding torus, 5: still no hot dust seen (but is it really expected? need rad. transfer)

4.7. Outlook

- A completion study is underway (087.B-0266, PI: K. Meisenheimer) to fill gaps in (u, v) planes caused by weather loss during the LP.
- VISIR data has been taken (P086.B-0919, PI: K. Tristram) of those sources where no good high-resolution single-spectra exist. This will lead to reduced uncertainties in the '0-baseline' points and help to constrain the models
- Many other programmes have been started that are connected to the Large Programme, e.g. a SINFONI programme (PI: M. Schartmann) with the objective to test the link between star formation and AGN tori that is being explored successfully in hydrodynamical models.

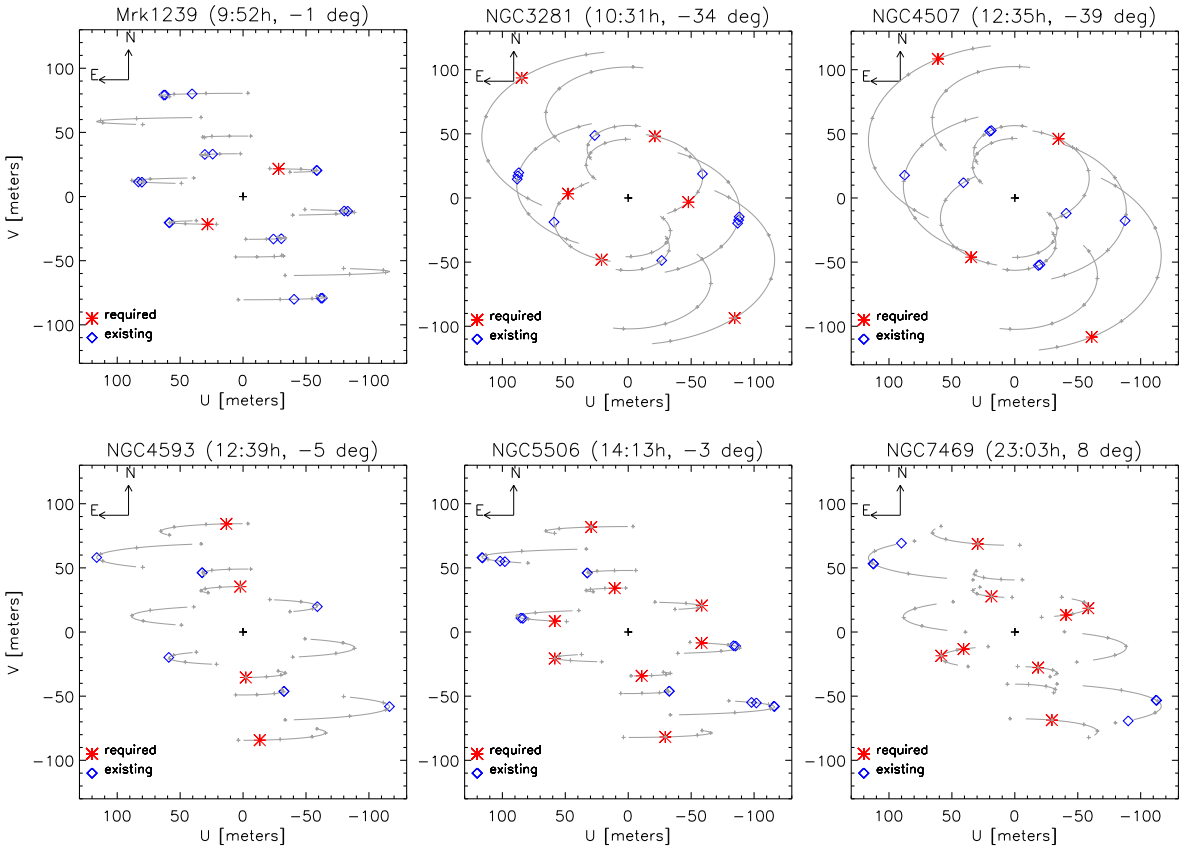

Figure 4.29.: The LP conclusion study (087.B-0266) is already scheduled and will help to fill the gaps in the (u, v) coverage that could not be observed during the LP due to bad weather.

- The selection criteria for the LP were obviously still very conservative: Since 12 of our 13 targets could be observed, we have probably not yet reached the limit of MIDI's sensitivity with this sample and even weaker sources seem to be observable.
- In the near future, we need more short baselines (and more sensitivity to do that with the ATs) to better constrain the relatively large sizes of the resolved emission found in many sources.
- In the more distant future, it would be desirable to observe these targets with even longer baselines to resolve the "point source" and see if it, in type 2 objects, really is a disk with a large axis ratio as seen in the nearby galaxies NGC 1068 and Circinus.

5. Conclusions

Methodical

- VLTI/MIDI / Interferometry at 10 micron has become a very powerful and relatively easy to use tool for bright sources; for weak sources, however, the amount of data processing before having scientifically useful spectra is still very large. Many tests and checks are necessary before an acceptable level of confidence in the results can be reached.

- A trustworthy determination of the errors of correlated and single-dish fluxes is the basis for any scientific modeling. From the re-observation of identical (u, v) points, confidence was gained that the flux of weak sources ($F_\nu \lesssim 500$ mJy) can actually be determined to better than 10 % under good conditions.

- An analysis of atmospheric fluctuations further indicated that, for good nights, the transfer function variations do not prohibit the use of correlated fluxes. For weak sources, the statistical errors of correlated fluxes are much smaller than for the single-dish fluxes. It was seen that the systematic error of calibrating correlated fluxes introduced by the calibration is also not much larger than when calibrating visibilities.

Astrophysical

In a multi-baseline campaign, the (u, v) coverage of the nearest radio galaxy and major merger, Centaurus A, was substantially extended compared to previous observations. The resulting visibility pattern defied any easy explanation, however. After a careful study of the statistical and systematic errors, we were convinced that the pattern was real and that the bad fits to simple smooth models of an elongated Gaussian emitter and an unresolved point-source actually indicated a more complex structure. A better fit was subsequently found if an offset was introduced between the unresolved point source and the extended source. Furthermore, a flux increase by about 50 % was detected in the mid-IR between 2005 and 2008 and an outburst was discovered in X-Ray monitoring data. Together with a time constraint from the X-Ray data, a scenario was constructed that allowed to fix the position of the resolved emitter very near to the front-facing part of the nuclear jet.

In successful, albeit challenging, observations of the brightest type 1 galaxy NGC 4151 a resolved thermal emitter was found. Its properties (size, temperature, emissivity, temperature gradient) were found to be similar to the tori that had been resolved in type 2

objects before, thereby confirming line-of-sight unification schemes. Tentative evidence for silicate emission on the parsec scale was found.

However, In the light of the very different nuclear dust properties of the two well studied type 2 objects, NGC 1068 and the Circinus galaxy, it was clear that the simple most unification models – employing a more or less identical torus in all galaxies – cannot hold. Unification has therefore to be studied statistically in a number of sources. This was the goal of the Large Programme, an observational campaign including 13 AGNs of various types and luminosities. More than twice as much data than during the whole GTO AGN programme was collected within less than a year. In most of the sources a resolved emitter was found and in many its size could be determined to $\approx$ 10 - 20%. It was noted that in the search for correlations in this dataset, a number of observational constraints must be taken into account in order to deduce astrophysical results. The detection of highly resolved (large) structures is favored in type 1 sources over type 2 source.

All in all, I have spent a good part of my doctoral studies with learning and understanding the details of mid-IR interferometry, a wonderfully elegant but challenging observational method. The results from the studies of NGC 4151 were a stepping stone to the much larger Large Programme where the preliminary data reduction has just been finished and first results have been obtained. Centaurus A is the only extragalactic target where an offset between components has been detected with MIDI so far. More data is urgently needed to constrain the models.

A. List of Abbreviations

CCW	Counter clockwise
CW	Clockwise
DIMM	DIfferential Motion Monitor (small telescope that measures the seeing on Paranal)
DDT	Director's Discretionary Time – an ESO category for observing programmes that require little observing time but might have great impact. DDT proposals can be submitted at any time.
# DOF	Number of degrees of freedom (in a χ^2 fit)
FWHM	Full width at half maximum
GTO	Guaranteed Time Observations – time rewarded to an institute or consortium for building an instrument
HWHM	Half width at half maximum
IRIS	Infrared Image Sensor
LP	Large Programme – an ESO category for observing programmes requiring more than 100 hours of observing time
MACAO	Multi-Application Curvature Adaptive Optics, the Coudé Adaptive Optics system on the VLT UTs
mas	milli-arcsecond(s), 1/1000 $''$= 4.848 $\cdot 10^{-9}$ rad
MIDI	MID-infrared interferometric Instrument
PSF	Point Spread Function
VLT(I)	Very Large Telescope (Interferometer)

B. Additional Large Programme material

B.1. Large Programme observing log

Legend

id Identifier used for the data reduction process

BL (Projected) baseline length

PA (Projected) baseline position angle

NDIT Number of frames (DIT = Detector Integration Time)

flags
- F (only for corr. fluxes) Number of points flagges as good by oirAutoFlag < 2000 (very often indicative of a problematic observation)
- R Data reduction problems, e.g. telescope was chopping during fringe track (systematic error of corr. flux unknown) or no suitable calibrator found because fringe track was taken in different MIDI mode
- O transmission in ozone feature > 0.85 in raw counts (too shallow, i.e. flux not dominated by science object)
- S Seeing > 1.5 (for corr. fluxes), > 2.0 (for photometries), (VLTI subsystems work unreliably at large seeing)
- Z Airmass > 2.0 (calibration is less reliable at large airmasses)
- M Data manually excluded (e.g. because of clouds or very uneven background)

Table B.1.: Log of all observations of IZwicky1

Dataset		Fringe track				Photometry		Associated calib
Time [UTC]	id	BL [m]	PA [°]	NDIT	flags	NDIT A/B	flags	id, name, time
2009-12-02		U2U4		184.B-0832(L)				
01:50:44	s1	88.0	79.5	8000		8000/ 8000		c2 (HD9138/02:43:22)
02:02:25	s2	87.2	78.7	8000	S	—/ —	—	c2 (HD9138/02:43:22)
02:06:02	s3	86.9	78.5	8000		—/ —	—	c2 (HD9138/02:43:22)
02:10:22	s4	86.5	78.2	8000		16000/16000	O	c2 (HD9138/02:43:22)
2010-01-02		U3U4		184.B-0832(Q)				
01:05:48	s1	43.7	104.1	4000		8000/ 8000	O	c3 (HD9138/01:29:47)
01:16:41	s2	41.6	104.2	4000		—/ —	—	c3 (HD9138/01:29:47)
2010-08-24		U1U2		184.B-0832(A)				
06:31:24	s4	44.0	26.5	8000		8000/ 8000		c4 (HD9138/06:49:02)
08:05:13	s6	50.3	34.3	8000		—/ —	—	c6 (HD9138/08:54:04)
08:28:00	s7	51.7	35.3	8000	OF	—/ —	—	c6 (HD9138/08:54:04)
08:35:12	s8	52.1	35.5	8000	OF	8000/ 8000	M	c6 (HD9138/08:54:04)
09:55:32	s12	55.4	36.0	8000		—/ —	—	c6 (HD9138/08:54:04)
2010-08-25		U2U3		184.B-0832(K)				
05:54:21	s1	34.7	40.9	12000		8000/ 8000		c1 (HD9138/05:30:03)
06:07:54	s2	35.9	42.3	12000		—/ —	—	c1 (HD9138/05:30:03)
09:17:13	s3	46.4	46.1	12000		8000/ 8000		c2 (HD9138/08:58:01)
09:30:53	s4	46.5	45.6	12000		—/ —	—	c2 (HD9138/08:58:01)
2010-08-26		U3U4		184.B-0832(T)				
06:03:56	s2	62.3	110.3	8000		16000/ 8000		c2 (HD9138/06:34:57)
06:22:26	s3	62.5	109.2	8000	R	—/ —	—	— (/)
06:25:55	s4	62.5	109.0	8000	R	—/ —	—	c2 (HD9138/06:34:57)
2010-08-28		U1U4		184.B-0832(G)				
06:30:22	s8	117.7	66.3	8000		16000/ 8000		c2 (HD9138/05:31:16)
06:41:07	s9	119.9	66.1	12000		8000/ 8000		c2 (HD9138/05:31:16)
09:23:27	s18	127.1	58.6	4000		—/ —	—	c5 (HD9138/09:06:16)
09:25:55	s19	126.9	58.4	8000		8000/ 8000		c5 (HD9138/09:06:16)
09:39:12	s20	125.3	57.2	12000		4000/ 4000		c5 (HD9138/09:06:16)

Table B.2.: Log of all observations of NGC1365

Dataset		Fringe track				Photometry		Associated calib
Time [UTC]	id	BL [m]	PA [°]	NDIT	flags	NDIT A/B	flags	id, name, time
2006-09-10		U2U3		077.B-0026(B)				
07:42:55	s2	46.6	31.0	8000	M	8000/ 8000	M	c2 (HD26967/07:00:40)
09:36:20	s3	45.1	45.6	8000	F	—/ —	—	c4 (HD36597/08:44:20)
09:41:27	s4	0.0	-NaN	8000	OFS	—/ —	—	c4 (HD36597/08:44:20)
2007-11-23		U3U4		080.B-0258(A)				
01:53:47	s3	54.2	92.4	8000		8000/ 8000		c2 (HD16815/02:38:26)
03:51:36	s5	62.1	108.6	12000		8000/ 8000		c2 (HD16815/02:38:26)
04:11:21	s6	62.4	111.5	12000		—/ —	—	c2 (HD16815/02:38:26)
04:18:56	s7	62.5	112.6	12000		—/ —	—	c2 (HD16815/02:38:26)
2009-12-02		U2U4		184.B-0832(L)				
03:10:08	s5	89.4	79.0	8000	S	8000/ 8000	S	c3 (HD23319/05:32:22)
03:30:13	s6	89.4	82.0	8000	S	—/ —	—	c3 (HD23319/05:32:22)
03:34:12	s7	89.3	82.6	8000	S	16000/16000		c3 (HD23319/05:32:22)
06:03:04	s8	75.0	105.8	12000		—/ —	—	c3 (HD23319/05:32:22)
06:09:30	s9	73.9	107.0	12000		16000/16000		c3 (HD23319/05:32:22)
06:31:35	s10	70.0	111.4	12000		8000/ 8000	O	c4 (HD23319/07:06:39)
06:44:27	s11	67.6	114.1	12000		8000/ 8000	M	c4 (HD23319/07:06:39)
07:37:13	s12	57.3	127.5	12000		8000/ 8000	O	c4 (HD23319/07:06:39)
07:50:05	s13	54.9	131.5	12000		8000/ 8000		c4 (HD23319/07:06:39)
08:09:56	s14	51.3	138.3	12000	Z	—/ —	—	c5 (HD26967/08:40:46)
08:20:30	s15	49.6	142.2	12000	Z	—/ —	—	c5 (HD26967/08:40:46)
2010-01-01		U1U3		184.B-0832(E)				
03:16:56	s3	94.0	43.9	8000		8000/ 8000	O	c3 (HD23319/02:41:01)
03:30:59	s4	92.6	45.1	4000	S	—/ —	—	c3 (HD23319/02:41:01)
2010-01-02		U3U4		184.B-0832(Q)				
04:21:29	s3	56.6	141.4	4000		8000/ 8000		c4 (HD23319/03:47:35)
04:32:21	s4	56.0	143.8	4000		—/ —	—	c4 (HD23319/03:47:35)
06:02:45	s7	51.8	167.0	4000		8000/ 8000	O	c6 (HD23319/05:38:51)
06:15:48	s8	51.5	170.7	4000	Z	—/ —	—	c6 (HD23319/05:38:51)
2010-08-24		U1U2		184.B-0832(A)				
05:17:31	s1	56.5	167.7	8000	Z	8000/ 8000	Z	c2 (HD23319/05:33:21)
05:50:45	s2	56.5	172.4	8000		—/ —	—	c2 (HD23319/05:33:21)
06:18:25	s3	56.6	176.4	8000		—/ —	—	c2 (HD23319/05:33:21)
07:32:42	s5	56.5	7.1	8000	OF	—/ —	—	c7 (HD23319/09:36:38)
09:14:13	s9	56.2	20.8	4000	OF	—/ —	—	c7 (HD23319/09:36:38)
09:19:08	s10	56.2	21.4	2000	OF	—/ —	—	c7 (HD23319/09:36:38)
09:20:53	s11	56.1	21.7	4000	R	8000/ 8000		c7 (HD23319/09:36:38)

Table B.3.: Log of all observations of NGC1365

Dataset		Fringe track				Photometry		Associated calib
Time [UTC]	id	BL [m]	PA [°]	NDIT	flags	NDIT A/B	flags	id, name, time
2010-08-26		U3U4		184.B-0832(T)				
08:35:44	s7	59.0	99.8	4000	F	—/ —	—	c5 (HD23319/09:03:29)
08:38:21	s8	59.2	100.1	12000		8000/ 8000	M	c5 (HD23319/09:03:29)
09:35:53	s10	62.0	108.0	12000		8000/ 8000		c5 (HD23319/09:03:29)
09:48:31	s11	62.2	109.8	12000	OF	8000/ 8000		c6 (HD23319/10:10:45)
2010-08-28		U1U4		184.B-0832(G)				
07:28:41	s10	125.5	38.7	4000		—/ —	—	c3 (HD23319/07:05:16)
07:31:13	s11	125.7	39.2	8000		8000/ 8000	O	c3 (HD23319/07:05:16)
07:44:43	s12	126.6	41.8	12000		8000/ 8000		c3 (HD23319/07:05:16)
10:08:36	s21	128.3	64.0	8000		—/ —	—	c6 (HD23319/10:24:25)
10:12:22	s22	128.0	64.5	12000		—/ —	—	c6 (HD23319/10:24:25)
2010-08-29		U2U3		184.B-0832(I)				
09:50:32	s4	45.9	41.8	12000		8000/ 8000		c3 (HD23319/09:34:04)
10:04:34	s5	45.6	43.4	12000		8000/ 8000		c3 (HD23319/09:34:04)

Table B.4.: Log of all observations of LEDA17155

Dataset		Fringe track				Photometry		Associated calib
Time [UTC]	id	BL [m]	PA [°]	NDIT	flags	NDIT A/B	flags	id, name, time
2007-11-23		U3U4		080.B-0258(A)				
03:10:23	s4	50.7	95.7	8000	FS	—/ —	—	c2 (HD16815/02:38:26)
2010-01-01		U1U3		184.B-0832(E)				
02:04:52	s1	101.7	23.9	8000		8000/ 8000	OM	c1 (HD36597/01:04:54)
02:18:30	s2	101.9	25.6	8000		—/ —	—	c3 (HD23319/02:41:01)
05:21:24	s6	97.4	42.3	4000	F	8000/ 8000		c5 (HD36597/05:49:16)
05:32:18	s7	96.4	42.9	4000		—/ —	—	c5 (HD36597/05:49:16)
2010-01-02		U3U4		184.B-0832(Q)				
05:12:17	s5	57.2	126.7	4000		8000/ 8000	O	c5 (HD36597/04:46:52)
05:23:23	s6	56.3	128.6	4000		—/ —	—	c5 (HD36597/04:46:52)
06:52:11	s9	48.5	147.9	4000		8000/ 8000	M	c7 (HD36597/06:29:15)
07:02:55	s10	47.6	150.8	4000	F	—/ —	—	c7 (HD36597/06:29:15)
2010-02-27		U2U4		184.B-0832(M)				
01:45:37	s1	77.2	95.8	8000		8000/ 8000	O	c1 (HD36597/01:21:01)
01:56:58	s2	75.1	97.2	8000	M	—/ —	—	c1 (HD36597/01:21:01)
02:03:02	s3	74.0	98.0	8000	F	8000/ 8000		c1 (HD36597/01:21:01)
2010-08-24		U1U2		184.B-0832(A)				
10:17:13	s13	56.2	15.1	4000	OF	—/ —	—	c7 (HD23319/09:36:38)
2010-08-25		U2U3		184.B-0832(K)				
09:45:29	s5	45.3	24.4	8000	F	8000/ 7120		c3 (HD36079/10:24:53)
10:09:14	s6	45.7	28.0	8000		8000/ 8000		c3 (HD36079/10:24:53)
2010-08-26		U3U4		184.B-0832(T)				
07:34:01	s5	35.8	87.0	4000	F	—/ —	—	c3 (HD36079/07:08:01)
09:23:04	s9	53.9	97.9	4000	OF	—/ —	—	c5 (HD23319/09:03:29)

Table B.5.: Log of all observations of MCG-5-23-16

Dataset		Fringe track				Photometry		Associated calib
Time [UTC]	id	BL [m]	PA [°]	NDIT	flags	NDIT A/B	flags	id, name, time
2005-12-18		U2U3		076.B-0038(A)				
06:39:51	s1	46.1	24.1	12000		16000/16000		c2 (HD90610/05:07:40)
2010-01-01		U1U3		184.B-0832(E)				
04:18:40	s5	101.2	3.7	4000		8000/ 8000		c4 (HD90610/04:44:13)
2010-01-31		U3U4		184.B-0832(R)				
03:38:05	s1	54.9	95.9	12000	S	8000/ 8000		c1 (HD82150/03:11:19)
03:51:36	s2	56.3	97.5	12000		8000/ 8000	O	c1 (HD82150/03:11:19)
2010-02-27		U2U4		184.B-0832(M)				
02:59:20	s4	87.7	73.6	8000		8000/ 8000	O	c3 (HD82150/02:38:35)
03:10:49	s5	88.3	75.2	8000		8000/ 8000	M	c3 (HD82150/02:38:35)
03:22:17	s6	88.8	76.7	8000		8000/ 8000	M	c3 (HD82150/02:38:35)
03:35:12	s7	89.2	78.4	8000		—/ —	—	c3 (HD82150/02:38:35)
03:42:02	s8	89.4	79.3	8000		8000/ 8000		c4 (HD82150/04:36:39)
03:53:30	s9	89.4	80.8	8000		8000/ 8000	O	c4 (HD82150/04:36:39)
04:08:12	s10	89.3	82.7	8000		—/ —	—	c4 (HD82150/04:36:39)
04:16:54	s11	89.1	83.8	8000		8000/ 8000	O	c4 (HD82150/04:36:39)
05:01:50	s12	86.5	89.5	8000	S	—/ —	—	c4 (HD82150/04:36:39)
2010-03-26		U1U2		184.B-0832(B)				
23:59:04	s1	56.5	9.3	8000		16000/ 8000		c1 (HD82150/23:31:09)
00:16:37	s2	56.5	11.8	8000		8000/ 8000		c2 (HD90610/00:36:05)
01:23:32	s3	56.5	20.5	8000	S	—/ —	—	c2 (HD90610/00:36:05)
01:43:10	s4	56.5	22.9	8000	FS	—/ —	—	c3 (HD90610/02:21:13)
01:49:58	s5	56.4	23.7	8000		8000/ 8000		c3 (HD90610/02:21:13)
02:01:51	s6	56.4	25.1	8000	S	8000/ 8000		c3 (HD90610/02:21:13)
2010-03-27		U1U4		184.B-0832(H)				
00:20:09	s1	125.6	45.0	8000	OFS	8000/ 8000	M	c1 (HD90610/23:32:32)
00:31:38	s2	126.6	46.9	8000	OFS	8000/ 8000	M	c1 (HD90610/23:32:32)
00:42:55	s3	127.5	48.7	8000	OF	—/ —	—	c1 (HD90610/23:32:32)
03:35:17	s9	122.2	70.3	8000	S	8000/ 8000	S	c5 (HD90610/04:37:48)
03:46:38	s10	120.3	71.5	8000		16000/ 8000		c5 (HD90610/04:37:48)
03:58:17	s11	118.1	72.6	8000		—/ —	—	c5 (HD90610/04:37:48)
2010-04-28		U2U4		184.B-0832(O)				
00:02:53	s1	89.4	81.5	8000		8000/ 8000		c1 (HD82150/23:32:22)
00:14:28	s2	89.3	83.0	12000		8000/ 8000		c1 (HD82150/23:32:22)
01:42:19	s3	82.6	94.3	12000	OFM	—/ —	—	c2 (HD82150/01:19:16)
01:49:32	s4	81.7	95.3	12000	M	8000/ 8000	M	c2 (HD82150/01:19:16)
02:06:16	s5	79.3	97.6	12000	M	8000/ 8000	M	c3 (HD82150/02:34:31)

Table B.6.: Log of all observations of MCG-5-23-16

Dataset		Fringe track				Photometry		Associated calib
Time [UTC]	id	BL [m]	PA [°]	NDIT	flags	NDIT A/B	flags	id, name, time
2010-05-27		U1U2		184.B-0832(C)				
00:44:04	s5	51.6	39.2	8000		8000/ 8000	O	c3 (HD90610/01:23:55)
00:55:21	s6	51.0	39.8	8000		—/ —	—	c3 (HD90610/01:23:55)
01:01:08	s7	50.6	40.0	8000		8000/ 8000		c3 (HD90610/01:23:55)
2010-05-31		U3U4		184.B-0832(S)				
23:21:33	s1	60.4	123.3	8000		8000/ 8000	O	c1 (HD82150/23:00:38)
23:33:05	s2	59.8	125.2	8000	OF	—/ —	—	c1 (HD82150/23:00:38)
01:14:34	s3	52.8	145.6	8000	M	8000/ 8000		c2 (HD82150/00:42:03)
01:26:05	s4	52.0	148.5	16000	O	—/ —	—	c3 (HD90610/01:49:02)
01:34:36	s5	51.4	150.6	8000	M	—/ —	—	c3 (HD90610/01:49:02)
02:15:43	s6	49.1	161.9	8000	R	—/ —	—	c4 (HD90610/02:28:29)

Table B.7.: Log of all observations of Mrk1239

Dataset Time [UTC]	id	Fringe track BL [m]	PA [°]	NDIT	flags	Photometry NDIT A/B	flags	Associated calib id, name, time
2005-12-18		U2U3		076.B-0038(A)				
07:31:59	s2	41.0	36.1	12000		16000/16000		c3 (HD83618/08:15:17)
08:47:23	s3	44.7	42.8	12000		16000/16000		c3 (HD83618/08:15:17)
2008-04-19		U1U4		381.B-0240(B)				
00:35:32	s1	127.3	62.3	12000	S	8000/ 8000		c2 (HD95272/01:17:48)
2008-04-20		U1U3		381.B-0240(A)				
01:33:06	s1	100.6	38.1	8000		8000/ 8000		c1 (HD95272/02:10:52)
01:44:35	s2	101.2	38.5	8000		8000/ 8000		c1 (HD95272/02:10:52)
2010-01-01		U1U3		184.B-0832(E)				
06:32:53	s8	89.8	26.9	4000		8000/ 8000		c6 (HD83618/06:56:15)
2010-01-30		U2U4		184.B-0832(N)				
07:27:33	s4	83.9	82.2	8000		8000/ 8000	M	c2 (HD83618/06:53:16)
07:46:09	s5	81.2	82.1	8000		8000/ 8000		c2 (HD83618/06:53:16)
2010-01-31		U3U4		184.B-0832(R)				
05:36:11	s6	62.2	109.1	8000		8000/ 8000	M	c3 (HD83618/06:10:48)
05:49:14	s7	61.8	109.3	8000		8000/ 8000	O	c3 (HD83618/06:10:48)

Table B.8.: Log of all observations of NGC3281

Dataset Time [UTC]	id	Fringe track BL [m]	PA [°]	NDIT	flags	Photometry NDIT A/B	flags	Associated calib id, name, time
2010-01-01		U1U3	184.B-0832(E)					
07:25:42	s9	102.3	25.2	4000	OF	—/ —	—	c7 (HD112213/08:17:07)
2010-01-02		U3U4	184.B-0832(Q)					
07:50:16	s11	61.6	106.2	4000		8000/ 8000	O	c8 (HD90610/07:21:17)
08:01:22	s12	61.9	107.7	4000		—/ —	—	c8 (HD90610/07:21:17)
2010-01-30		U2U4	184.B-0832(N)					
06:02:48	s1	89.2	77.2	8000		8000/ 8000	M	c1 (HD90610/05:33:14)
06:14:11	s2	89.4	78.9	8000		8000/ 8000	M	c1 (HD90610/05:33:14)
06:25:47	s3	89.4	80.6	8000		8000/ 8000		c1 (HD90610/05:33:14)
2010-03-26		U1U2	184.B-0832(B)					
03:00:53	s7	55.8	27.0	8000		8000/ 8000		c3 (HD90610/02:21:13)
03:16:22	s8	55.5	28.7	8000		8000/ 8000		c3 (HD90610/02:21:13)
2010-05-31		U3U4	184.B-0832(S)					
02:52:01	s7	51.8	160.6	8000	OFS	—/ —	—	c4 (HD90610/02:28:29)

Table B.9.: Log of all observations of 3C273

Dataset		Fringe track				Photometry		Associated calib
Time [UTC]	id	BL [m]	PA [°]	NDIT	flags	NDIT A/B	flags	id, name, time
2007-02-06		U2U3		078.B-0031(A)				
05:41:06	s1	35.1	26.8	8000	O	—/ —	—	c1 (HD98430/06:31:50)
05:50:44	s2	35.7	28.5	8000	O	—/ —	—	c1 (HD98430/06:31:50)
06:04:10	s3	36.6	30.8	8000	M	—/ —	—	c1 (HD98430/06:31:50)
06:08:32	s4	36.9	31.5	7120		—/ —	—	c1 (HD98430/06:31:50)
06:08:32	s5	36.9	31.5	4440	R	—/ —	—	c1 (HD98430/06:31:50)
2008-04-21		U3U4		081.B-0121(D)				
06:52:20	s7	30.9	126.3	8000	Z	8000/ 8000	OZ	c5 (HD107328/06:10:08)
07:03:47	s8	28.7	129.4	8000	Z	8000/ 8000	Z	c5 (HD107328/06:10:08)
2009-05-04		U3U4		282.B-5071(C)				
05:50:15	s1	33.2	123.5	8000		12000/12000		c6 (HD107328/06:23:15)
2010-01-30		U2U4		184.B-0832(N)				
09:16:32	s9	88.6	81.8	8000		8000/ 8000	M	c3 (HD112213/08:56:39)
09:28:12	s10	87.8	81.6	8000		8000/ 8000		c3 (HD112213/08:56:39)

Table B.10.: Log of all observations of NGC4507

Dataset		Fringe track				Photometry		Associated calib
Time [UTC]	id	BL [m]	PA [°]	NDIT	flags	NDIT A/B	flags	id, name, time
2010-01-01		U1U3		184.B-0832(E)				
07:59:57	s10	102.4	12.2	4000	OF	—/ —	—	c7 (HD112213/08:17:07)
08:31:34	s11	102.3	17.0	4000	F	—/ —	—	c7 (HD112213/08:17:07)
08:34:09	s12	102.3	17.4	4000	F	—/ —	—	c7 (HD112213/08:17:07)
2010-01-02		U3U4		184.B-0832(Q)				
08:17:24	s13	54.4	90.6	4000	F	8000/ 8000	O	c9 (HD112213/08:41:24)
08:28:04	s14	55.4	92.3	4000		—/ —	—	c9 (HD112213/08:41:24)
2010-01-30		U2U4		184.B-0832(N)				
08:16:38	s6	89.4	78.6	8000		8000/ 8000		c3 (HD112213/08:56:39)
08:28:06	s7	89.4	80.4	8000	OF	—/ —	—	c3 (HD112213/08:56:39)
08:33:50	s8	89.4	81.4	8000		8000/ 8000	O	c3 (HD112213/08:56:39)
2010-01-31		U3U4		184.B-0832(R)				
04:51:01	s3	42.6	73.7	8000		8000/ 8000		c2 (HD112213/04:30:41)
05:03:37	s4	44.4	76.4	8000	M	8000/ 8000		c2 (HD112213/04:30:41)
05:17:31	s5	46.4	79.2	8000		—/ —	—	c2 (HD112213/04:30:41)
2010-03-26		U1U2		184.B-0832(B)				
04:01:11	s9	55.8	19.6	8000		8000/ 8000		c5 (HD112213/04:37:40)
04:12:34	s10	55.7	21.1	8000		8000/ 8000		c5 (HD112213/04:37:40)
2010-03-27		U1U4		184.B-0832(H)				
01:18:12	s4	122.2	21.2	8000	OF	8000/ 8000	O	c2 (HD112213/02:00:28)
01:30:03	s5	122.8	23.8	8000	OF	8000/ 8000	M	c2 (HD112213/02:00:28)
01:41:25	s6	123.5	26.3	8000	F	—/ —	—	c2 (HD112213/02:00:28)
06:51:08	s17	114.7	77.6	8000	F	—/ —	—	c7 (HD123123/07:16:31)
2010-04-28		U2U4		184.B-0832(O)				
07:22:35	s9	56.4	138.1	4000	OF	—/ —	—	c6 (HD112213/06:20:46)
2010-05-30		U2U4		184.B-0832(P)				
04:15:22	s1	66.8	120.4	8000	OF	—/ —	—	c1 (HD108759/03:54:56)
04:22:04	s2	65.6	122.1	8000	OFS	—/ —	—	c1 (HD108759/03:54:56)

Table B.11.: Log of all observations of NGC4593

Dataset		Fringe track				Photometry		Associated calib
Time [UTC]	id	BL [m]	PA [°]	NDIT	flags	NDIT A/B	flags	id, name, time
2010-01-31		U3U4		184.B-0832(R)				
07:01:27	s8	60.2	108.1	8000		16000/16000	O	c4 (HD116870/08:12:57)
07:13:22	s9	60.9	108.2	8000	OF	—/ —	—	c4 (HD116870/08:12:57)
07:35:57	s10	62.0	108.4	8000		8000/ 8000	O	c4 (HD116870/08:12:57)
07:47:54	s11	62.3	108.6	8000		8000/ 8000	O	c4 (HD116870/08:12:57)
2010-03-26		U1U2		184.B-0832(B)				
07:13:41	s13	56.6	34.9	8000	OFS	—/ —	—	c7 (HD116870/07:58:33)
07:21:05	s14	56.6	35.0	8000		8000/ 8000		c7 (HD116870/07:58:33)
07:32:34	s15	56.5	35.2	8000		8000/ 8000		c7 (HD116870/07:58:33)
2010-03-27		U1U4		184.B-0832(H)				
05:55:38	s14	130.0	63.5	8000		8000/ 8000	O	c6 (HD116870/05:35:11)
06:07:00	s15	129.6	63.6	8000	F	8000/ 8000		c6 (HD116870/05:35:11)
06:19:00	s16	128.8	63.8	8000	F	—/ —	—	c6 (HD116870/05:35:11)
2010-05-27		U1U2		184.B-0832(C)				
23:58:18	s2	51.9	20.7	8000	OF	—/ —	—	c2 (HD116870/23:29:07)
00:04:38	s3	52.1	21.5	8000	F	8000/ 8000	O	c2 (HD116870/23:29:07)
00:16:21	s4	52.5	22.9	8000	OF	—/ —	—	c2 (HD116870/23:29:07)

Table B.12.: Log of all observations of IC4329A

Dataset		Fringe track				Photometry		Associated calib
Time [UTC]	id	BL [m]	PA [°]	NDIT	flags	NDIT A/B	flags	id, name, time
2007-02-06		U2U3	078.B-0031(A)					
08:43:55	s8	46.6	35.5	8000	M	4000/ 4000		c2 (HD123123/09:08:18)
08:49:02	s9	46.6	36.2	8000	R	—/ —	—	c2 (HD123123/09:08:18)
2008-04-19		U1U4	381.B-0240(B)					
02:47:35	s4	125.2	44.9	8000		8000/ 8000		c4 (HD123123/03:25:05)
02:58:55	s5	126.2	46.8	8000		8000/ 8000		c4 (HD123123/03:25:05)
04:54:48	s6	129.4	62.7	8000	S	8000/ 8000	S	c7 (HD123123/04:29:15)
05:06:13	s7	128.8	64.0	8000	S	8000/ 8000		c7 (HD123123/04:29:15)
2008-04-20		U1U3	381.B-0240(A)					
02:41:31	s3	102.0	18.1	8000		8000/ 8000	M	c2 (HD123123/03:16:56)
02:53:07	s4	102.1	19.8	8000		8000/ 8000		c2 (HD123123/03:16:56)
06:34:36	s5	95.5	43.3	8000	S	—/ —	—	c4 (HD123123/06:03:52)
06:43:36	s6	94.6	43.9	8000	S	—/ —	—	c4 (HD123123/06:03:52)
06:55:20	s7	93.4	44.6	8000	S	8000/ 8000		c4 (HD123123/06:03:52)
07:06:53	s8	92.0	45.2	8000	S	8000/ 8000		c4 (HD123123/06:03:52)
2010-03-26		U1U2	184.B-0832(B)					
04:57:12	s11	56.6	17.1	8000		8000/ 8000		c6 (HD123123/05:31:32)
05:08:34	s12	56.6	18.5	8000		8000/ 8000		c6 (HD123123/05:31:32)
2010-03-27		U1U4	184.B-0832(H)					
02:36:46	s7	114.2	24.0	8000		8000/ 8000	M	c4 (HD123123/03:13:59)
02:48:02	s8	115.3	26.6	8000	S	8000/ 8000		c4 (HD123123/03:13:59)
08:31:41	s20	111.1	75.4	8000		8000/ 8000		c9 (HD123123/08:58:27)
08:42:57	s21	108.2	76.4	8000		—/ —	—	c9 (HD123123/08:58:27)
2010-04-28		U2U4	184.B-0832(O)					
04:28:42	s6	88.9	84.6	12000		8000/ 8000		c4 (HD123123/04:52:41)
08:09:21	s10	54.2	120.3	8000		8000/ 8000		c7 (HD123123/07:48:01)
2010-05-29		U2U3	184.B-0832(J)					
00:20:54	s5	46.2	26.8	8000		8000/ 8000		c2 (HD112213/00:45:28)
02:59:52	s6	45.4	46.2	8000	S	8000/ 8000	O	c8 (HD112213/02:34:16)
04:04:38	s7	42.7	51.4	8000	S	—/ —	—	c9 (HD123123/04:38:17)
04:08:07	s8	42.5	51.6	8000	S	—/ —	—	c9 (HD123123/04:38:17)
04:11:43	s9	42.3	51.9	8000	S	—/ —	—	c9 (HD123123/04:38:17)
04:15:14	s10	42.1	52.1	8000	S	8000/ 8000	S	c9 (HD123123/04:38:17)
04:59:26	s11	39.1	54.5	8000	S	—/ —	—	c9 (HD123123/04:38:17)
05:02:57	s12	38.8	54.6	8000	S	—/ —	—	c9 (HD123123/04:38:17)
05:07:37	s13	38.4	54.8	8000	S	8000/ 8000	S	c10 (HD123123/05:38:16)
05:19:33	s14	37.4	55.3	8000	S	—/ —	—	c10 (HD123123/05:38:16)
05:23:38	s15	37.0	55.4	8000	OS	—/ —	—	c10 (HD123123/05:38:16)

Table B.13.: Log of all observations of NGC5506

Dataset		Fringe track				Photometry		Associated calib
Time [UTC]	id	BL [m]	PA [°]	NDIT	flags	NDIT A/B	flags	id, name, time
2010-03-26		U1U2		184.B-0832(B)				
09:20:14	s18	56.5	35.3	8000		8000/ 8000		c8 (HD126927/08:57:57)
09:31:35	s19	56.4	35.3	8000		8000/ 8000	O	c9 (HD126927/09:55:03)
2010-03-27		U1U4		184.B-0832(H)				
07:36:50	s18	129.9	63.5	8000		8000/ 8000	O	c8 (HD126927/08:10:22)
07:48:08	s19	129.4	63.5	8000		8000/ 8000	O	c8 (HD126927/08:10:22)
09:21:12	s22	115.8	61.5	8000		8000/ 8000	O	c10 (HD126927/10:02:00)
09:32:28	s23	113.2	61.0	8000	O	—/ —	—	c10 (HD126927/10:02:00)
09:35:58	s24	112.3	60.8	8000		8000/ 8000		c10 (HD126927/10:02:00)
2010-04-28		U2U4		184.B-0832(O)				
05:43:27	s7	86.0	82.7	12000		8000/ 8000	O	c5 (HD126927/05:17:12)
05:57:38	s8	84.4	82.8	12000		8000/ 8000		c5 (HD126927/05:17:12)
08:37:26	s11	46.1	80.0	12000	Z	—/ —	—	c8 (HD123123/09:05:03)
08:42:44	s12	44.3	79.7	12000	Z	8000/ 8000	OZ	c8 (HD123123/09:05:03)
2010-05-29		U2U3		184.B-0832(J)				
23:21:25	s1	35.7	16.5	8000	OS	—/ —	—	c1 (HD124294/23:01:09)
23:25:09	s2	35.8	17.3	8000	M	—/ —	—	c1 (HD124294/23:01:09)
23:28:38	s3	35.9	18.1	8000	F	—/ —	—	c1 (HD124294/23:01:09)
23:45:00	s4	36.6	21.4	8000	OF	—/ —	—	c1 (HD124294/23:01:09)

Table B.14.: Log of all observations of NGC5995

Dataset		Fringe track				Photometry		Associated calib
Time [UTC]	id	BL [m]	PA [°]	NDIT	flags	NDIT A/B	flags	id, name, time
2010-03-26		U1U2		184.B-0832(B)				
08:20:08	s16	55.9	27.3	8000		8000/ 8000	O	c8 (HD126927/08:57:57)
08:31:29	s17	56.1	28.3	8000		8000/ 8000	O	c8 (HD126927/08:57:57)
2010-03-27		U1U4		184.B-0832(H)				
05:00:11	s12	99.3	35.5	8000		8000/ 8000		c6 (HD116870/05:35:11)
05:12:07	s13	101.8	38.1	8000		8000/ 8000	M	c6 (HD116870/05:35:11)

Table B.15.: Log of all observations of NGC7469

Dataset		Fringe track				Photometry		Associated calib
Time [UTC]	id	BL [m]	PA [°]	NDIT	flags	NDIT A/B	flags	id, name, time
2006-09-10		U2U3		077.B-0026(B)				
06:09:20	s1	46.4	46.3	8000	M	8000/ 8000	M	c1 (HD220009/05:00:21)
2007-11-23		U3U4		080.B-0258(A)				
01:07:41	s1	52.2	106.8	8000	F	—/ —	—	c1 (HD220009/00:00:39)
01:12:56	s2	51.4	106.8	8000	F	—/ —	—	c1 (HD220009/00:00:39)
2010-04-28		U2U4		184.B-0832(O)				
10:05:28	s13	55.5	88.5	4000	F	4000/ 4000	O	c8 (HD123123/09:05:03)
10:17:53	s14	59.2	88.1	4000	FS	—/ —	—	c8 (HD123123/09:05:03)
2010-08-26		U3U4		184.B-0832(T)				
05:48:19	s1	59.7	107.1	8000	F	—/ —	—	c2 (HD9138/06:34:57)
07:47:31	s6	43.9	107.9	8000	F	8000/ 8000		c4 (HD213119/08:14:00)
2010-08-27		U1U3		184.B-0832(D)				
04:41:56	s1	85.7	34.2	4000	F	—/ —	—	c4 (HD220009/02:55:22)
04:49:38	s2	86.7	34.9	4000	F	8000/ 8000	M	c4 (HD220009/02:55:22)
05:02:34	s3	88.4	36.0	4000	F	—/ —	—	c4 (HD220009/02:55:22)
2010-08-28		U1U4		184.B-0832(G)				
04:43:08	s1	119.8	64.7	4000	S	—/ —	—	c1 (HD220009/04:16:46)
04:45:37	s2	120.3	64.7	8000	OF	—/ —	—	c1 (HD220009/04:16:46)
04:52:20	s3	121.5	64.7	4000		—/ —	—	c1 (HD220009/04:16:46)
04:54:50	s4	122.0	64.7	4000		8000/ 8000		c1 (HD220009/04:16:46)
05:05:09	s5	123.7	64.7	4000		—/ —	—	c1 (HD220009/04:16:46)
05:07:45	s6	124.1	64.7	8000		—/ —	—	c1 (HD220009/04:16:46)
05:11:24	s7	124.7	64.7	8000		8000/ 8000		c1 (HD220009/04:16:46)
08:24:22	s13	117.9	54.9	4000		—/ —	—	c4 (HD220009/08:08:22)
08:29:22	s14	116.9	54.4	4000		—/ —	—	c4 (HD220009/08:08:22)
08:31:46	s15	116.4	54.1	8000		8000/ 8000	M	c4 (HD220009/08:08:22)
08:43:17	s16	114.0	52.8	4000	FSZ	—/ —	—	c4 (HD220009/08:08:22)
08:46:47	s17	113.3	52.3	8000	Z	8000/ 8000	Z	c4 (HD220009/08:08:22)
2010-08-29		U2U3		184.B-0832(I)				
09:00:07	s1	45.1	39.6	4000	OFZ	—/ —	—	c2 (HD220009/08:35:46)
09:05:02	s2	44.9	39.2	4000	Z	8000/ 8000	Z	c2 (HD220009/08:35:46)
09:19:30	s3	44.4	37.8	4000	OFZ	—/ —	—	c2 (HD220009/08:35:46)

B.2. Large Programme spectra

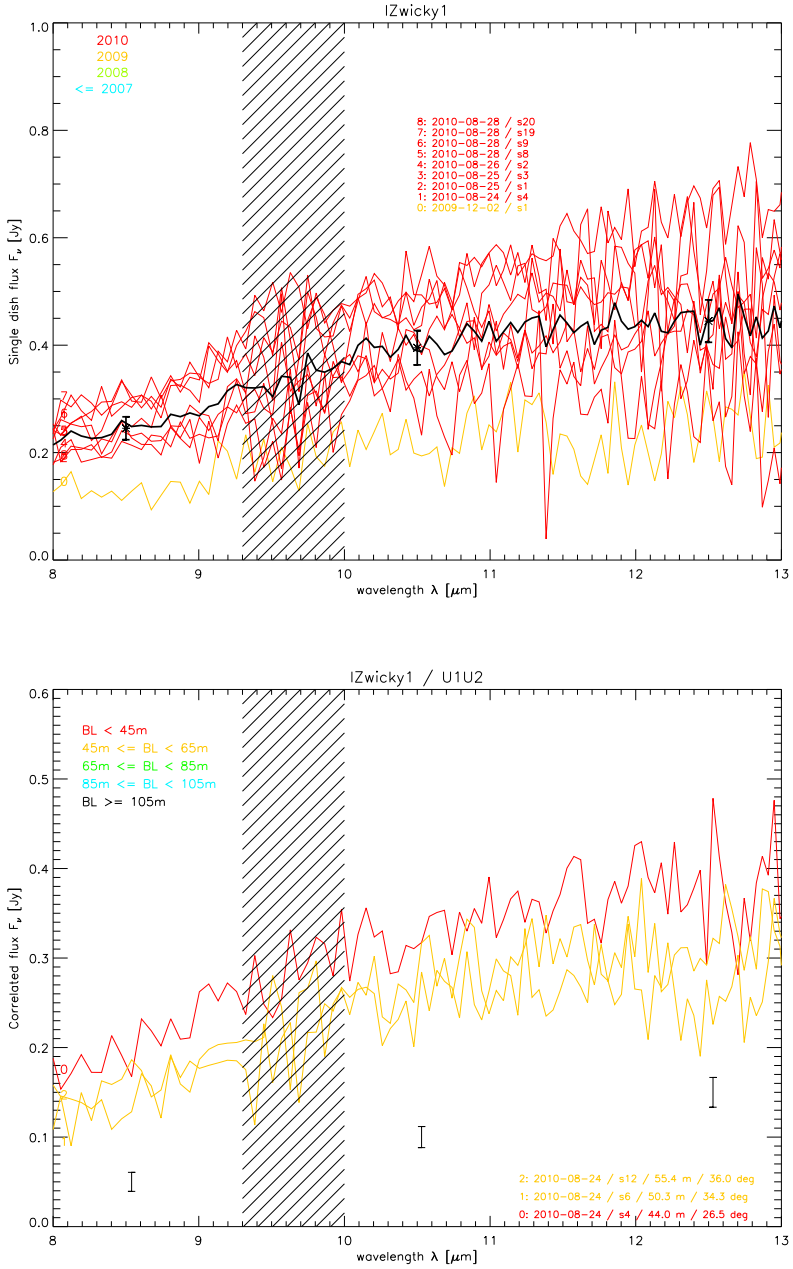

Figure B.1.: Single-dish and correlated flux spectra of **I Zwicky 1** (λ in observed frame). The average **single-dish flux** spectrum (top), that was used for the radial models described in Section 4.4, is plotted as a thick black line. The marked data points there denote the averaged fluxes at 8.5 ± 0.2 μm, 10.5 ± 0.2 μm and 12.5 ± 0.2 μm with the errors estimated as described in Section 4.2.5. Each individual spectrum's color denotes the year in which it has been observed.
The **correlated flux** spectra (bottom; continued on next page) are grouped by baseline (telescope combination). Typical errors ($\pm 1\sigma$) of the averaged fluxes at 8.5 μm, 10.5 μm and 12.5 μm on this baseline are plotted below or above the spectrum. In the correlated flux plots, the color of each line indicates the projected baseline length. *Continued on next page*

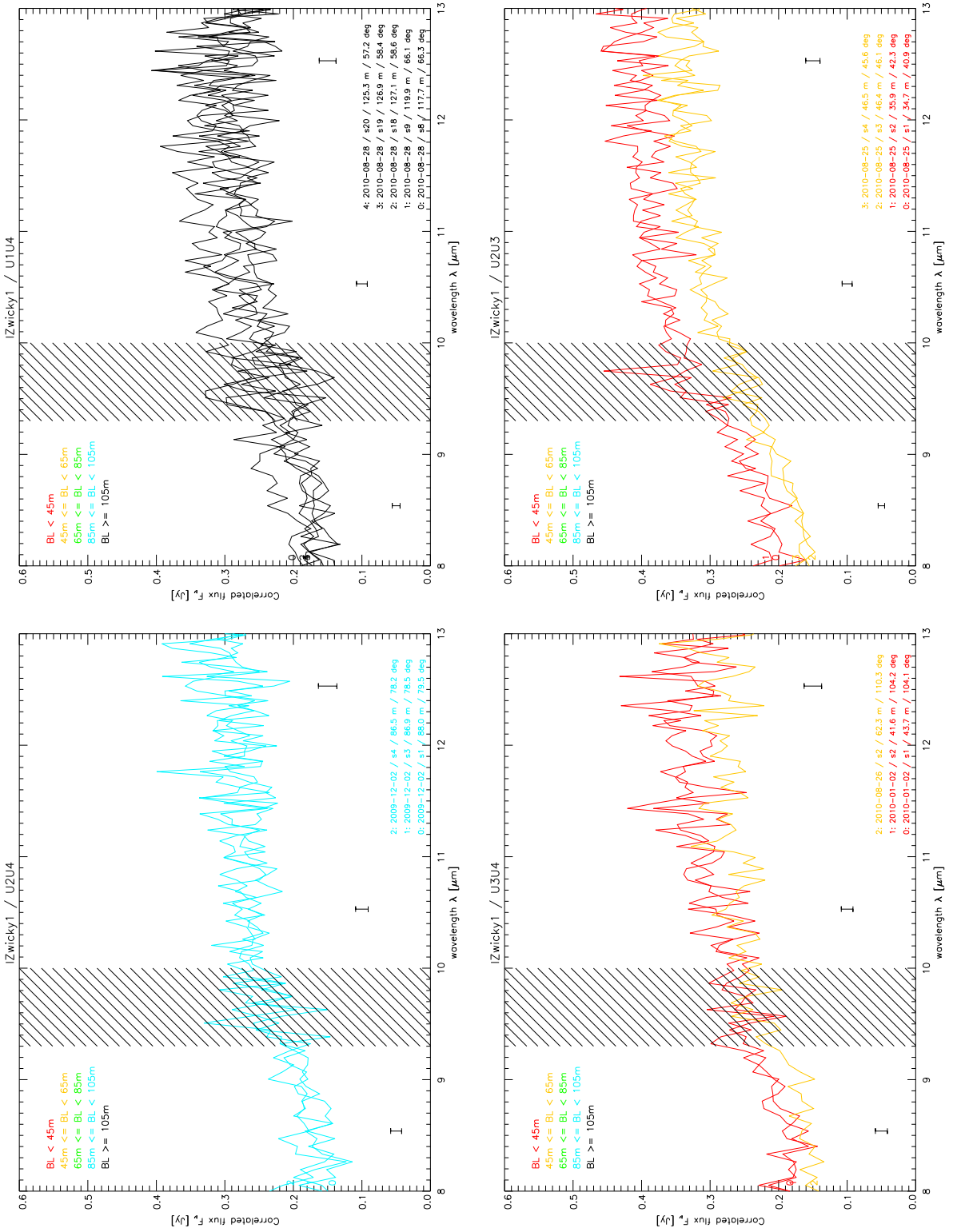

Figure B.1.: **I Zwicky 1** — *Continued*

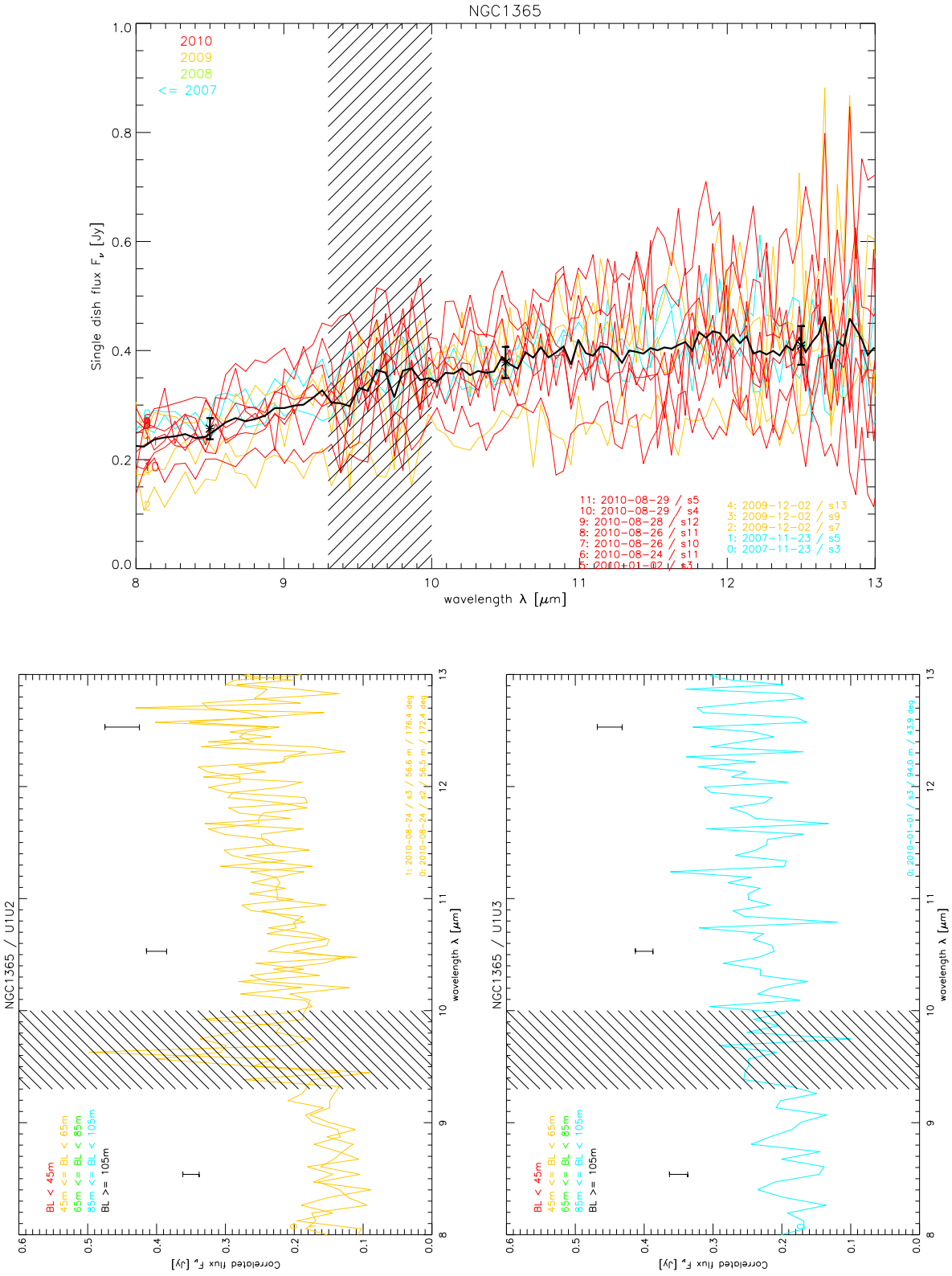

Figure B.2.: Single-dish (top left) and correlated flux spectra of **NGC 1365**, see caption of Figure B.1. *Continued on next page*

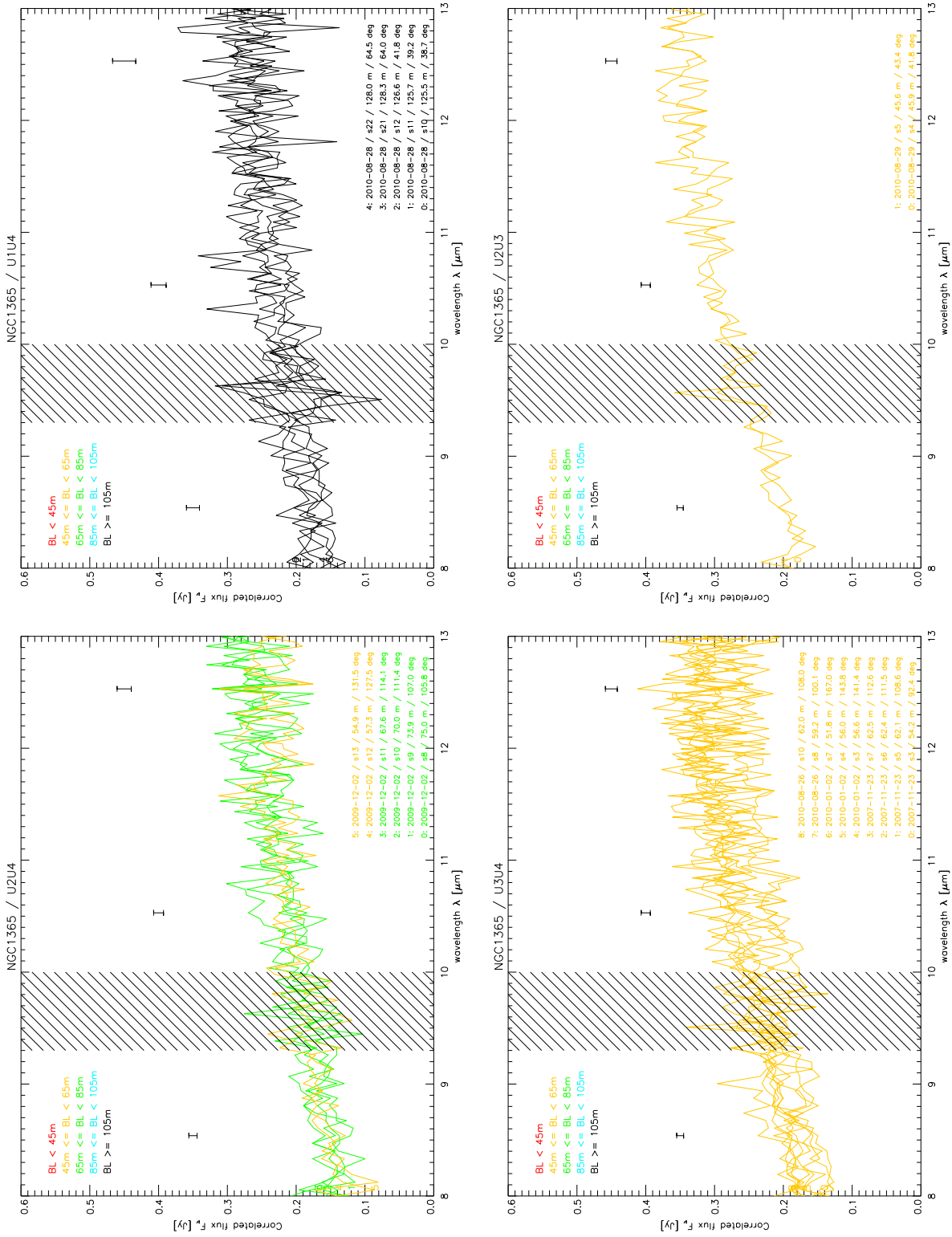

Figure B.2.: **NGC 1365** — *Continued*

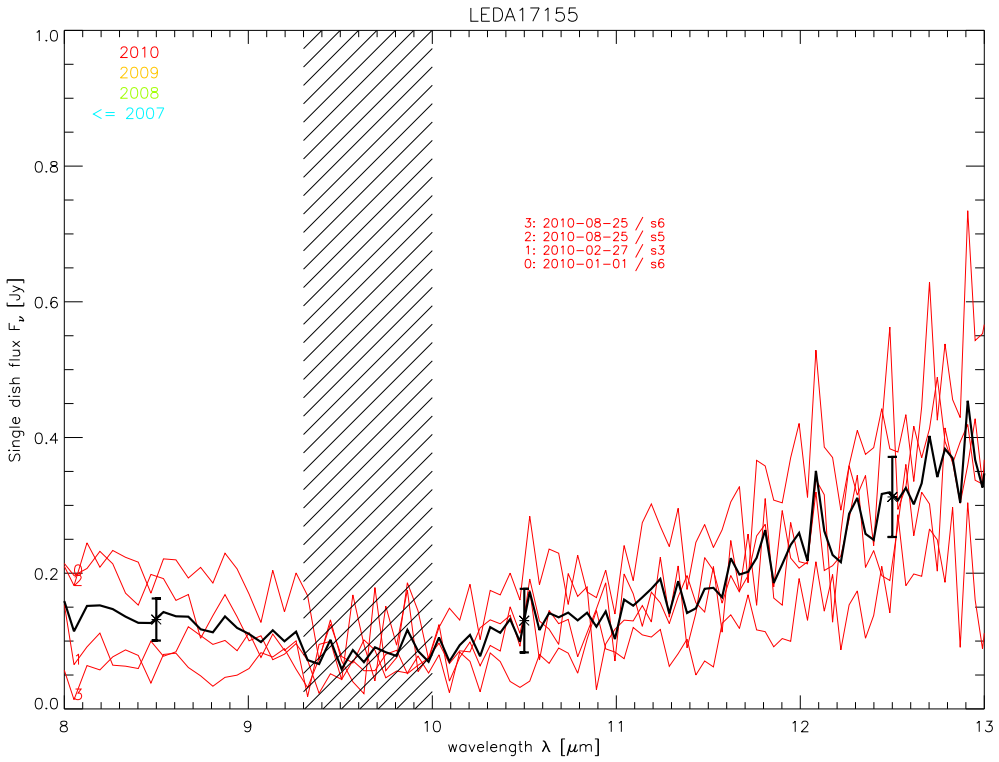

Figure B.3.: Single-dish spectra (this page) and correlated flux spectra (overleaf) of **LEDA 17155 / IRAS 05189-2524** (λ in observed frame), see caption of Figure B.1. *Continued on next page*

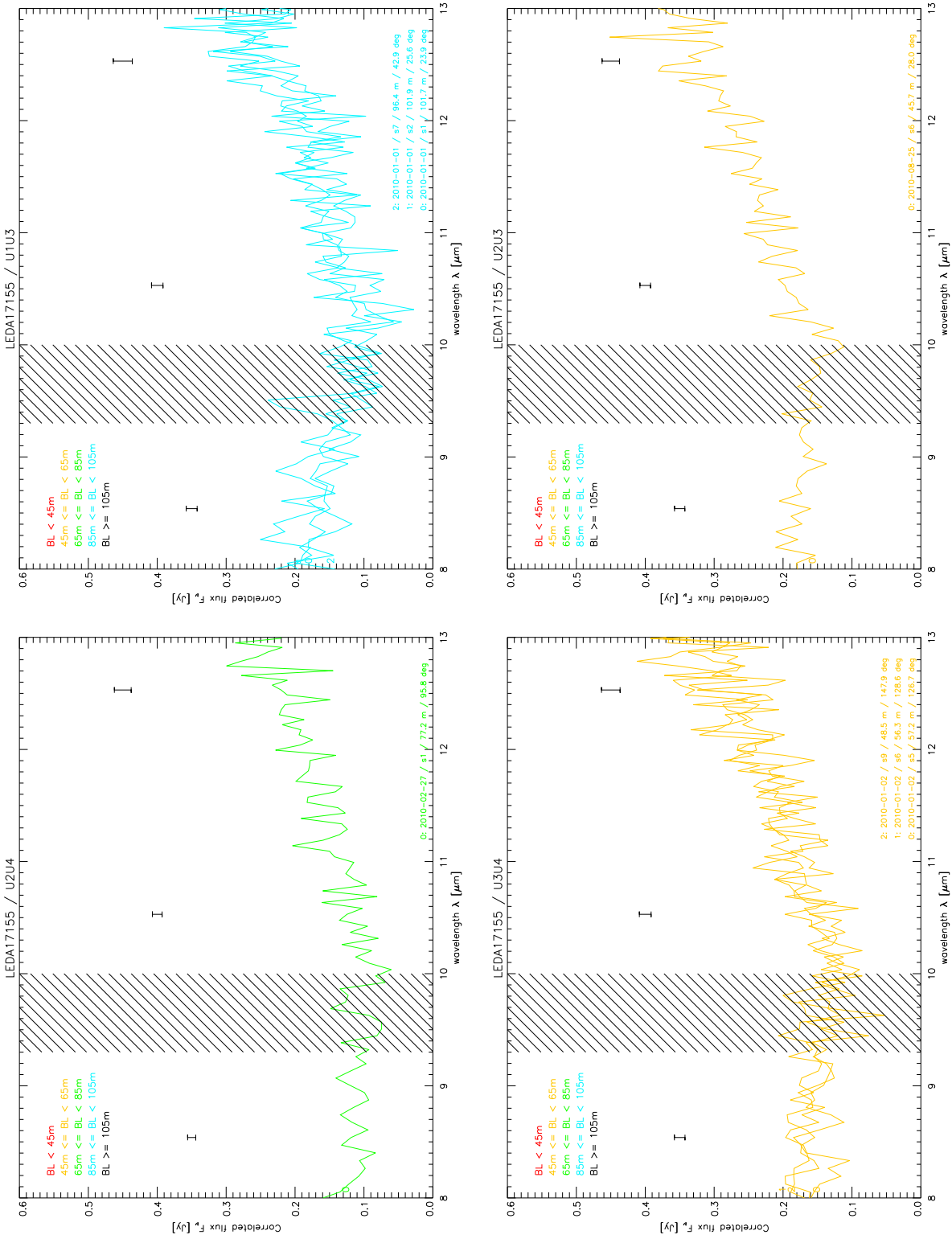

Figure B.3.: **LEDA 17155 / IRAS 05189-2524** — *Continued*

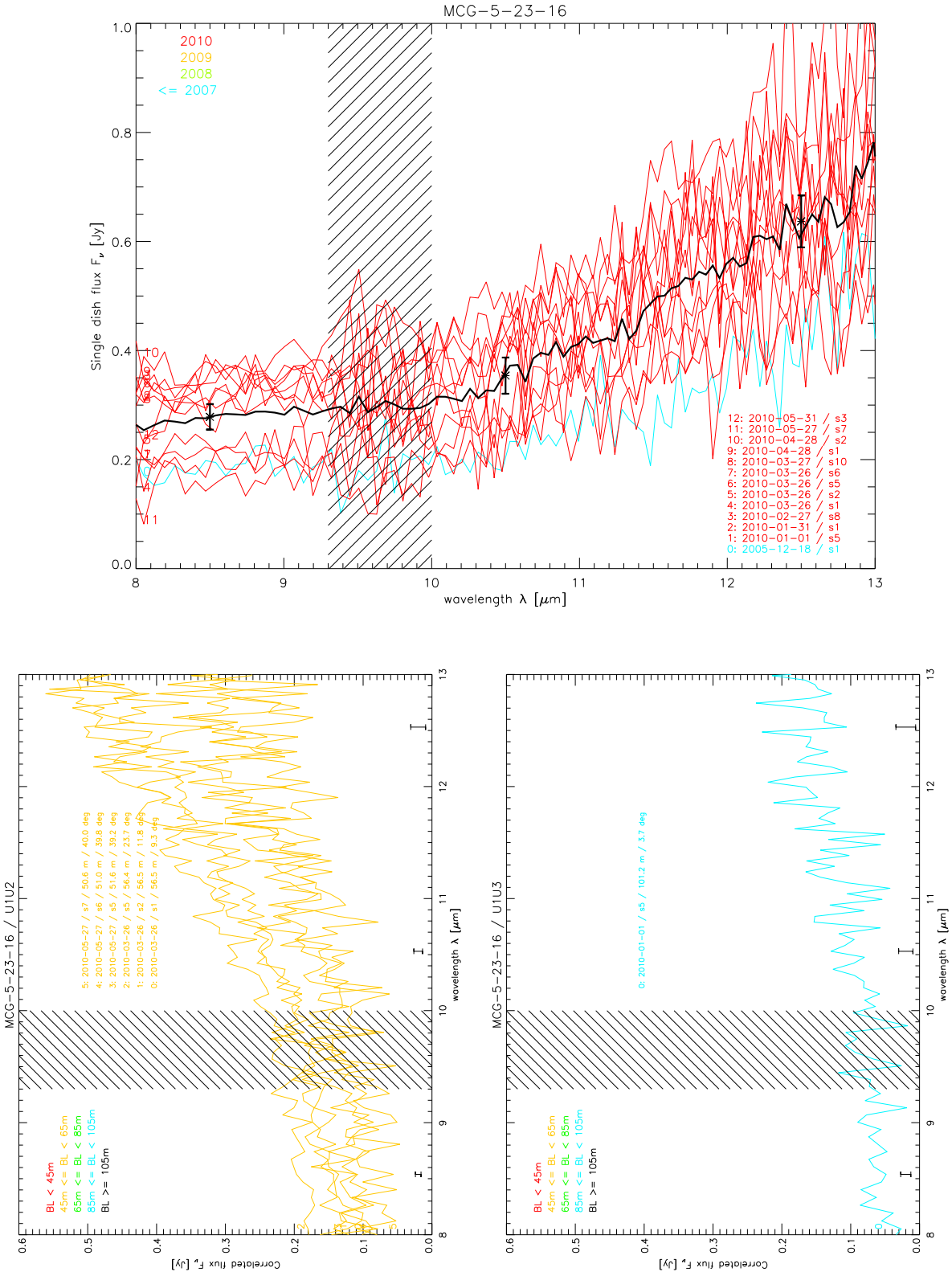

Figure B.4.: Single-dish (top left) and correlated flux spectra of **MCG-05-23-16**, see caption of Figure B.1. *Continued on next page*

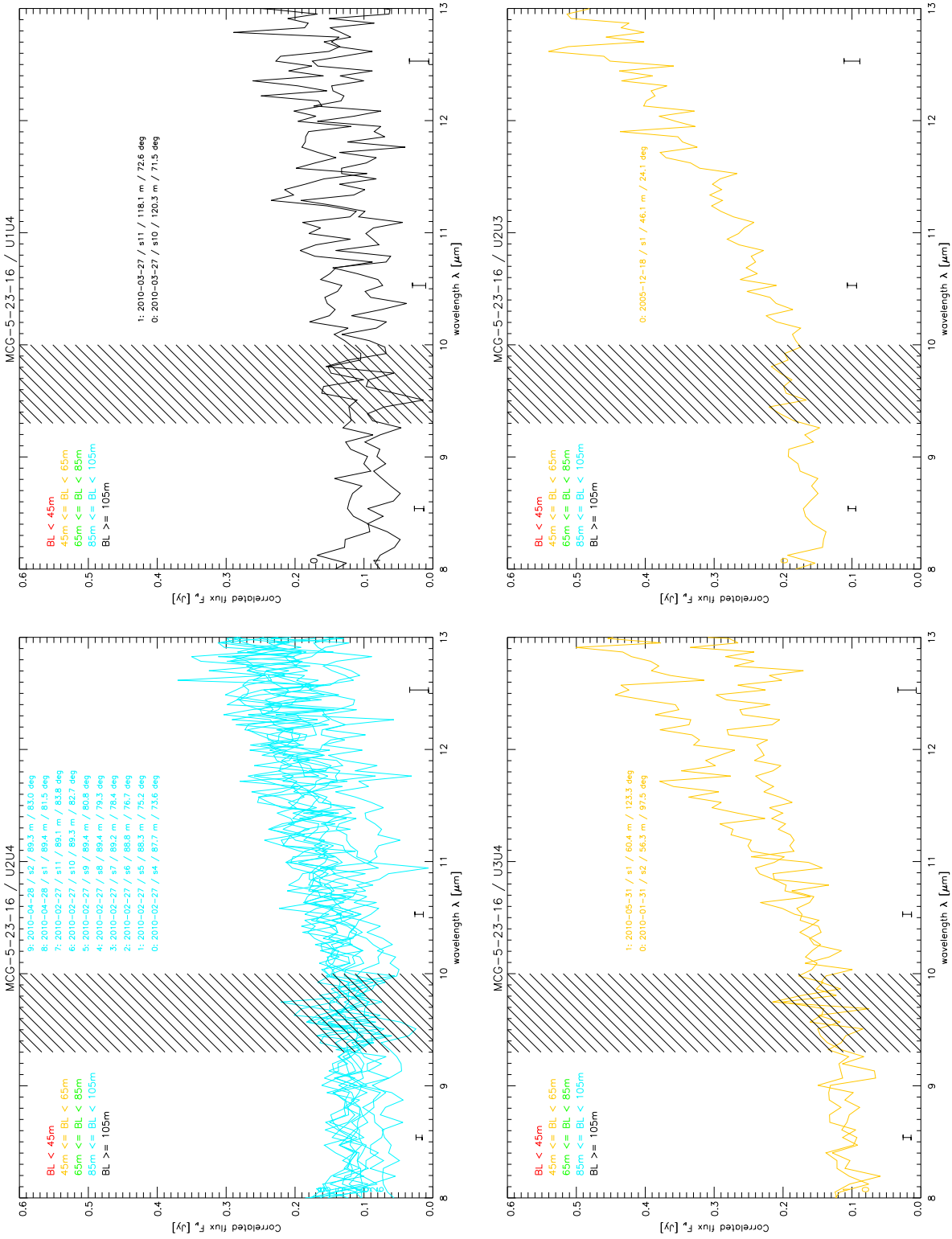

Figure B.4.: **MCG-05-23-16** — *Continued*

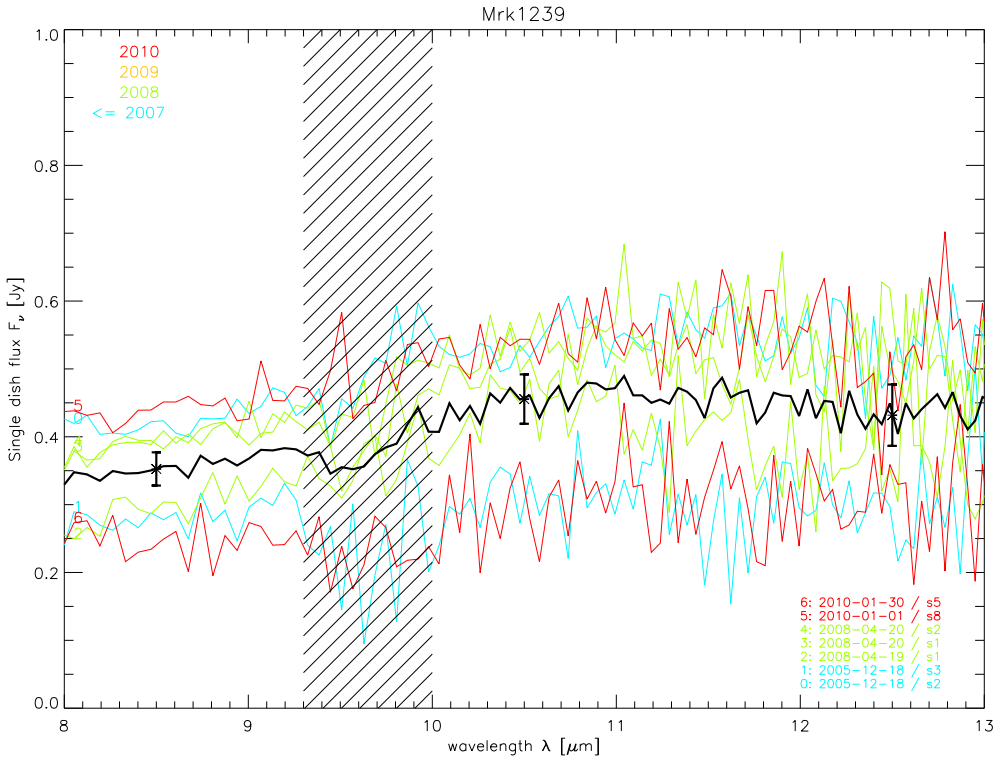

Figure B.5.: Single-dish spectra (this page) and correlated flux spectra (overleaf) of **Mrk 1239**, see caption of Figure B.1. *Continued on next page*

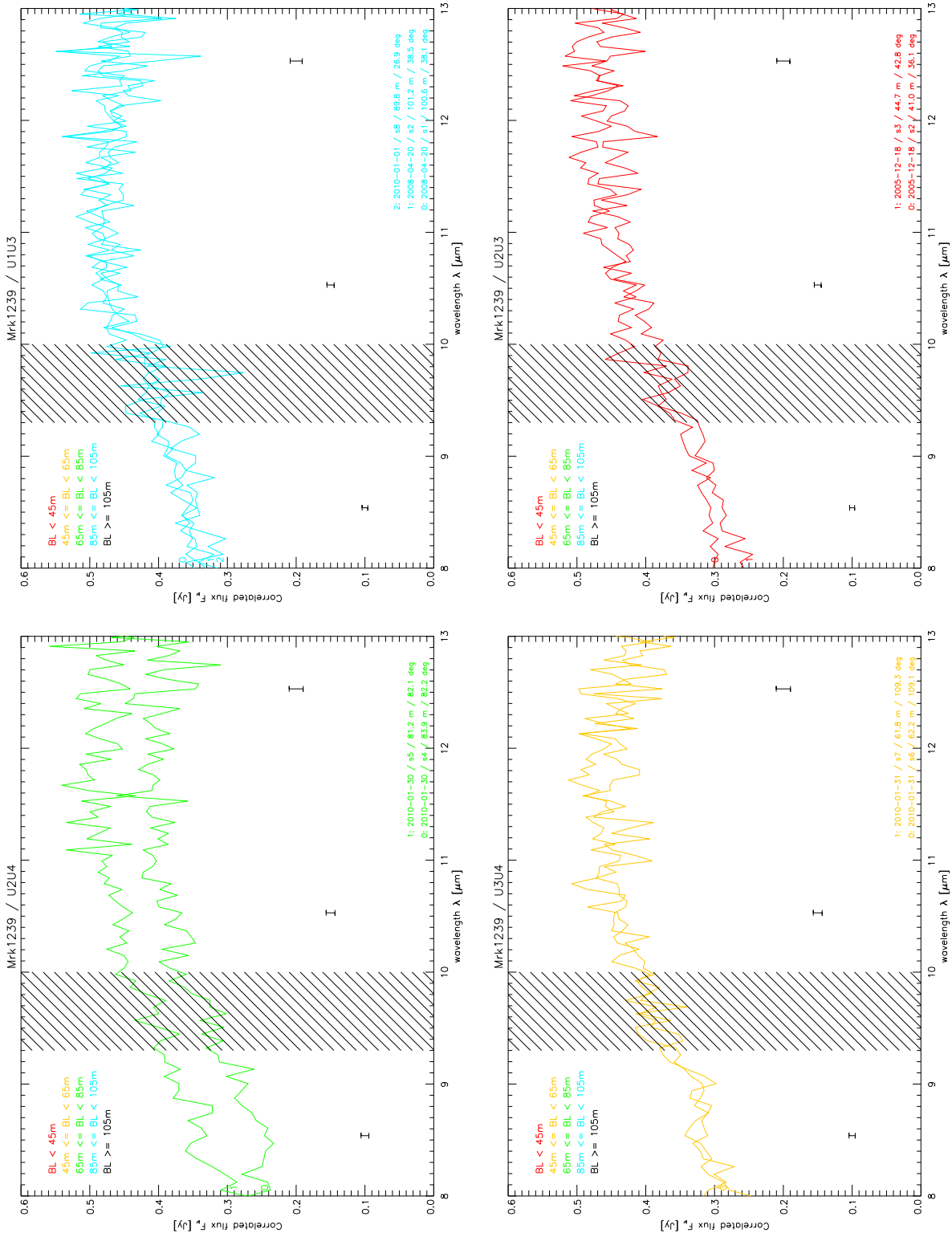

Figure B.5.: **Mrk 1239** — *Continued*

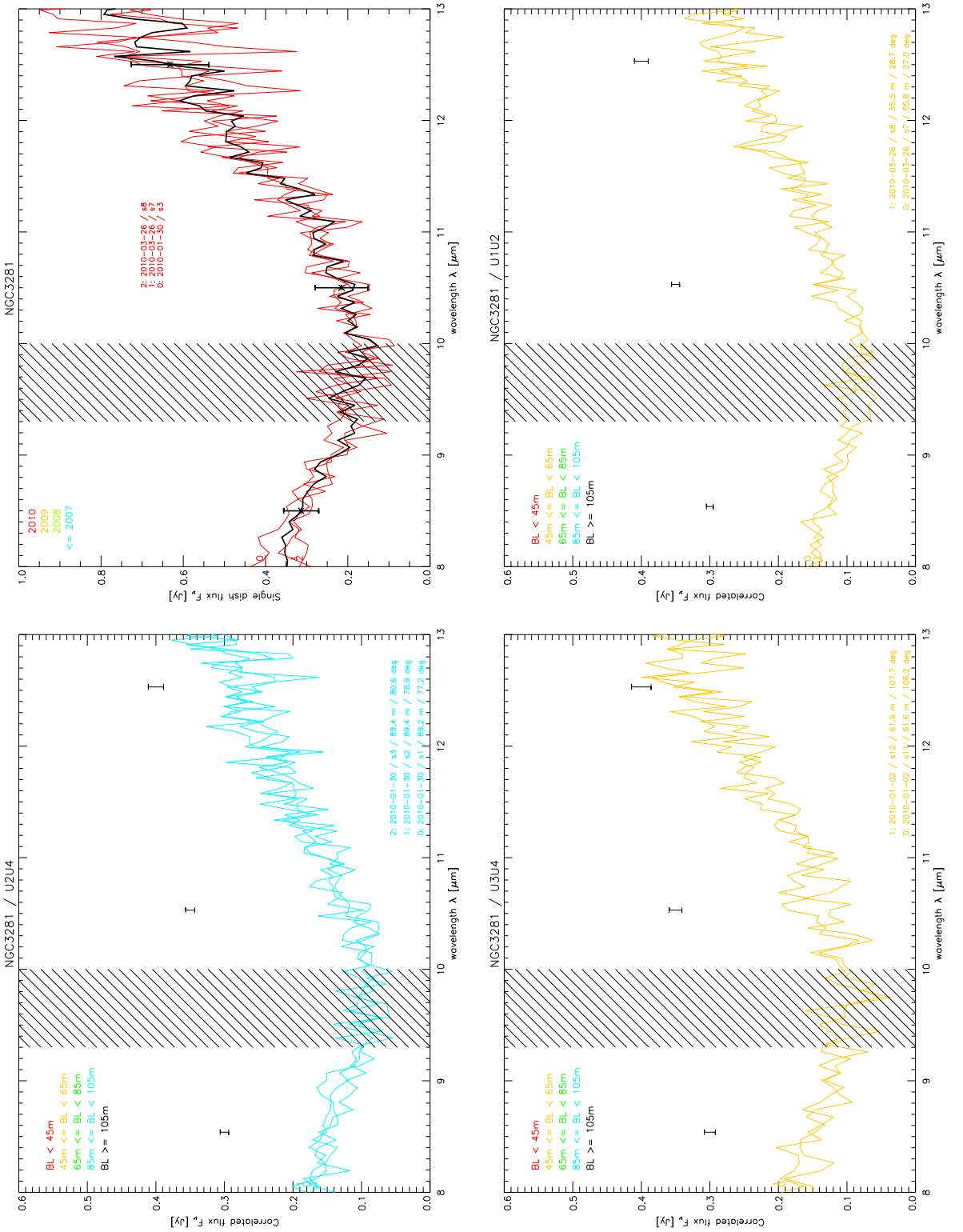

Figure B.6.: Single-dish (top left) and correlated flux spectra of **NGC 3281**, see caption of Figure B.1.

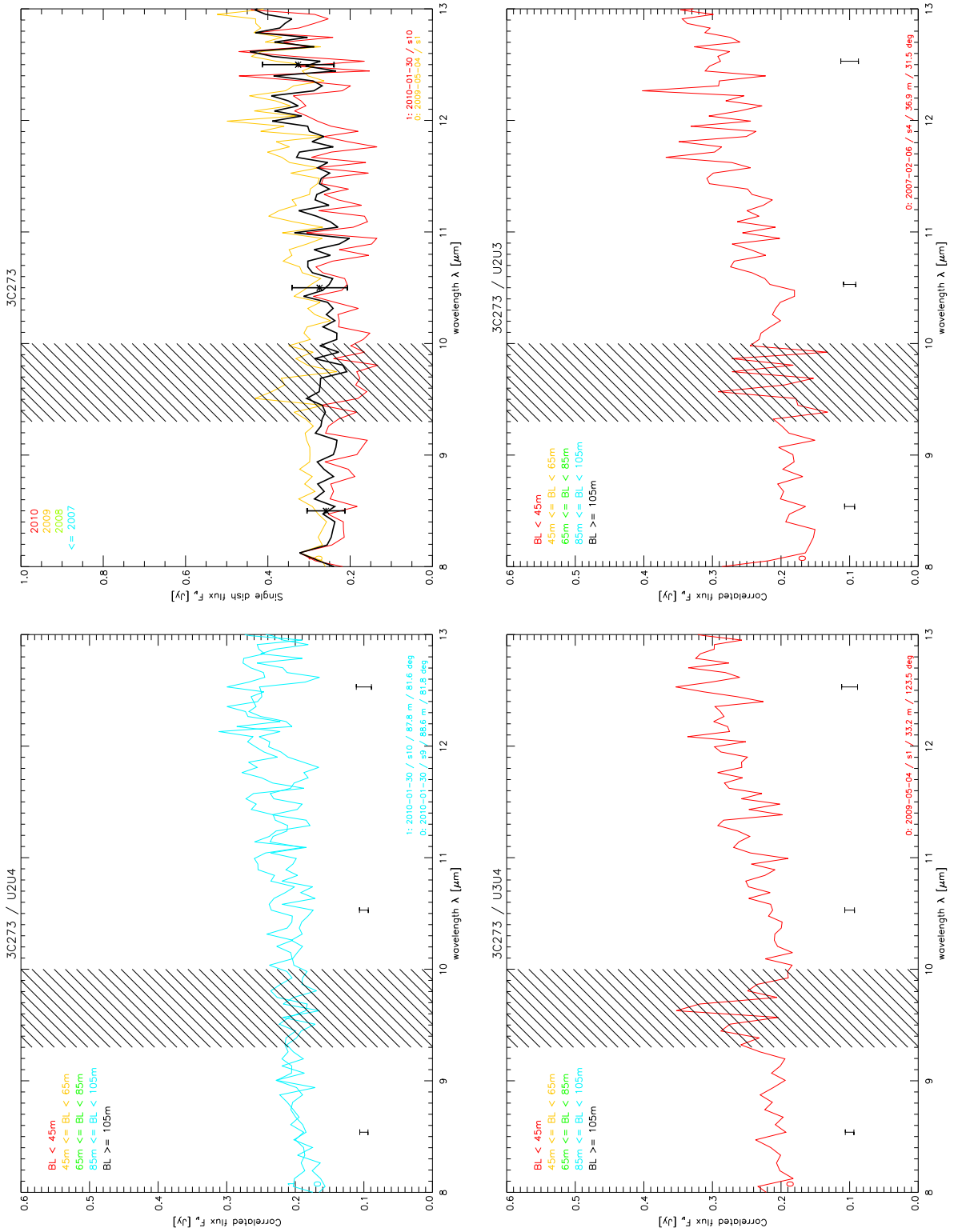

Figure B.7.: Single-dish (top left) and correlated flux spectra of **3C 273** (λ in observed frame), see caption of Figure B.1.

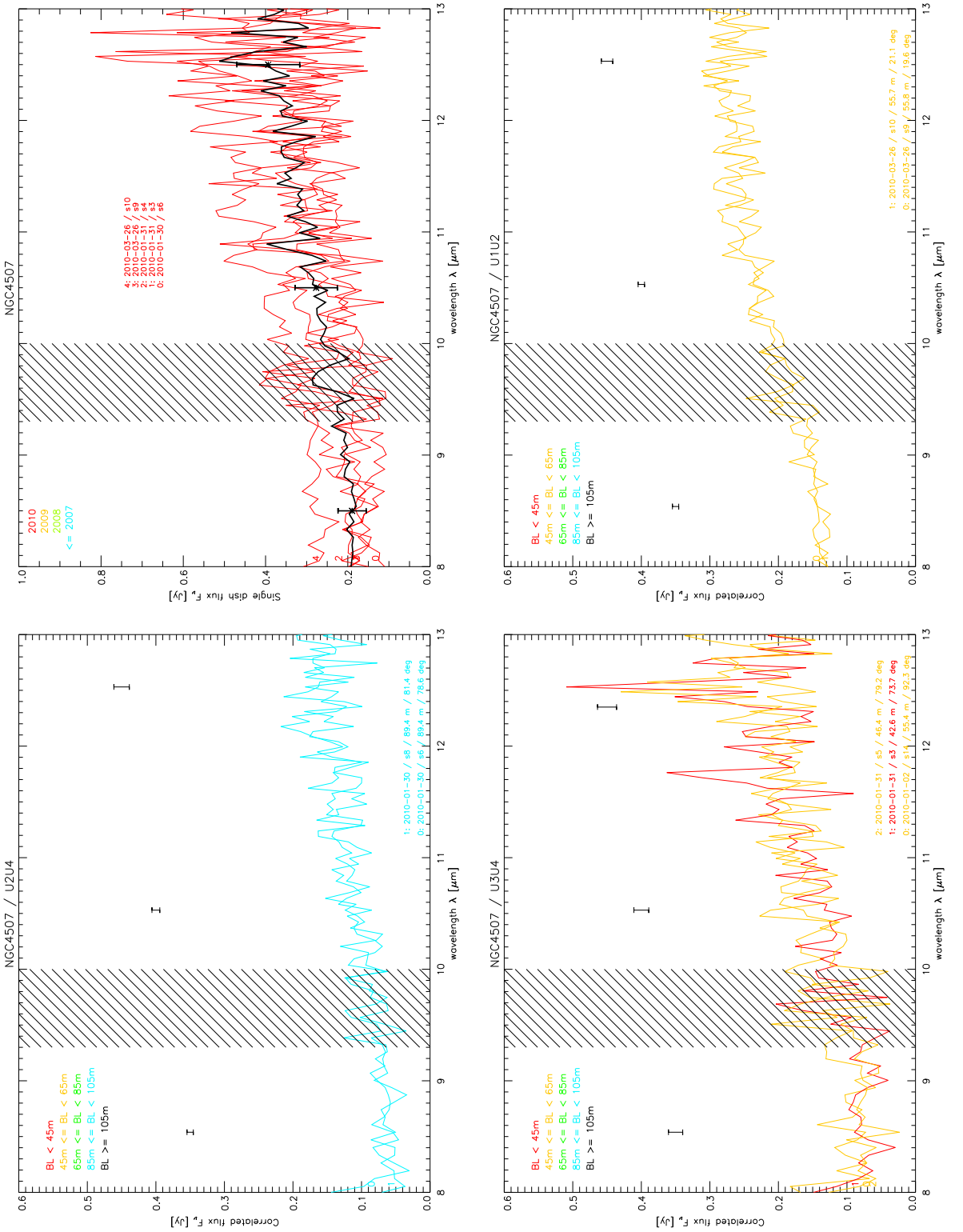

Figure B.8.: Single-dish (top left) and correlated flux spectra of **NGC 4507**, see caption of Figure B.1. The 12.5 μm error bar on the U3U4 plot has been slightly offset for clarity. The "feature" at $\lambda \approx 12.5\mu$m is a noise peak.

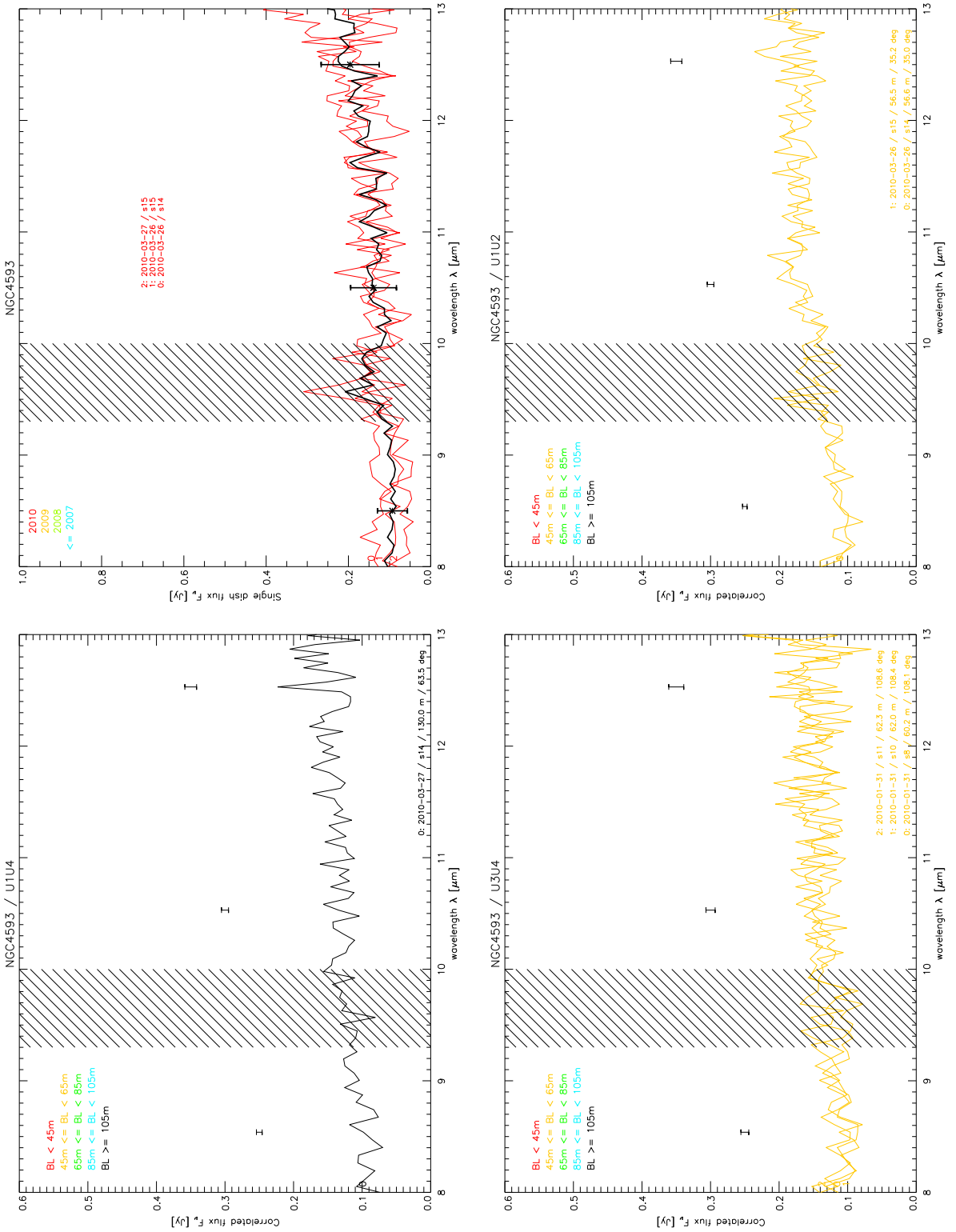

Figure B.9.: Single-dish (top left) and correlated flux spectra of **NGC 4593**, see caption of Figure B.1.

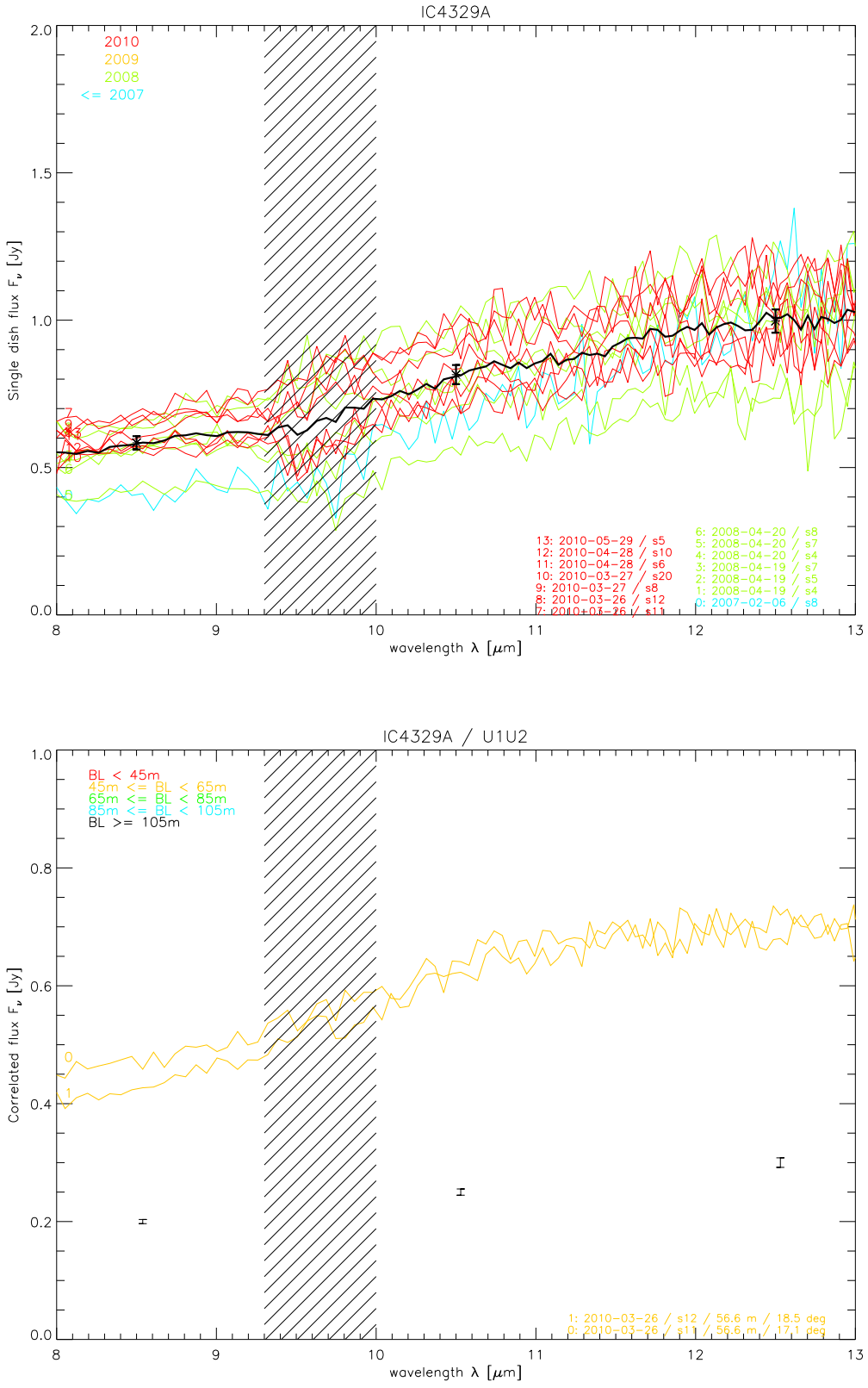

Figure B.10.: Single-dish (top) and correlated flux spectra of **IC 4329 A**, see caption of Figure B.1. *Continued on next page*

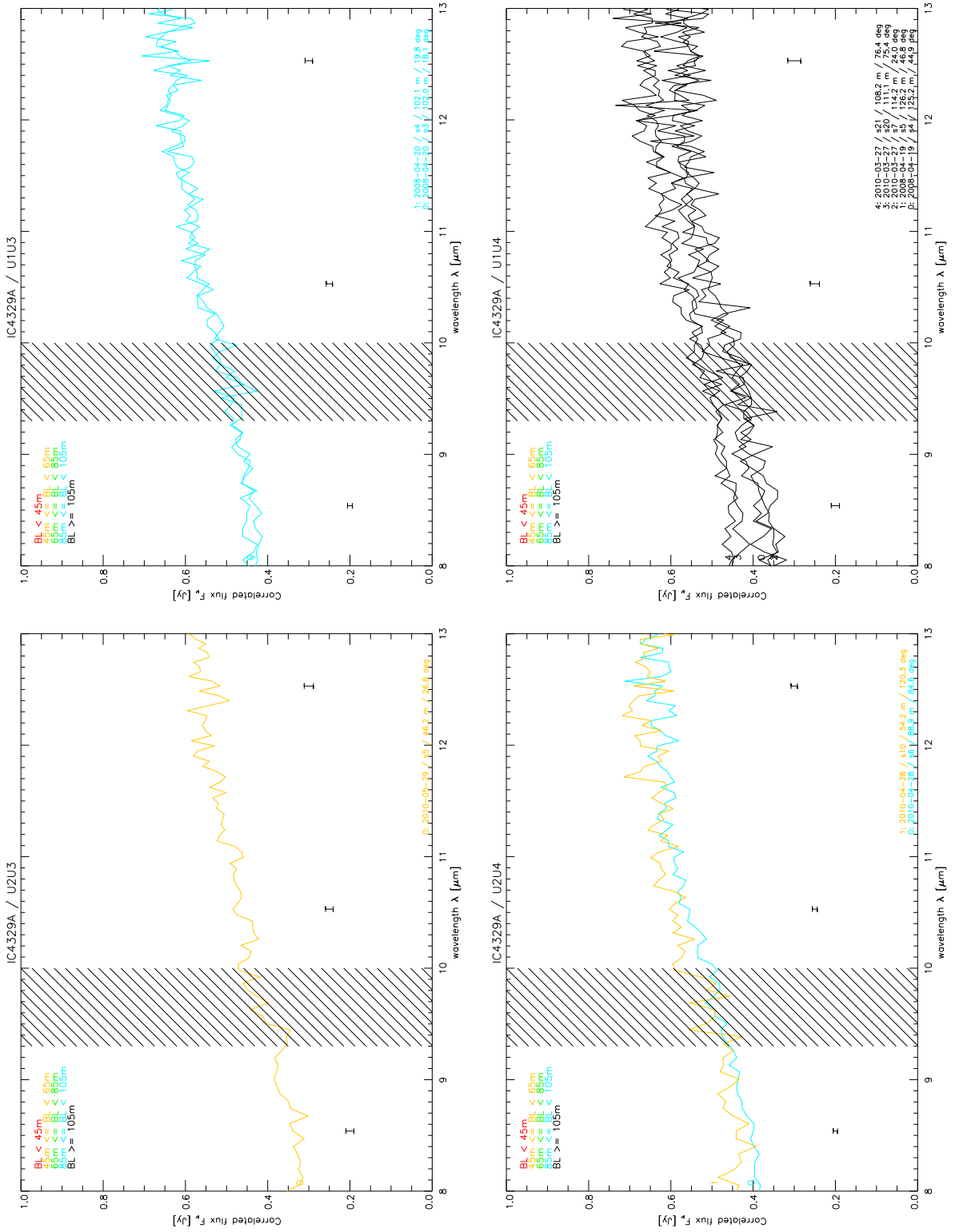

Figure B.10.: **IC 4329 A** — *Continued*

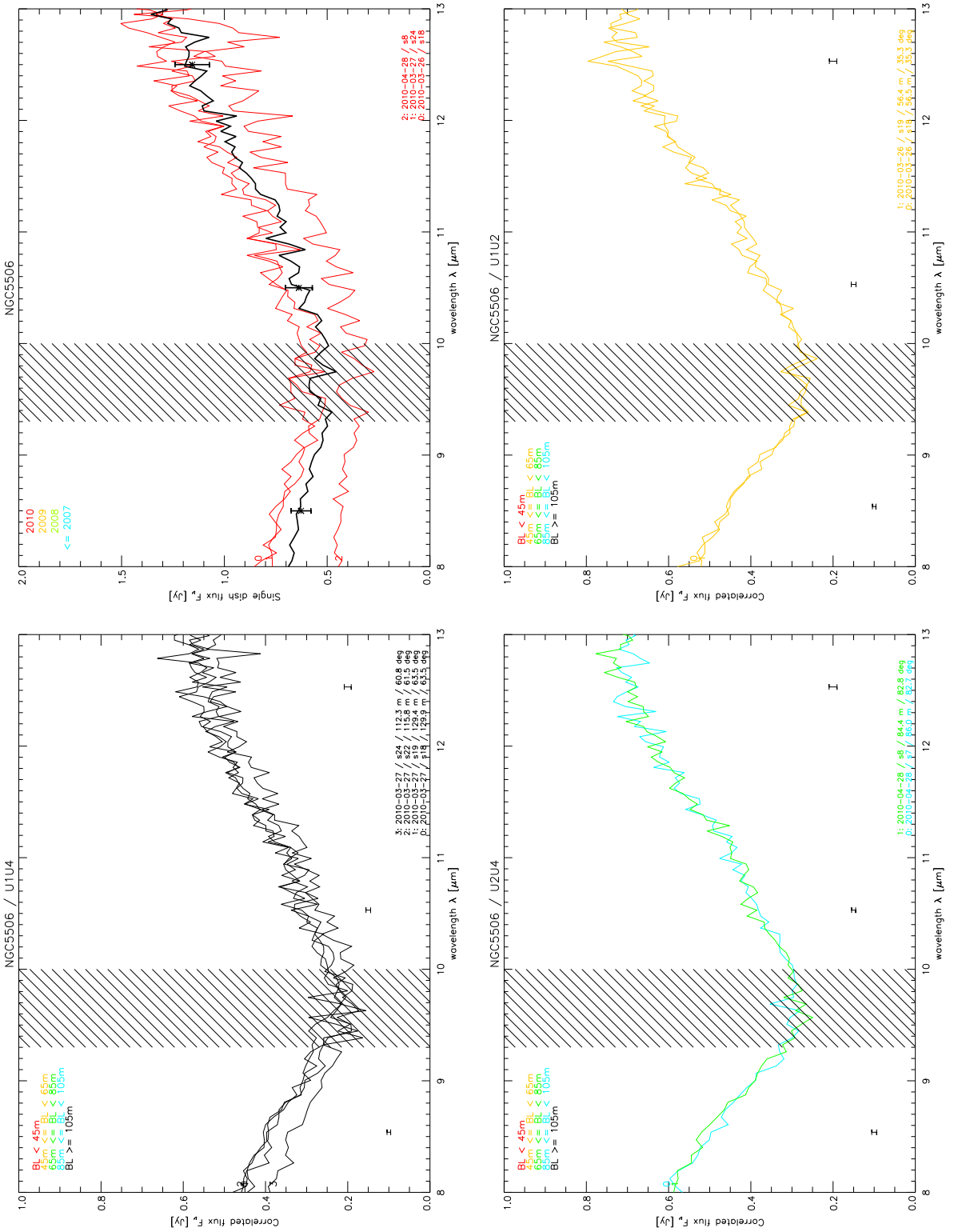

Figure B.11.: Single-dish (top left) and correlated flux spectra of **NGC 5506**, see caption of Figure B.1.

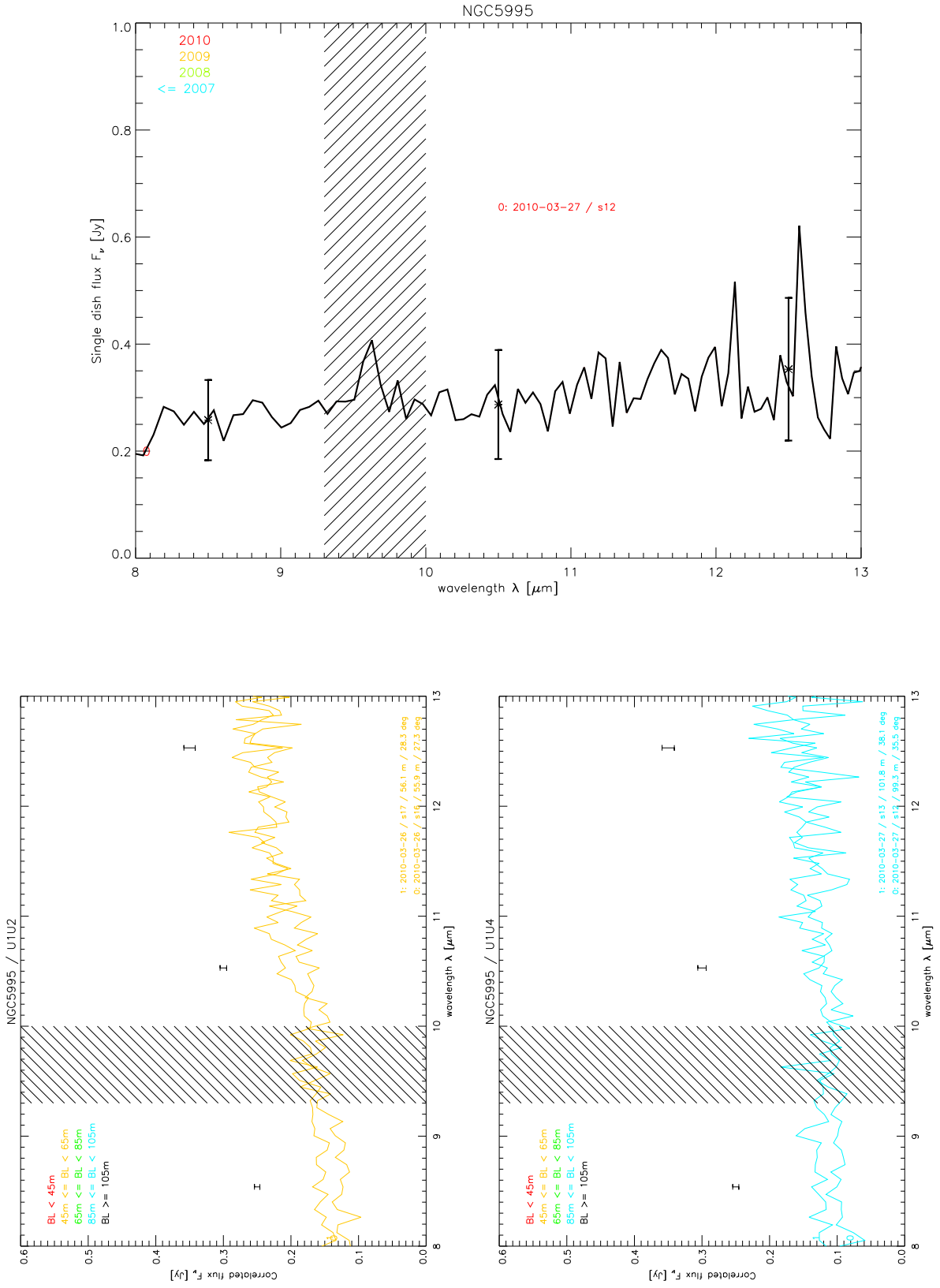

Figure B.12.: Single-dish (top) and correlated flux spectra of **NGC 5995**, see caption of Figure B.1.

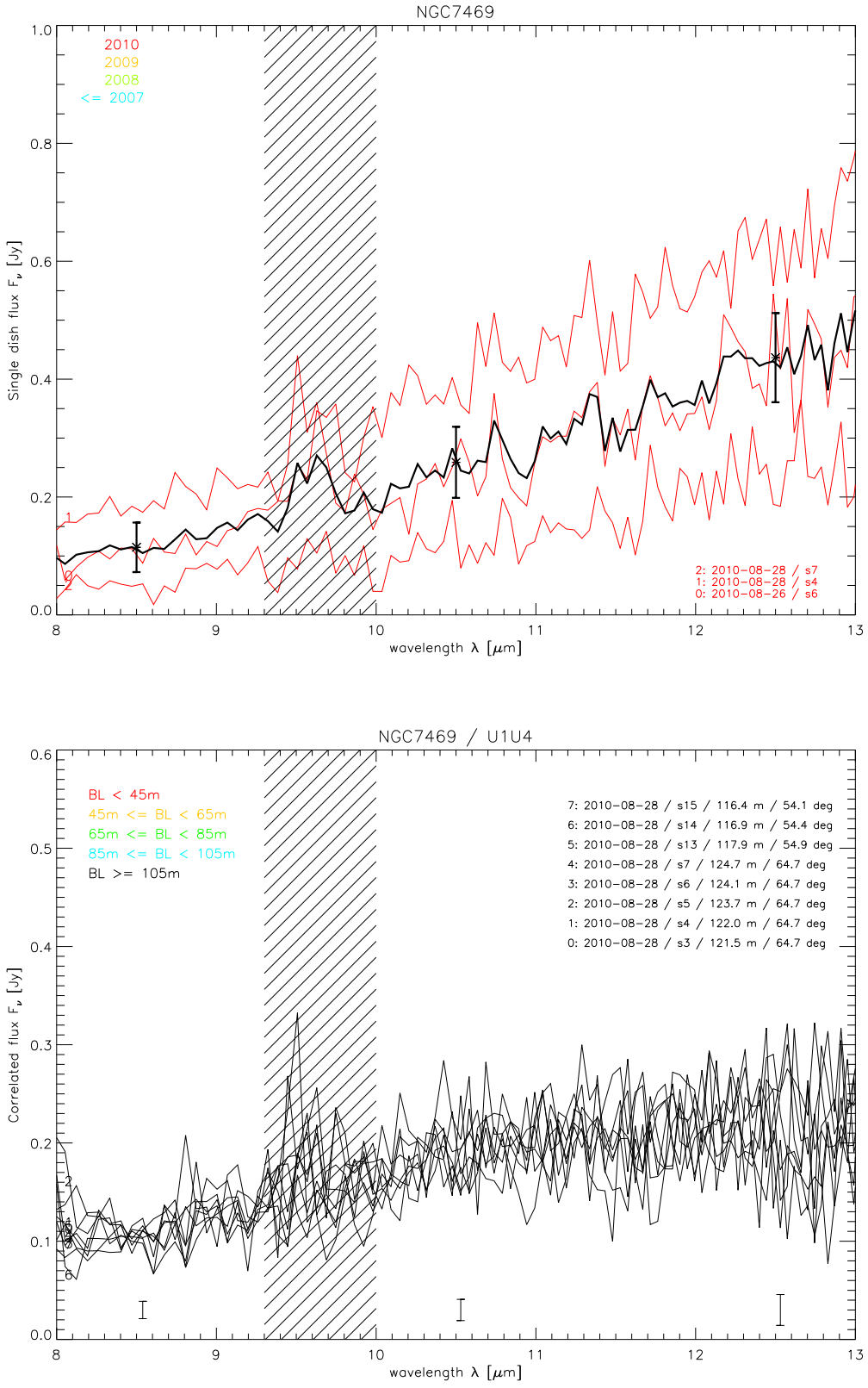

Figure B.13.: Single-dish (top) and correlated flux spectra of **NGC 7469**, see caption of Figure B.1.

B.3. Large Programme visibilities

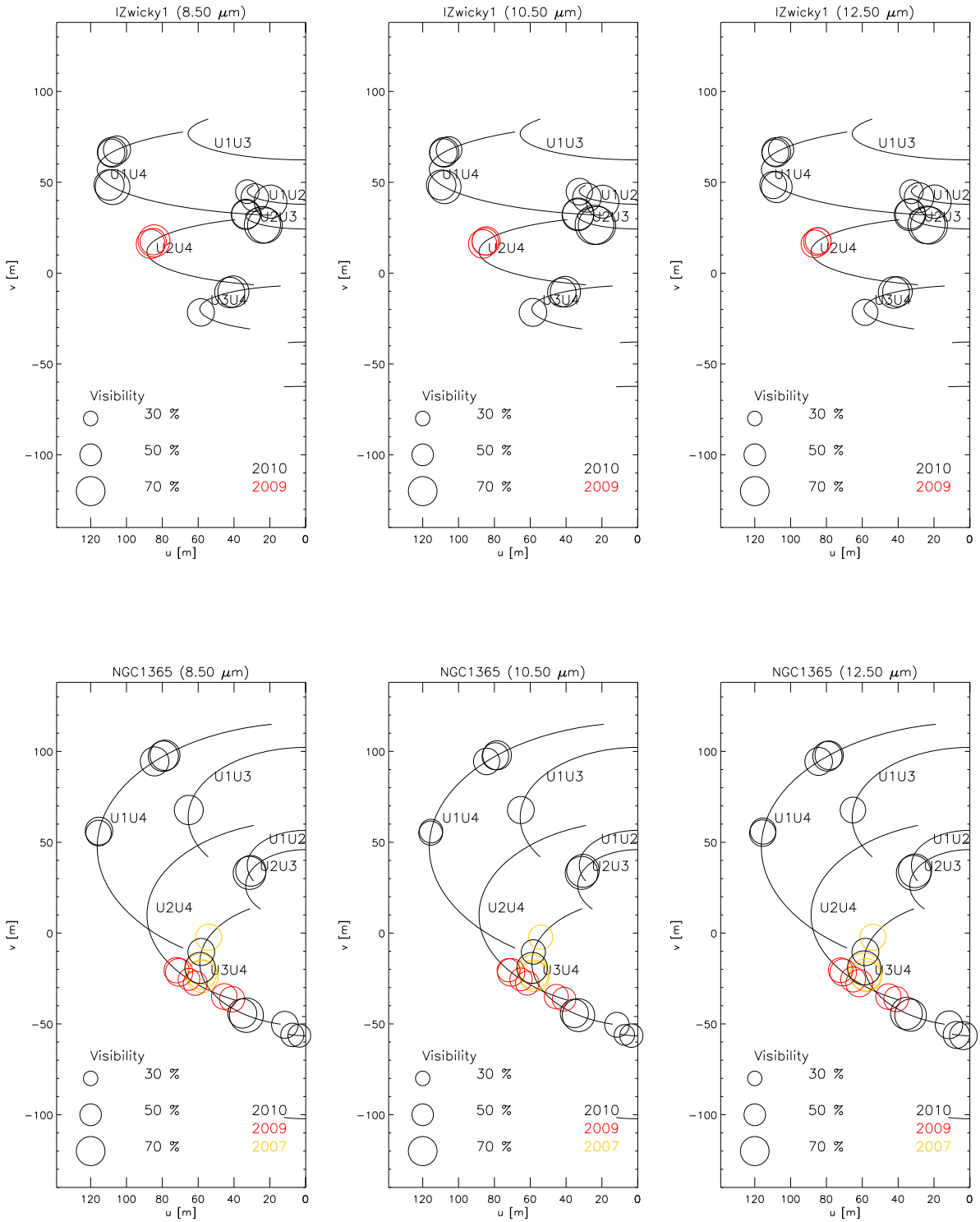

Figure B.14.: Visibilities in the (u, v) plane. Each symbol represents a visibility measurement, the radius denotes the visibility amplitude. Note that only half of the (u, v) plane is shown (the other half is point-symmetric to the one shown). For traditional (u, v) coverage plots, please refer to Figure 4.6. *Continued on next page*

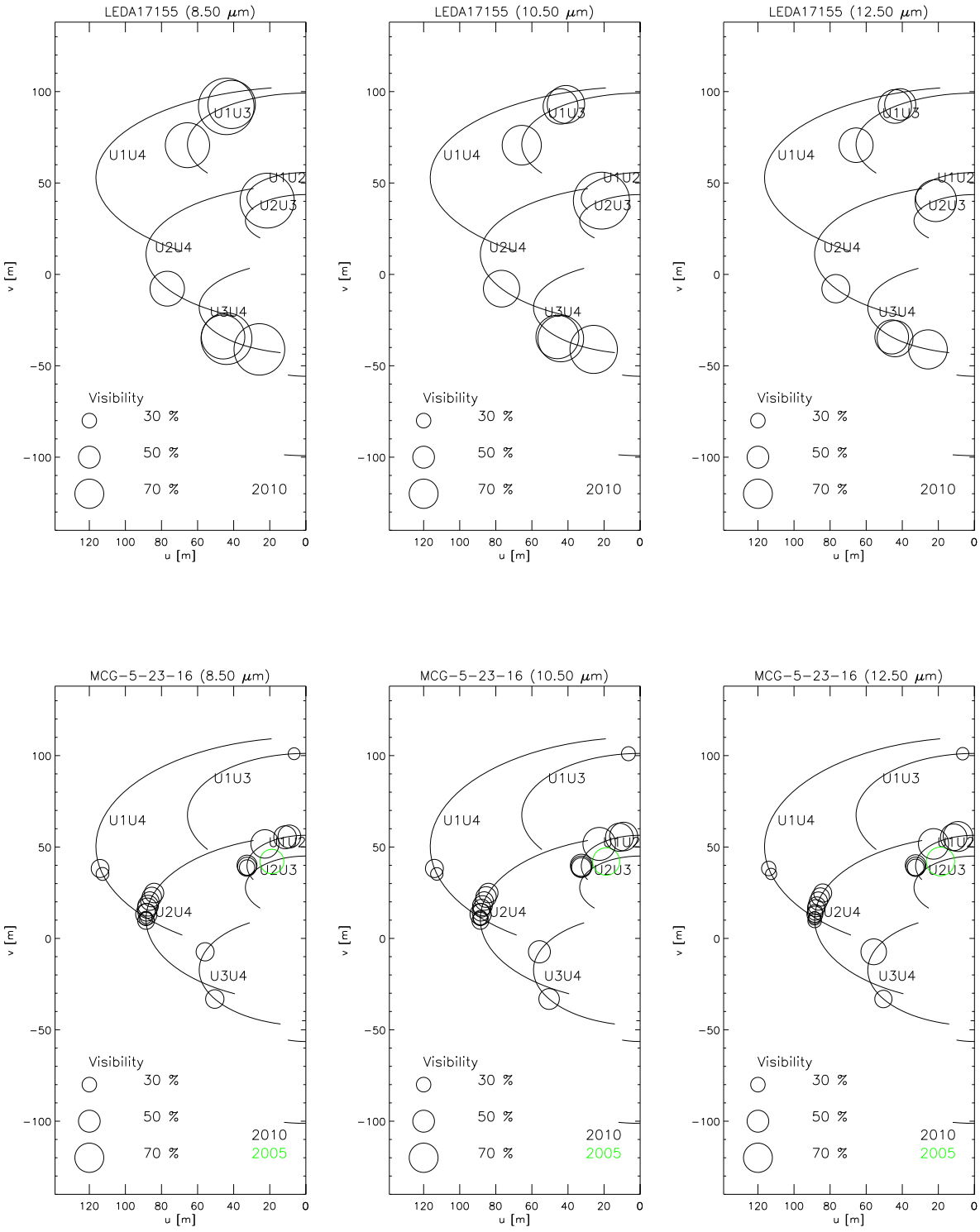

Figure B.14.: — *Continued*

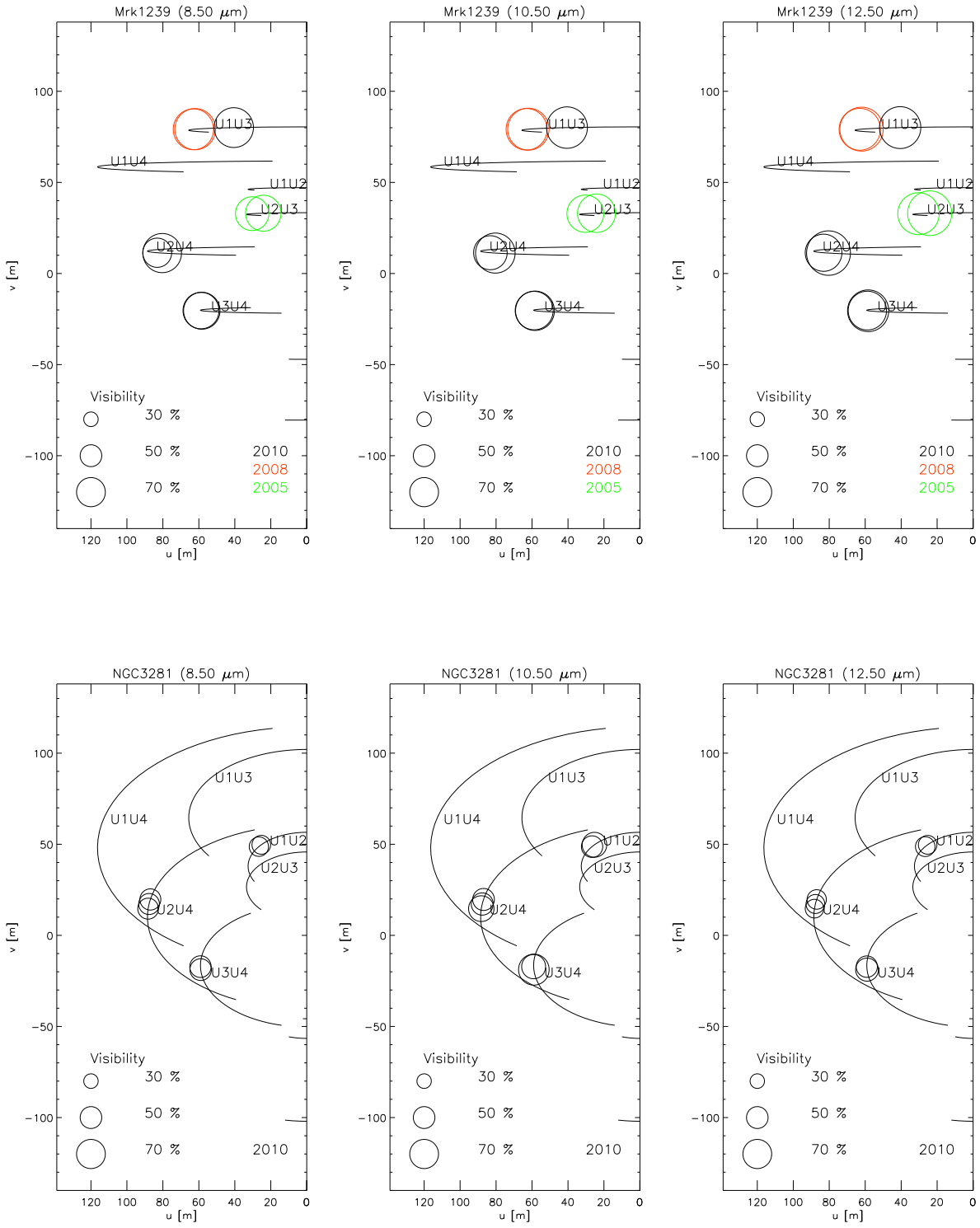

Figure B.14.: — *Continued*

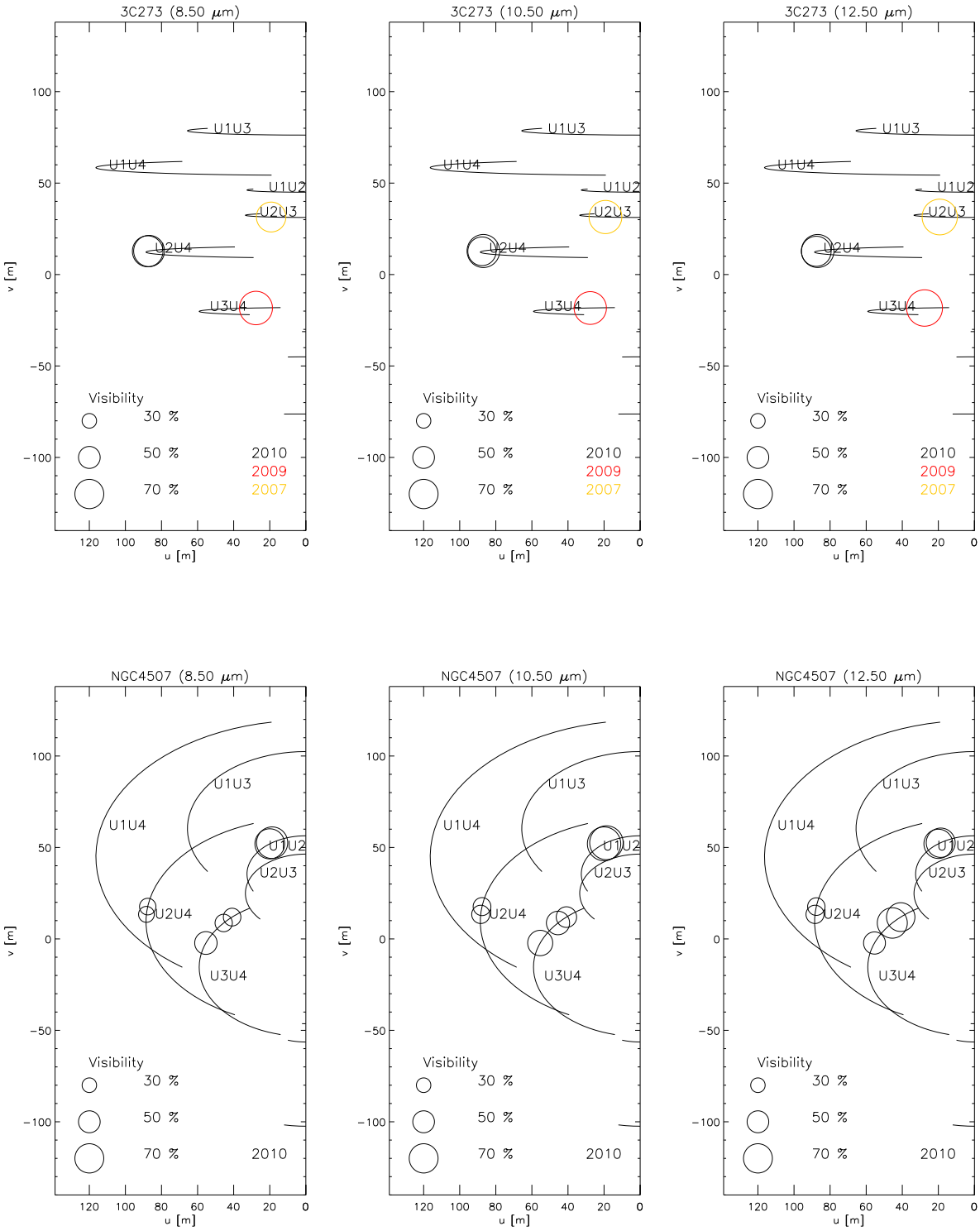

Figure B.14.: — *Continued*

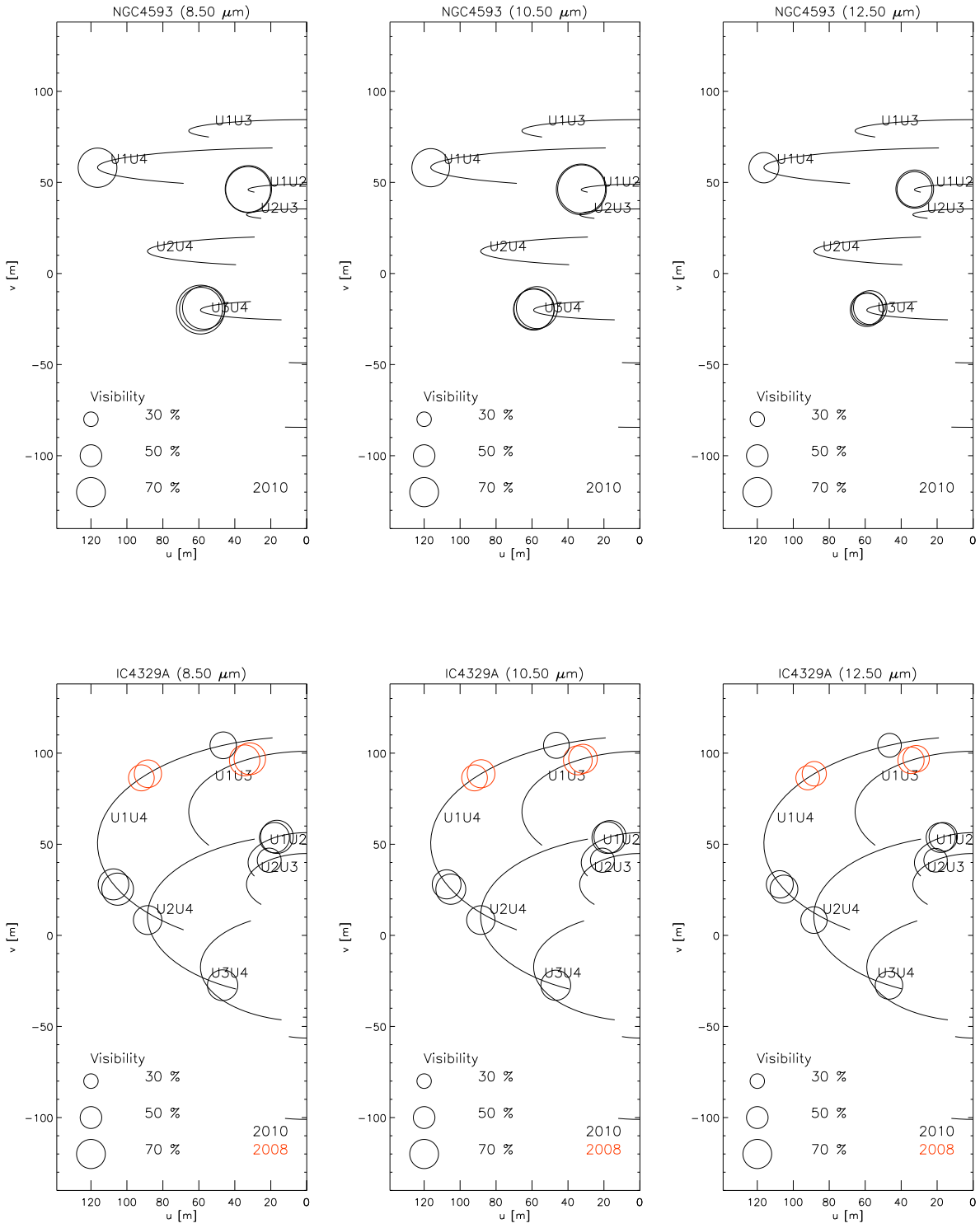

Figure B.14.: — *Continued*

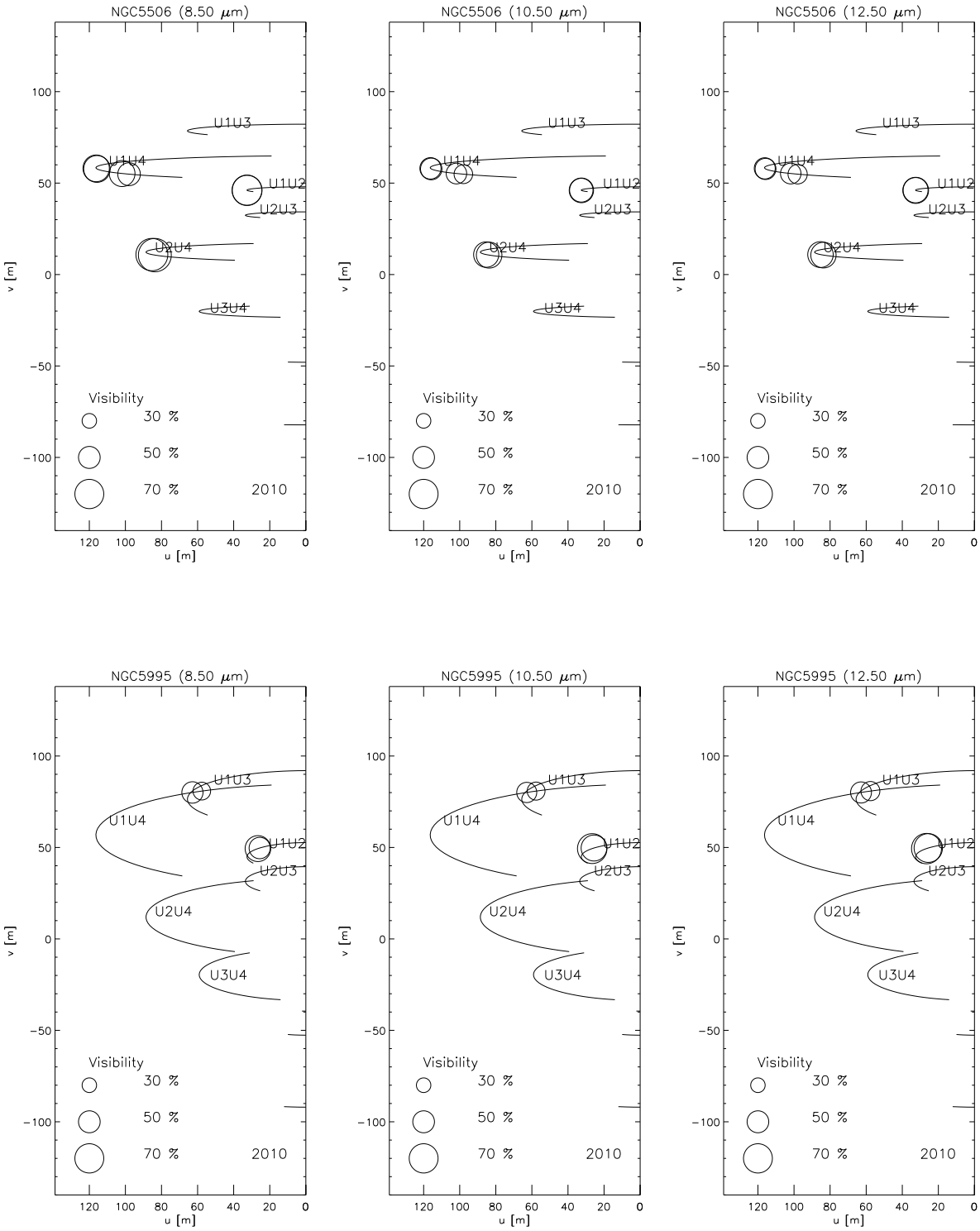

Figure B.14.: — *Continued*

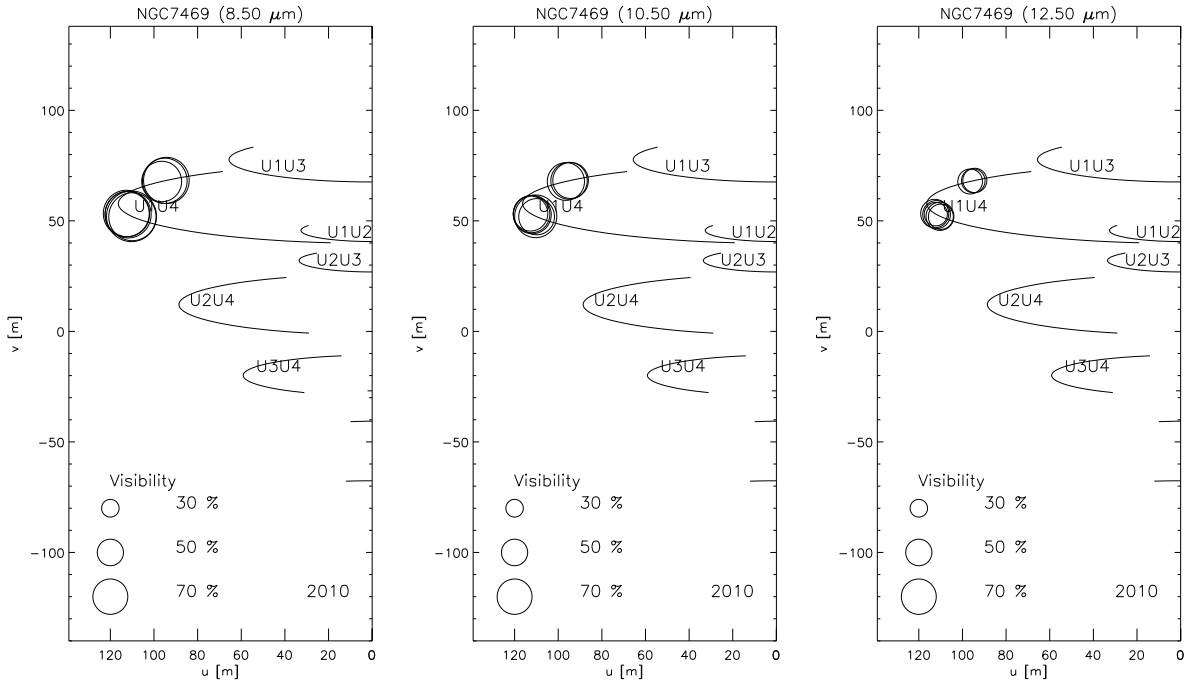

Figure B.14.: — *Continued*

Bibliography

Agudo, I., Gómez, J., Martí, J., Ibáñez, J., Marscher, A. P., Alberdi, A., Aloy, M., & Hardee, P. E. 2001, ApJ, 549, L183

Armstrong, J. T., et al. 1998, ApJ, 496, 550

Arsenault, R., et al. 2003, in Presented at the Society of Photo-Optical Instrumentation Engineers (SPIE) Conference, Vol. 4839, Society of Photo-Optical Instrumentation Engineers (SPIE) Conference Series, ed. P. L. Wizinowich & D. Bonaccini, 174–185

Bakker, E. J., et al. 2003, in Presented at the Society of Photo-Optical Instrumentation Engineers (SPIE) Conference, Vol. 4838, Society of Photo-Optical Instrumentation Engineers (SPIE) Conference Series, ed. W. A. Traub, 905–916

Baldwin, J. E., Haniff, C. A., Mackay, C. D., & Warner, P. J. 1986, Nature, 320, 595

Barlow, R. 1989, Statistics. A guide to the use of statistical methods in the physical sciences (The Manchester Physics Series, New York: Wiley, 1989)

Barvainis, R. 1987, ApJ, 320, 537

Beckert, T., Driebe, T., Hönig, S. F., & Weigelt, G. 2008, A&A, 486, L17

Bentz, M. C., et al. 2006, ApJ, 651, 775

—. 2008, ApJ, 689, L21

Berger, J. P., & Segransan, D. 2007, New Astronomy Review, 51, 576

Best, P. N. 2009, Astronomische Nachrichten, 330, 184

Bester, M., Danchi, W. C., & Townes, C. H. 1990, in Presented at the Society of Photo-Optical Instrumentation Engineers (SPIE) Conference, Vol. 1237, Society of Photo-Optical Instrumentation Engineers (SPIE) Conference Series, ed. J. B. Breckinridge, 40–48

Bland, J., Taylor, K., & Atherton, P. D. 1987, MNRAS, 228, 595

Blandford, R. D., & McKee, C. F. 1982, ApJ, 255, 419

Bolton, J. G., Stanley, G. J., & Slee, O. B. 1949, Nature, 164, 101

Braatz, J. A., Wilson, A. S., & Henkel, C. 1994, ApJ, 437, L99

Brown, R. H., & Twiss, R. Q. 1957, Royal Society of London Proceedings Series A, 242, 300

Bruhweiler, F., & Verner, E. 2008, ApJ, 675, 83

Buchanan, C. L., Gallimore, J. F., O'Dea, C. P., Baum, S. A., Axon, D. J., Robinson, A., Elitzur, M., & Elvis, M. 2006, AJ, 132, 401

Burtscher, L., Jaffe, W., Raban, D., Meisenheimer, K., Tristram, K. R. W., & Röttgering, H. 2009, ApJ, 705, L53

Burtscher, L., Meisenheimer, K., Jaffe, W., Tristram, K. R. W., & Röttgering, H. J. A. 2010, PASA, 27, 490

Capetti, A., et al. 2000, ApJ, 544, 269

Cappellari, M., Neumayer, N., Reunanen, J., van der Werf, P. P., de Zeeuw, P. T., & Rix, H.-W. 2009, MNRAS, 394, 660

Chiaberge, M., Capetti, A., & Celotti, A. 2001, MNRAS, 324, L33

Cohen, M., Walker, R. G., Carter, B., Hammersley, P., Kidger, M., & Noguchi, K. 1999, AJ, 117, 1864

Colavita, M. M., & Wizinowich, P. L. 2003, in Society of Photo-Optical Instrumentation Engineers (SPIE) Conference Series, Vol. 4838, Society of Photo-Optical Instrumentation Engineers (SPIE) Conference Series, ed. W. A. Traub, 79–88

Cornwell, T. J. 2009, A&A, 500, 65

Courvoisier, T. J.-L. 1998, A&A Rev., 9, 1

Cox, A. N., ed. 2000, Allen's astrophysical quantities (New York: AIP Press; Springer)

Díaz-Santos, T., Alonso-Herrero, A., Colina, L., Ryder, S. D., & Knapen, J. H. 2007, ApJ, 661, 149

Dyck, H. M. 2000, in Principles of Long Baseline Stellar Interferometry, ed. P. R. Lawson, 185–+

Elitzur, M., & Shlosman, I. 2006, ApJ, 648, L101

Espada, D., et al. 2009, ApJ, 695, 116

Evans, D. A., Kraft, R. P., Worrall, D. M., Hardcastle, M. J., Jones, C., Forman, W. R., & Murray, S. S. 2004, ApJ, 612, 786

Feain, I. J., et al. 2009, ApJ, 707, 114

Fienup, J. R. 1978, Optics Letters, 3, 27

Galliano, E., Alloin, D., Pantin, E., Lagage, P. O., & Marco, O. 2005, A&A, 438, 803

Gallo, L. C., Brandt, W. N., Costantini, E., Fabian, A. C., Iwasawa, K., & Papadakis, I. E. 2007, MNRAS, 377, 391

Gandhi, P., Horst, H., Smette, A., Hönig, S., Comastri, A., Gilli, R., Vignali, C., & Duschl, W. 2009, A&A, 502, 457

Gebhardt, K., Adams, J., Richstone, D., Lauer, T. R., Faber, S. M., Gültekin, K., Murphy, J., & Tremaine, S. 2011, ApJ, 729, 119

Glass, I. S. 1999, Handbook of Infrared Astronomy (Cambridge University Press)

Glindemann, A., et al. 2000a, in Society of Photo-Optical Instrumentation Engineers (SPIE) Conference Series, Vol. 4006, Society of Photo-Optical Instrumentation Engineers (SPIE) Conference Series, ed. P. Léna & A. Quirrenbach, 2–12

Glindemann, A., Hippler, S., Berkefeld, T., & Hackenberg, W. 2000b, Experimental Astronomy, 10, 5

Gorjian, V., Werner, M. W., Jarrett, T. H., Cole, D. M., & Ressler, M. E. 2004, ApJ, 605, 156

Greene, J. E., et al. 2010, ApJ, 723, 409

Guainazzi, M., Bianchi, S., Matt, G., Dadina, M., Kaastra, J., Malzac, J., & Risaliti, G. 2010, MNRAS, 406, 2013

Haas, M., Siebenmorgen, R., Pantin, E., Horst, H., Smette, A., Käufl, H.-U., Lagage, P.-O., & Chini, R. 2007, A&A, 473, 369

Hajian, A. R., et al. 1998, ApJ, 496, 484

Haniff, C. 2007, New Astronomy Review, 51, 565

Haniff, C. A., et al. 2000, in Society of Photo-Optical Instrumentation Engineers (SPIE) Conference Series, Vol. 4006, Society of Photo-Optical Instrumentation Engineers (SPIE) Conference Series, ed. P. Léna & A. Quirrenbach, 627–633

Hao, L., et al. 2005, ApJ, 625, L75

Hardcastle, M. J., Cheung, C. C., Feain, I. J., & Stawarz, Ł. 2009, MNRAS, 393, 1041

Hardcastle, M. J., Worrall, D. M., Birkinshaw, M., & Canosa, C. M. 2003a, MNRAS, 338, 176

Hardcastle, M. J., Worrall, D. M., Kraft, R. P., Forman, W. R., Jones, C., & Murray, S. S. 2003b, ApJ, 593, 169

Harris, G. L. H., Rejkuba, M., & Harris, W. E. 2010, PASA, 27, 457

Hecht, E. 2001, Optics 4th edition (Addison Wesley)

Henkel, C., Peck, A. B., Tarchi, A., Nagar, N. M., Braatz, J. A., Castangia, P., & Moscadelli, L. 2005, A&A, 436, 75

HESS Collaboration: F. Aharonian. 2009, ApJ, 695, L40

Högbom, J. A. 1974, A&AS, 15, 417

Hönig, S. F., Beckert, T., Ohnaka, K., & Weigelt, G. 2006, A&A, 452, 459

Horst, H., Duschl, W. J., Gandhi, P., & Smette, A. 2009, A&A, 495, 137

Horst, H., Gandhi, P., Smette, A., & Duschl, W. J. 2008, A&A, 479, 389

Israel, F. P. 1998, A&A Rev., 8, 237

Jaffe, W., et al. 2004, Nature, 429, 47

Jaffe, W. J. 2004, in Society of Photo-Optical Instrumentation Engineers (SPIE) Conference Series, Vol. 5491, Society of Photo-Optical Instrumentation Engineers (SPIE) Conference Series, ed. W. A. Traub, 715–+

Kaeufl, H. U., Bouchet, P., van Dijsseldonk, A., & Weilenmann, U. 1991, Experimental Astronomy, 2, 115

Kishimoto, M., Hönig, S. F., Beckert, T., & Weigelt, G. 2007, A&A, 476, 713

Kishimoto, M., Hönig, S. F., Tristram, K. R. W., & Weigelt, G. 2009, A&A, 493, L57

Köhler, R., & Jaffe, W. 2008, in The Power of Optical/IR Interferometry: Recent Scientific Results and 2nd Generation, ed. A. Richichi, F. Delplancke, F. Paresce, & A. Chelli, 569–+

Komossa, S. 2008, in Revista Mexicana de Astronomia y Astrofisica Conference Series, Vol. 32, Revista Mexicana de Astronomia y Astrofisica Conference Series, 86–92

Kormendy, J., Cornell, M. E., Block, D. L., Knapen, J. H., & Allard, E. L. 2006, ApJ, 642, 765

Koshida, S., et al. 2009, ApJ, 700, L109

Krabbe, A., Böker, T., & Maiolino, R. 2001, ApJ, 557, 626

Kraft, R. P., et al. 2000, ApJ, 531, L9

Labeyrie, A. 1970, A&A, 6, 85

Landt, H., Bentz, M. C., Peterson, B. M., Elvis, M., Ward, M. J., Korista, K. T., & Karovska, M. 2011, ArXiv e-prints

Lawrence, A. 1991, MNRAS, 252, 586

Leinert, C., et al. 2003, Ap&SS, 286, 73

Lindblad, P. O. 1999, A&A Rev., 9, 221

Lord, S. D. 1992, A New Software Tool for Computing Earth's Atmospheric Transmission of Near- and Far-Infrared Radiation, Tech. Rep. 103957, NASA

Lumsden, S. L., Heisler, C. A., Bailey, J. A., Hough, J. H., & Young, S. 2001, MNRAS, 327, 459

Maiolino, R., Marconi, A., Salvati, M., Risaliti, G., Severgnini, P., Oliva, E., La Franca, F., & Vanzi, L. 2001, A&A, 365, 28

Maiolino, R., & Rieke, G. H. 1995, ApJ, 454, 95

Malin, D. F., Quinn, P. J., & Graham, J. A. 1983, ApJ, 272, L5

Marconi, A., Schreier, E. J., Koekemoer, A., Capetti, A., Axon, D., Macchetto, D., & Caon, N. 2000, ApJ, 528, 276

Markowitz, A. 2009, ApJ, 698, 1740

Marquardt, D. 1963, SIAM Journal on Applied Mathematics, 11, 431

Mason, R., Wong, A., Geballe, T., Volk, K., Hayward, T., Dillman, M., Fisher, R. S., & Radomski, J. 2008, in Presented at the Society of Photo-Optical Instrumentation Engineers (SPIE) Conference, Vol. 7016, Society of Photo-Optical Instrumentation Engineers (SPIE) Conference Series

Matt, G., Bianchi, S., D'Ammando, F., & Martocchia, A. 2004, A&A, 421, 473

Mazzarella, J. M., & Boroson, T. A. 1993, ApJS, 85, 27

Meisenheimer, K., et al. 2007, A&A, 471, 453

Michelson, A. A., & Pease, F. G. 1921, ApJ, 53, 249

Minezaki, T., Yoshii, Y., Kobayashi, Y., Enya, K., Suganuma, M., Tomita, H., Aoki, T., & Peterson, B. A. 2004, ApJ, 600, L35

Moran, E. C., Barth, A. J., Kay, L. E., & Filippenko, A. V. 2000, ApJ, 540, L73

Morganti, R. 2010, PASA, 27, 463

Müller, C. 2010, Master's thesis, Friedrich-Alexander-Universität Erlangen-Nürnberg

Müller, C., Kadler, M., Ojha, R., Boeck, M., & Wilms, J. 2010, in COSPAR, Plenary Meeting, Vol. 38, 38th COSPAR Scientific Assembly, 2310–+

Mundell, C. G., Wrobel, J. M., Pedlar, A., & Gallimore, J. F. 2003, ApJ, 583, 192

Nagar, N. M., Oliva, E., Marconi, A., & Maiolino, R. 2002, A&A, 391, L21

Nemmen, R. S., Bonatto, C., & Storchi-Bergmann, T. 2010, ApJ, 722, 281

Neugebauer, G., Graham, J. R., Soifer, B. T., & Matthews, K. 1990, AJ, 99, 1456

Neugebauer, G., Oke, J. B., Becklin, E. E., & Matthews, K. 1979, ApJ, 230, 79

Neumayer, N., Cappellari, M., Reunanen, J., Rix, H.-W., van der Werf, P. P., de Zeeuw, P. T., & Davies, R. I. 2007, ApJ, 671, 1329

Panessa, F., & Bassani, L. 2002, A&A, 394, 435

Peng, E. W., Ford, H. C., Freeman, K. C., & White, R. L. 2002, AJ, 124, 3144

Peterson, B. M. 1993, PASP, 105, 247

Peterson, B. M., et al. 2004, ApJ, 613, 682

Pier, E. A., & Krolik, J. H. 1992, ApJ, 401, 99

Pott, J., Malkan, M. A., Elitzur, M., Ghez, A. M., Herbst, T. M., Schödel, R., & Woillez, J. 2010, ApJ, 715, 736

Prieto, M. A., Reunanen, J., Tristram, K. R. W., Neumayer, N., Fernandez-Ontiveros, J. A., Orienti, M., & Meisenheimer, K. 2010, MNRAS, 402, 724

PROCESSING, I., & ANALYSIS CENTER (IPAC), C. 2011, The Near, mid and far infrared

Przygodda, F. 2004, PhD thesis, Max-Planck-Institut für Astronomie

Quillen, A. C., et al. 2008, MNRAS, 384, 1469

Quillen, A. C., Brookes, M. H., Keene, J., Stern, D., Lawrence, C. R., & Werner, M. W. 2006, ApJ, 645, 1092

Quirrenbach, A. 2000, in Principles of Long Baseline Stellar Interferometry, ed. P. R. Lawson, 71–+

Quirrenbach, A. 2001, ARA&A, 39, 353

Raban, D., Heijligers, B., Röttgering, H., Meisenheimer, K., Jaffe, W., Käufl, H. U., & Henning, T. 2008, A&A, 484, 341

Raban, D., Jaffe, W., Röttgering, H., Meisenheimer, K., & Tristram, K. R. W. 2009, MNRAS, 394, 1325

Radomski, J. T., et al. 2008, ApJ, 681, 141

Radomski, J. T., Piña, R. K., Packham, C., Telesco, C. M., De Buizer, J. M., Fisher, R. S., & Robinson, A. 2003, ApJ, 587, 117

Ratzka, T. 2005, PhD thesis, Max-Planck-Institut für Astronomie

Ravi, V., Wishnow, E. H., Lockwood, S., & Townes, C. H. 2010, ArXiv e-prints

Read, A. M., & Pietsch, W. 1998, A&A, 336, 855

Reunanen, J., Prieto, M. A., & Siebenmorgen, R. 2010, MNRAS, 402, 879

Riffel, R. A., Storchi-Bergmann, T., & McGregor, P. J. 2009, ApJ, 698, 1767

Risaliti, G., Elvis, M., Fabbiano, G., Baldi, A., Zezas, A., & Salvati, M. 2007, ApJ, 659, L111

Risaliti, G., Maiolino, R., & Salvati, M. 1999, ApJ, 522, 157

Robberto, M., & Herbst, T. M. 1998, in Presented at the Society of Photo-Optical Instrumentation Engineers (SPIE) Conference, Vol. 3354, Society of Photo-Optical Instrumentation Engineers (SPIE) Conference Series, ed. A. M. Fowler, 711–719

Robson, E. I., et al. 1993, MNRAS, 262, 249

Rodríguez-Ardila, A., & Mazzalay, X. 2006, MNRAS, 367, L57

Rothschild, R. E., Markowitz, A., Rivers, E., Suchy, S., Pottschmidt, K., Kadler, M., Mueller, C., & Wilms, J. 2011, ArXiv e-prints

Saha, S. K. 1999, Indian Journal of Physics Section B, 73, 553

Sales, D. A., Pastoriza, M. G., & Riffel, R. 2010, ArXiv e-prints

Sanders, D. B., Soifer, B. T., Elias, J. H., Madore, B. F., Matthews, K., Neugebauer, G., & Scoville, N. Z. 1988, ApJ, 325, 74

Sandqvist, A. 1999, A&A, 343, 367

Sandqvist, A., Joersaeter, S., & Lindblad, P. O. 1995, A&A, 295, 585

Sarazin, M., Melnick, J., Navarrete, J., & Lombardi, G. 2008, The Messenger, 132, 11

Schartmann, M., Meisenheimer, K., Camenzind, M., Wolf, S., & Henning, T. 2005, A&A, 437, 861

Schartmann, M., Meisenheimer, K., Camenzind, M., Wolf, S., Tristram, K. R. W., & Henning, T. 2008, A&A, 482, 67

Schartmann, M., Meisenheimer, K., Klahr, H., Camenzind, M., Wolf, S., & Henning, T. 2009, MNRAS, 393, 759

Scharwächter, J., Eckart, A., Pfalzner, S., Moultaka, J., Straubmeier, C., & Staguhn, J. G. 2003, A&A, 405, 959

Scharwächter, J., Eckart, A., Pfalzner, S., Saviane, I., & Zuther, J. 2007, A&A, 469, 913

Schinnerer, E., Eckart, A., & Tacconi, L. J. 1998, ApJ, 500, 147

Schmidt, M. 1963, Nature, 197, 1040

Schreier, E. J., et al. 1998, ApJ, 499, L143+

Schuller, P. 2002, PhD thesis, Max-Planck-Institut für Astronomie

Schweitzer, M., et al. 2008, ApJ, 679, 101

Scoville, N. Z., et al. 2000, AJ, 119, 991

Shakura, N. I., & Syunyaev, R. A. 1973, A&A, 24, 337

Siebenmorgen, R., Krügel, E., & Spoon, H. W. W. 2004, A&A, 414, 123

Simpson, C. 1998, MNRAS, 297, L39

—. 2005, MNRAS, 360, 565

Soifer, B. T., Bock, J. J., Marsh, K., Neugebauer, G., Matthews, K., Egami, E., & Armus, L. 2003, AJ, 126, 143

Soldi, S., et al. 2008, A&A, 486, 411

Spoon, H. W. W., Keane, J. V., Tielens, A. G. G. M., Lutz, D., Moorwood, A. F. M., & Laurent, O. 2002, A&A, 385, 1022

Storchi-Bergmann, T., Wilson, A. S., & Baldwin, J. A. 1992, ApJ, 396, 45

Struve, C., Oosterloo, T. A., Morganti, R., & Saripalli, L. 2010, A&A, 515, A67+

Suganuma, M., et al. 2006, ApJ, 639, 46

Surace, J. A., Sanders, D. B., Vacca, W. D., Veilleux, S., & Mazzarella, J. M. 1998, ApJ, 492, 116

Swain, M., et al. 2003, ApJ, 596, L163

Tallon-Bosc, I., et al. 2008, in Presented at the Society of Photo-Optical Instrumentation Engineers (SPIE) Conference, Vol. 7013, Society of Photo-Optical Instrumentation Engineers (SPIE) Conference Series

ten Brummelaar, T. A., Bagnuolo, W. G., McAlister, H. A., Ridgway, S. T., Sturmann, L., Sturmann, J., & Turner, N. H. 2000, in Society of Photo-Optical Instrumentation Engineers (SPIE) Conference Series, Vol. 4006, Society of Photo-Optical Instrumentation Engineers (SPIE) Conference Series, ed. P. Léna & A. Quirrenbach, 564–573

Teng, S. H., et al. 2009, ApJ, 691, 261

Tingay, S. J., et al. 1998, AJ, 115, 960

Tingay, S. J., & Lenc, E. 2009, AJ, 138, 808

Tingay, S. J., Preston, R. A., & Jauncey, D. L. 2001, AJ, 122, 1697

Townes, C. H. 2000, in Principles of Long Baseline Stellar Interferometry, ed. P. R. Lawson, 59–+

Tristram, K. R. W. 2007, PhD thesis, Max-Planck-Institut für Astronomie, Königstuhl 17, 69117 Heidelberg, Germany

Tristram, K. R. W., et al. 2007, A&A, 474, 837

—. 2009, A&A, 502, 67

Tristram, K. R. W., & Schartmann, M. 2011, A&A, to be published

Türler, M., et al. 2006, A&A, 451, L1

Tuthill, P., et al. 2010, in Presented at the Society of Photo-Optical Instrumentation Engineers (SPIE) Conference, Vol. 7735, Society of Photo-Optical Instrumentation Engineers (SPIE) Conference Series

Tuthill, P. G., Monnier, J. D., Danchi, W. C., Wishnow, E. H., & Haniff, C. A. 2000, PASP, 112, 555

Ulrich, M.-H. 2000, A&A Rev., 10, 135

van der Wolk, G., Barthel, P. D., Peletier, R. F., & Pel, J. W. 2010, A&A, 511, A64+

Veilleux, S., Kim, D., Sanders, D. B., Mazzarella, J. M., & Soifer, B. T. 1995, ApJS, 98, 171

Veron, P., Lindblad, P. O., Zuiderwijk, E. J., Veron, M. P., & Adam, G. 1980, A&A, 87, 245

Véron-Cetty, M.-P., & Véron, P. 2006, A&A, 455, 773

Vignali, C., & Comastri, A. 2002, A&A, 381, 834

Weaver, K. A., Yaqoob, T., Mushotzky, R. F., Nousek, J., Hayashi, I., & Koyama, K. 1997, ApJ, 474, 675

Weedman, D. W., et al. 2005, ApJ, 633, 706

Weigelt, G. P. 1977, Optics Communications, 21, 55

Weiß, A., Kovács, A., Güsten, R., Menten, K. M., Schuller, F., Siringo, G., & Kreysa, E. 2008, A&A, 490, 77

Whysong, D., & Antonucci, R. 2004, ApJ, 602, 116

Young, S., Hough, J. H., Efstathiou, A., Wills, B. J., Bailey, J. A., Ward, M. J., & Axon, D. J. 1996, MNRAS, 281, 1206